PhD degree in Molecular Medicine (curriculum in Molecular Oncology)

European School of Molecular Medicine (SEMM),

University of Milan and University of Naples "Federico II"

Settore disciplinare: BIO/10

Novel IRSp53 (Insulin Receptor Substrate protein of 53 kDa) functions in actin capping, filopodia formation and polarity establishment

Sara Bisi

IFOM, Milan

Matricola n. R09843

Supervisor: Prof. Giorgio Scita

IFOM, Milan

Added Supervisor: Dr. Marina Mapelli

IEO, Milan

Anno accademico 2015-2016

Table of contents

List of abbreviations

3-D	three-dimensional
ABBA	Actin-bundling protein with BAIAP2 homology
ABI1	Abl-interactor 1
AMIS	apical membrane initiation site
aPKC	atypical protein kinase C
ARP2/3	Actin-related protein 2/3
BAIAP2	Brain-specific angiogenesis inhibitor 1-associated protein 2
BAR	Bin-Amphiphysin-Rvs167
CACO2	human colorectal adenocarcinoma cells
CDC42	cell division control protein 42 homolog
COCO	coiled-coil
CP	capping protein
CRB	Crumbs
CRIB	CDC42/Rac interactive binding
DLG	Disks large homolog
DLS	dynamic light scattering
ECM	extracellular matrix
ENA	Enabled
EPS8	Epidermal growth factor receptor kinase substrate 8
ER	endoplasmic reticulum
F-ACTIN	filamentous actin
F-BAR	FCH-BAR, Fes/CIP4 homology BAR
FAB	F-actin binding domain
FAK	focal adhesion kinase

FH1	formin homology 1 domain
FH2	formin homology 2 domain
FMNL3	formin-like 3
G-ACTIN	globular actin
GAB	G-actin binding domain
GAP	GTPase activating protein
GDI	guanine-nucleotide dissociation inhibitor
GEF	guanine nucleotide exchange factor
GUV	giant unilamellar vesicles
HUVEC	human umbilical vein endothelial cells
I-BAR	inverted BAR
IRSp53	Insulin Receptor Substrate protein of 53 kDa
IRTK	Insulin Receptor Tyrosine Kinase substrate
KD	knock down
KO	knock out
LGL	Lethal giant larvae
LIN7	Protein lin-7 homolog
MDCK	Madin Darby canine kidney cells
MEF	mouse embryonic fibroblast
MENA	Mammalian enabled
MIM	Missing-in-metastasis
N-BAR	N-terminal amphipathic helix BAR
NMDAR	N-methyl-D-aspartate receptor
NPF	nucleation-promoting factor
PALS1	Protein associated with LIN7
PAP	pre apical patch

PAR	partitioning defective
PATJ	PALS1-associated tight-junction homolog
PDZ	PSD95-DLG1-ZO-1
PH	pleckstrin homology
PINKBAR	Planar intestinal and kidney-specific BAR domain protein
PIP_2	phosphatidylinositol-(4,5)-bisphosphate
PIP_3	phosphatidylinositol-(3,4,5)-trisphosphate
PK	protein kinase
PP	protein phosphatase
PR	proline-rich
PRD	proline-rich domain
PSD	post synaptic density
PTB	phospho-tyrosine binding
ROCK	RHO-associated protein kinase
SDS-PAGE	SDS polyacrylamide gel electrophoresis
SH3	SRC homology 3 domain
SILAC	stable isotope labelling with amino acids in cell culture
SOS1	Son of sevenless homolog 1
TIRF	total internal reflection fluorescence
VASP	Vasodilator-stimulated phosphoprotein
WCA	WH2 Central Acidic
WH1	WASP homology domain 1
WH2	WASP homology domain 2
WHD	WAVE homology domain
WT	wild type
ZO-1	Zonula occludens protein 1

Figure index

Abstract

IRSp53 (Insulin Receptor Substrate protein of 53 kDa) is a multidomain scaffolding protein that possesses an inverted BAR (Bin-Amphiphysin-Rvs167) domain (responsible for protein dimerization and membrane deformation), a partial CRIB motif (for the interaction with active CDC42), a SH3 domain (through it binds actin-related proteins, such as the capping protein EPS8) and additional protein interaction modules at the C-terminus.

In this thesis we have studied a previously unknown capping role of IRSp53 and the functional consequences of its interaction with VASP (Vasodilator-stimulated phosphoprotein). In particular, we showed that following CDC42 binding and activation, IRSp53 is able to recruit and cluster VASP both *in vitro* and on the plasma membrane, thus fostering VASP processive elongation activity. The elongation of actin filaments by VASP, together with the membrane-deforming ability of IRSp53, combine to promote filopodia initiation downstream of CDC42. Thus, IRSp53 is essential for coordinating these activities *in vitro* and in cells in culture. Indeed, mouse embryonic fibroblasts (MEFs) devoid of IRSp53 form a reduced number of filopodia and are impaired in directional migration and wound healing. In keeping with a critical role of IRSp53 in these processes, we further showed that IRSp53 null mice are severely impaired in wound healing.

In the second part of this thesis, an IRSp53 role in the polarity program of epithelial cells was investigated. Few scattered reports had provided some evidence that: i) IRSp53 binds the polarity protein LIN7; ii) IRSp53 knock down affects the morphogenesis of MDCK (Madin Darby canine kidney) cysts by acting downstream of the polarity-regulating kinase PAR1b. The molecular and cellular processes controlled by IRSp53 in polarity remain, however, ill defined. Here we showed that

IRSp53 is apically localized in 3-D cyst models of epithelial cells, and IRSp53 depletion leads to a multilumen phenotype also in Caco2 (human colorectal adenocarcinoma) spheroids. The correct morphogenesis of Caco2 spheroids depends on the intact function of both I-BAR, CRIB and SH3 domains of IRSp53. Moreover, using MDCK cysts as a model system, we noted that IRSp53 is enriched early at the prospective lumen initiation site (called AMIS, apical membrane initiation site), even before the apical marker podocalyxin. This latter protein is known to be a critical factor in lumenogenesis. Finally, IRSp53 removal affects podocalyxin localization in MDCK cysts at the early stages.

We speculate that IRSp53 might be involved in the trafficking of the apical protein podocalyxin, and we are currently investigating the molecular mechanism responsible for this putative role. We are also exploring whether IRSp53 affects additional functions required for the correct execution of the polarity program, first and foremost the correct orientation of the spindle.

Introduction

The plasma membrane is a barrier, which separates the inside of the cell from its environment. But it has not only a passive role, it is actually involved in information transduction, entry of nutrients, receptor signalling, cell shaping and migration. The lipid bilayer is draped over a cortical network, composed by actin, septin, spectrin and microtubules. The coupling of the lipid membrane bilayer and the force generated by actin polymerization is essential for all the above-mentioned cellular processes.

Membranes are composed of more than 300 different lipid species, asymmetrically distributed in the bilayer and subjected to constant remodeling, their distribution is mediated by a variety of proteins, such as flippases, proteins able to transport lipids between the two leaflets that compose the plasma membrane. The chemical properties of the different lipids acyl chains can favor different membrane topologies, on the other hand membrane-associated proteins can actively change membrane curvature by sensing it and applying forces. For example, proteins can apply a localized pulling force. Alternatively, proteins can bend the membrane through scaffold mechanisms (meaning that the intrinsic curvature of the protein corresponds to the curvature that is induced on the membrane) or produce local deformations of the membrane, due to amphipathic moieties insertions [1] [2] [3].

Of note, actin architecture can modulate membrane composition. Conversely, changes in membrane composition can result in changes of cortex architecture. For example, membrane phospholipids, in particular PIP_2 (phosphatidylinositol-(4,5)-bisphosphate), activates proteins that promote actin assembly (e.g. vinculin, talin, ezrin, WASP, WAVE) and inhibits proteins involved in actin disassembly (such as gelsolin and villin) [4]. It is also important to consider that these systems are highly

dynamic and undergo to constant assembly and disassembly processes that are regulated in space and time.

In these events, of membrane and actin remodeling, crucial are the members of the Bin-Amphiphysin-Rvs167 (BAR) superfamily of protein. BAR proteins possess a multidomain structure, in which the BAR domain is able to regulate the shape and lipid organization of the plasma membrane, while additional protein-binding modules are able to recruit a plethora of proteins, including a variety of different actin-binding proteins [5] [6] [7] [8].

In this thesis, I will focus primarily on IRSp53 (Insulin Receptor Substrate protein of 53 kDa). IRSp53 possesses an inverted BAR domain (I-BAR) that deforms outward the plasma membrane, but it can also bind actin-binding proteins, such as EPS8 (Epidermal growth factor receptor kinase substrate 8) and VASP (Vasodilator-stimulated phosphoprotein) via its SH3 (SRC homology 3) domain [9]. These multiple functions are critical to account for the role that IRSp53 plays in filopodia formation: a topic that will be examined in detail in this thesis. In the second part of this dissertation, I will also highlight other potential roles of IRSp53, in particular I will discuss about its involvement in the establishment of polarity in the early steps of epithelial morphogenetic process.

Before touching these topics, I will start with a brief introduction on actin biochemistry and actin-binding proteins.

The actin cytoskeleton

Actin is one of the most abundant and conserved proteins in eukaryotes: in many cells, it accounts for more than the 10% of the total cellular protein content. Actin filaments (or F-actin) are composed by two intertwined chains, in which single units of globular actin monomers (or G-actin) are aligned. The two ends of the filaments are

very different: at the barbed or plus end, fast and active polymerization of ATP-bound monomers occurs; at the pointed or minus end, depolymerization is favored. As filaments grow, ATPase activity of actin monomers is activated, subsequently ATP is hydrolyzed and ADP-bound actin monomers are released from the minus end. Once ADP actin monomers are free in the cytoplasm, the ADP/ATP exchange occurs and new ATP actin monomers can be reassembled into the filaments. The two processes of polymerization and depolymerization are coordinated, so that, at the "steady state", a dynamic equilibrium exist between G-actin and F-actin, in a process called "actin treadmilling" (Figure 1) [10].

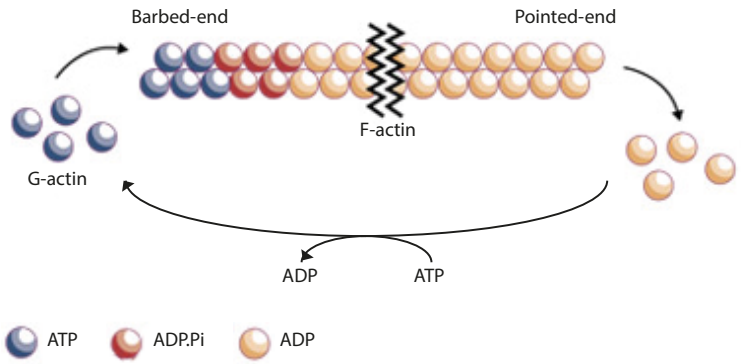

Figure 1. Model for "actin treadmilling".

ATP-bound G-actin monomers associate at the barbed ends, while ADP-bound G-actin monomers dissociate at the pointed ends, resulting in a flux of monomers through the F-actin filament. Dissociated monomers are then loaded with ATP and again used to sustain filament polymerization (modified from Littlefield et al., 2002 [11]).

From a cell-perspective, it can be imagined that actin filaments assemble at the leading edge, the front of cell migration, while there is an actin retrograde flow, from cell front to cell rear. In this way, barbed ends are directly exposed to the plasma membrane, and forces generated by actin polymerization are coupled with membrane deformation. Forces may be generated not only by polymerization, but

also by active crosslinking of actin filaments through myosin motor, which in turn generate contraction.

However, actin polymerization is not enough to produce forces able to generate active cell movement: it must be coupled to adhesion, using adhesive structures (as focal adhesions, that connect actin stress fibers with the extracellular matrix, ECM, through transmembrane proteins such as integrins) or friction, to transmit forces over the substrate [12].

Actin filaments, and the other components of the cytoskeleton, such as microtubules, are not only required for cell movement, but also, on a smaller scale, for vesicular transport inside the cell. In fact, a lot of motor proteins exist that mediate active transport of vesicles along cytoskeletal filaments routes (consuming energy from ATP hydrolysis). It was also suggested that large scale actin flow can contribute to intracellular transport in an unspecific way, particularly if the particle can at least transiently bind to actin [13]. Recently, for example, it has been shown that in cell migration there is an invariable coupling between cell velocity and cell persistence, which critically rely onto the polarized transport of actin binding and regulatory proteins, mediated by an active retrograde actin flow [14].

The actin monomer and the stages of actin polymerization

Actin is a 42 kDa globular protein that stably binds an atom of Ca^{2+} or Mg^{2+} and a molecule of ATP or ADP, inside an inner hydrophobic cleft. Four subdomains, named from one to four, can be identified in the G-actin structure (Figure 2 A). Actin monomers can assume an open or a close conformation, that differ in respect to the localization of a loop of the subdomain 2, called D-loop, and in the opening of the nucleotide binding cleft [15]. It has been hypothesized that the switch between the two forms is coupled to the ADP/ATP exchange: ADP-bound actin may adopt an open

conformation, that would be permissible for nucleotide exchange, while when bound to ATP the nucleotide binding cleft closes, allowing slow hydrolysis of the nucleotide [16].

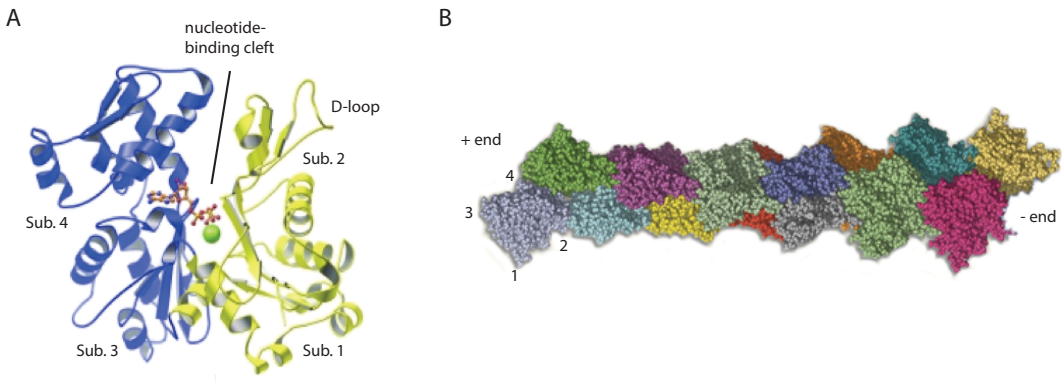

Figure 2. Structures of G-actin and F-actin.

A Ribbon diagram showing an actin monomer (Protein DataBase (PDB) code 2BTF). In the figure are highlighted the subdomains 1-4, the nucleotide binding cleft (where ATP is shown as a ball-and-stick model and the metal ion is in green) and the D-loop (modified from Aguda et al., 2005 [15]).
B Space-filling model of the F-actin helix: it is composed by repeats that contain 13 molecules each, measuring 35.7 nm. Note that the filament is polarized and different monomer subdomains are exposed at the two ends (modified from Holmes, 2009 [17]).

Actin monomers polymerize into a polarized filament, as already mentioned, formed by two parallel protofilaments, with 13 monomers per turn (Figure 2 B). From a biochemical point of view, actin polymerization can be divided into three phases:
1- nucleation (or lag phase): formation of an oligomer of two or three G-actin molecules, this is the kinetically unfavoured phase;
2- elongation (or log phase): oligomers act as seeds and filaments are rapidly assembled;
3- steady state (or equilibrium phase): during filament growth, the concentration of the free actin monomers that can assemble in the filament decreases, until reaching an equilibrium. At this stage, the polymerization at the plus end is counterbalanced by

the depolymerization at the minus end, without change in the net length of the filament (Figure 3).

At the steady state, an equilibrium between F-actin and G-actin is reached; at this stage the concentration of actin monomers is equal to the actin critical concentration (C_C), which is the minimal G-actin concentration required for filaments assembly. The critical concentration depends from the ratio of the constants of dissociation and association of monomers with each filament end, under typical *in vitro* conditions this value is equal to 0.1 μM at the plus end (C_C^+). The critical concentration is different at the pointed end, where is equal to 0.6 μM (C_C^-). At steady state this difference determines the net monomer association at the plus end and the net depolymerization that occurs at the minus end [10].

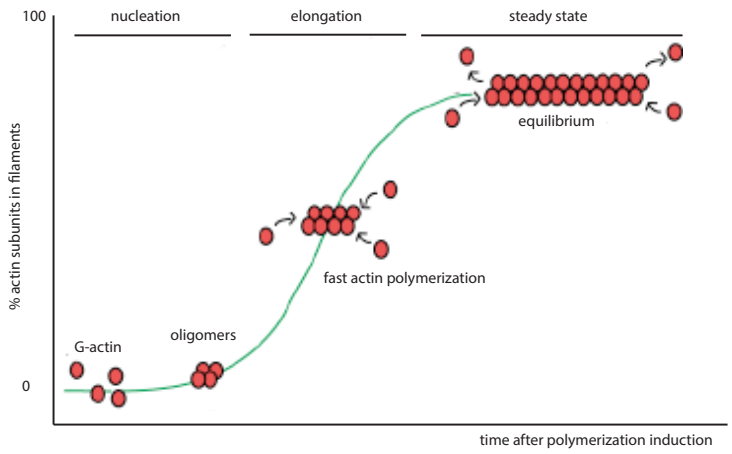

Figure 3. The phases of actin polymerization.

Actin polymerization can be divided in the following phases: nucleation (monomers slowly assemble, forming oligomers of two or three subunits), elongation (filament rapidly elongates) and steady state (in which no net growth of filaments is observed) (modified from: Molecular biology of the cell, Alberts, 2001).

Of note, the pool of actin monomers is constantly replenished in cells, it is thefore not-limited, and there is no competition for actin monomers between all the filaments in

active growth, while *in vitro* a finite and exhaustible pool of monomers is available [18].

Lamellipodia and filopodia

The actin cytoskeleton is tightly regulated in term of localization, composition and architecture. Examples of this control are to be found in lamellipodia and filopodia: protrusive structures that are assembled at the leading edge of motile cells (Figure 4). Lamellipodia are sheet-like projections containing a network of short branched filaments, which growth is terminated by capping proteins. WAVE2 mediated activation of Arp2/3 (Actin-related protein 2/3), downstream of Rac1-GTPase, is essential for the formation of branched actin filaments at the lamellipodium [19]. Filopodia are thin projections 8-15 μm long and 0.6-1.2 μm wide, with uniform tubular morphology, containing 15-20 long and parallel actin filaments, bundled together by crosslinking proteins, such as fascin. Filopodia extend and retract quickly (their lifetime is 79-142 seconds [20]).

Filopodia are sites for integrating signalling from ECM and external clues: they are involved in many cellular processes, such as cell migration, neuritogenesis, axon guidance in neuronal growth cones, receptor-ligand endocytosis, detection of pathogen targets for phagocytosis, angiogenesis, wound healing [12] [21] [22]. A lot of proteins are associated with filopodia, some examples are: the formin mDia2 [23], fascin (found along filopodia shalf) [24], Ena/VASP (located at tips) [25], myosin X (that transport Ena/VASP and other proteins to the tips, traveling towards actin filament barbed ends) [26].

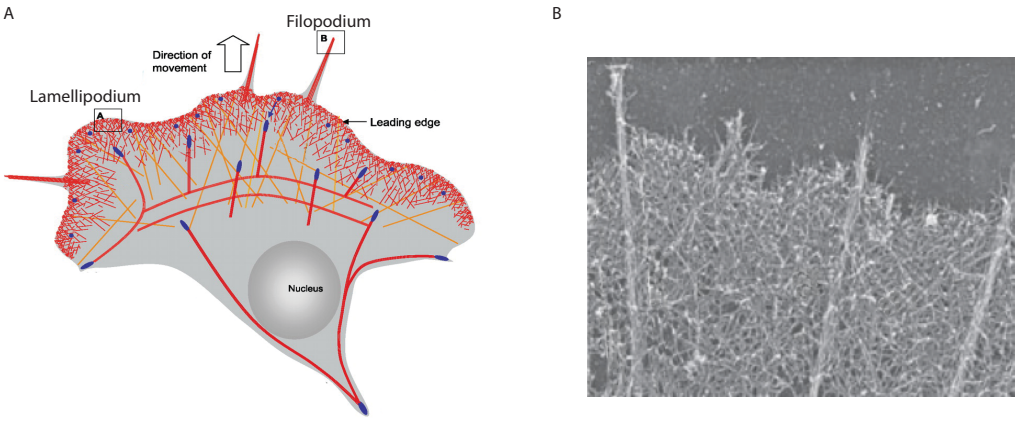

Figure 4. Lamellipodia and filopodia.

A Cartoon representing a moving cell, in which are highlighted, at the leading edge, lamellipodia and filopodia structures (modified from Le Clainche et al., 2008 [27]).

B Electron micrograph representing a neuron growth cone, in which filopodia actin bundle are visible (modified from Burnette et al., 2007 [28]).

Several small GTPases have been linked to filopodia formation, such as CDC42 (cell division control protein 42 homolog) [29], Rif [30] (both belonging to RHO family) and RAB35 (belonging to Ras family) [31].

Different models have been proposed to explain filopodia formation. According to the "convergent elongation model", filopodia emerge from a lamellipodial branched network. In particular, filopodial tip complex (Ena/VASP, mDia2) protects actin barbed ends from capping proteins, enabling Arp2/3-nucleated lamellipodial microfilaments to extend into long filaments, subsequently bundled together by fascin, to give rise to a filopodium [32]. However, filopodia can also form even in absence of lamellipodia. For this reason, a second, Arp2/3-independent, mechanism has been proposed. In the "*de novo* filament nucleation model", filopodial tip complex (containing proteins such as formins) nucleates and assembles unbranched actin

filaments, that are subsequently bundled together [33]. Filopodia stabilization is guaranteed by the formation of focal complexes and by the adhesion to the substrate. Filopodia extension and retraction are dependent on a balance between the actin polymerization rate and the retrograde flow: the assembly rate at the tips is the major determinant of filopodia dynamics, while the retrograde flow remains almost constant, but becomes the main force during retraction. Moreover, the plasma membrane exerts tension, inducing a passive inward retraction force [34]. Actin-binding proteins can modulate filopodia retraction: it has been observed that cofilin accumulates along filopodia shaft and becomes enriched at filopodia tips during their retraction. Of note, cofilin severing action is more efficient in presence of fascin-crosslinked actin bundles, promoting actin disassembly [35].

Note on GTPases

Kozma et al., 1995 [36], reported for the first time that CDC42 was able to regulate filopodia formation; in a variety of mammals cells CDC42 dominant negative inhibits filopodia formation. Moreover, CDC42 is a master regulator of cell polarity. CDC42 is prenylated, and in this way is tethered to the membrane.

CDC42 and others small GTPases (20-30 kDa in weight) are molecular switches that are able to cycle between an active GTP-bound form (at the plasma membrane), to an inactive GDP-bound form (at the cytoplasm), thus regulating the formation and disassembly of protein complexes at the plasma membrane. RHO GTPases switch ability makes them ideal molecules to control changes in the cytoskeleton dynamics, allowing a spatial and timing restricted response to extracellular stimuli [37].

GTPases itself are tightly regulated by guanine nucleotide exchange factors (GEFs) and GTPase activating proteins (GAPs). GEFs promote GDP to GTP transition. In addition, it is possible that GEFs can aid in selecting downstream GTPase effectors,

through direct binding or scaffolding mechanisms, and to organize a specific signalling pathway downstream of GTPase activation. GAPs are responsible for controlling GTP hydrolysis activity, in particular favoring the GDP-loaded pool. Finally, guanine-nucleotide dissociation inhibitors (GDIs) inhibit the dissociation of GDP from the protein, keeping the GTPases soluble in the cytoplasm, thus acting as negative regulators of the protein activity.

Interestingly, RHO family members can modify the local distribution of phospholipids in the plasma membrane, acting on the regulation of lipid-modifying enzymes, thus are able to influence the cytoskeletal dynamics also in this indirect way [38].

Actin-binding proteins

Actin polymerization is an energy-demanding process, in particular the nucleation of filaments is thermodynamically counteracted, meaning that the addiction of the first two or three monomers is discouraged. A class of proteins, called "nucleators" exists *in vivo* to overcome this energetic barrier.

Moreover, the polymerization rate of actin *in vivo* differs from the one reached *in vitro* by orders of magnitude: *in vivo* actin treadmilling is 100 time faster with respect to pure actin *in vitro* [10]. This is due to the fact that polymerization and depolymerization are tightly regulated in cells by a variety of proteins that influence filament dynamics, stability and architecture (Figure 5). It should be noted that actin-binding proteins work in tandem, binding together the actin filament, thus mutually influencing their affinities and dissociation rates, allowing a tighter control of filament polymerization [18]. Some examples of actin-binding proteins will be briefly reviewed in this section.

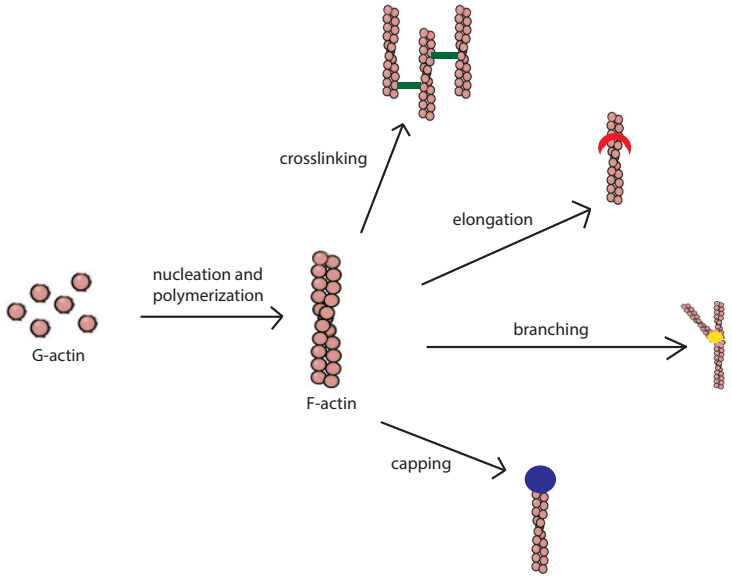

Figure 5. Roles of actin-binding proteins.

Actin-binding proteins can affect actin polymerization acting on nucleation, elongation or filament stability, but can also influence filaments architecture through capping, branching and crosslinking functions.

Profilin

Profilin binds to G-actin (between subdomains 1-3) with 0.1 μM affinity, while the affinity of profilin for F-actin is significantly lower (25 μM). Due to its higher concentration with respect to G-actin, the main actin monomer in cells is actually a G-actin:profilin complex. *In vitro*, profilin accelerates actin treadmilling: it catalyses the exchange from ADP to ATP and inhibits ATP hydrolysis; when bound to profilin, actin monomers are preferentially added to the barbed ends. Even though the overexpression of profilin in cells inhibits cell migration [39] and causes disappearance of filaments in lamellipodia [40]. This could be due to the fact that profilin bound to the barbed ends competes with capping proteins, formins, WASP-Arp2/3 complex, thus inhibiting nucleation and branching *in vitro* [41].

Of note, profilin can also bind a variety of proteins, mostly related with cystoskeleton dynamics, using its proline-rich region: some examples will be discussed later and include WASP, formins and VASP family proteins.

Nucleation and branching of actin filaments

The Arp2/3 was the first nucleating complex to be identified, but it is also able to branch actin filaments, with a typical angle of 70°[42-44]. It is a complex of 220 kDa, composed by seven proteins (Arp2, Arp3 and five additional subunits, named ARPC1-ARPC5) [45, 46]. It has been recently observed that Arp3, ARPC1 and ARPC5 are actually present in two distinct isoforms inside the cells. Interestingly, isoform composition of the Arp2/3 complex influences its actin assembly properties, as well as the stability of the formed filaments [47].

The isolated Arp2/3 complex is an inefficient nucleator, that requires the action of activators, called nucleation-promoting factors (NPFs). Among the NPFs, there is the WASP family, which includes WASP, N-WASP, and WAVE. All of them have a C-terminal WCA (WH2 Central Acidic) module, necessary and sufficient to interact with the Arp2/3 complex and to stimulate actin nucleation and branching [48]. In particular, WCA is composed by a WH2 (WASP homology domain 2), able to bind G-actin and deliver it to the nascent filament [49], an amphipathic connector region (C) and an acidic polypeptide (A). The CA portion is able to contact different subunits of the Arp2/3 complex, causing a conformational change required for its activation [50]. Members of the WASP family also share a central poly-proline region. The N-terminus of the proteins diverges: WASP and N-WASP have a WH1 (WASP homology domain 1), followed by a short basic region and a CRIB domain. WAVE (also called SCAR) instead possesses a WHD (WAVE homology domain) and a stretch of basic residues, but lacks the ability to bind directly small RHO GTPases. WAVE exists in 3 isoforms

(WAVE1-3), WAVE1 and 3 are expressed mainly in neural tissues, while WAVE2 isoform is ubiquitous. All WAVE proteins are present in both lamellipodia and filopodia tips. WAVE2 exists in a multiprotein complex, that contain Nap1 (NCK-associated protein), PIR121/Sra1 (p53 inducible protein), HSCP300, ABI1/2 (Abl-interactor 1/2). The assembly of the complex is required for WAVE to correctly localize and interact with activated Rac, as well as for its ability to activate Arp2/3 [51] [52]. WAVE2 null mice show embryonic lethality, fibroblasts derived from them show defect in lamellipodia formation, ruffling and cell migration [53].
Filaments branching can be also down regulated in cells: some proteins exist (such as Gadkin or Arpin) that sequester Arp2/3 into a non-branching complex, competing with WASP proteins [54] [55].

Formins

Formins can nucleate and polymerize linear actin filaments. There are 15 formins in mammalian cells which are currently subject of intense investigation [56] [57]. Two of the most studied, primarily for historical reason, are mDia1/2 formins, acting downstream of the small GTPases of the RHO family. The N-terminal basic domain of formins binds phospholipids and localize the protein to the plasma membrane. Formins then possess a FH1 (formin homology 1) domain, which is a proline-rich region, able also to recruit profilin-actin complexes, and a FH2 (formin homology 2) domain, a donut-shaped dimer required and sufficient for promoting actin assembly *in vitro*. In fact, FH2 associates with the barbed end of the filament and it is assisted, in its nucleation function, by the adjacent DAD (diaphanous autoregulatory domain), able to bind actin monomers [58]. Formins are processive nucleators: they bind barbed ends with high affinity, and display a low dissociation rate, so that a formin dimer can catalyze thousands cycles of actin polymerization *in vitro* [59] [60]. An

intramolecular interaction between the N-terminal DID (diaphanous inhibitory domain) with the C-terminal DAD autoregulatory domain, locks the protein in an inactive conformation; the transition to the active state occurs upon RHO GTPase binding and the disruption of this intramolecular interaction [61]. Of note, FH2 itself is not a dimer, but the active form of the formin is: a coiled coil and additional dimerization elements contribute to the overall assembly of the molecule.

In vivo, formin activity can be controlled influencing the rate of processive assembly or enhancing formin dissociation from the barbed ends. Some formins are instead poor nucleators and require an activator for their function. Of note, formins often act in membrane-bound sites, as at the tips of filopodia, some reports suggest that this tension could affect formin activity [62].

Cappers

Capping proteins are able to bind barbed ends with nanomolar affinity, thus inhibiting further addiction of monomers (or nucleation). In the cytoplasm, stable capping of actin filaments prevents any unproductive polymerization and the associated futile ATP consumption.

Different families of cappers exist, as the gelsolin superfamily, whose members (gelsolin, adseverin, villin, advillin, supervillin, flightless I homolog, CapG) are composed by gelsolin-type domains, that sever and cap actin filaments with high affinity and are calcium-dependent.

Another example are the capping protein (CP) and the homolog CapZ in striated muscle: CP is an heterodimer of alpha and beta subunits and is the major barbed ends capper. It binds the two terminal actin subunits with high affinity and has very slow dissociation rates.

CP has a “mushroom” shape: the N-terminal regions of the two subunits create a six-helix bundle structure that forms its “stalk”, while the C-terminal part forms an intertwined β-sheet that creates the “cap”. At the very C-terminus of each subunit, an alpha-helix emerge: they are the “tentacles” that extend perpendicularly from the “mushroom” structure and bind the barbed end of the filament [63].

If all the CP present in the cytoplasm were active, barbed ends will be permanently capped in cells, for this reason CP are finely regulated. In particular,

* V-1 (or myotrophin), present in micromolar amounts, sequester free CP. V-1 binds CP with high affinity, directly competing with barbed ends binding activity, due to a steric hindrance effect [64];

* CARMIL and CPI (capping protein interaction)-motif-containing proteins (CapZIP, FAM21, CIN85) lower the affinity of CP for the barbed ends, through an allosteric mechanism [64]. They can bind both free CP then CP bound to the barbed ends, this results in an enhanced rate of dissociation of CP from the barbed ends (called “uncapping”). CARMIL can also bind CP:V-1 complex, promoting V-1 release. Interestingly, proteins of the CPI family act in a site-specific manner, as CARMIL is an Arp2/3-myosin I linker and localizes at the protruding cell edges.

Of note, others uncapping proteins exist, that upon the transient formation of the ternary complex barbed ends:CP:uncapper, result in CP dissociation, while the “uncapper” remains bound. Examples are: the WH2 domain of VopF and the FH2 domain in formin, both WH2 and FH2 domains possess a short amphipathic α-helix, that inserts in the hydrophobic cleft between subdomains 1-3 of actin at the barbed ends [65] [66].

Another family of capper exist: the EPS8 family [67]. EPS8 is a 97 kDa protein identified as a substrate of receptor tyrosine kinase (RTK). It possesses a modular structure: a N-terminal PTB domain (phospho-tyrosine binding domain), a central

SH3 domain, two proline-rich regions and a C-terminal region, which is able to bind actin. The SH3 domain of EPS8 binds ABI1/2 and RN-tre, indicating a role of EPS8 both in the RHO GTPase signalling cascade and in endocytosis. EPS8, together with ABI1 and SOS1 (Son of sevenless homolog 1), forms a trimeric complex that possesses a specific Rac GEF activity *in vitro* and *in vivo*, essential for ruffling induced by oncogenic Ras [68]. RN-tre, instead, is a GAP for RAB5, RAB33 and RAB4, connecting EPS8 with RTKs internalization and recycling [69].

EPS8 C-terminal region instead affects actin cytoskeleton remodelling, in particular it contains an amphipathic H1 helix, homologous to WH2 domains, that is responsible for EPS8 interactions with the barbed end and is crucial for its capping activity. EPS8 C-terminus also possesses a four helix bundle (H2-H5), that represents a second interaction surface which mediates EPS8 contacts with the filament side and is responsible for its bundling activity [70]. These two actin binding surfaces are spatially coordinated by a flexible linker, that ensures a bimodal topological arrangement of EPS8 around the actin filaments. Of note, EPS8 capping activity is auto inhibited in the full-length protein and can only be induced upon binding to ABI1, while full-length EPS8 remains functional as a crosslinker [67].

Crosslinking

Actin bundling or crosslinking proteins mediate the interaction between different actin filaments, thus affecting their three-dimensional (3-D) organization. A variety of crosslinking proteins exist, that allow a fine-tuning of the mechanical properties of the actin bundles they generate. Crosslinking proteins need at least two F-actin binding regions to work, or alternatively dimerization of the protein is needed if it contains just one actin-binding module. The distance and the orientation of the two

actin-binding sites are crucial in determining the structural properties of the actin network.

Fascin is a monomeric bundling protein of great relevance for filopodia formation: it organizes actin in very tight and stiff bundles of around 20 filaments [71], exclusively oriented in a parallel fashion [35]. The rigidity that fascin confers to actin filaments is due to the close proximity of the two actin-binding site located in the N- and in the C-terminus of the protein. Fascin is specifically localized along the filopodia shaft, supporting them with the rigidity required to efficiently push against the membrane. Interestingly, fascin rapidly associates and dissociates from actin filaments, allowing an efficient coordination between elongation and bundling inside the filopodium. Fascin knock down (KD) in B16F1 mouse melanoma cells cause a decrease in filopodia number, while the remaining ones contained loosely arranged actin filaments [24].

Depolymerization

ADF (actin depolymerizing factor) or cofilin bind cooperatively to the side of ADP-bound actin filaments, it alters the mechanical properties of the filament, increasing its helical twist, thus weakening the contacts between actin monomers and promoting filament severing and depolymerization [72]. This mode of action does not affect the rate of actin polymerization *per se*, but causes an increase of the pool of G-actin, indirectly sustaining the growth of filaments. Other proteins can work with ADF/cofilin to enhance filament disassembly, such as: Aip1, coronin, twinfilin, cyclase-associated proteins [73] [74] [75] [76].

VASP

I dedicated a separated subchapter to the actin-binding protein VASP, since it will be an important player in our research that will be described later on. VASP belongs to the Ena/VASP family proteins, that includes Mena (Mammalian enabled) and EVL (Ena-VASP-like). In *Drosophila* just one member of the family is present: Enabled (Ena) (Figure 6) [77].

These proteins localize to focal adhesions, actin stress fibers, tips of filopodia and lamellipodia at the leading edge; interestingly VASP is lost from the leading edge during membrane retraction [78] [79] [80]. From *in vivo* cell imaging, it has been observed that GFP-VASP increases locally in sites that subsequently give rise to filopodia [32]. Ena/VASP proteins are implicated also in cell-cell contact maturation: they localize with E-cadherin/catenin puncta in primary keratinocytes [81] and Ena/VASP distruption perturbs cadherin-associated actin bundles in CHO cells [82]; in *Drosophila* Ena is essential for dorsal closure, influencing epithelial zippering by the modulation of filopodial number and length [83]. Finally, VASP is a protein kinase A (PKA) substrate in platelets, where PKA inhibits platelet activation [84].

The multidomain structure is conserved in Ena/VASP family and comprises the N-terminus EVH1 (Ena-VASP-homology-1) domain, a central proline-rich sequence and a C-terminal EVH2 domain (Ena-VASP-homology-2) (Figure 6). EVH1 interacts with proteins containing the consensus sequence (D/E)FPPPPX(D/E)(D/E); through EVH1, VASP binds its upstream regulators, palladin (an organizer of dorsal stress fibers) [85] and also zyxin and vinculin, responsible for VASP subcellular targeting on focal adhesions [86] [87]. Other EVH1 interactors are FYB/SLAP (through which VASP goes to immunological synapses in T-cells and phagocytic cups in macrophages) [88] and lamellipodin/Mig-10/RIAM (involved in the recruitment of VASP to filopodia tips) [89]. Moreover, EVH1 domain interacts, with lower affinity, with

proteins containing a LPPPPP motif, as mDia formins [90] and ABI1, a previously cited component of the WAVE complex [91].

VASP proline-rich domain (PRD) binds proteins containing SH3 and WW domains (as Abl, IRSp53, FE65), as well as profilin and actin-profilin complex [92]. Monomeric VASP binds two molecules of profilin, with nanomolar affinity [93], and the biochemical properties of profilin:actin complex are altered when bound to Ena/VASP.

EVH2 is required for Ena/VASP tetramerization, through the C-terminal coiled-coil (COCO) motif, and for actin binding. Actually, Ena/VASP possess both a G-actin binding domain (GAB), related to the WH2 domain, and a F-actin binding domain (FAB). Profilin and profilin:actin complex, that bind the central PRD region, can be directly transferred to GAB to promote actin filament elongation [92] [94]. EVH2 domain is sufficient to direct GFP-EVH2 to the leading edges of spreading cells, but EVH1 can cooperate to refine VASP localization to the very tip of lamellipodia and filopodia; moreover, EVH2 contains all the determinants required to regulate fibroblast lamellipodia dynamics. The activity of Ena/VASP proteins is regulated by phosphorylation: they are targets of cAMP/cGMP-dependent protein kinases (PKA, PKG). In particular VASP phosphorylation occurs at Ser-153, near EVH1-PRD junction, and at two sites in EVH2 (Ser-235, Thr-274). Mutation of any of PKA/PKG site has no effect on Ena/VASP localization, but if Mena is mutated in the serine flanking PRD (into alanine), fails to support normal motility [95].

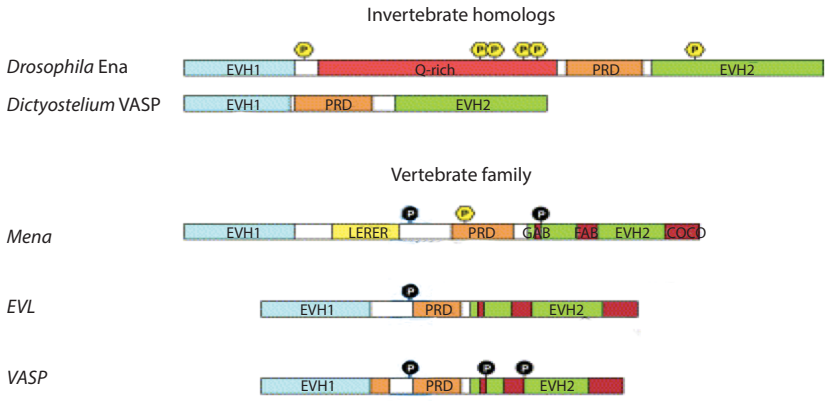

Figure 6. The Ena/VASP family.

Ena/VASP ortholog are found in *Drosophila melanogaster* (Ena, Enabled) and *Dictyostelium discoideum* (VASP, vasodilator-stimulated-phosphoprotein). In vertebrates, the Ena/VASP family includes three highly related proteins: Mena (mammalian Enabled), VASP and EVL (Ena-VASP-like). All the family members share a conserved domain structure: EVH1, Ena-VASP-homology domain 1, PRD, proline-rich domain, EVH2, Ena-VASP-homology domain 2. The vertebrate EVH2 contains GAB (G-actin binding) domain, FAB (F-actin binding) domain, and a coiled-coil domain (COCO). *Drosophila* Ena possesses an additional glutamate-rich region (Q-rich), vertebrate Mena contains repeats of the amino acid sequence LERER. All vertebrate Ena/VASP are substrate for the protein kinases PKA and PKG (modified from Kwiatkowski et al., 2003 [77]).

Deletion of all Ena/VASP family members in mice is embryonic lethal. Ena/VASP triple knock out (KO) embryos show disrupted vessel integrity and modified endothelial barrier function, leading to edema and hemorrhages, while single KO have more subtle phenotypes [96].

The role of Ena/VASP proteins has been highly debated in the past in the literature [97]: it has been proposed to act both in promoting and inhibiting actin-dependent processes. For example, the amount of GFP-VASP in lamellipodia correlates with their protrusion velocity in B16F1 melanoma cells [80], moreover, delocalization of VASP in Jurkat T-cells abolished the reorganization of their actin cytoskeleton in response

to antigens, while in macrophages impairs phagocytosis. Filopodia fail to form in *Dictyostelium* cells lacking VASP [98] and are severely reduced in neuronal cells lacking all the Ena/VASP family members [99]. Also in fibroblast, VASP removal reduces filopodia formation, promoting instead lamellipodia assembly [100]. *In vitro* purified Ena/VASP proteins stimulate actin nucleation, but at low and non physiological salt concentrations [101], however, EVL can reduce the lag phase in *in vitro* actin polymerization assays at physiological salt concentrations. It has also been proposed that VASP can act as a bundling protein *in vitro* [101]. Finally, EVH1:ABI1 interaction acts cooperatively with Rac1 to promote WAVE complex activation, and subsequently Arp2/3 stimulation *in vitro* [91].

In apparent contrast, Ena/VASP proteins have also been proposed to have a negative role in actin-dependent processes: platelets isolated from VASP-KO mice show an increased rate of collagen-dependent platelet activation and fibroblast devoid of Ena/VASP proteins exhibit increased rates of cell motility [102]. Moreover, neutralization of Ena/VASP in neurons caused neurons to migrate farther then normal neurons in neocortex [103]. Finally, Ena/VASP deficient lamellipodia contain shorter and denser [100] branched actin filaments, that protrude slower but persist longer, causing cells to move faster.

Additionally, other papers suggest an anti-capping role, proposing that VASP is able to associate near the barbed ends of actin filaments and, in this way, antagonize CP [100]. In Trichet et al., 2008 [104], it is proposed that Ena/VASP could detach the actin cytoskeleton from the surface in which active actin polymerization occurs, due to its anti-branching activity, which reduces the number of barbed ends growing towards the surface. Pasic et al., 2008 [105], observed VASP-mediated barbed end capture, without detecting acceleration of filament assembly, using a 100 mM KCl buffer (high ionic strength).

The current view suggests that VASP is a processive actin elongator, that accelerates filament polymerization by delivering G-actin to the barbed ends, if clustered on a surface [106]. In solution, VASP accelerates F-actin elongation in a concentration-dependent manner, but it is inhibited by low doses of CP. In contrast, VASP clustered on functionalized (carboxylated) polystyrene beads, to mimic actin assembly on a surface, promotes processive filament elongation, which is insensitive to high CP concentrations. This suggests that VASP remains attached to the barbed ends and sterically prevents the interaction with CP.

The effect of VASP-coated beads on actin polymerization was analysed through TIRF (total internal reflection fluorescence) microscopy: fluorescence initially increases around the beads, due to fluorescent actin accumulation, then filaments start to grow. Two populations of filaments can be identified: one population growing at the same rate of control filaments, the other with higher elongation rate. These latter filaments, presumably assembled by VASP, also show buckling, meaning that the elongation of actin filaments is subjected to resistance, in other words barbed ends stayed attached to a fixed point, indicating a processive behavior of VASP [106]. Note that these experiments were not made at the physiological salt concentration of 50 mM KCl. Profilin had not effect on actin polymerization from VASP-coated beads, moreover, extensive buckling occurs only when VASP is close to saturation on beads surface. Processive filament elongation is seen in even presence of the mutants lacking (Δ) GAB or the tetramerization domain (only ΔGAB mutant produces less buckling filaments); while ΔFAB mutant is not able to perform elongation, in presence of high concentrations of CP short filaments detach from the beads, so FAB is critical for the anchorage of filaments to the beads surface, in the region immediately flanking the barbed ends. In cells, ΔFAB mutant fail to localize to filopodia tips and to trigger filopodia formation in VASP null cells, that present also defects in migration [106].

Profilin-PRD interaction is not required for filament elongation, in fact both VASP wild type (WT) and VASP-ΔPRD elongate actin filaments at comparable levels, in presence or absence of profilin, even if VASP has higher affinity for profilin-actin than actin alone [107].

The model proposed in Breitspecher et al., 2008 [106], suggests that VASP oligomers cluster to the plasma membrane, then use GAB and FAB domains to tether actin filaments and promote their processive elongation. In particular, VASP binds barbed ends and then stays attached to filament side while it continues to growth, by the addiction of G-actin molecules delivered by other VASP proteins (Figure 7). Decoration of barbed ends by multiple VASP molecules could prevent CP access to the barbed ends.

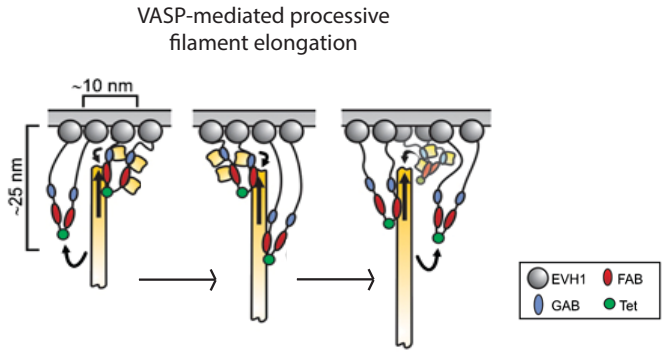

Figure 7. Model for VASP processive elongation activity.

When clustered on a surface, VASP acts as a processive elongator 1) VASP tetramers tethered to the surface bind actin and deliver monomers to the barbed end, using GAB and FAB domains. (2) VASP remains bound to the side of the filament, as it elongates by other VASP molecules. (3) Stretched VASP molecules eventually detach from the filament, due to its continuous elongation, and are then available for a new cycle of actin addition. During the detachment period, the growing filament is constantly tethered to the surface by other VASP molecules, that also prevent access of CP to the filament barbed end (modified from Breitspecher et al., 2008 [106]).

Later observations, reported in Hansen et al., 2010 [93], describe three binding modes for VASP tetramers: 1) static side binding, 2) side binding with one-dimensional diffusion (mainly contributed by FAB) and 3) processive barbed end tracking (in 50 mM ionic buffer), that is enhanced by the presence of profilin. Contrary to Breitspecher et al., 2008 [106], using TIRF microscopy they rarely observe VASP transition from barbed ends to lateral side: VASP dissociated directly from barbed ends, while molecules from solution frequently bind filament sides. The model proposed [93] is then slightly changed: GAB binds actin monomer, if FAB allows VASP binding enough close to the barbed ends, actin is included in the growing filament and GAB contributes to filament binding. Since GAB affinity for G-actin is higher than the affinity for filament side, if another G-actin is available it will be captured by GAB in an additional cycle of polymerization. In a VASP tetramer, multiple GAB near the barbed ends further increase G-actin capture and consequently filament elongation rate. Recently, it has been observed that lamellipodin, beside recruiting Ena/VASP proteins to the plasma membrane, also promotes VASP clustering and simultaneously interacts directly with actin filaments. The combination of these activities, in turn, increases the delivery of Ena/VASP proteins to the barbed ends and promotes VASP processive elongation activity [108].

IRSp53: protein at the interface between membrane and actin

Proteins that sit at the membrane-actin interface are in a critical position to couple forces generated by actin polymerization machinery and membrane deformations. The I-BAR containing protein IRSp53 is one of these key proteins, and will be extensively analysed in this thesis.

IRSp53, known also as BAIAP2 (Brain-specific angiogenesis inhibitor 1-associated protein 2), has been identified in a screen for substrates of insulin and insulin-like growth factor 1, that are capable of phosphorylating it on tyrosine residues. IRSp53 is widely expressed in different tissues in mammals, as spleen, lung, liver, testis, but is enriched in brain, in particular in cortex, hippocampus, striatum and cerebellum [109] [110] [111].

IRSp53 is abundant in postsynaptic density (PSD, multi-protein complexes in the postsynaptic side of excitatory synapses, that couple receptor activation with downstream signalling) and regulates actin-rich dendritic spines. IRSp53 is enriched during the first three weeks of postnatal brain development, when active synaptogenesis occur. Not surprisingly, IRSp53 KO mice display enhanced NMDAR (N-methyl-D-aspartate receptor) function, defects in learning, memory, synaptic plasticity, social and cognitive defects, despite no obvious structural defects being apparent in dendritic spines from their brain [110] [112].

Actin filaments in IRSp53 KO hippocampal neurons are abnormally stable, which may promote synaptic localization of NMDAR and suppress their activity-dependent removal (cofilin resistance); mice lacking EPS8 and WAVE1, two IRSp53 interactors, also show altered NMDAR function [113]. Moreover, lens-retina inter-epithelial filopodium formation is impaired in IRSp53 KO mice [114].

In humans, IRSp53 has been implicated in diverse psychiatric disorders: autism spectrum disorder, schizophrenia, attention deficit/hyperactivity disorder [112].

IRSp53 protein contains different domains, that will be reviewed in the next subchapters (Figure 8). Different IRSp53 isoforms exist, called S- L- M- T-, differentiated by their C-termini [9]. Isoform S is the sorter, it contains a PDZ (PSD95-DLG1-ZO-1)-binding domain, while M and L isoforms contain a WH2-like motif (with actin-binding function), isoform T role is unclear, it lacks both the PDZ-binding and

the WH2-like domains. Isoforms S and L are phosphorylated by insulin stimulation, T by IGF-1 stimulation.

Figure 8. The structure of IRSp53.

IRSp53 S isoform: it contains I-BAR domain, CRIB-PR domain, SH3 domain, WW-binding domain, PDZ-binding domain (modified from Kast et al., 2014 [115]).

I-BAR domain

The I-BAR domain, at IRSp53 N-terminus, has been reported to be able to bind Kank [116], Tir (required for pedestral formation in enterohemorragic *E. coli* infection) [117], Rac1 (when GTP bound, with a Kd of 3.2 μM) [118] and synaptopodin [119]. However, the most relevant function of this domain is linked to its dimeric structure and ability to bind and sense membrane curvature [120] [121]. Indeed, I-BAR domain belongs to the bigger family of BAR (Bin-Amphiphysin-Rvs167) domains. More then 50 types of BAR proteins are present in humans that are able to generate membrane deformation. BAR-containing proteins also possess protein-binding modules, consequently they can work as platforms to allow a unique coordination of complex processes, such as endocytosis, migratory protrusion, epithelial morphogenesis. It has been hypothesized that different BAR proteins, generating a variety of membrane deformations, can adapt and bind to all the different membrane topologies that are formed during endocytosis: from the low curvature membrane invaginations to vesicles fission [6] [122].

The BAR domain was identified in Bin1 and Aphiphysin, it can induce membrane tubulation *in vitro* [123]. Its crystal structure [124] revealed a banana-shaped dimer, formed by three kinked antiparallel alpha helices for each monomer, creating a

concave surface able to bind negatively charged membranes. For this reason, it induces positive membrane curvature and is usually involved in membrane invaginations. Moreover, the BAR domain induce homodimerization of the protein [5].

BAR family comprises members with different geometrical properties: N-BAR, F-BAR, I-BAR domains (Figure 9). Less common are BAR-PH, in which BAR is associated with a PH (pleckstrin homology) domain, and PX-BAR, associated with PX (phox homology) domain, present in certain protein of the sorting nexin family. Both PH and PX domains can bind various phosphoinositides, but may also be involved in protein–protein interactions, adding specificity to BAR protein function and localization.

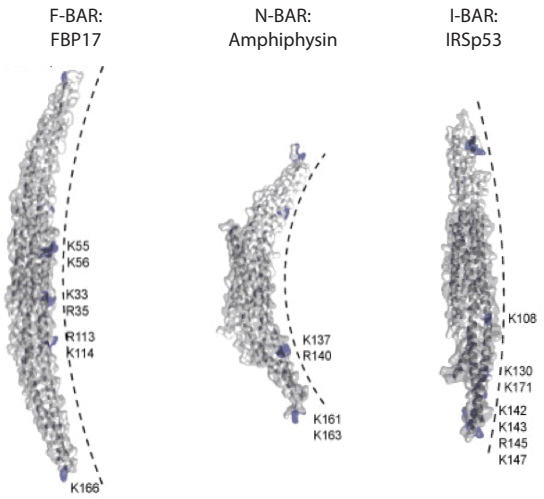

Figure 9. Structure and geometrical properties of selected BAR family proteins.

In the figure are shown: F-BAR domain from FBP17, N-BAR from *Drosophila* amphiphysin and IRSp53 I-BAR domain. The amino acids responsible for lipid binding are colored blue (modified from Suetsugu et al., 2010 [5]).

* N-BAR domain contains amino acids that form an N-terminal amphipatic helix. This helix is thought to insert into the membrane, thus enhancing protein-membrane interaction. One member of this family is amphiphysin, whose BAR domain was the

first to be solved. Amphiphysin contains also a SH3 domain able to bind dynamin and N-WASP, it has been hypothesized that this protein acts in the later stages of fission for clathrin-mediated endocytosis.

* F-BAR (FCH-BAR, Fes/CIP4 homology BAR, or also EFC, extended Fes-CIP4 homology) subfamily comprises Toca-1, FBP17, CIP4, Fes. F-BAR is "banana"-shaped dimer, but more extended in comparison to the others BAR domains, it contains 5 α -helices per monomer and induces curvature with larger diameter. It has been hypothesized that these proteins correspond to the curvature of the initial stages of clathrin-coated pits. F-BAR self-assemble into a helical coat around the membrane tubules, for F-BAR it is known that they form both end-to-end and lateral homointeractions [125]. Of note, in mammals srGAP 1-3 (slit-robo GAP) exist, which possess F-BAR domains that promote plasma membrane protrusions, instead of invaginations.

* I-BAR domain (inverse-BAR, also IMD, IRSp53-MIM homology domain) binds phosphoinoside-rich vesicles with high affinity, in particular binds liposomes enriched in PIP_2 (content major than 5-10%) [120], the most abundant phosphoinositol in the cytosolic leaflet of the plasma membrane. I-BAR is able to deform membrane into tubular structures [120], binding their internal leaflet [126]. Moreover, I-BAR domain induces PIP_2 clustering at the membrane [126]. In presence of artificial liposomes, I-BAR binds their outer leaflet and generates membrane invaginations, in contrast, N-BAR domain induced long outward protrusions of smaller diameter [120].

I-BAR, and IRSp53, overexpression in cells induces actin containing filopodia-like protrusions, requiring F-actin binding and PIP_2 binding [127] [120]. I-BAR induced protrusion are frequently characterized by the presence of aberrant actin aggregates, and a lifetime of more than 10 minutes [20], but are positive for filopodial marker,

such as fascin, VASP and myosin X [126]. The substitution of the I-BAR terminal loop residues K142,143,146,147 to glutamic acid (4K I-BAR mutant) does not really affect the global conformation of the dimer, but the overexpression of this mutant in COS7 cells abrogates filopodia formation (as ΔI-BAR mutant overexpression) [128].
Even if I-BAR was proposed to be a bundling domain [127], in physiological salt conditions it does not possess a strong crosslinking activity: the previously reported actin bundling activity appears to result from protein aggregation in low salt buffers [120].

I-BAR containing proteins

I-BAR proteins are present in lower eukaryotes, such as *Dictyostelium*, but not in yeast. In mammals, I-BAR containing proteins can be divided in two evolutionary diverged subfamilies: the first including MIM (Missing-in-metastasis) and ABBA (Actin-bundling protein with BAIAP2 homology); the second instead comprises IRSp53, IRTK (Insulin Receptor Tyrosine Kinase substrate, also BAIAP2L1, BAIAP2-like protein 1) and PINKBAR (Planar intestinal and kidney-specific BAR domain protein, or BAIAP2L2, BAIAP2-like protein 2) (Figure 10). Tubules induced by MIM and ABBA are thicker in comparison to the ones induced by the other group. In fact, MIM and ABBA possess a critical 11 amino acids N-terminal helix, that inserts into the acyl chain region of the bilayer, absent in IRSp53 and IRTK. MIM and ABBA are also more efficient in inducing filopodia in cells and contain an actin-binding WH2 domain [126].
IRTK is closer to IRSp53, it is expressed at low levels in brain, but present in liver, bladder, testes, heart, lung. IRTK binds the small GTPase Rac and induces clusters of short actin bundles [129]. More peculiar is PINKBAR: it possesses a shorter I-BAR domain (164 amino acids long, in comparison to IRSp53 I-BAR, which is long 182

amino acids) that, due to its flat arrangement, deforms membrane into planar structures. PINKBAR is expressed predominantly in intestinal and kidney epithelial cells, it interacts with PIP_2-rich vesicles through electrostatic interactions [130].

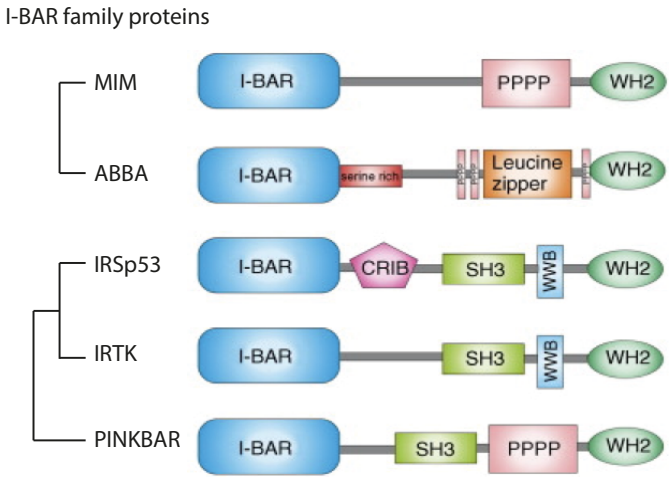

Figure 10. The I-BAR family.

Domain structures of mammalian I-BAR containing proteins: subfamily 1, including MIM and ABBA; subfamily 2, including IRSp53, IRTK, PINKBAR (I-BAR: I-BAR domain, WH2: WH2 domain, SH3: SH3 domain, PPPP: proline-rich region, Serine rich: serine-rich region, CRIB: CRIB domain, WWB: WW binding domain) (modified from Zhao et al., 2011, [131]).

I-BAR structure

The I-BAR structure resembles the one of the BAR domain, it forms an alpha-helical antiparallel and elongated dimer. Each monomer is made by a three helix bundle, with a shorter C-terminal helix, which is separated by 8-residue linker from the preceding helix 3. The C-terminus of helix 4 is adjacent to the N-terminus of helix 1 from the opposite monomer, helices 2 and 3 protrude beyond the central region, and the poorly ordered 2-3 loops define the extreme ends of the dimer [128] (Figure 11). Some structural differences, however, exist between the two monomers.

The extreme ends of the dimer present a strong positive charge (on the N-terminal side), and correspond to PIP_2 binding site, elsewhere charge distribution is even, with a slightly prevailing positive charges.

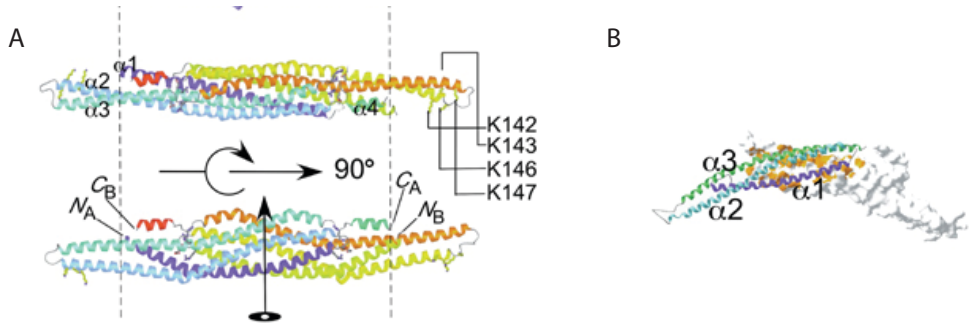

Figure 11. Structure of the I-BAR domain from IRSp53.

A Two orthogonal views of the I-BAR dimer in ribbon representation. The helices are colour ramped blue to green (chain A) and yellow to red (chain B). Vertical dashed lines indicate the core region of the dimer.

B Structure of amphiphysin BAR domain, indicated for comparison with A. Note that I-BAR dimer is flatter than amphiphysin BAR domain (modified from Millard et al., 2005 [128]).

I-BAR domain possesses an extensive dimer interface, which is solvent accessible: it encloses a cavity that contains several water molecules. Hydrophobic and polar surfaces contribute to nearly equally to the contact surface, which involves all the four helices [128] [132]. Dimerization of the proteins has been also confirmed by sedimentation velocity experiments [128] and coimmunoprecipitation approaches [127].

I-BAR signature sequence [127] ALXEE[R/K][R/G]RFC$X_{0\text{-}1}$F[I/L] is mostly buried in the dimer, with the EERRR core segment making contacts with the other conserved parts in the opposite monomer.

The I-BAR domain displays a convex geometry, thus generating negative membrane curvatures, through a scaffolding mechanism: the protein domain has a rigid surface

with an intrinsic curvature that forces membrane to adopt a similar conformation (Figure 12).

Moreover, positive residues over the I-BAR surface fit well with negatively charged lipids that BAR selects for binding.

I-BAR domain is able both to sense and generate membrane curvature. Using proteins encapsulated in GUV (giant unilamellar vesicles), from which membrane tubes of controlled radius are pulled, it has been demonstrated that I-BAR dimers can sense membrane curvature, in fact I-BAR is enriched on membrane portions with an induced negative curvature [121].

Additionally, I-BAR encapsulated in GUVs can generate membrane tubes, if concentrated enough: it reduces the force needed to sustain and stabilize the tubules. Tubulation induced by I-BAR proteins seems to be concentration-dependent, suggesting that I-BAR dimers can associate into high order oligomers [120] [133].

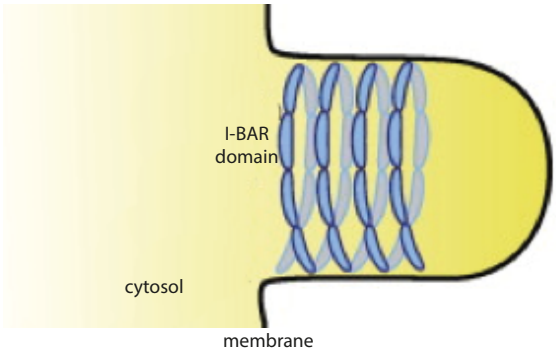

Figure 12. Model of I-BAR localization in membrane protrusions, such as filopodia.

I-BAR binds to the inner surface of the protruding membrane, a spiral arrangement is hypothesized for the domains (modified from Suetsugu et al., 2010 [5]).

CRIB

IRSp53 possesses a non-canonical, short, CRIB (CDC42/Rac interactive binding) region (Figure 8), able to bind CDC42 (with 16.1-23 uM affinity) [115] and Tiam1

[134]. The partial CRIB-like region is followed by a proline-rich region, together indicated as CRIB-PR. CRIB-PR is specifically adapted to bind active CDC42 and not Rac, probably because only few residues are shared with canonic CRIB domains, while the region in which CRIB-PR diverge from canonical CRIB binds the portion of CDC42 that highly differs from Rac. Moreover, the PR portion of the domain is able to bind switchI-switchII region of CDC42, that undergoes conformational change in response to the nucleotide binding: PR is thus involved in CDC42 binding and is important for nucleotide-state sensing [115].

Since CDC42 contains prenylated residues that tether it to the plasma membrane, both I-BAR and CRIB domain are involved in membrane localization of IRSp53.

IRSp53 mutant in the CRIB region is no longer able to induce neuritis (extensive lamellipodium, filopodium and ruffles) in N1E115 mouse neuroblastoma cells [135].

SH3

IRSp53 SH3 domain binds to the proline-rich sequences of a number of actin-related and neuronal proteins: WAVE2 [136], WAVE1 [20], N-WASP [20], Mena [137], EPS8 (EPS8/ABI1/SOS1) [138], Shank3 [111], Shank1 [109] [139], SH2B1 [140], NESH [141], espin [142], SPIN90 [143], DRPLA/atrophin-1 [144], BAI1 [145], EspFU [117], IQ-ArfGEF/BRAG1 [146], WIRE [147], huntigtin [148], cypin [149], synaptopodin [119], mDia [150] [20], dynamin1 [151]. For this reason, IRSp53 can be seen as an adaptor, that allows the recruitment of protein complexes (using its SH3 domain) to specific sites along the membrane (bounded through its I-BAR domain).

SH3 interactors are implicated in different biological processes. For example, Mena, EPS8 and mDia have been linked to filopodia formation, while WAVE proteins are connected to lamellipodia extension [9]. Additionally, Shank proteins are postsynaptic scaffolding proteins that regulate spine morphogenesis [109] [111].

Active CDC42 can induce filopodia even alone, but in combination with IRSp53 or IRSp53 SH3 mutant (W413R or F428A/P429A) allow the formation of even longer filopodia [137].

The region between CRIB-PR and SH3 contains several phosphorylation sites, involved in Tiam1 and 14-3-3 binding. When 14-3-3 binds IRSp53, the protein is maintained inactive in the cytoplasm and the interaction with SH3 binders of IRSp53 is abrogated [152] [153].

C-terminus

As introduced previously, the very C-terminal portion of IRSp53 differs among the different isoforms. Isoform S contains a PDZ-binding motif that binds CIPP [154], LIN7 (or MALS) [155], PSD-95 [156], PSD-93/Chapsyn-110 [156], SAP97 [155], SAP102 [155], S-SCAM [155]. Through its PDZ-binding domain, IRSp53 can participate to big scaffolding/signalling complexes in PSD.

M and L isoforms instead possess a WH2 domain. It is dissimilar to canonical WH2 domain and has unclear functions. The C-terminal portion of WH2 is very similar to MIM WH2, while the N-terminal portion possesses a non-canonical sequence [9].

Conformational changes of IRSp53

An intramolecular interaction between IRSp53 N-terminus and C-terminus has been proposed since 2001 [137], through a co-immunoprecipitation approach, but it has been formally demonstrated to occur just recently using a FRET approach in Kast et al., 2014 [115]. IRSp53 adopts a "closed"/inactive conformation, involving the reciprocal binding of CRIB-PR and SH3 domains; IRSp53 opens upon active CDC42 binding to CRIB-PR region and the subsequent binding of one effector to the SH3 domain (Figure 13). The release of this intramolecular interaction is synergistic, in

fact the conformational changes induced by CDC42 and SH3 binders are different in nature but have an additive character: both the interactors can bind simultaneously to IRSp53 and additively modify its structure to full activate it in an "open" conformation [115].

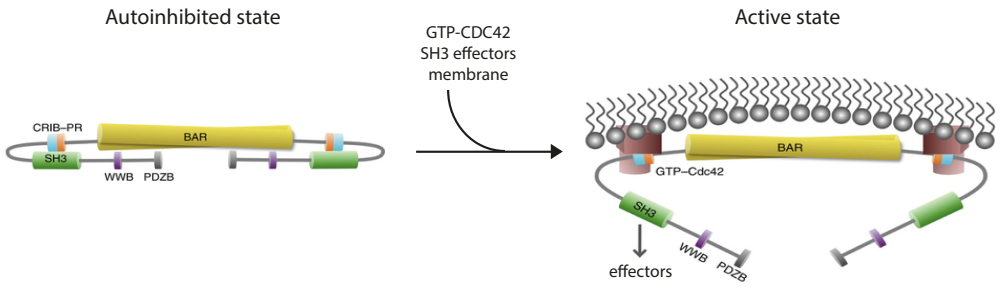

Figure 13. Model for IRSp53 activation.

In the autoinhibited state, IRSp53 is in a "closed" conformation, due to an intramolecular interaction between CRIB-PR and SH3 domains. IRSp53 activation requires the combinatorial binding of GTP-CDC42 and SH3 effectors (modified from Kast et al., 2014 [115]).

In Kast et al., 2014, the crystal structure of CDC42 bound to CRIB-PR allowed also the description of IRSp53 mutants in the CRIB-PR region, able to decouple its interaction with CDC42 and the SH3 domain, in particular I267A/S268A mutant failed to bind CDC42 (constitutively inactive mutant), while P278D/P281D mutant failed to form the intramolecular interaction with the SH3 domain ("open" mutant) [115].

IRSp53 cellular functions

IRSp53 is a scaffolding protein enriched at the plasma membrane. It participates in processes as neurite extension, dendritic spine morphogenesis, cell motility, tumor invasion, cell polarity, eye lens formation, myogenic differentiation and pathogen invasion [9]. IRSp53 is involved in the formation of lamellipodia [135] [137] [127]

and filopodia [157] [158], and localizes at tips of both these structures; GFP-IRSp53 is absent from cell edges undergo retraction [159].

IRSp53 acts in filopodia formation downstream of CDC42 signalling, working synergistically with Mena [137]. Synaptopodin, an actin-associated protein that has been linked also to synaptic plasticity, binds directly to IRSp53 and suppresses CDC42-IRSp53-Mena initiated formation of filopodia in kidney podocytes [119]. IRSp53 failed to induce filopodia formation in N-WASP KO fibroblasts, as well as in Ena/Mena/VASP KO cells [20]. Similarly, it has been observed that IRSp53 overexpression, in combination with the sequestering of VASP family proteins away from the plasma membrane, causes a reduction of filopodia formation in cells [160]. Moreover, in presence of an excess of IRSp53, VASP has an increased capacity to bundle actin filaments in *in vitro* bulk experiments [161].

Formation of filopodia precedes the formation of dendrites and axons; it has been proposed that IRSp53 can recruit SH2B1, a scaffolding protein that interacts with several neurotrophin receptors and regulates signalling and gene expression, IRSp53:SH2B1 complex can enhance the formation of filopodia and dendrites of hippocampal and cortical neurons [140].

Primary cultured neurons from IRSp53 null mice show changes in morphology: a reduction in primary dendrites and dendritic branches and a delayed formation of post synaptic clusters. IRSp53 overexpression in cultured hippocampal neurons, on the other hand, increases spine density and size [111].

IRSp53 N-terminus binds Ras (in a domain distinct from CRIB) and, through the SH3 domain, to WAVE2 proline-rich region, this complex is involved in membrane ruffling and lamellipodia formation [157]. Tiam1 (a Rac-GEF) enhances the signalling of IRSp53-WAVE2 axis, promoting IRSp53:Rac-GTP bound:WAVE2 complex [162]. Moreover, IRSp53 KD inhibits lamellipodia formation [163]. Also in macrophages,

IRSp53, WAVE2 and ABI1 are required for CSF-1 dependent actin remodeling, involved in cell migration and formation of protrusions, but not in podosome/filopodia formation nor phagocytosis, requiring a mechanism more complex than simple WAVE2 relocalization to the membrane [164].

IRSp53 is involved, as IRTK, in the formation of actin pedestals: actin-rich membrane protrusions, developed during enterohemorragic *E. coli* infections.

The major binder of IRSp53 in fibroblasts and cancer cells is EPS8; IRSp53 interaction with EPS8 enhances EPS8-ABI1-SOS1 signalling to Rac1, promoting motility and invasiveness of the malignant tumor cells [138]. The affinity between IRSp53 and EPS8 is in the nanomolar range, their interaction is mediated by IRSp53 SH3 domain and two distinct N-terminal proline-rich sequences in EPS8 [138], their association is constitutive and does not require stimulation by growth factors [160].

EPS8:IRSp53 complex localization is regulated by CDC42. In cells, the concomitant expression of IRSp53 and EPS8 enhances IRSp53 protrusive activity, promoting the formation of long and branched protrusion, which were not observed in presence of I-BAR only or EPS8 alone [160]. *In vitro*, EPS8 bundling activity is synergistically enhanced by the presence of full-length IRSp53, but not ΔI-BAR IRSp53 mutant. In neurons Shank competes with EPS8 for IRSp53 binding, abrogating the bundling function of the complex [111].

Further roles of IRSp53 in junctions assembly and cell polarity

In the second part of this thesis, the role of IRSp53 in cell polarity will be discussed. It is already known that IRSp53 contributes to assembly and maintenance of cell tight junctions, through its association with LIN7 (Protein lin-7 homolog) [155] [165],

small protein containing a single L27 (LIN2-LIN7) domain and a PDZ domain. LIN7 is also involved in epithelial polarization by stabilization of PALS1 (Protein associated with LIN7, or stardust). Moreover, IRSp53 KD causes abnormalities in the development of 3-D epithelial model system that will be described in the next section.

Models of epithelial polarity: MDCK and Caco2 cells

Epithelial organ development requires cell to polarize, forming a monolayer of epithelial cells, surrounding a central lumen, in which apical and basal layer acquire different properties. Polarization occurs through different mechanisms: differential expression of specific markers and transporters of nutrient and fluid; creation of intercellular junctions and sealing junctions between apical and basal layer, to segregate the two compartments; epithelial-specific cytoskeletal rearrangements and polarized trafficking (involving endoplasmic reticulum (ER), Golgi and endosomal compartements).

Polarity proteins can be divided in three groups [166]:

* PAR (partitioning defective) proteins: PAR1, PAR4, PAR5, PAR3, PAR6, aPKC (atypical protein kinase C) and CDC42, identified in a screen in *C. elegans* as required for correct partitioning between anterior and posterior cells of the early embryo, involved also in proliferation and differentiation;

* Crumbs: CRB (Crumbs), PALS1 and PATJ (PALS1-associated tight-junction homolog), localized both at apical membrane than at tight junctions;

* Scribble: DLG (Disks large homolog), Lgl (Lethal giant larvae), Scribble, at lateral membrane of epithelial cells.

RHO GTPases have key roles in defining the polarity program, even independently from their actin-organizing role [167]. Also phosphoinosides and other lipids are implicated in the generation of polarity signals, for example PIP_3

(phosphatidylinositol-(3,4,5)-trisphosphate) is involved in basolateral plasma membrane identity [168], while PIP_2 in apical plasma membrane identity [169].

One important mechanism in polarity definition is the mutual exclusivity: for example, aPKC at the apical cortex excludes basolateral proteins, while PAR1 at the basolateral side exclude apical proteins; both aPKC than PAR1 act promoting phosphorylation of partner proteins.

In the initial phases of epithelial polarization, aPKC associates with active CDC42 and PAR6, causing the apical recruitment of the complex and aPKC activation [170]. aPKC then phosphorylates PAR3, PAR1 and LGL, to exclude them from the apical domain [171]. When aPKC positioning is lost in epithelium, also E-cadherin, Numb (involved in endocytosis) and Pins/Lgn (involved in spindle orientation) are mislocalized [172] [173]. PAR3 stays at tight junctions in epithelial cells and is not part of the apical complex, but it is necessary for aPKC apical delivery, since it binds PAR6. Basolateral PI3K (phosphatidylinositol 3-kinase) is recruited at junctions by E-cadherin. PI3K recruits, in turn, DLG and generates PIP_3, which binds Scribble [166] (Figure 14).

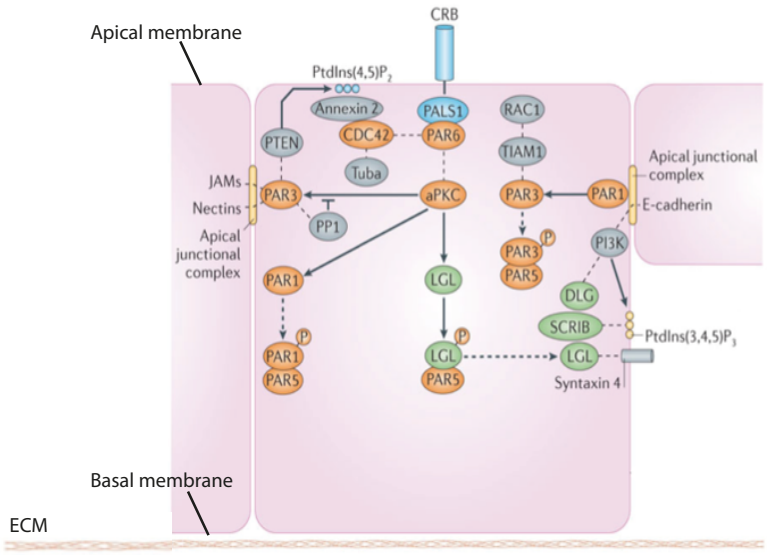

Figure 14. Players of the epithelial polarity program.

The apical polarity protein Crumbs (Crb) recruits PALS1, which in turn recruits PAR6 and aPKC to phosphorylate PAR3, the kinase PAR1 and LGL and exclude them from the apical domain. Conversely, PAR1-mediated phosphorylation prevents basal localization of the apical polarity determinants, such as PAR3. PTEN is recruited to the junctional area through interaction with PAR3 and generates PIP_2, which helps recruit CDC42 via annexin 2. CDC42 participates in the activation of aPKC via PAR6. Basolateral PI3K recruits DLG and generates PIP_3, which additionally contributes to basal membrane identity through the recruitment of Scribble (modified from Rodriguez-Boulan et al., 2014 [166]).

Polarity program proteins are also involved in tight junctions assembly and maintenance, tight junctions are essential to form a barrier that separates apical and basolateral domains. Loss of CRB3 or PALS1 causes defects in tight junctions assembly [174] [175]. CDC42 is involved in adherens junction assembly, through PAR3-PAR6-aPKC. Also cadherin-based adhesions are required for cell polarization.
Newly synthetized cargo proteins may traffic through the endosome compartment: apical and basolateral plasma membrane proteins are synthetized at ER, transferred to Golgi and trans-Golgi network to be sorted to the plasma membrane.
Although there is conservation among the key players of polarity program, considerable variations exist among different tissues and developmental contexts.
A key advantage for the comprehension of epithelial polarity program has been the development of 3-D methods of cell culture: MDCK (Madin Darby canine kidney) and Caco2 (human colorectal adenocarcinoma) cells, when plated on an appropriate ECM substrate, spontaneously growth as cysts. Cysts are polarized spherical monolayer, with an apical site surrounding a central lumen, a lateral and a basal layer contacting ECM. All the cells involved in MDCK and Caco2 cysts formation require a coordinated acquisition of apical-basal polarity, but they do not need apoptosis.
One of the first protein to be relocalized to the nascent lumen is podocalyxin, also called GP135. Podocalyxin is a transmembrane glycoprotein. It is heavily glycosylated in its extracellular portion, thus acts as an anti-adhesive protein, inducing

electrostatic repulsion that favors lumen formation. Podocayxin that accumulates at the nascent apical site at least partially comes from transcytosed peripheral protein [176]. Podocalyxin null mice display kidney developmental defects and perinatal lethality [177].

Here after are described the key steps in MDCK cysts formation:

* when single MDCK cells are plated in 3-D basement membrane culture, apical and basolateral proteins are distributed over the entire plasma membrane, as podocalyxin;

* polarity inversion occurs: podocalyxin relocalizes at the forming lumen, while β-catenin and Na/K-ATPase localize at the baso-lateral side;

* a central patch at cell-cell contact at two-cells stage emerges, it is called AMIS (apical membrane initiation site). It is the nascent apical surface, where apical proteins start to localize, as podocalyxin (while aPKC stays both at AMIS than at the plasma membrane);

* opposing plasma membrane start to separate in PAP (pre apical patch), when tight junctions markers become separated from podocalyxin, but podocalyxin doesn't give an optically resolvable signal;

* cyst further expand by the action of pumps and channels [176] (Figure 15).

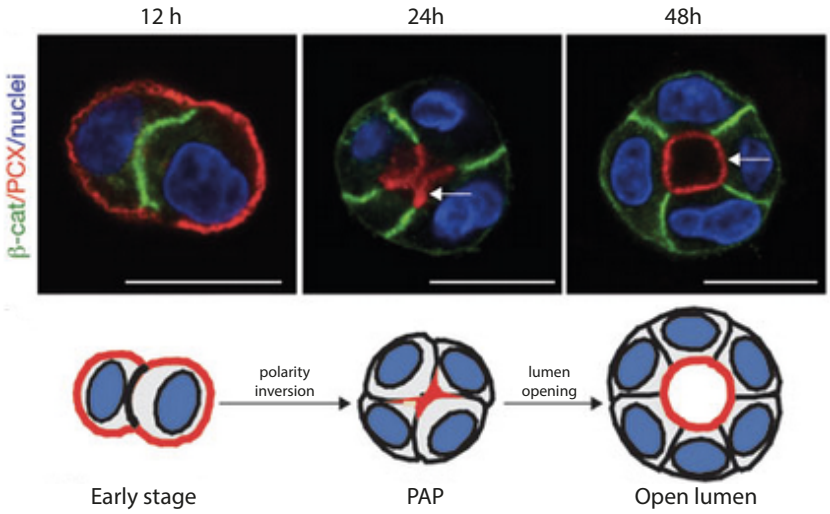

Figure 15. Stages of MDCK cyst development.

Initially the apical marker podocalyxin (in red) is located at the ECM-contacting region of early aggregates (12 h after plating), while β-catenin (in green) is at cell-cell junctions. Polarity inversion then occurs (24 h) and a pre apical patch (PAP) is formed, where podocalyxin stays at the cyst interior. Finally, the lumenal space is opened (48 h). In the lower panel, a cartoon of cyst development is presented (modified from Bryant et al., 2010 [176]).

Molecular mechanism of MDCK cyst generation

Polarity proteins, lipids and RHO GTPases (CDC42, RAC1 and RHOA) organize trafficking and generate junctions, to set apical-basal axis in the developing cyst. Before reorientation of polarity, cells are really motile and use an inverted front-rear polarity to move. Upon single cells plating on matrigel and/or collagen, collagen-mediated activation of β1 integrin occurs, promoting the activation of the complex FAK (focal adhesion kinase)/p190A-RHOA GAP, followed by RAC1 activation.
The activation of RHOA and its effectors ROCK1 (RHO-associated protein kinase) and myosin 2 light chain is then suppressed; if they are active, as before the induction of polarization, they promote ezrin phosphorylation and its association with podocalyxin and NHERF1/EBP50, stabilizing their localization at the cell surface. Later, PKCβII (protein kinase C) phosphorylates podocalyxin and NHERF1, causing the dissociation of the complex podocalyxin:NHERF1:ezrin, podocalyxin is then transcytosed to the AMIS through RAB11a positive vescicles (while NHERF1 is maintained cytoplasmic) [178]. RAB11a regulates apical trafficking and lumen formation [176] together with RAB8a, that localizes in podocalyxin containing vesicles, too. RAB8 is recruited through Rabin8 (a RAB GEF). Vescicle transport is facilitated both by microtubules and actin motors; RAB8a/11a cooperatively bind the actin-based motor protein myosin Vb to transport these vesicles to the AMIS [179]. Also annexin2, a protein that binds PIP_2, transiently associates with RAB11a positive vescicles; RAB11a interacts with Sec15 exocyst subunit (linking also Sec10 subunit), exocyst in turn interacts with PAR3 and aPKC, driving PAR3 to the apical surface and

allowing CDC42 activation. The CDC42 GEF tuba is required for CDC42 apical targeting.

The initial landmark for the formation of the apical region is the site of abscission: following entry into mitosis, RAB11a positive vesicles are accumulated at the cleavage furrow. Apical concentration of PTEN (Phosphatase and tensin homolog on chromosome 10, phosphatase whose substrates are PIP_3 and, with lower affinity, PIP_2), recruited at junctions by PAR3, causes the exclusion of PIP_3 and the apical enrichment of PIP_2, followed by the recruitment of annexin and CDC42 [169]. Apical vesicles then undergo fusion, which is mediated, for example, by syntaxin 3, SLP4 (synaptotagmin-like protein 4), RAB27/RAB3/RAB8 [180].

The exocyst is required for docking of RAB11a positive vesicles to the AMIS, but PAR3 localization and Crumbs3-PALS1-PATJ complex are also required: Crumbs may function to restrict PAR3 to the side of developing lumen.

At the nascent lumen, podocalyxin and NHERF1 are dephosphorylated by PP2A (protein phosphatase), so podocalyxin associates back with NHERF1 and ezrin [176] (Figure 16). Once the lumen is formed, RAB11a vesicles stay in the sub-apical region, as CDC42; CDC42 also stays partially at cell-cell contact. Of note, CDC42 also regulates orientation of cell division with PAR6 and aPKC.

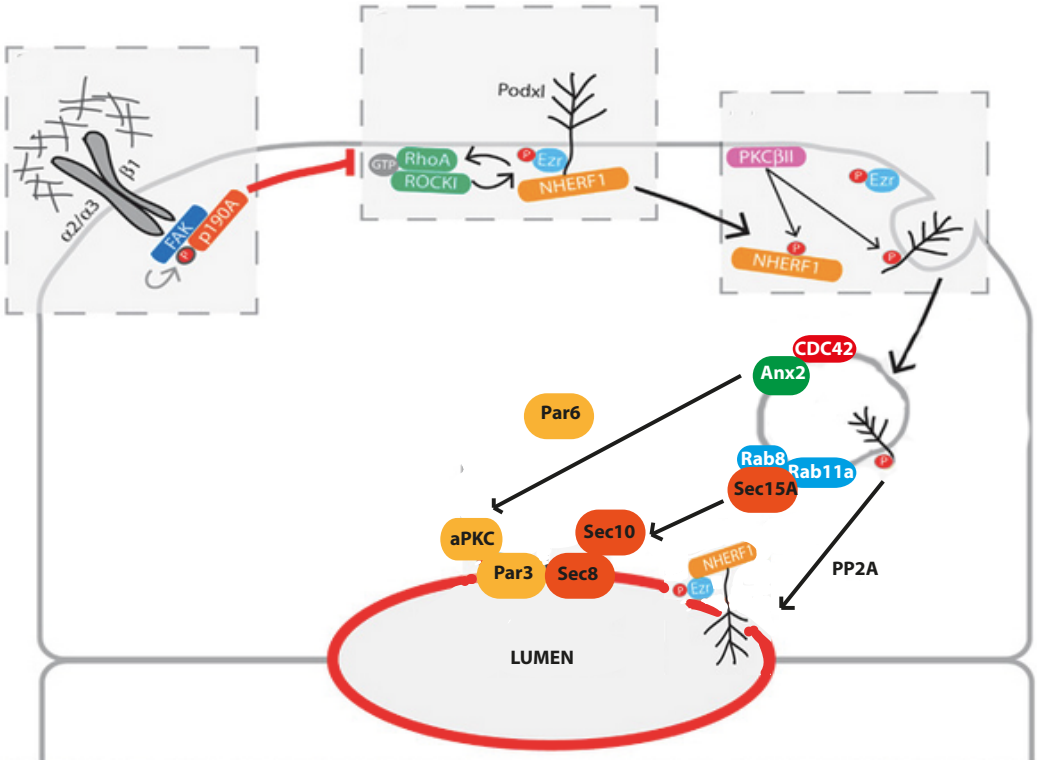

Figure 16. Model of the first events in MDCK cells polarization.

Initially, the podocalyxin (Podxl)-NHERF1-pEzrin (Ezr) complex is stabilized at the cell periphery, by RHOA-ROCKI. After integrin activation, an α2/α3/β1-integrin/FAK/p190A RHOA GAP module down regulates RHOA-GTP at the periphery. PKCβII phosphorylates and dissociates the podocalyxin-NHERF1-Ezrin complex, triggering peripheral podocalyxin endocytosis. Podxl and NHERF2 transcytose to the AMIS; after PP2A action the podocalyxin-NHERF1-Ezrin complex associates back. Podocalyxin positive vesicles transport also CDC42 and annexin2 to the AMIS, CDC42 in turn interacts with PAR3 and PAR6 and activates aPKC. These vescicles are also RAB8 and RAB11a positive, the latter interacts with Sec15 exocyst subunit (modified from Bryant et al., 2010, [176]).

CDC42 KD perturbs single lumen formation in MDCK, causing the accumulation of podocalyxin in vesicles. The same happens in Caco2 cysts, where CDC42 KD causes a multilumen phenotype and spindle misorientation, leading to aberrant cleavage furrow orientation and consequently anomalous positioning of the cells in the cyst [181].

RAB8, RAB11a, aPKC KD also cause defective lumenogenesis and podocalyxin accumulation into vesicles close to the cell surface. aPKC inhibition moreover partially affects podocalyxin internalization from the plasma membrane [176]. Interestingly, the KO of RAB8 or RAB11a in the mouse intestine leads to defective trafficking of apical proteins, illustrating the importance of the RAB11a/RAB8 recycling endosome system *in vivo* [182, 183]. PAR3 KD causes the formation of multiple lumen cysts, which are positive for podocalyxin staining in their apical region [184].

As observed before, differences exist among polarity signalling in different tissues, however, similar events also occur at mouse dorsal aorta, where podocalyxin is targeted to a central patch and stabilized at cell-cell contact by moesin (protein of ERM, ezrin-radixin-moesin, family) to initiate the apical region [185]. In contrast, the mechanism of lumen formation in Caco2 cysts is different from the one used by MDCK cells: it does not involve podocalyxin trafficking. Instead the lumen forms through a process of internal expansion due to fluid accumulation, driven by polarized ion transport. However, also in Caco2 cysts the relocalization of apical markers is observed: for example aPKC is localized around the cell periphery in single cells, while later accumulates in the nascent apical surface [181].

IRSp53 role in cyst development

As mentioned before, it has recently been shown that silencing of IRSp53 leads to a multiple lumen phenotype in MDCK spheroids and other defects in polarity establishment, including disrupted laminin staining around the cyst and retention of podocalyxin at the plasma membrane (indicative of an inverted polarity phenotype) [152]. In Cohen et al., 2011 [152], they observe the same phenotype in PAR1b overexpressing MDCK cells. PAR1B is a serine/threonine kinase that regulates

epithelial lumen [186] and is involved in spindle positioning together with LGN and Numa [187]. Consequently, Cohen et al., 2011 [152] propose a model in which the polarity protein PAR1b regulates IRSp53. In particular, PAR1b directly phosphorylates IRSp53 on S366, and indirectly phosphorylates the cluster S453, S454, S455. These residues, when phosphorylated, are able to recruit 14-3-3, that in turn sequesters IRSp53 and impairs its functions by masking the SH3 domain [152].

Aim of the project

IRSp53 have previously been suggested to act downstream of CDC42 in the regulation of filopodia dynamics. However, the molecular mechanisms exploited by this axis and the players controlling actin dynamics and architectural organization have remained, by and large, elusive. Hence, we set out to investigate more in details the role of IRSp53 on actin dynamics and asked whether IRSp53 interactors, other than Mena, were involved in modulating IRSp53 role in filopodia formation.

To this end, we will use a combination of biochemical assays, to analyse the effect of IRSp53 and its interactors on actin polymerization, and cell biology approaches by taking advantage of IRSp53 null and reconstituted cell lines, to explore the biological relevance of our findings.

In the second part of this thesis, an additional, novel role of IRSp53 will be discussed. Following the sparse evidences in literature pointing to the involvement of IRSp53 in the polarity program, we decided to investigate the role of this protein in the establishment of 3-D cysts. In particular we will exploit the epithelial cell lines MDCK and Caco2 as *in vitro* models that recapitulate the morphogenetic program of gland formation: both these cells lines have been vastly used in literature to unveil the mechanisms of polarization and lumenogenesis.

Materials and methods

1 Common laboratory solutions

Phosphate-buffered saline (PBS)

137 mM NaCl

2.7 mM KCl

10 mM Na_2HPO_4

2 mM KH_2PO_4

The solution is prepared by dissolving 8 g of NaCl, 0.2 g of KCl, 1.44 g of Na_2HPO_4, and 0.24 g of KH_2PO_4 in 800 mL of distilled water. The pH is adjusted to 7.4 with HCl and distilled H_2O is added to 1 litre.

Tris HCl (1 M)

Prepared by dissolving 121.1 g of Tris base in 800 mL distilled H_2O. The pH is adjusted (depending on the case) with HCl, and distilled H_2O is added to 1 litre.

10X Tris EDTA (pH 7.4-8.0)

100 mM Tris HCl (pH 7.4-8.0)

10 mM EDTA (pH 8.0)

50X TAE (Tris-Acetate-EDTA)

242 g/L Tris base

57.1 mL/L Acetic acid

20 mL/L 0.5 M EDTA pH 8

The pH is adjusted to 8.5 with HCl and distilled H_2O is added to 1 litre.

Tris-buffered saline (TBS)

137 mM NaCl

2.7 mM KCl

25 mM Tris base

It is prepared by dissolving 8 g of NaCl, 0.2 g of KCl and 3 g of Tris base in 800 mL of distilled H2O. The pH is adjusted to 7.4 with HCl and distilled H_2O is added to 1 litre final volume.

1.4X JS lysis buffer

50 mM HEPES pH 7.5

50 mM NaCl

1% glycerol

1% Triton X-100

1.5 mM $MgCl_2$

5 mM EGTA

To this solution phosphatases and proteases inhibitors were freshly added:

Protease inhibitor cocktail (Roche, Basel, Switzerland)

1 mM DTT

20 mM Na pyrophosphate pH 7.5

50 mM NaF

0.5 M Na-vanadate in HEPES pH 7.5

5X (2X) SDS-PAGE Sample Buffer

10% (4%) SDS

500 mM (200mM) Tris HCl pH 6.8

30% (12%) glycerol

0.03% (0.0012%) saturated bromophenol blue

15% (6%) (v/v) β-mercaptoethanol (14M)

10X SDS-PAGE Running Buffer

144 g/L Glycine

30 g/L Tris base

1% SDS

10X Western Transfer Buffer

144 g/L Glycine

30 g/L Tris base

Diluted at 1X concentration in 10% of EtOH.

Ponceau S

0.1% (w/v) Ponceau ($C_{22}H_{12}N_4Na_4O_{13}S_4$) (Sigma)

5% Acetic acid

2 Basic cloning techniques

Agarose gel electrophoresis

DNA samples were loaded on 0.8%-2% agarose gels along with DNA markers. Gels were made in TAE buffer containing 0.3 μg/mL ethidium bromide or GelRed™ Nucleic Acid 1:10000 (Biotium, Italy) and run at 80-100 V until desired separation was achieved. DNA bands were visualized under a UV lamp.

Minipreps

E. coli Top10 Cells (Thermo Fisher Scientific) were picked from individual transformed colonies, then used to inoculate 6 mL LB (containing the appropriate antibiotic) and grown overnight at 37°C in 15mL Falcon tubes. Cells were pelleted for 15 minutes at 2500 rpm. Minipreps were performed according to the manual instructions (Promega, Wizard Plus SV Minipreps). The final elution was made in 80μl of milli-Q water. DNA was checked performing an agarose gel electrophoresis using 5μl of the eluate.

LB

1% Bactotryptone

0.5% Yeast extract

1% NaCl

pH 7.25

DNA digestion

Between 0.5 and 2 μg of DNA was digested for 2 hours at 37°C with 10 units of the needed restriction enzymes (NEB). Reaction volume was adjusted to 20 μl with the appropriate 10X NEB buffer and ddH_2O.

Ligation

Ligation was performed with Quick Ligation kit (NEB), according to the manual instructions.

Large Scale Plasmid Preparation

E. coli Top10 Cells (Thermo Fisher Scientific) containing the desired DNA vector were expanded into 500 mL cultures overnight with the appropriate antibiotics. Plasmid DNA was isolated from these cells using the Qiagen Maxi-prep kit (Qiagen,Valencia, CA) according to the manufacturer's instructions and finally resuspended in Tris EDTA buffer.

Transformation of competent cells

E. coli one shot Top10 cells (Thermo Fisher Scientific) were used for cloning and large scale DNA preparation, while *E. coli* BL21 Rosetta (DE3) cells (Promega) were used for proteins production. The transformation protocol used was the same for both strains.

50 μl of fresh competent cells were thawed on ice for approximately 10 minutes prior to the addition of plasmid DNA. Cells were incubated with DNA on ice for 20 minutes

and then subjected to a heat shock for 45 seconds at 42°C. Cells were then returned to ice for 2 minutes. Then, 0.2 mL of SOC were added and the cells were left at 37°C for 60 minutes (with 200 rpm shaking) before plating them onto plates with the appropriate antibiotic. 50 μl of the transformed bacteria were usually plated. Plates were incubated overnight at 37°C.

SOC

2% Bactotryptone

0.5% Yeast extract

10 mM NaCl

2.5 mM KCl

10 mM $MgCl_2$

10 mM $MgSO_4$

20 mM glucose

pH 7.5

DNA elution from agarose gel

DNA elution from agarose gel was performed using the Wizard SV Gel and PCR Clean-Up System (Promega), following manufacturer's instructions.

PCR (Polymerase Chain Reaction)

Sense and antisense oligos, of 20-30 nucleotides each, were generated, one annealing in 5' (forward) and the other in 3' (reverse) to the target sequence. The primers were designed of similar length and annealing temperature. Melting temperature of the primers was calculated according to the formula: Tm = 81.5+0.41(%GC) - 675\N - % mismatch. These primers were used in a PCR reaction together with the DNA template and the Phusion High-Fidelity DNA Polymerase (NEB).

Reaction mixture

5x Phusion HF buffer	10 µl
DNA template	10-20 ng
primer forward	0.5 µM
primer reverse	0.5 µM
dNTPs mix	0.2 mM
Phusion Polymerase (NEB)	1 U
ddH_2O	to a final volume of 50 µl

Cycling parameters:

Step	Temperature	Time	N° of cycles
A)	denaturation at 98°C	30 seconds	1
B)	denaturation at 98°C	10 seconds	
	annealing at X°C	30 seconds	25
	extension at 72°C	(30 seconds/each kb of target length)	
C)	extension at 72°C	10 minutes	1

This was done on an automated cycler (GeneAmp PCR system 9700, Applied Biosystems).

Site directed mutagenesis

Site directed mutagenesis was performed using the Quick Change mutagenesis kit (Stratagene), following manufacturer's instructions. Briefly, a sense and an antisense oligo of about 30-45 nucleotides each, carrying the desired mutation in the middle of the sequence, were generated and used in a PCR reaction using the wild type construct as template. PCR was performed using the Pfu DNA Polymerase (Promega).

Reaction mixture

10X Pfu buffer	10 µl
DNA template	10-100 ng
primer forward	0.125 µM
primer reverse	0.125 µM
dNTPs mix	0.2 mM
Phusion Polymerase (NEB)	3 U
ddH_2O	to a final volume of 50 µl

For the amplification step, 18 PCR cycles were performed with a denaturation step of 30 seconds at 95°C, followed by an annealing step of 1 minute at 55°C and an extension step at 68°C of 2 minutes/each kb of plasmid length.

After amplification, 2 µl of DpnI restriction enzyme (NEB), which selectively cuts methylated DNA at the GATC sequence, was added to digest the wild type parental DNA. After one hour incubation at 37°C, the PCR product was checked by DNA electrophoresis and used to transform competent *E. coli* Top10 cells (Thermo Fisher Scientific). Single colonies were sequenced for the presence of the desired mutation and the absence of other, unwanted, base changes.

Generation of IRSp53 constructs

All the used constructs encode for the S (short) isoform of IRSp53, that possesses a PDZ binding domain at the C-terminus. Flag–IRSp53 was a gift from S. Ahmed (Neural Stem Cell Laboratory, Institute of Medical Biology, Singapore) and it was used to subclone IRSp53 in pBABE vector (Cell Biolabs). pEGFP–IRSp53 was a gift from H. Nakagawa (Austrian Academy of Sciences, Vienna Austria) and used to subclone IRSp53 in pTrcHis-A (Thermo Fisher Scientific) or pmCherry-C1 (Clonetech) vectors, performing BamHI-BamHI digestions.

IRSp53 deletion constructs were generated by PCR, using as a template pTrcHisA-IRSp53 vector. To clone the different constructs, specific primers were designed, flanked by BamHI and EcoRI sites (or EcoRI and SalI sites). DNA fragments were then subcloned in an empty pGEX-6P-1 (Amersham) vector. Used primers are listed in the table below:

1-250 aa	Fwd: 5'-GCGGATCCTCTTTGTCTCGCTCAGAGGA-3' Rev: 5'-GCGAATTCTCAGTTGCTGGCCACCTGCTG-3'
1-290 aa	Fwd: 5'-GCGGATCCTCTTTGTCTCGCTCAGAGGA-3' Rev: 5'-GCGAATTCTCACATCCGCCCCACGAACG-3'
1-309 aa	Fwd: 5'-GCGGATCCTCTCTGTCTCGCTCAGAGGA-3' Rev: 5'-GCGAATTCGTCCTCGCCATCCGGGCC-3'
1-339 aa	Fwd: 5'-GCGGATCCTCTCTGTCTCGCTCAGAGGA-3' Rev: 5'-GCGAATTCGTTGGAGTAGGAGTCGCTGA-3'
1-374 aa	Fwd: 5'-GCGGATCCTCTCTGTCTCGCTCAGAGGA-3' Rev: 5'-GCGAATTCATTGCGCTCCAGGCCGGC-3'
1-437 aa	Fwd: 5'-GCGGATCCTCTTTGTCTCGCTCAGAGGA-3' Rev: 5'-GCGAATTCTCAACTGCCATCGCTGTCCA-3'
290-521 aa	Fwd: 5'-GCGGATCCATGTCTGCCCAGGAGAGCAC-3' Rev: 5'-GCGAATTCTCACACTGTGGACACCAGC-3'
375-437 aa	Fwd: 5'-GCGAATTCGGCCGTATGCGGGTGAAGGC-3' Rev: 5'-GCGTCGACTCAACTGCCATCGCTGTCCA-3'

IRSp53 W413G mutant was generated by site directed mutagenesis

Other constructs

CDC42 N17 and L61 were cloned in pRK5 vector (with a myc tag) for mammalian expression, CDC42 was cloned in pGEX vector for bacterial purification. VASP was cloned in pEGFP vector for mammalian expression or pGEX/pTRCHisA for bacterial purification. EPS8 was cloned in pFL vector (kindly given by A. Musacchio, Max Planck Institute, Dortmund) carrying His tag motif for baculovirus expression. pFUW lentiviral vectors encoding GFP, GFP-IRSp53 WT and GFP-IRSp53 mutants (in I-BAR domain: 4KtoE on positions 142, 143, 146, 147, CRIB domain: I268N, SH3 domain: I403P, PDZ domain: V522G) were gifts from Hans-Jurgen Kreienkamp (University of Hamburg). Apple-RAB11a was kindly given by K. Mostov (University of California, San Francisco).

3 Reagents and antibodies

The monoclonal anti-IRSp53 was generated against the full-length His-tagged purified protein (Disanza et al., 2006 [160]). Others antibodies used were: rabbit polyclonal anti-IRSp53 (Sigma), monoclonal anti-EPS8 (Transduction Laboratories), anti-vinculin (Sigma), anti-tubulin (Sigma), anti-myc (Babco), anti-VASP (Cell Signaling), rabbit polyclonal anti-aPKC ζ (C-20, Santa Cruz Biotechnology), anti-ZO-1 (Thermo Fisher Scientific), anti-podocalyxin (3F2/D8, DSHB, University of Iowa, deposited by G. Ojakian), anti-βcatenin (Sigma), anti-GFP (gift from Jan Faix, Hannover), anti-EEA-1 (N-19, Santa Cruz Biotechnology), anti-Giantin (Covenance), anti-RAB7 (Cell Signaling), anti-Lamp1 (Sigma).

Secondary antibodies conjugated to horseradish peroxidase were from Bio-Rad; FITC- and Cy3-secondary antibodies from Jackson ImmunoResearch, AlexaFluor 488 was from Molecular Probes, TRITC- and FITC-conjugated phalloidin were from Sigma. Growth Factor Reduced Matrigel™ Matrix Basement Membrane and Collagen I were from BD Biosciences. Laminin, gelatin and fibronectin were from Sigma.

4 Biochemical procedures

SDS polyacrylamide gel electrophoresis (SDS-PAGE)

Gels for resolution of proteins were made from a 30%, 37.5:1 mix of acrylamide:bisacrylamide (Sigma). As polymerisation catalysts, 10% ammonium persulphate (APS) and TEMED (Fluka) were used.

Running gel mix

	7.5%	8%	10%	15%
acrylamide mix (ml)	5.625	6	7.5	11.25
1.5M Tris pH 8.8 (ml)	7.5	7.5	7.5	7.5
distilled water (ml)	16.275	15.9	14.4	10.65
10% SDS (ml)	0.3	0.3	0.3	0.3
10% APS (ml)	0.3	0.3	0.3	0.3
TEMED (ml)	0.03	0.03	0.03	0.03
Total (ml)	30	30	30	30

Stacking gel mix

acrylamide mix (ml)	1.7
1M Tris pH 6.8 (ml)	1.25
distilled water (ml)	6.8
10% SDS (ml)	0.1
10% APS (ml)	0.1
TEMED (ml)	0.01

Western blot

The desired amounts of proteins were added with 5X SDS-PAGE sample buffer and loaded onto 0.75-1.5 mm thick polyacrylamide gels for electrophoresis (Bio-Rad). Proteins were transferred in a Western transfer tanks (Bio-Rad) to Protran Nitrocellulose Transfer membrane (Whatman) in Western Transfer buffer 1X (diluted in 10% ethanol) at constant voltage (100 V for 1 hour, 80 V for 2 hours or 30 V overnight). Ponceau S was used to reveal the amount of proteins transferred onto the filters. Filters were blocked 1 hour (or overnight) in 5% milk in TBS 0.1% Tween (TBS-T).

After blocking, filters were incubated with the primary antibody, diluted in TBS-T 5% milk, for one hour at room temperature, or overnight at 4˚C; followed by three washes of five minutes each in TBS-T and then incubated with the appropriate peroxidase-conjugated secondary antibody diluted in TBS-T for 1 hour. After the incubation with the secondary antibody, the filter was washed three times in TBS-T and the bound secondary antibody was revealed using the ECL (Enhanced Chemiluminescence) method (Thermo scientific).

GST-fusion and His-fusion protein production

His-tagged IRSp53 WT and W413G

E. coli BL21 bacteria transformed with pTrcHis-A vector (Thermo Fisher Scientific) in which IRSp53 WT or W413G has been cloned, were used to inoculate 50 ml LB containing ampicillin 25 μg/ml and were grown overnight at 37°C. 5 ml of the overnight culture were diluted in 500 ml LB and grown at 37°C (240 rpm shaking) till it reached approximately OD=0.6, then induced with 1 mM IPTG at 37°C for 3.5 hours. Bacteria were then pelleted down at 2000 rpm for 25 minutes at 4°C and pellets were resuspended in His-lysis buffer (10 ml every liter of culture)

His-lysis buffer

50 mM Tris pH 8

300 mM NaCl

10 mM imidazole

1 mM β-mercaptoethanol

protease inhibitors

10% glycerol

Samples were sonicated and ultracentrifugated (at 40000 rpm for 45 minutes at 4°C, using a 50.2 Ti Beckman rotor), finally the supernatant was incubated with Ni-NTA agarose beads (Qiagen), pre-equilibrated in His-lysis buffer (600 µl slurry every liter of culture), for 1.5 hours at 4°C, rocking. Beads were then washed two times in buffer 1 and once in buffer 2

Buffer 1

20 mM imidazole

600 mM NaCl

50 mM Tris pH 8

1 mM β-mercaptoethanol

10% glycerol

Buffer 2

40 mM imidazole

300 mM NaCl

50 mM Tris pH 8

1 mM β-mercaptoethanol

10% glycerol

Beads were then packed in Poly-Prep Chromatography columns (Bio-Rad), His-fusion proteins were eluted from beads in elution buffer, collecting 8-10 fractions of 500 µl each, in clean tubes.

Elution buffer

200 mM imidazole

50 mM Tris pH 8

200 mM NaCl

1 mM β-mercaptoethanol

10% glycerol

(1 mM EDTA was added directly to the tube)

The eluted fractions were evaluated through SDS-PAGE, selected fractions were collected together and their buffer was exchanged using PD10 columns (GE Healthcare).

Exchange buffer

50 mM Tris pH 6.8

100 mM NaCl

5% glycerol

1 mM DTT

0.5 mM EDTA

The sample was diluted in dilution buffer just before the injection on Resource S column (GE Healthcare), on an AKTA purifier system (Amersham Bioscience), elution was performed following a 0→50% B gradient of 60 CV (column volume) length.

Dilution buffer

50 mM Tris pH 6.8

5% glycerol

0.5 mM EDTA

ResS buffer A

50 mM NaCl

50 mM Tris pH 6.8

5% glycerol

1 mM EDTA

1 mM DTT

ResS buffer B

1 M NaCl

50 mM Tris pH 6.8

5% glycerol

1 mM EDTA

1 mM DTT

Fractions (1.2 ml each) were evaluated through SDS-PAGE, the selected one were collected and concentrated with Vivaspin concentrators (Vivaspin 20 MWCO 100000, Sartorius Stedim Biotech). Sample was then loaded on a Superdex 200 10/300 gel filtration column (GE Healthcare), equilibrated in storage buffer, on an AKTA purifier system (Amersham Bioscience).

Storage buffer

50 mM Tris pH 7.5

200 mM NaCl

1 mM DTT

10% glycerol.

The best fraction identified in SDS-PAGE gel were collected together, concentrated, flash frozen using liquid nitrogen and stored at -80°C until use.

GST-VASP

E. coli BL21 bacteria transformed with pGEX-6P-1 vector in which VASP has been cloned, were used to inoculate 50 ml LB containing ampicillin 25 μg/ml and were grown overnight at 37°C. 5 ml of the overnight culture was diluted in 500 ml LB and grown at 37°C (240 rpm shaking) till it reached approximately OD=0.6, then induced with 0.5 mM IPTG at 16°C overnight. Cells were then pelleted down at 2000 rpm for 25 minutes at 4°C and pellets were resuspended in buffer A

Buffer A

50 mM Tris pH 7.4

500 mM NaCl

1 mM $MgCl_2$

1 mM DTT

0.1% Triton X-100

protease inhibitors

Samples were sonicated and ultracentrifugated (at 40000 rpm for 45 minutes at 4°C, using a 50.2 Ti Beckman rotor), finally the supernatant was incubated with Glutathione Sepharose 4B beads (GE Healthcare), pre-equilibrated in buffer A without Triton X-100 nor protease inhibitors, for 1 hour at 4°C, rocking. Beads were then washed with the same buffer. Proteins were cleaved from the GST using the PreScission protease (Amersham Pharmacia Biotech) according to the manufacturer's instructions, otherwise eluted by competition with glutathione. Cleaved protein was then loaded on a Superdex 200 10/300 gel filtration column (GE healthcare), equilibrated in dyalisis buffer, on an AKTA purifier system (Amersham Bioscience).

Dialysis buffer

50 mM Tris pH 7.5

200 mM NaCl

1 mM DTT

5% glycerol

The best fraction identified in SDS-PAGE gel were collected together, concentrated with Vivaspin concentrators (Vivaspin 20 MWCO 100000, Sartorius Stedim Biotech), flash frozen using liquid nitrogen and stored at -80°C until use.

GST-IRSp53 mutants and GST-SH3

IRSp53 truncated constructs were cloned in pGEX-6P-1 vectors and purified following the same protocol as indicated in GST VASP, with the only exception that *E. coli* BL21 bacteria were induced at OD=0.6 with 1 mM IPTG at 37°C for 3 hours.

His-VASP and His-VASP-DdGAB

E. coli BL21 bacteria transformed with pTrcHis-A vector (Thermo Fisher Scientific) in which VASP had been cloned, were used to inoculate 50 ml LB containing ampicillin 25 μg/ml and were grown overnight at 37°C. 5 ml of the overnight culture was diluted in 500 ml LB and grown at 37°C (240 rpm shaking) till it reached approximately OD=0.6, then induced with 0.5 mM IPTG at 16°C overnight. Cells have been resuspended in His-lysis buffer, sonicated, ultracentrifugated, and supernatant was incubated with Ni-NTA agarose beads (Qiagen), as written in *His-tagged IRSp53 WT* purification protocol.

Beads were then washed in washing solution and eluted.

Washing solution

20 mM imidazole

1 M NaCl

50 mM Tris pH 8

1 mM β-mercaptoethanol

Elution buffer

200 mM imidazole

150 mM NaCl

50 mM Tris pH 8

1 mM β–mercaptoethanol

(1 mM EDTA directly added to the tube)

Eluted fractions were subjected to SDS-PAGE and dialyzed in dialysis buffer. The sample was then concentrated using Vivaspin concentrators (Vivaspin 20 MWCO 100000, Sartorius Stedim Biotech) before loading on a Superdex 200 10/300 gel filtration column (GE healthcare), equilibrated in dialysis buffer, on an AKTA purifier system (Amersham Bioscience). The best fraction identified in SDS-PAGE gel were collected together, concentrated with Vivaspin concentrators, flash frozen using liquid nitrogen and stored at -80°C until use.

GST-CDC42 purification and loading

E. coli BL21 bacteria transformed with pGEX-CDC42 were grown and induced as described for GST-IRSp53 mutants. Purification was performed as previously described for GST-VASP; GST-CDC42 was detached from Glutathione Sepharose 4B beads (GE Healthcare) by competition with glutathione (20 mM Tris pH 8, 50 mM NaCl, GSH 10 mM), since the vector do not contain a PreScission protease cleavage site.

The loading was performed mixing

30 μM of purified protein

15 mM GTP-γ-S or GDP (Sigma)

5 mM EDTA

for 20 minutes at room temperature. The exchange reaction was stopped adding 20 mM $MgCl_2$.

His-EPS8

His-EPS8 protein was produced in Baculovirus system, EPS8 was cloned in pFL vector. Transposition was made using DH10MultiBac-YFP electro competent cells (a gift from A. Musacchio) that were electroporated in presence of 1 µl of DNA from an average yield miniprep. Selection of the recombinant bacteria was made after plating on LB plates containing 50 µg/mL kanamycin, 7 µg/mL gentamycin, 10 µg/mL tetracycline, 200 µg/mL X-gal, 40 µg/mL IPTG at least 48 hours. White recombinant colonies were selected and bacmid DNA was isolate using the Wizard Plus SV Minipreps kit (Promega) with a slight protocol modification: because the bacmid DNA is too big to be eluted with the kit columns, DNA was extracted using isopropanol precipitation.

Bacmid DNA was then used to transfect Sf21 insect cells (Thermo Fisher Scientific) in order to produce the virus. Sf21 cells were plated at $0.5*10^6$/mL in a six well plate and transfected using Insectogene reagent (Biontex Laboratories), according to manufacturer's instruction. Cells transfection was monitored looking at the appearance of YFP positive cells. After 72 hours the surnatant was collected (this was the V0, primary stock virus production). The virus was amplified in H5 cells (Thermo Fisher Scientific). 25 mL of H5 cells at $0.5*10^6$/mL were infected using 1.5 mL of the V0 virus. Cells infection was monitored looking at the appearance of YFP positive cells and the cells growth arrest, that is caused by the viral infection. After 72 hours from the cell growth arrest the surnatant was collected (this is the V1 generation). The virus was amplified a second time using 200 mL of H5 cells infected with 2.5 mL of the V1 virus.

Protein production was finally began, starting from 500 mL of H5 cells at $0.5*10^6$ cells/mL infected with 12.5 mL of V2 virus. For protein purification, the cells were harvested three days after infection. Cells pellet was resuspended in phosphate buffer.

Phosphate buffer

20 mM phosphate buffer pH 8

10 mM imidazole

500 mM NaCl

1 mM β–mercaptoethanol

5% glycerol

protease inhibitors

After sonication and ultracentrifugation, the supernatant was incubated with Ni-NTA agarose beads (Qiagen) (previously washed twice in phosphate buffer) for one hour. Beads were then washed in washing buffer and eluted (as described for His IRSp53).

Washing buffer

20 mM phosphate buffer pH 8

20 mM imidazole

1 M NaCl

1 mM β–mercaptoethanol

5% glycerol

Elution buffer

20 mM phosphate buffer pH 8

100 mM imidazole

500 mM NaCl

1 mM β–mercaptoethanol

5% glycerol

(1 mM EDTA was added directly to the tube).

Eluted fraction were evaluated through SDS-PAGE, selected fractions were pulled and loaded on a Superdex 200 10/300 gel filtration column (GE Healthcare), equilibrated in storage buffer, on an AKTA purifier system (Amersham Bioscience).

Storage buffer

100 mM Tris pH 8

20 % glycerol

1 mM DTT

1 mM EDTA

500 mM NaCl

The best fractions identified in SDS-PAGE gel were collected together, flash frozen using liquid nitrogen and stored at -80°C until use.

Alexa labelling

Purified protein was concentrated until at least 2 mg/ml, dyalized O/N against PBS pH 7. The following day, protein was incubated for 1 hour at room temperature in the dark with Alexa Fluor 488 or 555 (succinimidyl ester, that reacts with primary amines, or maleimide, that reacts with thiols, diluted in DMSO) 0.1 mg every 1 mg of total protein, with gentle rocking. Finally the labelled protein was gel filtered and treated accordingly to the procedures described before.

Other proteins

The proteins CP, profilin and spectrin-actin seeds were a kind gift from Dr. Marie-France Carlier (LEBS-CNRS-Gif sur Yvette, France). IRSp53 mutants P278D/P281D and I267A/S268A were from D. Kast (University of Pennsylvania, Perelman school of medicine, Philadelphia, USA). VASP ΔPRD, VASP $\Delta(GP5)_3$, VASP DdGAB were from J.

Faix (Hannover Medical School, Germany) and purified as in Breitsprecher et al., 2008 [106].

Co-immunoprecipitation assay

HeLa cells were transfected with the appropriate vectors using lipofectamine, lysed after 24 hours in JS buffer with the indicated antibody, in presence of sepharose beads IgA or IgG coupled, for two cycles of 2 hours each at 4°C with rocking. After washing steps, beads were resuspended in SDS-PAGE sample buffer, boiled for 10 min at 95°C and then loaded onto polyacrylamide gels. Proteins were detected via immunoblotting.

In vitro binding assay

The indicated proteins (tipically at around 0.5 μM) were mixed together with Ni-NTA agarose beads (Qiagen) or Glutathione sepharose beads (GE Healthcare) for one hour at 4°C, in mild agitation. After washing steps, beads were collected and eluted with SDS-PAGE Sample Buffer. Samples were then boiled for 10 min at 95°C and loaded onto polyacrylamide gels. Proteins were detected using Ponceau staining or the indicated antibodies.

IVB buffer

50 mM Tris pH 7.5

300 mM NaCl

1 mM DTT

0.1% Triton X-100

(20 mM imidazole was used to prevent unspecific binding when Ni-NTA beads were used; 20 mM $MgCl_2$ was used to preserve the nucleotide-loaded state of CDC42, when added)

Dynamic light scattering (DLS)

Purified proteins were dialysed for at least 6 hours in DLS buffer.

DLS buffer

50 mM Tris pH 7.5

100 mM NaCl

1mM DTT.

Prior to the experiment, mixtures of proteins were incubated for 30 min at 20°C to allow for the formation of the complexes. DLS was carried out at 20°C on a Malvern Viscothek instrument equipped with a 633 nm He-Ne laser. The measurement duration was 4 sec, and 100 measurements were averaged for each analysis. The distributions of the mean apparent translational diffusion coefficients (D_T) were determined by fitting the DLS autocorrelation functions using nonnegative constrained least squares (Hayes 1995, Program Sednterp: Sedimentation Interpretation Program version 1.09. Alliance Protein Laboratories, Thousand Oaks, CA, USA.). The distribution of apparent diameters D_h was obtained from the distribution of mean apparent translational diffusion coefficients (D_T) via $D_h = 2kT/(6\pi\eta D_T)$ where k is the Boltzmann constant, and η is the solvent viscosity calculated from the buffer composition using SEDNTERP (Hayes 1995, Program Sednterp: Sedimentation Interpretation Program version 1.09. Alliance Protein Laboratories, Thousand Oaks, CA, USA.).

Liposomes flow cytometry

Liposome preparation. A plasma membrane-like mixture of membrane lipids, including 0, 2.5, 5 or 10% PIP_2 (phosphatidylinositol-(4,5)-bisphosphate) was prepared from individual chloroform stock solutions (Avanti Polar Lipids). The mix composition (in mol%) was the following: 17.5% PC (phosphatidylcholine), 5% PS (phosphatidylserine), 5% PI (phosphatidylinositol), 9% PE

(phosphatidylethanolamine), 50% CL (cholesterol), 12.5% SM (sphingomyelin), 1% rhodamine-labelled PE (PE-N-(lissamine rhodamine B sulfonyl), rhod-PE), and 0, 2.5, 5 or 10% PIP_2. The PIP_2 content was increased at the expense of phosphatidylcholine. A homogeneous lipid film was obtained by drying the lipid mixture in a round bottom glass flask at room temperature under nitrogen and an additional 45 min under vacuum. The lipid film was rehydrated in reconstitution buffer (50 mM Tris HCl pH 7.4, 200 mM NaCl) containing 10% sucrose. The obtained solution was subjected to 10 freeze/thaw cycles and 21 size extrusion steps (mini extruder; Avanti Polar Lipids, pore size 1000 nm). Liposomes were checked for homogeneity using DLS, stored at 4°C and used within 5 days.

Flow Cytometry. Liposomes were incubated with the indicated proteins and analysed with a FACS Calibur instrument, and data were processed with CellQuest Pro software (Becton Dickinson) as described Temmerman et al., 2009 [188].

Solid-phase binding assays

Solid phase assays to probe the interactions between VASP, GST-IRSp53 SH3 and profilin IIa were done as described in Veniere et al., 2009 [189]. Profilin IIa was coated in microplates, ligand binding was monitored using an antibody-based method.

5 Biochemical actin-based assays

Common buffers

G buffer was used to keep actin in the monomeric state (G = globular)

G Buffer

5 mM Tris-HCl pH 7.8

0.2 mM ATP pH 7.0

1 mM DTT

0.1 mM $CaCl_2$

F buffer was used to keep actin in the polymerized state (F = filamentous)

F Buffer

5 mM Tris-HCl pH 7.8

0.2 mM ATP pH 7.0

1 mM DTT

0.1 mM $CaCl_2$

1 mM $MgCl_2$

0.2 mM EGTA

0.1 M KCl

Actin purification

Actin was purified starting from Rabbit muscle acetone powder (Pel-Frezez Biologicals, Rogrs, Arkansas) according to the following protocol.

Nine gr of acetone powder were extracted with 270 ml cold buffer X on ice in a 500 ml beaker. Buffer was slowly added with gentle stirring with a glass rod to thoroughly wet powder. The resuspension was set on ice for 30 min and stirred gently once every 10 min. The preparation was then centrifuged at 25000 g at 4˚C for 45 min. Supernatant was filtered using a cotton lint into a graduated cylinder and transferred into a beaker. Solid KCl was added to a final concentration of 3.3 M while stirring (at room temperature until the sample reaches 15˚C) and moved back on ice without stirring until temperature returned to 5˚C. The sample was centrifuged at 25000 g, for 30 min at 4˚C. Tight white pellets, if any, is actinin. Supernatant was dialyzed against 32 volumes of buffer D overnight. Final KCl concentration was 0.1 M.

After overnight dialysis 4M KCl was added to give a final concentration of 0.8 M and the preparation was stirred for 1.5 hours at 4˚C in order to solubilize tropomyosin. The preparation was then centrifuged at 100000 g for 3.5 hours at 4˚C. Supernatant

was discarded. Pellets were homogenized with a potter in 25 ml buffer X. Once added 0.075 ml $MgCl_2$ 1 M and 0.375 ml KCl 4 M, the volume was adjusted to 38.6 ml with buffer X and the prep was left at 4˚C overnight without stirring.

The day after 9 ml KCl 4 M and 2.37 ml of buffer X were added and the preparation was stirred for 1.5 hours at 4˚C and then centrifuged at 100000 g for 3.5 hours at 4˚C. Pellet was homogenized in buffer X (20-30 ml) and the resuspension was dialyzed against 1 liter of G buffer.

The day after the prep was briefly sonicated in the dialysis bag, 1 x 10 seconds and the dialysis buffer was changed.

After two days of dialysis in G buffer (with daily change of the buffer) actin was clarified at 230000 g for 2 hours at 4˚C. The prep was loaded onto a Superdex 200 26/60 column (GE Healthcare) and run using an Amersham Biosciences AKTA Purifier. Fractions of 5 ml were collected. Protein concentration was measured using UV absorbance (290 nm instead of 280 nm because ATP interferes at 280 nm wavelength). Actin concentration was calculated using the following formula:

[μM] = (OD 290 nm/0.617) * (1/42)

where 0.617 is the OD of actin at 290 nm when concentrated 1mg/ml, and 42 is the actin molecular weight (kDa).

X Buffer

2 mM Tris-HCl pH 7.8

0.5 mM ATP pH 7.0

0.1 mM $CaCl_2$

1 mM DTT

D Buffer

2 mM Tris-HCl pH 7.8

1 mM $MgCl_2$

1 mM DTT

Pyrenyl-actin labelling

Actin was purified as described above and the labelling protocol was started at the end of the third day. Actin is labelled on cysteine 374.

After centrifugation the pellet was resuspended in buffer A to a final concentration of 2 mg/ml. 1:100 volume of N-(1-pyrenyl)iodoacetamide (Molecular Probes, Thermo Fisher Scientific) at 14 mg/ml in DMF was added and the sample was gently mixed until it became white. Actin was then incubated overnight at 4°C rocking. From this moment actin has to be kept always in the dark.

After overnight incubation, DTT was added to 1 mM final concentration and the sample was centrifuged at 4000 g for 15 min. Supernatant was then centrifuged again at 100000 g for 3.5 hours at 4˚C. Pellet was homogenized in 5 ml of buffer G and dialyzed against one liter of buffer G overnight at 4˚C.

The day after the prep was briefly sonicated in dialysis bag, 1 x 10 seconds and the dialysis buffer was changed.

After 2 days of dialysis in G buffer (with daily change of the buffer) actin was clarified at 230000 g for 2 hours at 4˚C. The prep was loaded onto a Superdex 200 26/60 column (GE Healthcare) and run using an Amersham Biosciences AKTA Purifier. Fractions of 5 ml were collected. Protein concentration was measured using UV absorbance (290 nm instead of 280 nm because ATP interferes at 280 nm wavelength). Actin concentration was calculated using the following formula:

$[\mu M] = (OD\ 290\ nm/0.617) * (1/42)$

where 0.617 is the OD of actin at 290 nm when concentrated 1mg/ml, and 42 is the actin molecular weight (kDa).

To evaluate the actin labelling OD was measured at 343 nm, that is the wavelength of maximum absorbance for pyrene (N-(1-pyrenyl)iodoacetamide).

The following formula was used to calculate the concentration of the labelled actin:

[μM] labelled actin = OD 343 nm/54000

where 54000 (M-1 cm-1) is the Pyrene ξ value at 343 nm.

To evaluate the percentage of actin labelling the ratio between labelled and total actin concentration was then calculated.

A Buffer

5 mM Tris-HCl pH 7.8

0.5 mM ATP pH 7.0

1 mM DTT

0.1 mM $CaCl_2$

2 mM $MgCl_2$

0.1 M KCl

Atto-488 labelled actin

Atto-488 actin labelling was essentially performed as described in Kuhn et al., 2005 [190]. Actin was labelled with succinimidyl ester atto-488 (ATTO-TEC GmbH, Germany) on random lysine residues. Actin labelling was performed under polymerization conditions (50 mM KCl and 2 mM $MgCl_2$) followed by depolymerization and gel filtration in G buffer.

Actin polymerization assays

Initial rate of filament growth was monitored by the increase in fluorescence of 10% pyrenyl-labelled actin using a Perkin Elmer (LS55) or Safas Sfx fluorescence spectrophotometer. Pyrenyl fluorescence increases of about 25 times from G- to F-actin, filaments growth can thus be followed looking to the increase in fluorescence. The used wavelengths are 366 nm for the absorption, 407 nm for the emission.

Actin polymerization was induced starting from spectrin-actin seeds: these are preformed nuclei of 2 or 3 actin subunits from which the polymerization can start avoiding the first lag phase, moreover they have only free barbed ends, allowing actin polymerization only from these ends.

Seeded polymerization was induced by addition of 0.05 M KCl, 1 mM $MgCl_2$ and 0.5 mM EGTA to a solution of Ca-ATP–G-actin (1.25 μM) in G-buffer containing 0.16 nM spectrin-actin seeds, 5 μM profilin and the desired amount of purified protein (as indicated in the figure legends) in a final volume of 100 ml.

Total Internal Reflection Fluorescence (TIRF) Microscopy.

TIRF microscopy was performed esentialy as described in Breitsprecher et al., 2008 [106]. For coating 0.1% v/v of 3 μm diameter Ni-NTA magnetic beads (Novagen), the beads were incubated with 5 μM His-IRSp53 WT or W413G mutant or His-tagged VASP for 90 min at 4° C in coating-solution (CS) (10 mM HEPES pH 7.5, 50 mM KCl, and 20 mM β-mercaptoethanol). Subsequently, the beads were washed three times in CS containing 1% v/v BSA to prevent unspecific binding.

Coated beads were then mixed with 1 μM 20% Atto-488 labelled actin and the indicated proteins in TIRF buffer (20 mM imidazole pH 7.4, 50 mM KCl, 1 mM $MgCl_2$, 1 mM EGTA, 20 mM β-mercaptoethanol, 0.2 mM ATP, 15 mM glucose, 2.5 mg/ml methylcellulose, 20 μg/ml catalase, 100 μg/ml glucose-oxidase). Analysis were performed in flow cells, as described in Breitsprecher et al., 2008 [106]. Fluorescence was excited at 488 nm with a Sapphire laser, and images from an Olympus IX-81 inverted microscope equipped with an Apo N 60x TIRF objective captured every 2 with exposure times of 80 ms by a cooled Hamamatsu Orca-R2 CCD camera (Hamamatsu Corp.). Using 2x2 binning mode, the pixel size corresponded to 0.21 μm. The elongation rates of filaments were calculated by manual tracking of growing barbed ends after post processing the time lapse movies by background subtraction

(30 px rolling ball radius) using ImageJ software. 16-24 filaments from three movies per condition were analysed.

6 Cells culture

Cells culture

HeLa cells were grown in Minimum Essential Medium (MEM Thermo Fisher Scientific) supplemented with 10% FBS (EuroClone), 1% non essential ammino acids and 1% Sodium Pyruvate. Immortalized fibroblasts from *Irsp53 +/+* and *Irsp53 -/-* embryos were generated as described in Weiss et al., 2009 [117]. Immortalized mouse embryo fibroblasts (MEFs) were grown in Dulbecco's Modified Eagle Medium (DMEM, Lonza) supplemented with 10% FBS (EuroClone) and 2 mM L-Glutamine (EuroClone). MDCK cells were grown in Dulbecco's Modified Eagle Medium (DMEM, Lonza) supplemented with 5% FBS (EuroClone) and 2 mM L-Glutamine (EuroClone). MDCK Tet-Off cell line T23 containing IRSp53 shRNAmir (kind gift of A. Musch, Albert Einstein College of Medicine, New York), described in Cohen et al., 2011 [152], were grown in Dulbecco's Modified Eagle Medium (DMEM, Lonza) supplemented with 10% FBS (EuroClone) and 2 mM L-Glutamine (EuroClone) and doxycycline 200 ng/ml. IRSp53 KD was induced by doxycycline removal (in presence of 50 μM enoxacine). Caco2 cells were grown in Dulbecco's modified Eagle's medium (DMEM, Thermo Fisher Scientific) supplemented with 20% FBS (EuroClone) and 1% non-essential aminoacids. HEK-293T and phoenix cells were grown in Dulbecco's modified Eagle's medium (DMEM, Lonza) supplemented with 10% FBS (EuroClone) and 2 mM L-Glutamine. Cells were grown at 37°C in humidified atmosphere with 5% CO_2.

Transfection

Transfections were performed using the calcium phosphate method, electroporation, Lipofectamine (Thermo Fisher Scientific), Lipofectamine2000 (Thermo Fisher Scientific) or FuGENE (Thermo Fisher Scientific).

HEK-293T cells were transfected using the calcium phosphate procedure. In this case DNA (10 µg for a 10 cm plate) was diluted in 439 µl of ddH_2O and 61 µl of 2M $CaCl_2$ were added. This solution was added, drop-wise, to 0.5 mL of HBS 2X. Then, the precipitate was added to the cells and removed after 12-16 hours.

Electroporation was used to transfect MEF cells for the expression of GFP-VASP, myc-CDC42 or mCherry-IRSp53, using NEON™ trasfection system (Thermo Fisher Scientific) according to manufacturer's instructions. Cells were microporated with one pulse of 20 ms at 1650 V, with a cell density of $5*10^6$ cells.

Lipofectamine (Thermo Fisher Scientific), according to manufacturer's instruction, was used to transfect HeLa cells. Caco-2 cells were transfected using Lipofectamine2000 (Thermo Fisher Scientific), according to manufacturer's instructions, to perform CRISPR/Cas9 genome editing. MDCK were transfected using Lipofectamine2000 (Thermo Fisher Scientific), according to manufacturer's instructions, for Apple-RAB11a expression and selected with Neomycin. MEF cells were transfected with FuGENE for the expression of myc-CDC42 in Figure 34.

2X HBS pH 7.5

50 mM HEPES pH 7.5

10 mM KCl

12 mM dextrose

280 mM NaCl

1.5 mM Na_2HPO_4

Retroviral infection

Stable MEF *Irsp53 -/-* cells were subjected to retroviral infection with pBABE control, pBABE IRSp53 WT and pBABE IRSp53 W413G vectors. Retroviruses were produced by transfecting Phoenix cells with the above mentioned constructs, using the calcium phosphate procedure. 48 and 72 hours after transfection, supernatants were collected and passed through a 0.45 μm filter. Viral supernatant was supplemented with 8 μg/ml Polybrene (Sigma) and added to cultured MEF *Irsp53 -/-* cells. Two cycles of infection were performed, of four hours each, for two days. Infected cells were selected with Puromycin. Expression of the different constructs was controlled by Western blot analysis.

Lentiviral infection

MDCK and Caco2 cells were subjected to lentiviral infection with pFUW vectors encoding for GFP-IRSp53 WT or mutated. Lentivirus were produced transfecting HEK-293T cells with 25 μg of the vector of interest, 9 μg ENV, 16.25 μg pMDL, 6.25 μg REV (for virus packaging). 48 and 72 hours after transfection, supernatants containing virus particles were collected and passed through a 0.45 μm filter. Supernatants were supplemented with 8 μg/ml Polybrene (Sigma) and added to cultured cells, four cycles of infection were performed. GFP-constructs expression was checked by Western blot analysis and immunofluorescence.

Short interfering RNA (siRNA) experiments

MDCK cells were seeded the day before trasfection (150000 cells/well in 6 well format). siRNAs (small interfering RNAs) delivery was achieved by mixing 10 nM of specific siRNAs with Optimem and Lipofectamine RNAiMAX Transfection Reagent (Thermo Fisher Scientific) according to manufacturer's instruction. Negative control was performed with the same amount of scrambled siRNA. KD efficiency was controlled by Western blot analysis. Oligoes were purchased from Thermo Fisher

Scientific, oligos details as follows:

IRSp53 (canine): CCAAGGAACTCGGAGACGTTCTCTT

Scrambled: TCGAATACGAACATTTATTT

Cell lysis

After washing twice with PBS 1X, cells were lysed in JS buffer directly on the plates using a cell-scraper. About 400 μl of JS buffer for 10 cm plates were used. Lysates were incubated on ice for 10 minutes and cleared by centrifugation at 13200 rpm for 10 min at 4°C (Eppendorf 5424 refrigerated tabletop centrifuge). The supernatant was transferred into a new eppendorf and protein concentration was measured by the Bradford assay (Bio-Rad), following manufacturer's instructions.

CRISPR/Cas9 KO cell clones

CRISPR vector was purchased from DNA 2.0, containing the following guide RNA sequence:
CTGGAGAATTACGTGTCCGA

(selected as the best for annealing vs off-target probability).

After 48 hours transfection with the CRISPR vector expressing both Cas9-RFP and the gRNA targeting IRSp53, RFP positive Caco2 cells were selected by FACS (MoFlo Astrios, Beckman Coulter) equipped with 405 nm, 488 nm, 561 nm and 642 nm lasers.

To obtain clones, serial dilution of the mass population was performed, the expression of IRSp53 was finally evaluated for each clone by Western blot analysis.

Caco-2 cyst formation assay (embedded cultures)

This protocol was adapted from Jaffe et al., 2008 [181]. Growth Factor Reduced Matrigel™ Matrix Basement Membrane (BD Biosciences) should be thawed overnight in ice at 4°C and handled in ice with cold tips. Caco2 cells were detached with trypsin and carefully re-suspended to single cells by pipetting and flowing through a cell

strainer (size 40 μm). Cells were then mixed to 60000 cells/ml final concentration with:

20 mM Hepes

1 mg/ml Collagen I (BD)

50 % Matrigel™ (BD)

The mixture was then plated 250 μl/well in one μ-slide 8 Wells chamber slide (Ibidi). After 30 minutes at 37°C, to allow matrix polymerization, each well was overlayed with 250 μl of media. Media was replaced every two days. At day 6, 0.1 μg/ml cholera toxin was added, to favour lumen swelling. Cells were fixed approximately 24 hours later.

MDCK cyst formation assay (on top cultures)

MDCK cells were splitted the day before, to obtain cells in the growing state the day of the experiment. Growth Factor Reduced Matrigel™ Matrix Basement Membrane (BD Biosciences) should be thawed overnight in ice at 4°C and handled in ice with cold tips. Every well from μ-slide 8 Wells chamber slide (Ibidi) was pre-coated with 15 μl Matrigel and allowed to solidify for 30 minutes at 37°C. Cells were detached with trypsin and carefully re-suspended to single cells by pipetting and flowing through a cell strainer (size 40 μm). Cells were then mixed to 40000 cells/ml final concentration with 2% Matrigel and plated 250 μl/well in the chamber slide. Media was replaced every two days. Cysts were fixed after 6 days or at earlier time points, as indicated in the figure legends.

7 Imaging techniques

Microscope equipment

Wide-field fluorescence images were taken by an AX70 (Olympus) microscope equipped with a 12 bit b/w camera (FviewII, Olympus). Confocal images were taken

with a Leica TSC SP2 AOBS confocal microscope controlled by Leica Confocal Software and equipped with violet (405 nm laser diode), blue (argon, 488 nm), yellow (561 nm Solid State Laser), and red (633 nm HeNe Laser) excitation laser lines. A 40x oil-immersion objective lens (Leica) was used for image acquisition of MDCK and Caco2 organoids. Timelapses analysis were performed as indicated in the following subchapters.

Immunofluorescence

Cells were plated on glass coverslips (pre-incubated with 0.5% gelatin in PBS at 37˚C for 30 minutes in the case of MEFs). After 24 h, cells were processed for epifluorescence or indirect immunofluorescence microscopy. Cells were fixed in 4% paraformaldehyde for 10 minutes, washed with PBS and permeabilized in PBS 0,1% Triton X-100 and 1% BSA (to prevent non-specific binding of the antibodies) for 10 minutes at room temperature (RT). After three washes in PBS, the coverslips were gently deposited, face down, on 50 µl of primary antibody diluted in PBS 1% BSA, spotted on Parafilm™. After 40 minutes of incubation at room temperature, coverslips were washed three times with PBS. Cells were then incubated for 40 minutes at room temperature with the appropriate secondary antibody. FITC- or TRITC-phalloidin (Molecular Probes) was added in the secondary antibody step, where applicable. After three washes in PBS, coverslips were incubated in PBS containing 0.5 ng/ml DAPI (1:3000) for 5 minutes at RT. Coverslips were washed two times in PBS and then in deionized water, finally coverslips were mounted in mowiol (20% Mowiol (Sigma), 5% Glycerol, 2.5% DABCO (Molecular Probes), 0.02% NaN_3 in PBS) and examined by fluorescent wide field microscopy, or mounted in Vectashield mounting medium (Vector Laboratories) for confocal acquisition. Images were further processed with Image J software.

Note that for EEA1 and Lamp1 antibodies, permeabilization was done in presence of 0.02% saponin, saponin was then added in all the following passages.

3-D cyst staining

Cysts were fixed in 2% paraformaldehyde for 4 minutes in case of MDCK cysts or 30 minutes for embedded Caco2 spheroids. To remove paraformaldehyde, samples were washed three times with 1% glycine diluted in 1X PBS, with gentle agitation. Permeabilization was performed in 1X PBS containing 0.5 % Triton X-100 for 10 minutes at room temperature, then cells were rinsed once with IF buffer and blocked in IF buffer plus 5% BSA for 1.5 hours. After 5 minutes wash in IF buffer, samples were incubated with primary antibodies diluted in IF buffer for few hours at room temperature or overnight at 4°C, with gentle agitation. Samples were rinsed three times with IF buffer and incubated 1.5 hours at room temperature with AlexaFluor-secondary antibodies (and eventually phalloidin) diluted in IF Buffer at room temperature. After one wash in IF buffer and two washes in 1X PBS, nuclei were stainined with 0.5 ng/ml DAPI diluted in PBS, for 5 minutes at room temperature. After 2 washes in 1X PBS, images were acquired with a Leica TSC SP2 AOBS confocal microscope and a HCX PL APO 40X/1.25-0.75NA oil-immersion objective lens. ImageJ software was used for image analysis.

IF buffer

PBS

0.2% Triton X-100

0.05% Tween-20

0.1% BSA

Epifluorescence time-lapse microscopy

Cells electroporated with various expression vectors, using Neon™ transfection system (Thermo Fisher Scientific) according to the manufacturer's instructions, were

seeded on laminin (40 µg/ml). After 24 h, images were acquired for 5 min at 10 sec time interval using an Leica inverted Microscope DMI6000B with adaptive focus control system driven by Leica Las AF software; a HCX PLAPO 63x n.a. 1.47 objective was used with an Andor camera iXon DU-885 EM CCD. All experiments were performed using an environmental microscope incubator set to 37°C and 5% CO_2 perfusion.

Confocal spinning-disc time-lapse microscopy

Cells were electroporated and seeded on laminin as described above. After 24 h, images were acquired (10 min, 0.55 sec time interval) with an UltraVIEW VoX (Perkin Elmer) spinning disk confocal unit, equipped with an EclipseTi inverted microscope (Nikon), a C9100-50 emCCD camera (Hamamatsu) and driven by Volocity software (Improvision, Perkin Elmer). Images were acquired with a 100x oil immersion objectives (Nikon Apo TIRF, NA 1.49). All the experiments were performed using an environmental microscope incubator (OKOLab) set to 37°C and 5% CO_2 perfusion.

Quantification of VASP at filopodia tips in IRSp53 MEFs and reconstituted cells expressing activated CDC42

To evaluate the frequency of VASP localization at the tips of filopodia, GFP-VASP-and myc-CDC42 L61-expressing IRSp53 KO and reconstituted cells (with either WT-IRSp53 or IRSp53W413G mutant) were plated, fixed and stained to detect F-actin and processed for epifluorescence to visualize VASP foci. Filopodia were scored for the presence of VASP at their tip. Typically, > 80% of cells filopodia display VASP at their tip in more than 90% of filopodia. The remaining ones are presumably also positive for VASP, but we may have failed in detecting it as some filopodia tips may be out of the focal plane. In the fewer filopodia of IRSp53 KO MEFs, ~ 80% of cells do not show any VASP at filopodia tips, the other have at least one positive filopodia.

Transwell assay

Cells were seeded on fibronectin-coated chambers of 6.5 mm diameter and 8.5 μm pore size (Corning Incorporated Life Science, Tewksbury, MA). 20% Serum or 10 ng/ml PDGF were added in the lower chamber as chemoattractant. Cells were fixed after seeding with 4% paraformaldehyde, stained with Chrystal violet and visualized by wide field microscopy.

Invasion assay

Cells were seeded on BD BioCoat™ Growth Factor Reduced BD Matrigel™ Invasion Chamber, 8.0 μm PET Membranes (BD, Franklin Lakes, NJ). PDGF (10 ng/ml) was added in the lower chamber as chemoattractant. Cells were fixed 16 h after seeding with 4% paraformaldehyde, stained with DAPI to detect nuclei and visualized by confocal microscopy.

Scratch assay

Cells seeded and grown till confluence were scratched with a pipette tip and carefully washed with 1X PBS to remove floating cells and create a cell-free wound area, then fresh media was added. Cells were subjected to DIC time-lapse analysis (20 h, 5 min time interval) using an Olympus IX81 Inverted microscope, driven by an "Olympus Scan^R" software and equipped with a "Hamamatsu Orca-AG" CCD camera 12 bit (pixel size = 6.45 μm). Objective, PlanC N 10X/0.25 (N.A.), Ph1. Single cell migration was analysed using Image J software. The directional migration index and the average speed of the cells were calculated. The directional migration index represents the ratio between the total distance covered by cells and the distance covered longitudinally toward the center of the wound. All the experiments were performed using an environmental microscope incubator set to 37°C and 5% CO_2 perfusion.

8 Other techniques

Irsp53 null mice generation

Irsp53 -/- mice were generated by a transgenic insertion ("exon trap") of a β-geo (β -galactosidase–Neo^R fusion) cassette between exons 3 and 4 of mouse *Irsp53* (embryonic stem cell clone Accession Number XG-757, BayGenomics, S. Francisco) (described in Sawallisch et al., 2009 [111]).

Wound surgery

Mice were treated accordingly to ethical procedures. Experiments were performed on 10 weeks-old littermate mice IRSp53 WT and KO mice. Mice were anesthetized by intraperitoneal injection of 2.5% Avertin solution and their back skin was shaved, cleaned with alcohol and disinfected with Betadine. Using a sterile 4-mm biopsy punch, 4 bilateral full-thickness skin wounds were created on the back skin without injuring the underlying muscle. Wounds were separated by a minimum of 6 mm of uninjured skin. Wounds were photographed at 0, 1, 2, 4, 5, 6, 7 days after wounding (0, 2 and 5 days are shown in Figure 38), using a Canon EOS D-600 digital camera. Wound area was measured using ImageJ software, and the relative wound closure at each time point was derived by following formula: current wound size/initial wound size. Mice were sacrificed by CO_2 euthanasia at day 7 after wounding. Wound tissue biopsies were collected for histology and immunohistochemistry.

9 Statistical analysis

In case of re-infection with GFP constructs, only GFP-positive cells were considered for the analysis. All data are presented as the mean±standard errors of mean (s.e.m.), except when specified in figure legend, from at least three independent experiments. A Student's t-test was used to calculate the P-values.

In the cyst formation assay at least 30 cysts were counted for each sample.

Results

Part one: CDC42:IRSp53:VASP axis is involved in filopodia formation

IRSp53 possesses a weak capping activity, in seeded polymerization assay, that is relieved by binding to active CDC42

To explore the role of IRSp53 on actin dynamics, we employed initially *in vitro* actin polymerization assays reconstituted with purified minimal components. Actin polymerization can be easily followed using pyrenyl-labelled G-actin (see "Material and methods"). Since fluorescent signal from pyrenyl-group is 25-fold higher for F-actin with respect to G-actin, the emitted fluorescence increases proportionally to the increase of actin polymerization. In particular, these assays were performed in the presence of seeds, short preformed actin oligomers, in order to overcome the rate-limiting step of actin nucleation. After the addition of seeds, actin polymerization immediately starts, following an exponential phase of activity.

We observed a slow down of actin barbed end growth by around 10-fold, upon addition of increasing concentrations of IRSp53 (Figure 17). IRSp53 was added in substoichiometric concentration with respect to G-actin, suggesting that IRSp53 effect is due to its interaction with barbed ends and not with G-actin itself and further revealing a potentially novel and unexpected role for IRSp53, that may act as a capping protein in solution. IRSp53 capping is less efficient than other known cappers. Indeed, IRSp53 calculated Kd for barbed ends is around 0.29 μM, while other

known cappers, including EPS8 and CP, bind to and block barbed ends with nanomolar affinity.

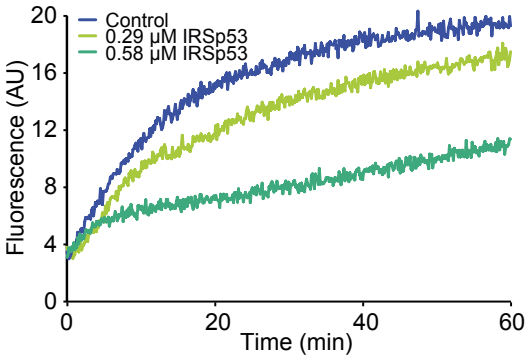

Figure 17. IRSp53 slows down barbed ends growth.

Kinetics of actin polymerization in presence of the indicated concentrations of IRSp53 purified protein. Control sample contained no IRSp53. Barbed end growth was measured in bulk pyrenyl-actin polymerization assays using 1.25 µM Mg-ATP-G-actin (5% pyrenyl-labelled), 5 µM profilin and 0.16 nM spectrin-actin seeds (modified from Disanza et al., 2013 [191]).

IRSp53 is an effector of CDC42. Binding of the former protein to the GTPase has been shown to promote a conformational change of IRSp53, opening the protein to an "active" conformation [115]. We then tested the effect of IRSp53 and CDC42 addition in our seeded actin polymerization assays. As shown in Figure 18, in the presence of IRSp53 and inactive GDP-CDC42, IRSp53 retains its weak capping activity. However, upon the addition of active GTP-CDC42, IRSp53 capping activity is abrogated.

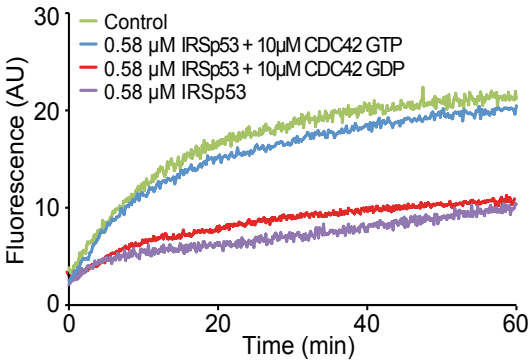

Figure 18. Active CDC42 relieves IRSp53 capping activity.

Kinetics of actin polymerization in presence of 0.58 μM IRSp53 purified protein alone or with 10 μM GTP-CDC42 or GDP-CDC42. Control sample contained no IRSp53. Barbed end growth was measured in bulk pyrenyl-actin polymerization assays using 1.25 μM Mg-ATP-G-actin (5% pyrenyl-labelled), 5 μM profilin and 0.16 nM spectrin-actin seeds (modified from Disanza et al., 2013 [191]).

Next, we performed a structure-function analysis to identify the minimal region or domain of IRSp53 involved in capping. We designed and purified a series of truncated or mutated IRSp53 constructs, and tested their capping ability in seeded actin polymerization assays. Results are summarized in Figure 19. A functional SH3 domain is not required, since IRSp53 W413G mutant, which is unable to bind SH3 interactors, inhibited barbed ends growth. The truncated protein I-BAR-IRSp53 and ΔI-BAR-IRSp53 displayed no capping, indicating that the I-BAR domain is required but not sufficient for this activity.

The activity profile of mutants truncated between CRIB-PR and SH3 domains revealed that a second region is required by IRSp53 to perform capping: this region comprises the amino acids 339-374, just before the SH3 domain. Of note, by sequence alignment, we observed no similarities between 339-374 IRSp53 region and any other known actin-binding protein, suggesting that IRSp53 uses a novel mode of action in binding and blocking barbed ends growth.

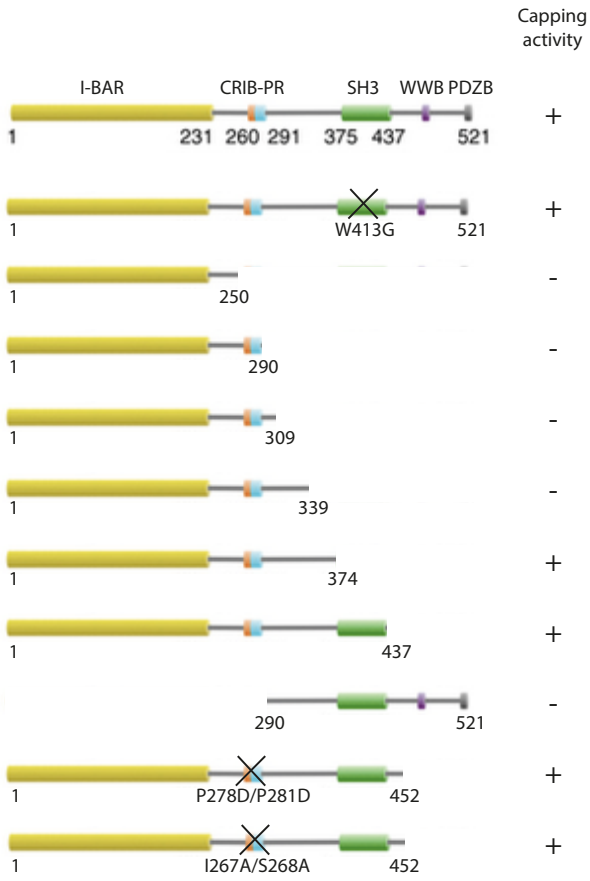

Figure 19. Barbed end growth inhibition by the indicated IRSp53 mutants.

All the indicated constructs were tested for their capping ability in bulk pyrenyl-actin polymerization assays using 1.25 µM Mg-ATP-G-actin (5% pyrenyl-labelled), 5 µM profilin and 0.16 nM spectrin-actin seeds (modified from Disanza et al., 2013 [191]).

These results further suggest that IRSp53 either requires multiple interaction surfaces to act as a capper, or it needs to adopt an appropriate 3-D conformation. For this reason, we also tested two IRSp53 conformational mutants, that have recently been described in Kast et al., 2014 [115]. IRSp53 P278D/P281D mutant is no longer able to form the intramolecular interaction between the CRIB-PR and the SH3 domains ("open" mutant), while IRSp53 I267A/S268A no longer binds to CDC42 (constitutively inactive mutant).

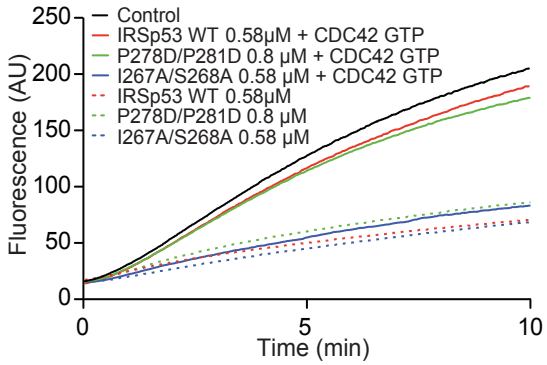

Figure 20. Capping activity of IRSp53 P278D/P281D and I267A/S268A mutants.

Kinetics of actin polymerization in presence of the indicated concentrations of IRSp53 WT or P278D/P281D or I267A/S26 mutated, alone or with 2.5 μM GTP-CDC42. Control sample contained no IRSp53. Barbed end growth was measured in bulk pyrenyl-actin polymerization assays using 1.25 μM Mg-ATP-G-actin (5% pyrenyl-labelled), 5 μM profilin and 0.16 nM spectrin-actin seeds (modified from Disanza et al., 2013 [191]).

As shown in Figure 20, both P278D/P281D and I267A/S268A IRSp53 mutants can act as cappers, indicating that this activity is unlikely due to the status of its "open" or "close" conformation. The finding that IRSp53 I267A/S268A mutant retains its capping proficiency, even in the presence of CDC42-GTP, indicates that their interaction is necessary to regulate barbed end capping, further suggesting that CDC42 may act through a steric hindrance effect.

It is also of note that the inhibition of barbed ends elongation by IRSp53 developed slowly during filament growth. Interestingly, comparing actin polymerization curves in the presence of IRSp53 full length or IRSp53 1-374, truncated just before the SH3 domain, we observed that the two proteins have a different kinetic behavior. As can be noticed from the magnification of the firsts few seconds of actin polymerization, in Figure 21, IRSp53 1-374 inhibited instantaneously barbed end growth, while IRSp53 displayed a time lag delay.

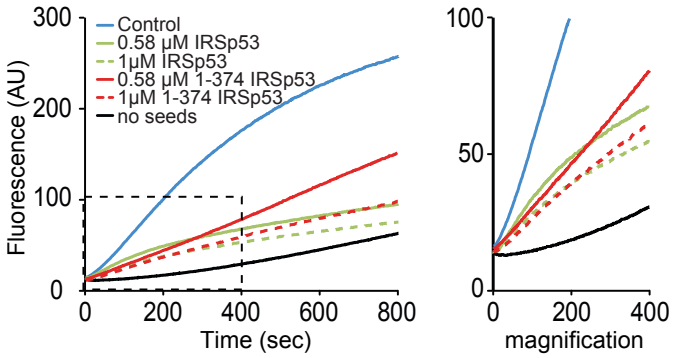

Figure 21. Comparison of the capping activity of IRSp53 WT or 1-374 truncated.

Kinetics of actin polymerization in presence of the indicated concentrations of IRSp53 WT or truncated (1-374). On the right, magnification of the region boxed in the left graph. Control sample contained no IRSp53. Barbed end growth was measured in bulk pyrenyl-actin polymerization assays using 1.25 µM Mg-ATP-G-actin (5% pyrenyl-labelled), 5 µM profilin and 0.16 nM spectrin-actin seeds (modified from Disanza et al., 2013 [191]).

The slow kinetic of IRSp53 association to the barbed ends again suggests that IRSp53 may need a slow conformational change to efficiently cap actin filaments, while all the surfaces required for capping are presumably unmasked in the mutant lacking the SH3 domain. Alternatively, these small conformational changes might follow the binding of IRSp53 to the actin filaments, thus affecting the rate of filament growth.
In summary, the data reported here suggest a novel capping function for IRSp53, which is relieved by active CDC42 and dependent on two regions of IRSp53: the I-BAR domain and a 30 amino acids patch just before the SH3 domain.

IRSp53 and VASP directly interacts, using IRSp53 SH3 domain and VASP proline-rich region

IRSp53 is able to bind Mena *in vitro*, and their interaction has been shown to be critical for filopodia formation in cells [137]. FRET and co-immunoprecipitation

approaches suggest that VASP, another member of the ENA/VASP family, is also able to bind IRSp53[20] [161]. Hence we next tested whether IRSp53 and VASP proteins are capable of forming a complex using *in vitro* purified components and asked whether their interaction has a functional role in cells.

We started performing simple *in vitro* binding assays. As shown in Figure 22 A, IRSp53, as well as its isolated SH3 domain, bound to VASP. Conversely, an IRSp53 point mutant in the SH3 region, IRSp53 W413G, was no longer able to interact with VASP. As negative control, we used EPS8, which also contains a SH3 domain, but did not display any binding ability to VASP (Figure 22 B).

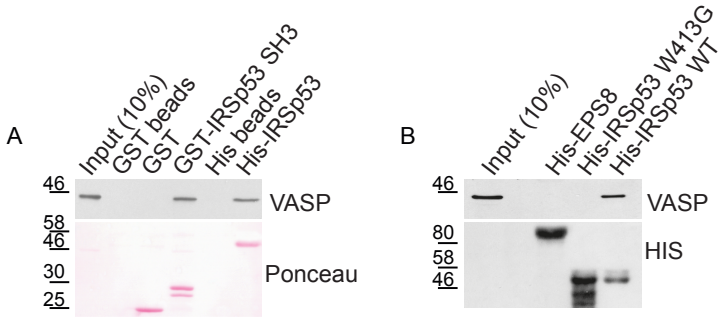

Figure 22. IRSp53 binds VASP through its SH3 domain.

A Recombinant purified VASP was incubated with glutathione-sepharose (GST) or Ni-NTA agarose beads (His beads) as control, or in presence of GST, GST-IRSp53-SH3 or His-IRSp53. Input (10% of total) and bound material were immunoblotted with VASP antibody. Ponceau staining was used to detect recombinant GST, GST-IRSp53-SH3 and His-IRSp53.

B Recombinant purified VASP was incubated with purified His-EPS8, His-IRSp53-W413G mutant or His-IRSp53 WT immobilized onto Ni-NTA agarose beads. Input (10% of total) and bound material were immunoblotted with the indicated antibodies (modified from Disanza et al., 2013 [191]).

These results indicate that the SH3 domain of IRSp53 is required and sufficient to bind to VASP. We further estimated that the apparent Kd of the IRSp53:VASP interaction was around 0.6 μM. Next, we set out to determine the region of VASP involved in this interaction. SH3 domains are known to interact with proline-rich

sequence. We, therefore, took advantage of VASP mutant in which the central PRD was deleted (VASP ΔPRD). As shown in Figure 23, VASP ΔPRD was no longer able to bind to the SH3 domain of IRSp53. Also the construct lacking the three central GP5 motif included in PRD (VASP $\Delta(GP5)_3$) failed to associate with the SH3 domain of IRSp53.

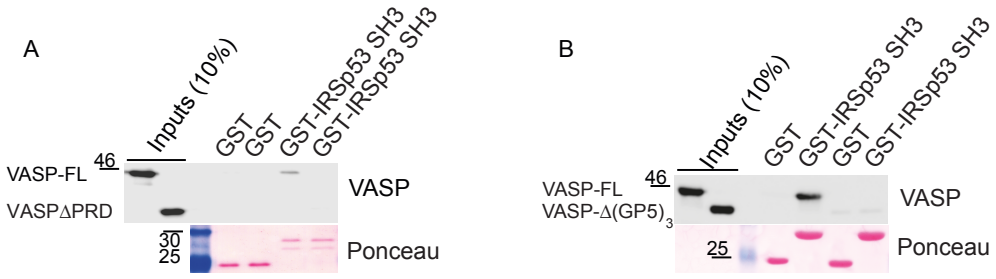

Figure 23. VASP binds IRSp53-SH3 through its PRD.

A Recombinant purified VASP or VASP ΔPRD was incubated with GST, as control, or GST-IRSp53-SH3. Inputs (10% of total) and bound material were immunoblotted with VASP antibody. Ponceau staining was used for recombinant GST and GST-IRSp53-SH3.

B Recombinant purified VASP or VASP $\Delta(GP5)_3$ was incubated with GST, as control, or GST-IRSp53-SH3. Inputs (10% of total) and bound material were immunoblotted with VASP antibody. Ponceau staining was used for recombinant GST and GST-IRSp53-SH3 (modified from Disanza et al., 2013 [191]).

Since the PRD from VASP also binds to profilin, we next asked whether profilin could compete with VASP for binding to IRSp53. In collaboration with C. Ampè (Ghent University, Belgium), we exploited an ELISA-based assay to test this hypothesis [189]. The results obtained suggest that no competition exist between profilin and IRSp53 to bind with VASP, and further imply that the three proteins may form a ternary complex (Figure 24).

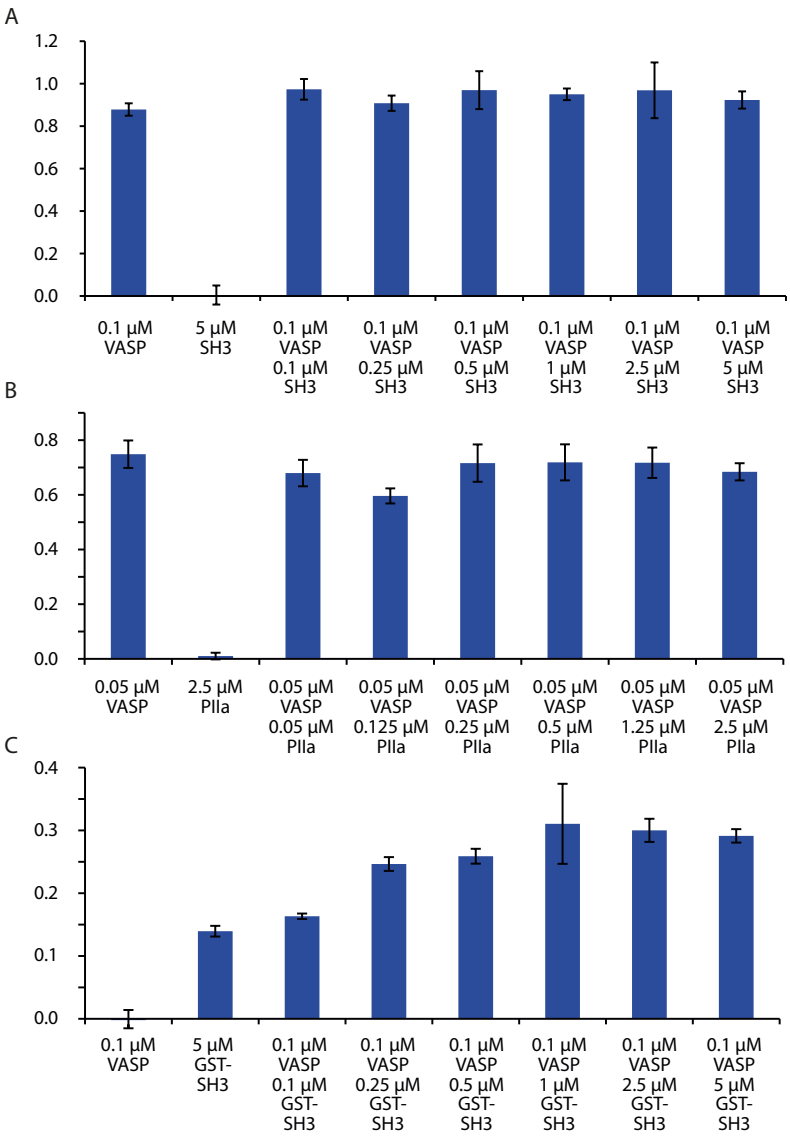

Figure 24. IRSp53, VASP and profilin may form a ternary complex.

A Solid-phase binding assays. His-VASP (0.1 µM) pre-incubated or not with cleaved IRSp53 SH3 (0.1 to 5 µM SH3) was added to profilin IIa-coated ELISA plates (0.06 nmol in 100 µl). After blocking and washing, His-VASP was detected. Profilin IIa without VASP and IRSp53 SH3 was used for back ground correction. The negative control was the highest concentration of IRSp53 SH3 (5 µM) in the absence of VASP.

B His-VASP (0.05 µM) pre-incubated or not with profilin IIa (0.05 to 2.5 µM PIIa) was added to GST-IRSp53 SH3 coated ELISA plates (0.04 nmol in 100 µl). After blocking and washing, His-VASP was detected. Blanc was GST-IRSp53 SH3 without VASP and profilin IIa, used for back ground correction. The negative control was the highest concentration of profilin IIa (2.5 µM) in the absence of VASP.

C His-VASP (0.1 µM) pre-incubated or not with GST-IRSp53 SH3 (0.1 to 5 µM) was added to profilin IIa-coated ELISA plates (0.06 nmol in 100 µl). After blocking and washing, GST-IRSp53-SH3 was detected. Profilin IIa without VASP and IRSp53 SH3 was used for back ground correction. The negative controls were the highest concentration of IRSp53-SH3 in the absence of VASP and VASP in the absence of GST-IRSp53-SH3. Positive controls were concentration series of VASP (experiment 1 and 2) and GST-IRSp53-SH3 (experiment 3) coated directly (not shown). In each case data (OD_{450nm}) are the averages from three independent experiments for each condition. Error bars are SD (modified from Disanza et al., 2013 [191]).

To better investigate the molecular and physical property of the IRSp53:VASP complex, we performed dynamic light scattering (DLS) analysis. When both IRSp53 than VASP were present, species with high hydrodynamic radius emerged (at about 200 nm), indicating that the two proteins in solution can associate and form large clusters. When IRSp53 was incubated in the presence of VASP ΔPRD mutant, the two proteins were not able to interact and no large clusters could be detected (Figure 25).

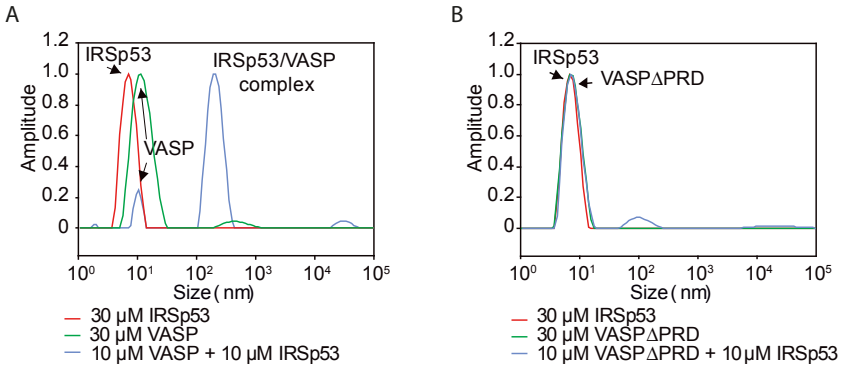

Figure 25. IRSp53 and VASP form large clusters in solution.

A Intensity weighted diameter distrubutions for 30 µM IRSp53 or 30 µM VASP showed a single species with hydrodynamic radius of 7.2 nm or 14.3 nm respectively. Mixing of 10 µM IRSp53 and 10 µM VASP gives aggregates with 200 nm hydrodynamic radius.

B Intensity weighted diameter distrubutions for 30 µM IRSp53, 30 µM VASP ΔPRD or the mixture of 10 µM IRSp53 and 10 µM VASP ΔPRD, in this latter condition no clusters were observed (modified from Disanza et al., 2013 [191]).

In summary, our data indicate that IRSp53 and VASP interact directly. The SH3 domain of IRSp53 binds specifically to the VASP PRD domain. This interaction leads to the formation of high-order oligomers in solution.

IRSp53 promotes VASP processive elongation activity by clustering VASP on surfaces

Next, we aimed at understanding whether IRSp53:VASP interaction had any effect on their biochemical functions. VASP is a processive elongator of actin filaments, particularly when clustered on functionalized beads. We hypothesized that if IRSp53 is able to mediate VASP clustering in solution (as emerged from DLS data), the same might happen when IRSp53 is immobilized onto beads. This hypothetical mode of action is schematically illustrated in Figure 26.

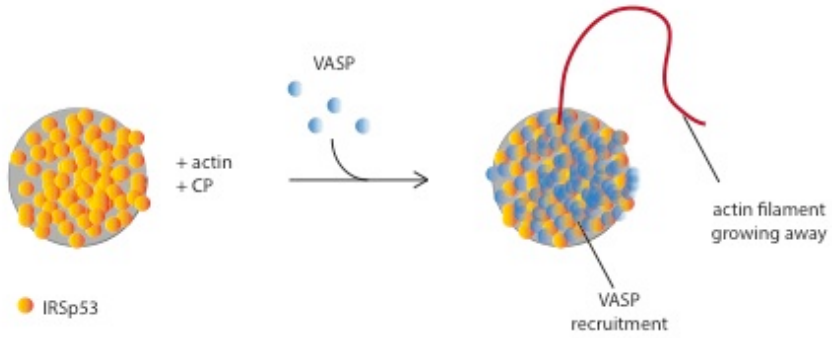

Figure 26. Scheme of the experimental setup.

Magnetic Ni-NTA beads were coated with His-IRSp53, then added to TIRF buffer containing Atto-488 labelled monomeric actin, capping protein (CP) and VASP. According to our hypothesis, if IRSp53 was able to cluster VASP on the beads surface, it would promote VASP processive elongation activity.

To test this hypothesis, we performed TIRF assays in collaboration with J. Faix (Hannover Medical School, Germany). Purified proteins where incubated in TIRF buffer, in the presence of Ni-NTA micro beads, fluorescently labelled actin monomers and CP. The addition of CP prevents spontaneous actin polymerization in solution. Recombinant and purified His-VASP was directly recruited and clustered on beads: a step that led to the activation of its processive elongation activity. Indeed, when we used a VASP tagged with GST, and thus no longer able to bind to Ni-NTA beads, no enhancement of filament growth could be detected. Only in presence of Ni-NTA beads saturated with IRSp53, we observed GST-VASP clustering on beads and, subsequently, processive elongation of actin filaments (Figure 27).

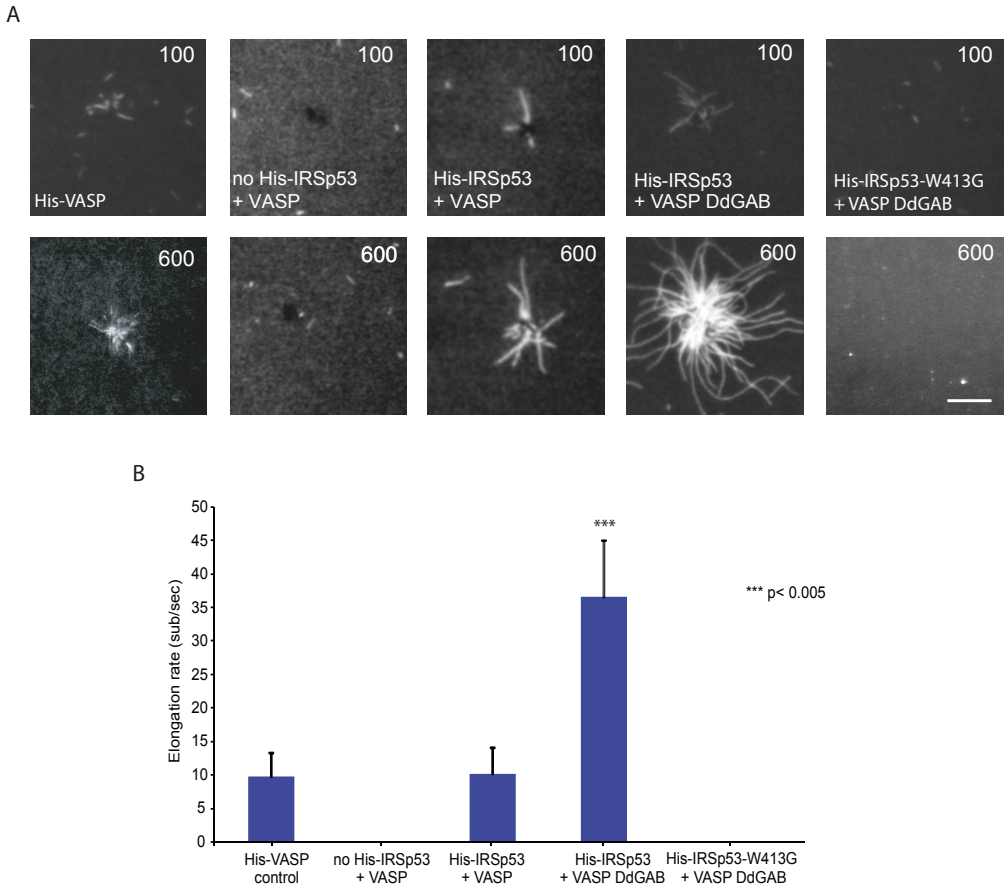

Figure 27. IRSp53 recruits and clusters VASP, to drive processive actin filament elongation.

A TIRF micrographs of the assembly of 1 μM G-actin (20% Atto-488 labelled) on Ni-NTA beads uncoated or saturated with His-VASP or His-IRSp53 or His-IRSp53-W413G. Reactions were run in

presence of 50 nM CP and 200 nM VASP or VASP DdGAB. Only filaments that were attached with their barbed ends to the beads were observed, since CP abolished filament growth in solution. Time is indicated in seconds in the upper right corner of each frame. Scale bar: 10 μm.
B Quantification of actin filament elongation rates from experiments shown in A. Data are presented as mean ± s.d. of three independent experiments, in which at least 16 filaments/experiment were measured (modified from Disanza et al., 2013 [191]).

We also performed the same assay in the presence of a VASP chimera, in which the human GAB domain was substituted with the GAB domain from *Dictyostelium discoideum*. VASP DdGAB chimera promotes a 3- to 4-fold higher rate of filament elongation as compared to hVASP, due to its higher affinity for G-actin [192]. Even under these conditions, IRSp53 was able to recruit and to cluster VASP DdGAB on beads and, by doing so, to promote actin filament elongation. The IRSp53 W413G mutant, instead, as expected, did not permit VASP clustering on beads, reinforcing the functional importance of this domain in mediating the interaction between the two proteins and the activation of VASP.

IRSp53 is able to recruit and cluster VASP on membranes

Our TIRF data support the hypothesis that IRSp53 can recruit and cluster VASP on solid supports, we next wandered if the same could also occur on the plasma membrane. To mimic the plasma membrane, we used PIP_2-containing liposomes (since IRSp53 shows a preference for PIP_2 lipids [120]), and tested their ability to bind fluorescently labelled proteins, exploiting a FACS based approach, in collaboration with W. Nickel (Heidelberg University, Germany) [188].
As shown in Figure 28, labelled IRSp53 WT and W413G mutant were both recruited to PIP_2 liposomes, that in fact showed an increased associated fluorescence signal. In contrast, VASP did not directly bind PIP_2 liposomes. Only in the presence of IRSp53,

fluorescently labelled-VASP could be recruited to liposomes. If IRSp53 was mutated in the SH3 domain, VASP was no longer recruited to PIP_2 liposomes.

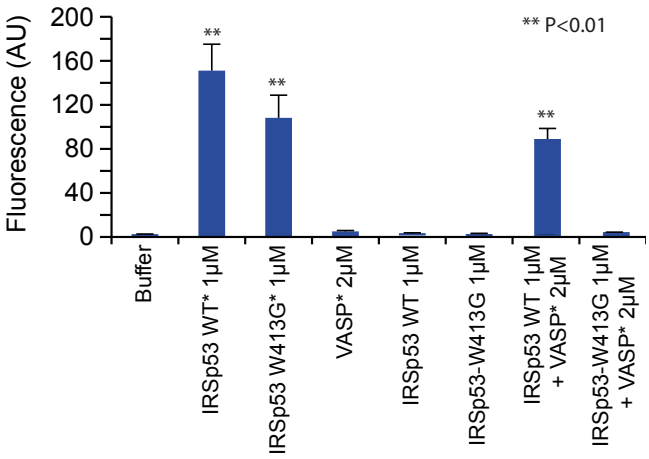

Figure 28. IRSp53 is necessary for VASP recruitment to PIP_2-containing liposomes.

Unlabelled and labelled (*Alexa-488) IRSp53 WT, IRSp53 W413G and VASP, at the indicated concentrations and combinations, were added to 1 mM of 10% PIP_2-containing liposomes. Interactions were analysed by FACS and data were processes with CellQuest Pro software (Becton Dickinson) and expressed as mean ± s.e.m. of at least three independent experiments performed in duplicate (modified from Disanza et al., 2013 [191]).

Next, we asked whether IRSp53 mediates VASP recruitment to the plasma membrane. VASP is generally enriched at the plasma membrane, localizing in discrete foci, that invariably mark the emergence of a microspike or a filopodia [32].

We took advantage of MEF cells derived from *Irsp53* KO mice [117]. MEFs were infected with pBABE empty vector, pBABE-IRSp53 WT or pBABE-IRSp53 W413G, in which the functionality of the SH3 domain is abrogated. To visualize VASP dynamics, the same cells were also electroporated with GFP-VASP encoding vector (Figure 29).

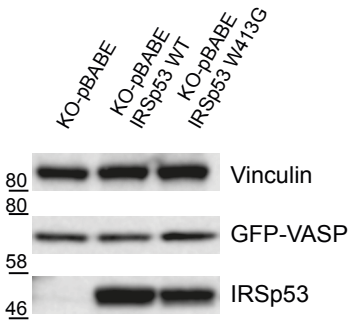

Figure 29. Expression levels of IRSp53 and VASP in MEFs.

MEF cells derived from *Irsp53* KO mice were infected with pBABE, pBABE IRSp53 WT or pBABE IRSp53 W413G, and electroporated with GFP-VASP. Cell lysates were immunoblotted with the indicated antibodies (modified from Disanza et al., 2013 [191]).

We then plated GFP-VASP-expressing MEFs, with or without IRSp53, on laminin and monitored them by time-lapse imaging. In all the conditions tested, GFP-VASP was enriched along the lamellipodia and at focal adhesions. Clear VASP foci emerged at the leading edge of MEF cells reconstituted with IRSp53 WT, that frequently moved laterally, merged and fused, but always preceded filopodia formation. In the absence of IRSp53 or in cells reconstituted with its mutant version W413G, no GFP-VASP foci were seen, reinforcing the hypothesis that functional IRSp53 is required to recruit VASP also at the cell membrane (Figure 30).

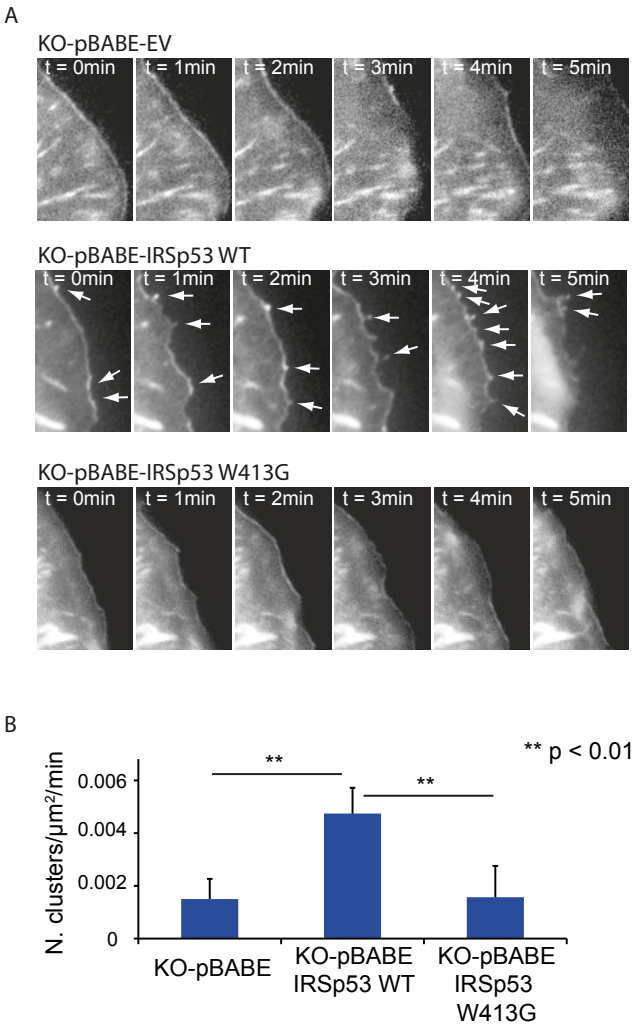

Figure 30. IRSp53 is required for VASP recruitement and clustering at the plasma membrane.

A Still images from fluorescence time-lapse analysis of migrating cells. MEF cells from IRSp53 KO mice were infected with empty vector (KO-pBABE), KO-pBABE-IRSp53 WT or KO-pBABE-IRSp53 W413G. Cells were then electroporated with GFP-VASP and plated on laminin (40 µg/ml). Twenty hours after electroporation, cells were analysed by time-lapse imaging (5 minuts, time interval 5 seconds). Arrows indicate VASP puncta.

B Quantification of the number of clusters (mean ± s.e.m.) formed by GFP-VASP for all the conditions tested in A. 20 cells for each conditions were analysed (modified from Disanza et al., 2013 [191]).

Next we also electroporated IRSp53-KO MEF cells with GFP-VASP and mCherry-IRSp53, plated them on laminin and subjected to time lapse analysis. We observed that also IRSp53 accumulated in discrete foci, that were also positive for VASP and fascin (not shown) and were preluding the formation of filopodia. To get more

insights into the timing of IRSp53 and VASP recruitment at the plasma membrane, we performed a careful, fast-acquisition time lapse analysis to follow the accumulation of the two fluorescent proteins over time. We observed that IRSp53 accumulation in foci slightly, but reproducibly, preceded (1.4 seconds on average) VASP accumulation (Figure 31).

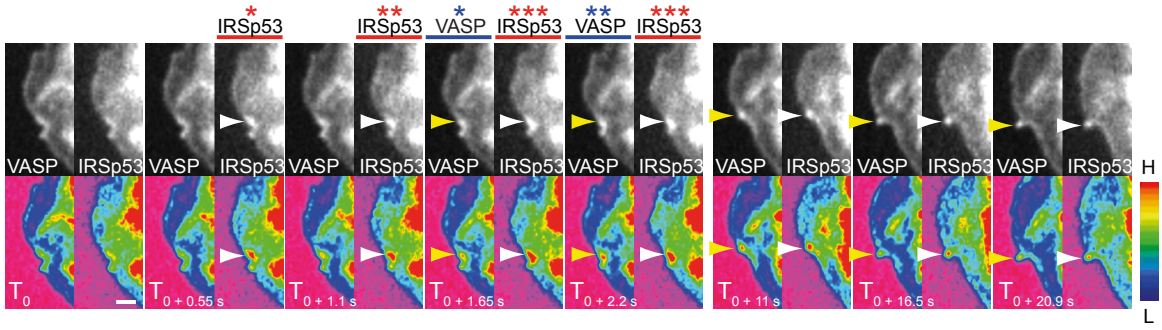

Figure 31. IRSp53 accumulation into foci at the plasma membrane slightly precedes VASP recruitment.

Still images from fluorescence spinning-disk confocal analysis of migrating cells. MEF cells were electroporated with GFP-VASP and mCherry-IRSp53 and plated on laminin (40 µg/ml). 24 hour after electroporation, cells were subjected to time lapse analysis (time interval 0.55 sec). Upper panels represent GFP-VASP and mCherry-IRSp53 signal as grew colours, lower panels represent the same images elaborated with the spectrum colour filter from ImageJ software, used to highlight local accumulation of fluorescent signals (highest intensities are in red, the lowest one in blue). White and yellow arrowheads indicate IRSp53 and VASP accumulation. Bar is 5 µm (modified from Disanza et al., 2013 [191]).

Summing up this section, we found that IRSp53 is required for VASP accumulation at the plasma membrane in small foci, which are markers of filopodia initiation.

CDC42 increases the apparent affinity between IRSp53 and VASP and this axis promotes efficient filopodia formation

Since CDC42 is a known IRSp53 interactor, we next investigated whether CDC42 influences IRSp53:VASP interaction and modulates their biological activity.

We started by performing *in vitro* binding assays using purified IRSp53, VASP and CDC42 proteins. We observed that in presence of 100 nM or 250 nM IRSp53, the amount of VASP that IRSp53 could bind increased in the presence of saturating concentrations of GTP-bound CDC42. At 500 nM these difference was lost, probably because saturation was achieved (Figure 32).

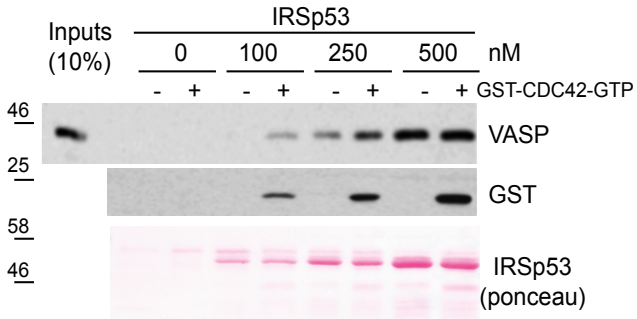

Figure 32. CDC42 modulates the interaction between purified IRSp53 and VASP.

Equal amounts of VASP were incubated with Ni-NTA agarose beads coated with increasing concentrations of recombinant purified His-IRSp53 (0, 100, 250, 500 nM), in absence or in presence of saturating concentrations of GTP-loaded GST-CDC42. Inputs (10% of total) and bound material were immunoblotted with the indicated antibodies. Ponceau staining was used to visualize IRSp53 (modified from Disanza et al., 2013 [191]).

We then tested if IRSp53:VASP interaction was enhanced in the presence of active CDC42 exploiting a co-immunoprecipitation approach. HeLa cells were transfected with an empty vector or vectors encoding CDC42 L61 (constitutively active) or CDC42 N17 (dominant negative), and immunoprecipitated with a control or a VASP antibody. In the presence of CDC42 L61, the amount of IRSp53 co-

immunoprecipitating with VASP was higher than the amount of IRSp53 co-immunoprecipitated in presence of CDC42N17 or an empty vector (Figure 33).

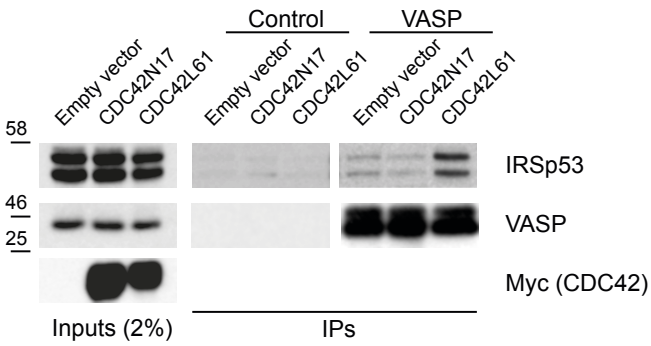

Figure 33. CDC42 favours the formation of an IRSp53:VASP complex in HeLa cells.

Lysates (2 mg) of HeLa cells, transfected with an empty vector as control or CDC42 N17 (dominant negative) or CDC42 L61 (constitutively active), were immunoprecipitated with an anti-VASP or a control antibody. Input lysates (40 μg) and immunoprecipitates (IPs) were immunoblotted with the indicated antibodies (modified from Disanza et al., 2013 [191]).

Both *in vitro* binding assays than co-immunoprecipitation approaches further confirmed that in the presence of active CDC42, the apparent affinity between IRSp53 and VASP is increased. The next question was to understand whether active CDC42 also affected IRSp53-dependent cell phenotypes. Active CDC42 causes the explosion of filopodia formation. IRSp53 null MEFs, reconstituted with empty pBABE or pBABE-IRSp53, were transfected with a construct encoding active CDC42 (CDC42 L61). Under these conditions, IRSp53 null MEF cells formed a limited number of filopodia (around 4 filopodia/cell), while IRSp53 null MEF cells reconstituted with IRSp53 displayed a significantly higher number of filopodia (26 filopodia/cell) (Figure 34).

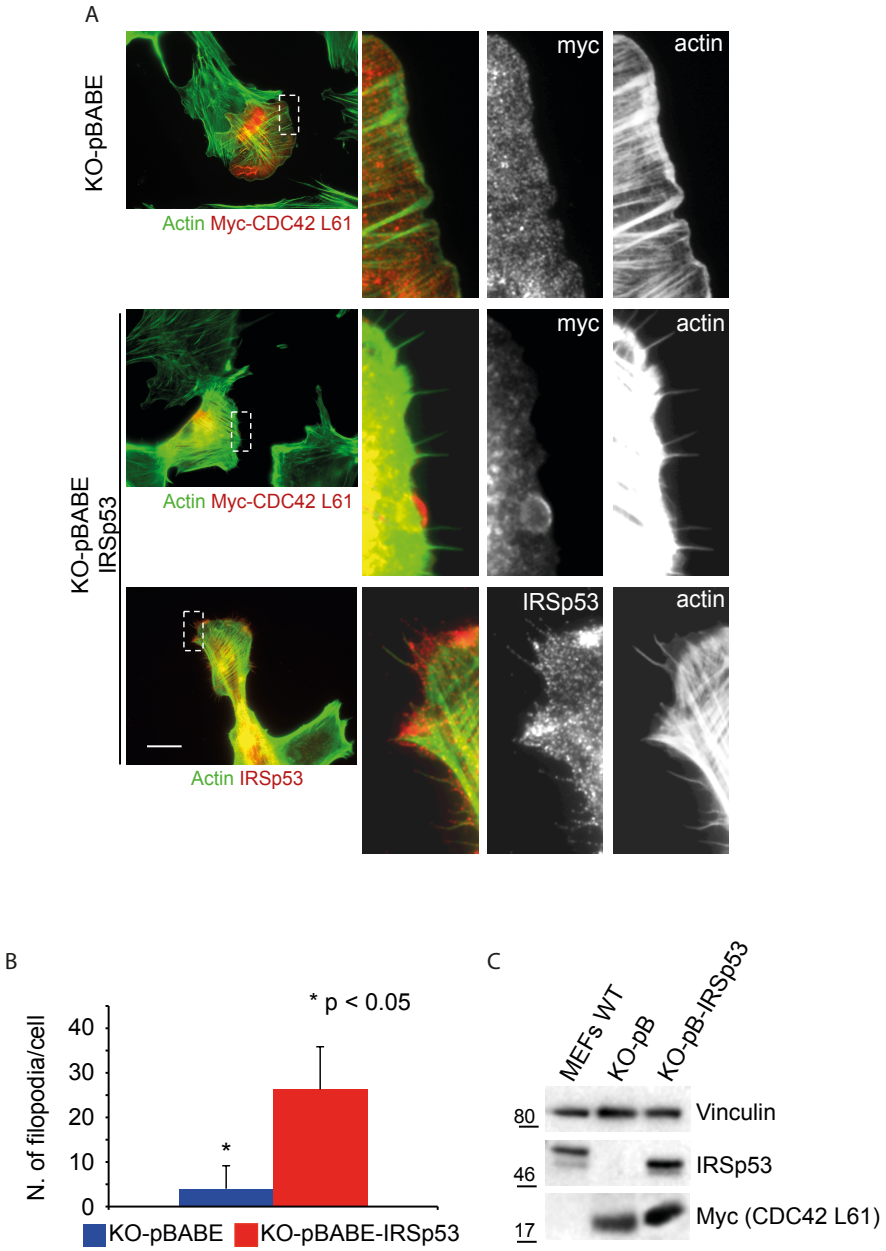

Figure 34. IRSp53 is required for CDC42-induced filopodia formation.

A MEF cells IRSp53 KO-pBABE and IRSp53 KO-pBABE-IRSp53 were transfected with a constitutively active myc-tagged CDC42 (myc-CDC42 L61). As control, also not trasfected IRSp53 KO-pBABE-IRSp53 cells were analysed. Cells were then fixed and stained with anti-myc or anti-IRSp53 antibodies and FITC-phalloidin. Right panels represent magnification of the boxed areas of each corresponding image. Scale bar is 10 μm.

B Quantification of the number of filopodia induced per cell, in MEF cells IRSp53 KO-pBABE and IRSp53 KO-pBABE-IRSp53, transfected with myc-CDC42 L61. At least, 100 cells were analysed in each experiment and three independent experiments were performed. Data are mean ± s.e.m.
C Expression levels of IRSp53, myc-CDC42 L61 and vinculin were analysed by immunoblotting (modified from Disanza et al., 2013 [191]).

These data support the hypothesis that CDC42:IRSp53 (and possibly VASP) axis is important in filopodia formation. IRSp53 is also required for VASP localization at filopodia tips. As shown in Figure 35, VASP localized at filopodia tips only in IRSp53 null MEFs reconstituted with pBABE-IRSp53 WT. This localization of VASP was lost in MEFs infected with pBABE empty vector or pBABE-IRSp53 W413G mutant. Of note, IRSp53 localized along the shafts of protruding filopodia (see Figure 35).

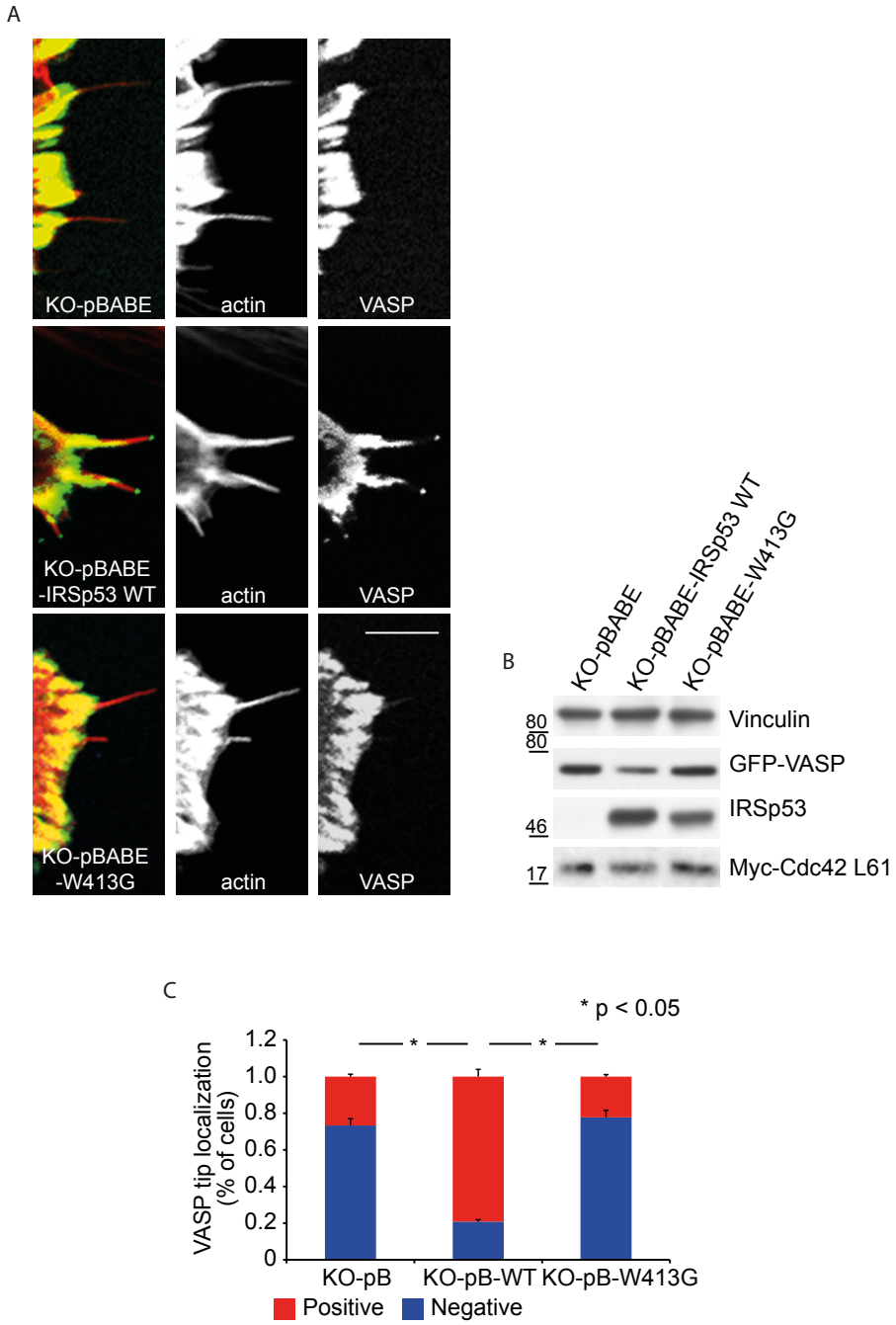

Figure 35. IRSp53 removal impairs VASP localization at filopodia tips.

A MEF cells derived from IRSp53 null mice and infected with pBABE empty vector, pBABE-IRSp53 or pBABE-IRSp53 W413G mutant, were electroporated with a constitutive active myc-tagged CDC42 mutant (myc-CDC42 L61) and GFP-VASP. Cells were fixed and stained with anti-myc antibody to detect CDC42 L61 (not shown) and rhodamine-phalloidin to detect actin. Right panels show single channels for actin and VASP. Scale bar is 5 µm.

B Expression levels of myc-CDC42 L61, GFP-VASP, IRSp53 and vinculin were analysed by immunoblotting in IRSp53 null MEFs infected with pBABE empty vector, pBABE-IRSp53 WT and pBABE-IRSp53-W413G.

C The number of cells expressing CDC42 L61 and presenting VASP at tips of filopodia was counted. Data are mean ± s.e.m. from three independent experiments (modified from Disanza et al., 2013 [191]).

Genetic removal of IRSp53 affects directional cell migration and invasion

Filopodia are important to drive cell directional migration and ECM invasion [22]. IRSp53 is known to be involved in filopodia formation, a notion reinforced and extended by the data presented so far.

We, then, asked whether IRSp53 null MEFs display any migration defect. We subjected MEFs to scratch wound assays. We observed that IRSp53 null MEFs were defective in wound closure, as compared to MEFs reconstituted with pBABE-IRSp53, due to their reduced speed and migration directionality (Figure 36). Of note, they were also impaired in extending polarized protrusions in the wound space (not shown).

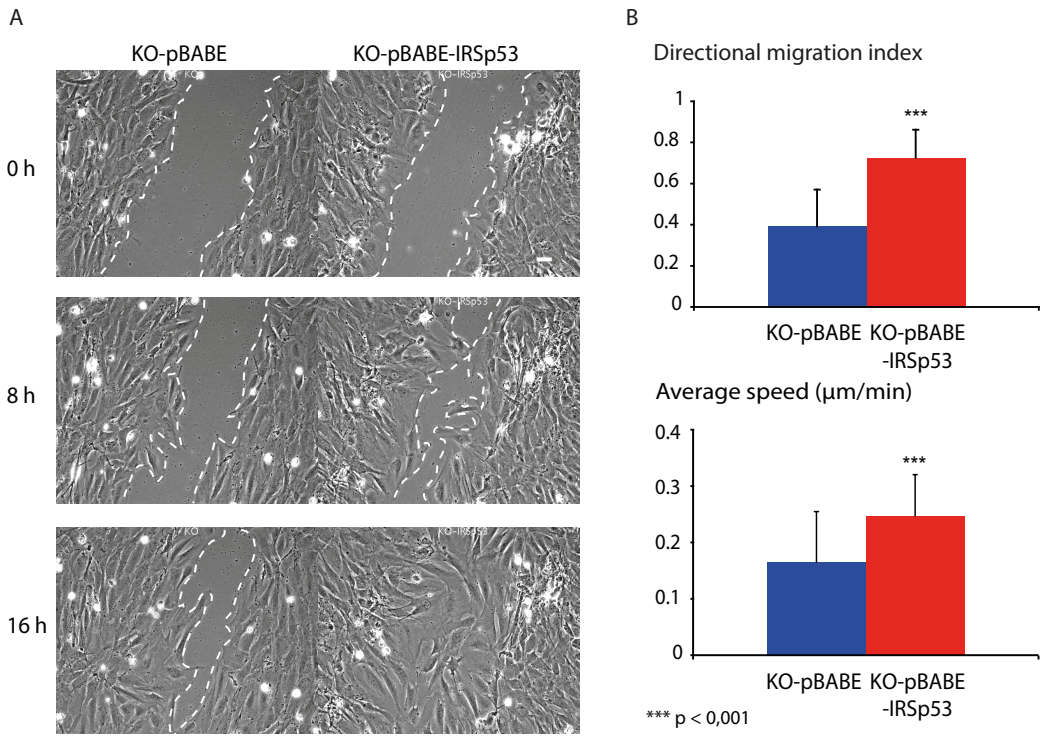

Figure 36. IRSp53 removal affects wound healing closure in MEFs.

A IRSp53 null MEF cells, infected with pBABE empty vector of pBABE-IRSp53 WT vector were seeded and grown to confluence. Cells were then scratched with a tip and analysed by DIC time-lapse imaging (20 hours, 5 minutes time interval). In the panels are represented still images taken at the indicated time points. White-dashed lines mark the front of migrating cells, bar is 50 µm.
B Single-cell migration was analysed from time-lapse data presented in A, using the ImageJ software. Upper panel: the directional migration index was calculated, it represents the ratio between the total distance covered by the cells and the distance covered longitudinally towards the centre of the wound. Lower panel: calculated average speed. At least 20 cells were analysed for each condition, in three independent experiments (modified from Disanza et al., 2013 [191]).

We also subjected IRSp53 null MEFs to different trans-well migration and invasion assays: we observed that these cells were defective in migration (both in serum or PDGF chemotactic conditions, shown in Disanza et al., 2013 [191]) and matrigel invasion (Figure 37), with respect to MEF cells infected with pBABE-IRSp53.

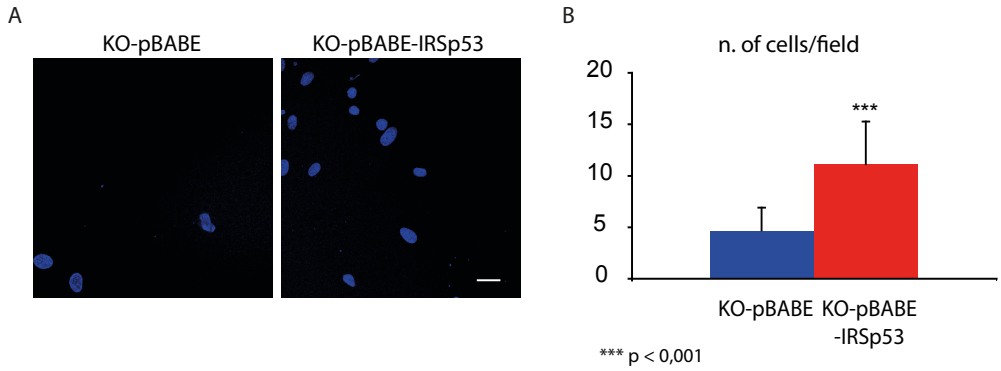

Figure 37. IRSp53 removal affects MEFs invasion.

A KO-pBABE and KO-pBABE-IRSp53 MEF cells were subjected to invasion assay and plated on Matrigel-coated chambers. PDGF was added in the lower chamber to generate a chemo-attractive gradient. Cells were fixed after 16 hours and stained with DAPI to detect nuclei. Bar is 10 µm.
B Quantification of the number of cells passing the semi-permeable membrane. At least 10 fields were analysed for each condition, data are mean ± s.e.m. from three independent experiments (modified from Disanza et al., 2013 [191]).

Finally, we took advantage of *Irsp53* null mice, and subjected them to dermal punch wound as model of wound healing. During tissue repair, cells migrate to the wound area, including keratinocytes, endothelial cells, macrophages and mesenchymal cells. We observed that *Irsp53* null mice displayed a delayed wound closure when compared to WT mice (Figure 38).

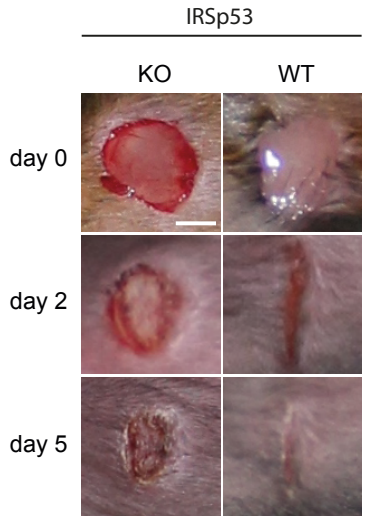

Figure 38. Genetic removal of IRSp53 in mice impairs wound repair.

10-week-old *Irsp53* KO and WT littermate mice were subjected to dermal punch wound model, performing four wounds on their back skin. Wounds closure were monitored over a 7-days period, microphotographs of wounds were captured to determine the degree of wound closure (modified from Disanza et al., 2013 [191]).

Hematoxyilin and eosin and immunohistochemical analysis (shown in Disanza et al., 2013 [191]) revealed that there were no differences in cellular composition and overall morphology between wounds in KO and WT mice, suggesting that IRSp53 is not required for skin development, but affects the re-epithelialization process. We observed that endothelial cells were recruited in similar numbers to wounds from KO or WT mice, while macrophages recruitment was reduced in IRSp53 null mice. These findings support the hypothesis that IRSp53 is crucial for efficient cell directional migration both in cells and *in vivo*.

Part two: IRSp53 is involved in the early steps of lumenogenesis

IRSp53 is apical and junctional localized in MDCK cells monolayer, but it stays at the lumen in MDCK cysts

Scattered set of evidence suggest an involvement of IRSp53 in polarity establishment. To explore further this possibility, we initially selected MDCK cells as model system, since these cells can be easily grown as cysts, with clearly defined apical and basal surfaces, able to recapitulate *in vitro* the polarity morphogenetic program. Noteworthy, a lot of information are available in literature about the molecular mechanism of lumenogenesis in MDCK cells [176] [178].

MDCK cells were infected with lentiviral vectors encoding for GFP-IRSp53, or GFP as control. Cells were grown at confluence to allow the formation of a mature and polarized monolayer. Under these conditions, we assessed the localization of GFP-IRSp53: it was enriched on both the apical and junctional lateral area, and partially co-localized with β-catenin and podocalyxin (Figure 39).

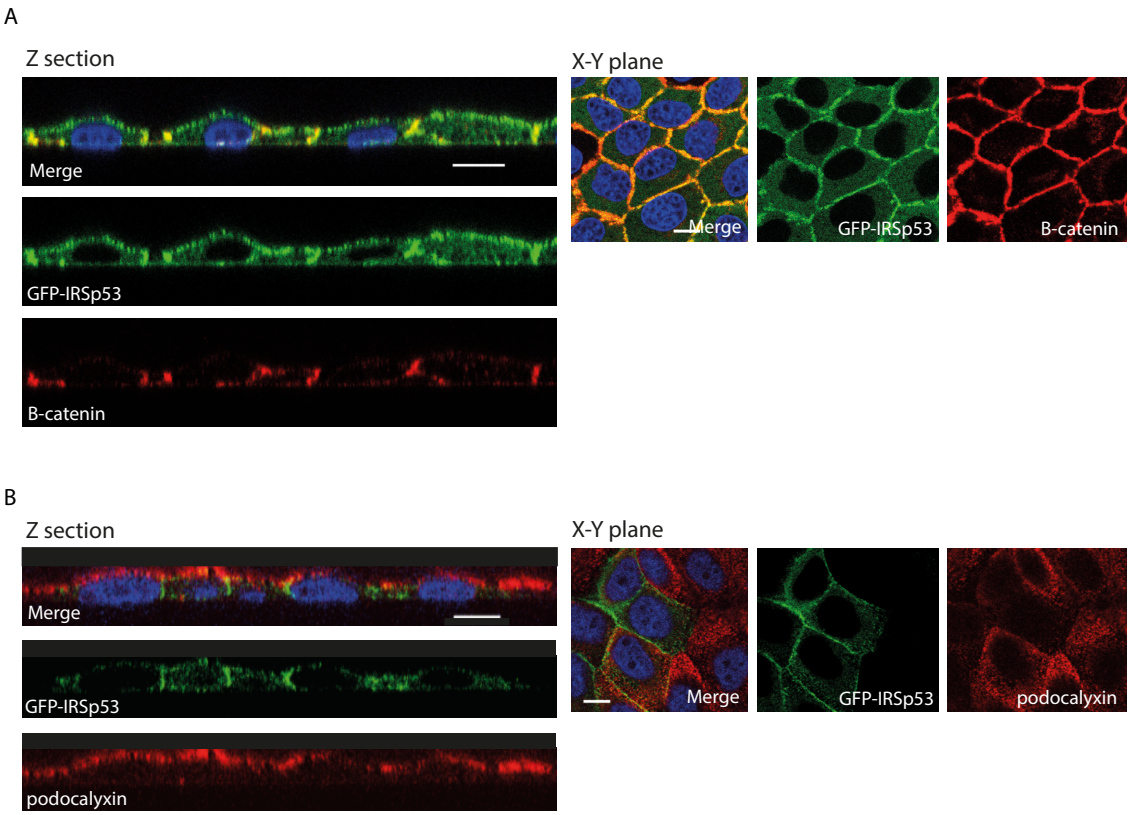

Figure 39. IRSp53 localizes to apical and junctional areas in MDCK monolayer.

A MDCK cells were infected with GFP-IRSp53 and grown at confluency. Cells were then fixed and stained with anti-β-catenin antibody, DAPI was used to detect nuclei. Z and X-Y sections were taken using a confocal microscope. Scale bar is 10 μm.

B MDCK cells were infected with GFP-IRSp53 and grown at confluency. Cells were then fixed and stained with anti-podocalyxin antibody, DAPI was used to detect nuclei. Z and X-Y sections were taken using a confocal microscope. Scale bar is 10 μm.

When MDCK cells were plated on top of a Matrigel layer, to form a polarized cyst, GFP-IRSp53 was restricted to the apical/lumenal side, co-localizing with the apical marker phalloidin, but not with β-catenin. Importantly, endogenous IRSp53 also displayed a pattern similar to the ectopically expressed GFP-tagged protein, validating the relevance of the latter approach to gain clues about the distribution of IRSp53 in epithelial cells and tissues. Of note, GFP alone was diffused in the cytoplasm, as expected (Figure 40).

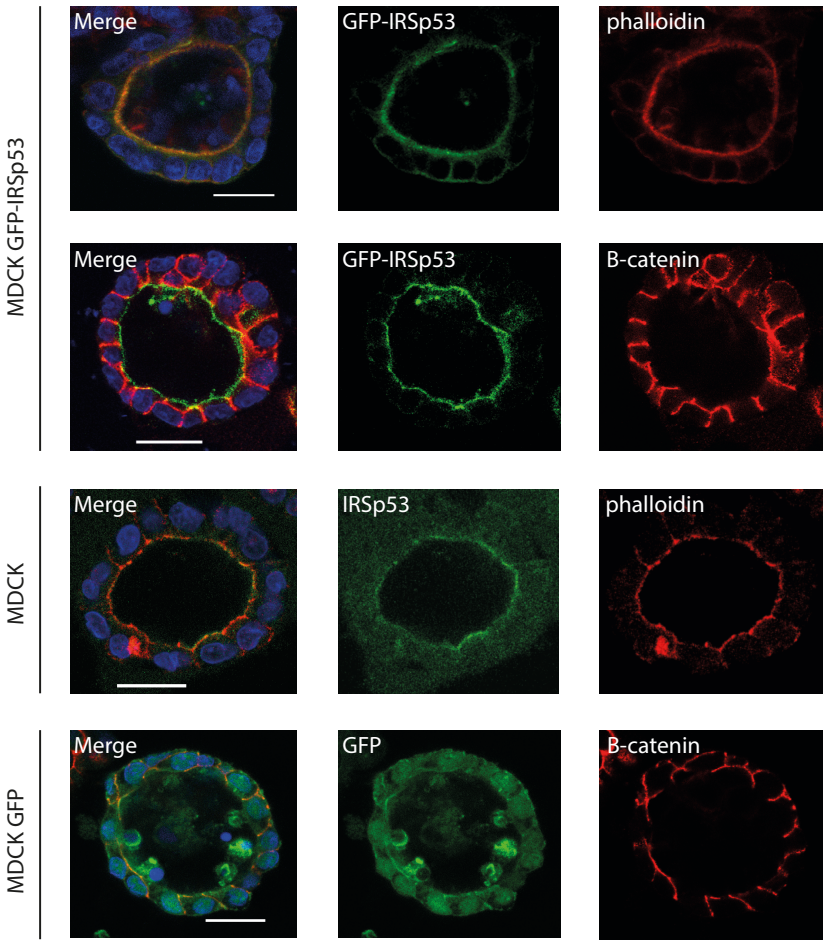

Figure 40. IRSp53 localizes at the lumenal region in MDCK cysts.

MDCK cells WT or infected with GFP or GFP-IRSp53 were resuspended as single cells and plated on a Matrigel layer for 6 days, to form a polarized cyst. Cysts were then fixed and stained with phalloidin, anti-β-catenin or anti-IRSp53 antibody, DAPI was used to detect nuclei. Images are confocal section of the central region of each cyst. Scale bar is 18 μm.

To validate these findings, we selected another cell line, of human origin, that forms spheroids when embedded in a Matrigel-collagen matrix: Caco2. We again tested GFP-IRSp53 localization in Caco2 spheroids: as seen in MDCK, we found that IRSp53 was prominently enriched in the apical region of the organoids (Figure 41).

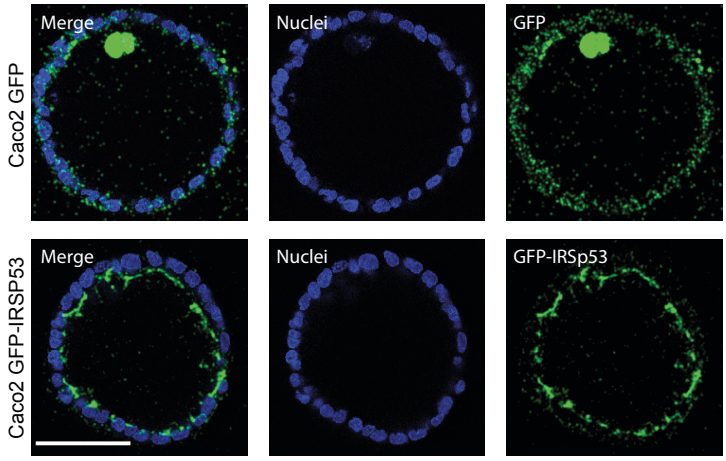

Figure 41. IRSp53 localizes at the lumenal region in Caco2 cysts.

Caco2 cells have been infected with GFP or GFP-IRSp53 encoding vectors. Single cells were then embedded in Matrigel-collagen mixture to form Caco2 spheroids. Spheroids were then fixed, stained with DAPI to detect nuclei and analysed by confocal microscopy. Images are confocal section of the central region of each cyst. Scale bar is 70 μm.

IRSp53 KD affects the morphogenesis of MDCK cysts

Next, we took advantage of IRSp53 Tet-off system to knock down IRSp53 in MDCK cells [152]. We found that removal of IRSp53 caused the formation of cysts with an aberrant morphology (Figure 42). We quantified the percentage of cyst presenting a multilumen phenotype in both IRSp53 WT than IRSp53 KD background: in the presence of IRSp53 WT, only 11% of cyst possessed an aberrant phenotype, while when IRSp53 was knocked down, ~55% of cysts showed a multilumen phenotype.

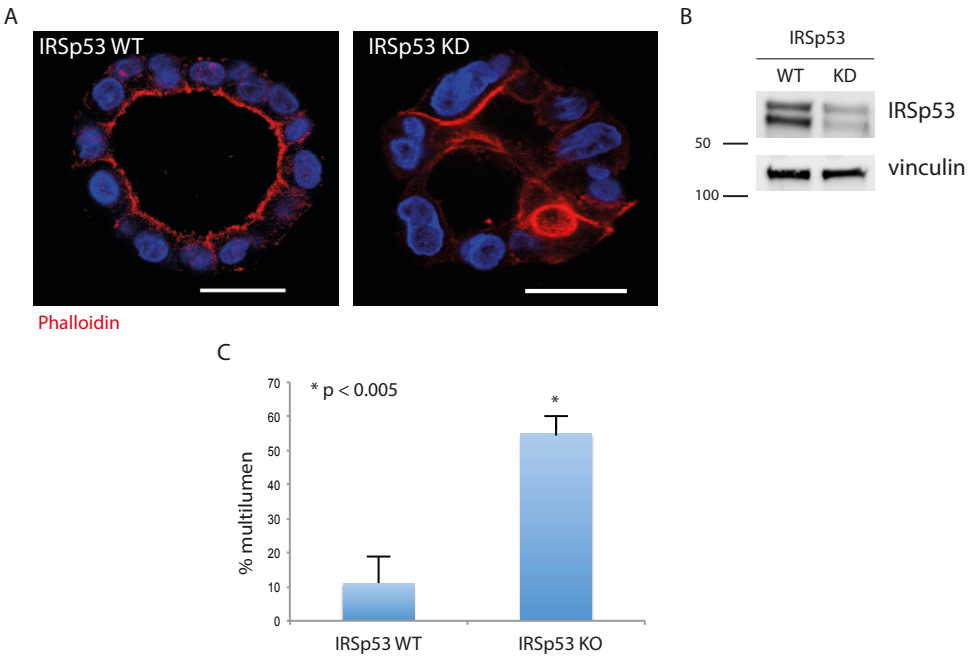

Figure 42. IRSp53 KD causes multilumen phenotype in MDCK cysts.

A MDCK IRSp53 Tet-off cells were treated with or without doxycycline, to induce IRSp53 depletion. Single cells were plated on Matrigel to form cysts and fixed at day 6. Cysts were then incubated with TRIC-phalloidin to highlight the lumen and DAPI to stain nuclei. Images are confocal section of the central region of each cyst. Scale bar is 18 μm.

B Levels of IRSp53 expression in MDCK IRSp53 Tet-off cells treated with or without doxycycline, to induce IRSp53 depletion.

C Percentage of cyst presenting a multilumen phenotype, formed by MDCK IRSp53 Tet-off cells treated with or without doxycycline, to induce IRSp53 depletion. Experiments were performed in triplicate, counting at least 30 cysts for each condition. Data are mean ± s.d.

We then checked the effect of IRSp53 depletion also in Caco2 cysts. We decided to use the CRISPR/Cas9 genome editing approach to permanently KO IRSp53 in Caco2 cells. Two clones were derived (#3, #12) and used to form organoids: again, we observed a multilumen phenotype in the cysts originated from IRSp53 KO Caco2 cells (with a frequency of 55% and 35% of multilumen cysts, respectively, in the two derived clones, in comparison with WT cells that form ~17% of aberrant cysts) (Figure 43).

Noteworthy, both in control and KO cysts, the lumens were stained for the apical marker aPKC, suggesting that IRSp53 removal does not affect the apical localization of this latter protein.

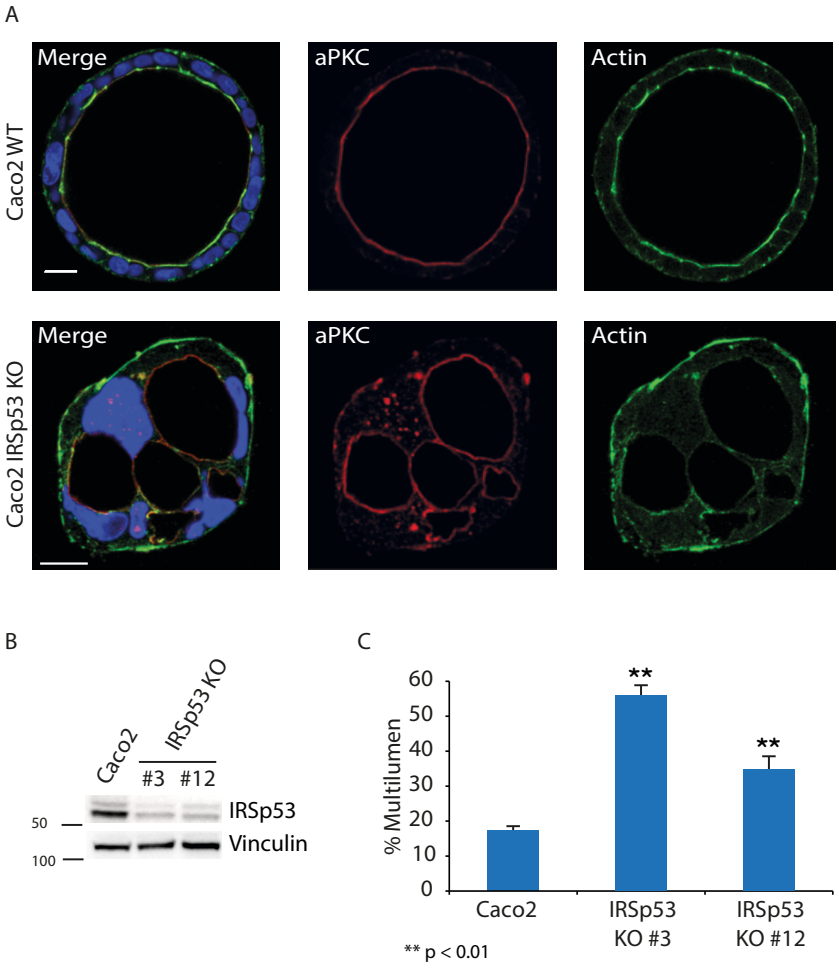

Figure 43. Multilumen cysts originate from IRSp53 KO Caco2 cells.

A Caco2 cells WT or IRSp53 KO (through CRISPR/Cas9 genome editing) were embedded in Matrigel-collagen matrix to form cysts. Cysts were then fixed, stained with aPKC, phalloidin and DAPI to detect nuclei and analysed by confocal microscopy. Images are confocal section of the central region of each cyst. Scale bar is 20 µm.

B Caco2 WT or IRSp53 KO (clones #3 and #12, originated by CRISPR/Cas9 genome editing) cells were lysated and immunoblotted with the indicated antibodies.

C Percentage of multilumen cysts originated from Caco2 WT or IRSp53 KO (clones #3 and #12, originated by CRISPR/Cas9 genome editing) cells, as described in A. At least 30 cysts were counted in 3 independent experiments.

To confirm that the multilumen phenotype in Caco2 IRSp53 KO cells was specifically due to the absence of IRSp53 protein, and not to spurious effects, we infected Caco2 IRSp53 KO clones with lentiviral vectors encoding for GFP or mouse GFP-IRSp53. In presence of GFP-IRSp53, the multilumen phenotype of IRSp53 KO cysts was rescued (24% of multilumen frequency), while GFP was not able to do the same (50% of multilumen frequency) (in Figure 44 A, images relatives to clone #12).

We then decided to perform a structure-function analysis, to understand which domain from IRSp53 was required for the correct organization of Caco2 cysts and start to get clues about the underlying mechanism. We infected IRSp53 KO clones with lentiviral vectors encoding for GFP-IRSp53 carrying a point mutation in the I-BAR, CRIB, SH3 or PDZ-binding domains and used these cells in our organoids assay. We observed a multilumen phenotype in presence of both IRSp53 mutated in I-BAR, CRIB and SH3 domain (multilumen frequency of 53%, 55% and 47% respectively), indicating that all of them are required for the correct execution of Caco2 polarity program. Only PDZ-binding domain is dispensable: Caco2 IRSp53 KO cells infected with GFP-IRSp53 PDZ mutant, in fact, formed cysts with a correct morphology (multilumen frequency reduced to 25%) (Figure 44 C, images relative to clone #12).

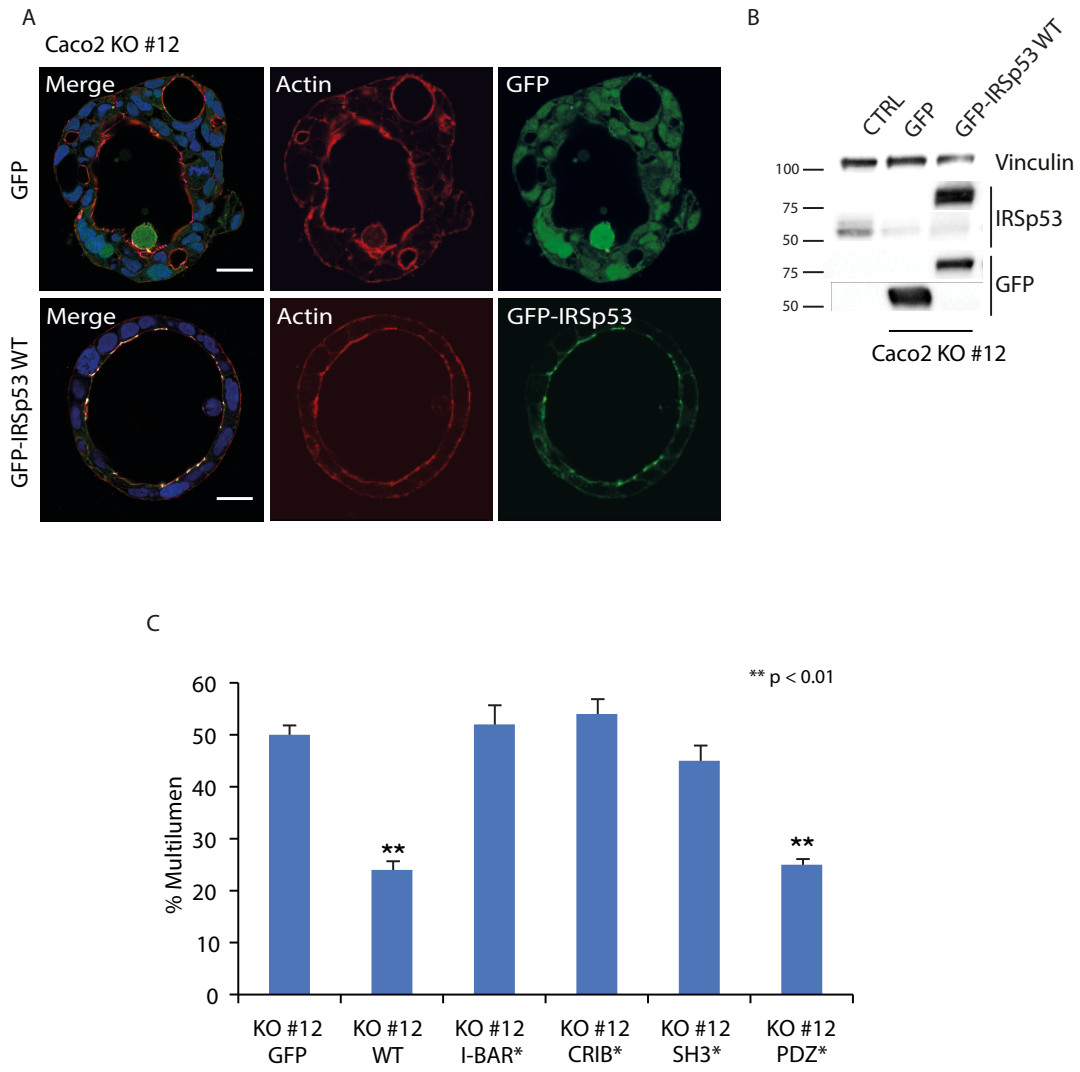

Figure 44. I-BAR, CRIB and SH3 domains are required for the correct lumenogenesis of Caco2 cysts.

A Caco2 cells IRSp53 KO (CRISPR/Cas9 derived clone #12) were infected with lentiviral vectors encoding for GFP or GFP-IRSp53. Cells were then embedded in Matrigel-collagen matrix to form cysts. Cysts were fixed, stained with phalloidin and DAPI to detect nuclei and analysed by confocal microscopy. Scale bar is 20 µm.

B Caco2 cells WT or IRSp53 KO (CRISPR/Cas9 derived clone #12) infected with lentiviral vectors encoding for GFP or GFP-IRSp53 were lysated and immunoblotted with the indicated antibodies.

C Percentage of multilumen cysts originated from Caco2 IRSp53 KO (CRISPR/Cas9 derived clone #12), and infected with lentiviral vectors encoding for GFP, GFP-IRSp53 WT or mutated (*) in I-BAR, CRIB, SH3 and PDZ-binding domains. Cysts were formed as described in A. At least 30 cysts were counted in 3 independent experiments.

Looking at the localization of GFP-IRSp53 mutants in Caco2 cysts, we observed a peculiar localization of IRSp53 I-BAR and SH3 mutants: both of them possessed a dotted localization in the apical portion, perfectly co-localizing with the tight junction protein ZO-1 (Zonula occludens protein 1) (Figure 45). Also IRSp53 WT and mutated in CRIB and PDZ-binding domains partially co-localize with ZO-1, but these dots were connected by regions of weaker signal along all the apical surface of the organoid (Figure 45).

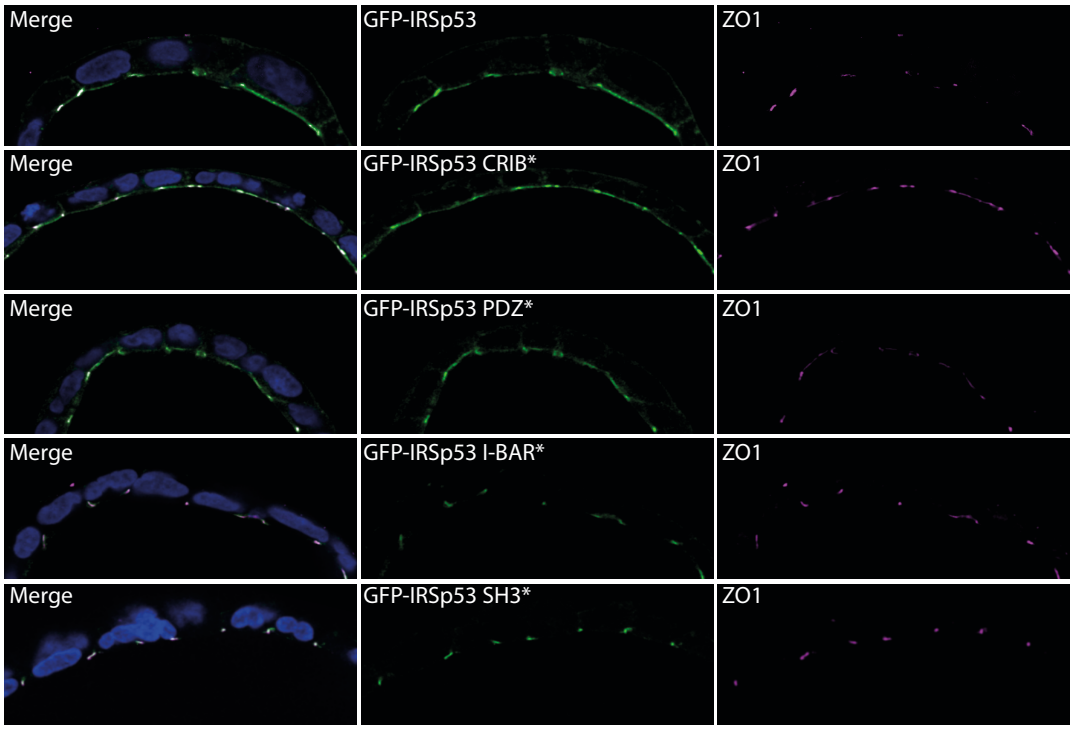

Figure 45. IRSp53 WT or mutated in I-BAR, CRIB, SH3 and PDZ-binding domains co-localize with ZO-1.

Caco2 cells IRSp53 KO (CRISPR/Cas9 derived clone #12) were infected with lentiviral vectors encoding for GFP-IRSp53 WT or mutated (*) in I-BAR, CRIB, SH3 and PDZ-binding domains. Cells were then embedded in Matrigel-collagen matrix to form cysts. Cysts were fixed, stained with ZO-1 and DAPI to detect nuclei and analysed by confocal microscopy. Images are magnification of confocal sections in the center of the cysts.

In summary, we observed that IRSp53 localizes to the apical region of MDCK and Caco2 organoids; the reduced expression of IRSp53 causes the formation of

multilumen cysts in both the cell lines. I-BAR, CRIB and SH3 domains are all required for IRSp53 to exert its role in the correct establishment of a polarized cyst. Finally, both I-BAR and SH3 domains are necessary for the continuous apical localization of IRSp53.

IRSp53 is early recruited at cell-cell junctions in the early stages of MDCK cyst formation

The above mentioned results pointed out an involvement of IRSp53 in pathways leading to polarization and acquisition of apical features, although the actual role of IRSp53 in lumenogenesis remains elusive. To get insights into the timing of IRSp53 involvement in the polarity program, we next decided to investigate if it was necessary in the early phases of MDCK cysts formation. We observed that in single cells IRSp53 was enriched at the plasma membrane, while at two-cells stages IRSp53 re-localized at cell-cell contact, overlapping with β-catenin (Figure 46). Of note, the region in the middle between the two cells has been identified as the so called AMIS, in which all the apical proteins will be recruited to form a mature cyst (see "Introduction").

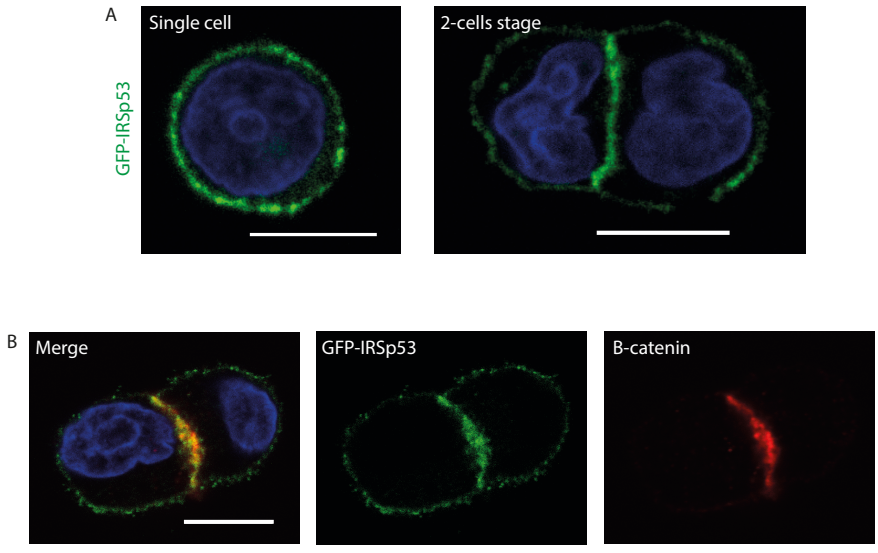

Figure 46. IRSp53 localizes to cell-cell contacts in early stage MDCK cysts.

A GFP-IRSp53 localization in MDCK cysts at one- or two-cells stages. MDCK cells infected with GFP-IRSp53 were resuspended as single cells, plated on a Matrigel layer and fixed at 6-12 hours. DAPI was used to detect nuclei. Images are confocal section of the central region of each cyst. Scale bar is 10 μm. **B** GFP-IRSp53 localization in two-cells stage MDCK cysts. MDCK cells infected with GFP-IRSp53 were resuspended as single cells, plated on a Matrigel layer and fixed at 16 hours. Cysts were stained with anti-β-catenin, DAPI was used to detect nuclei. Images are confocal section of the central region of the cyst. Scale bar is 10 μm.

We then performed a time-course analysis, following GFP-IRSp53 and podocalyxin localization in the early steps of cysts formation. The latter protein is a known apical marker that is rapidly translocating from the plasma membrane to the apical region, during cystogenesis (see "Introduction") via membrane trafficking [176].
We observed GFP-IRSp53 enrichment at cell-cell contact, already 8 hours after MDCK cells plating on Matrigel (Figure 47). Under the same conditions, podocalyxin was still at the plasma membrane. We also observed GFP-IRSp53 partially localized into vesicular-like structures, that were, at least in part, also positive for podocalyxin, which is known to undergo exocytic recycling through RAB8 and RAB11a positive vesicles (see "Introduction"). At 20h, both GFP-IRSp53 and podocalyxin accumulated in the AMIS region, and later on the apical side of the opening lumen. After 6 days a complete cyst was formed, with GFP-IRSp53 and podocalyxin co-localizing in the lumen (Figure 47).

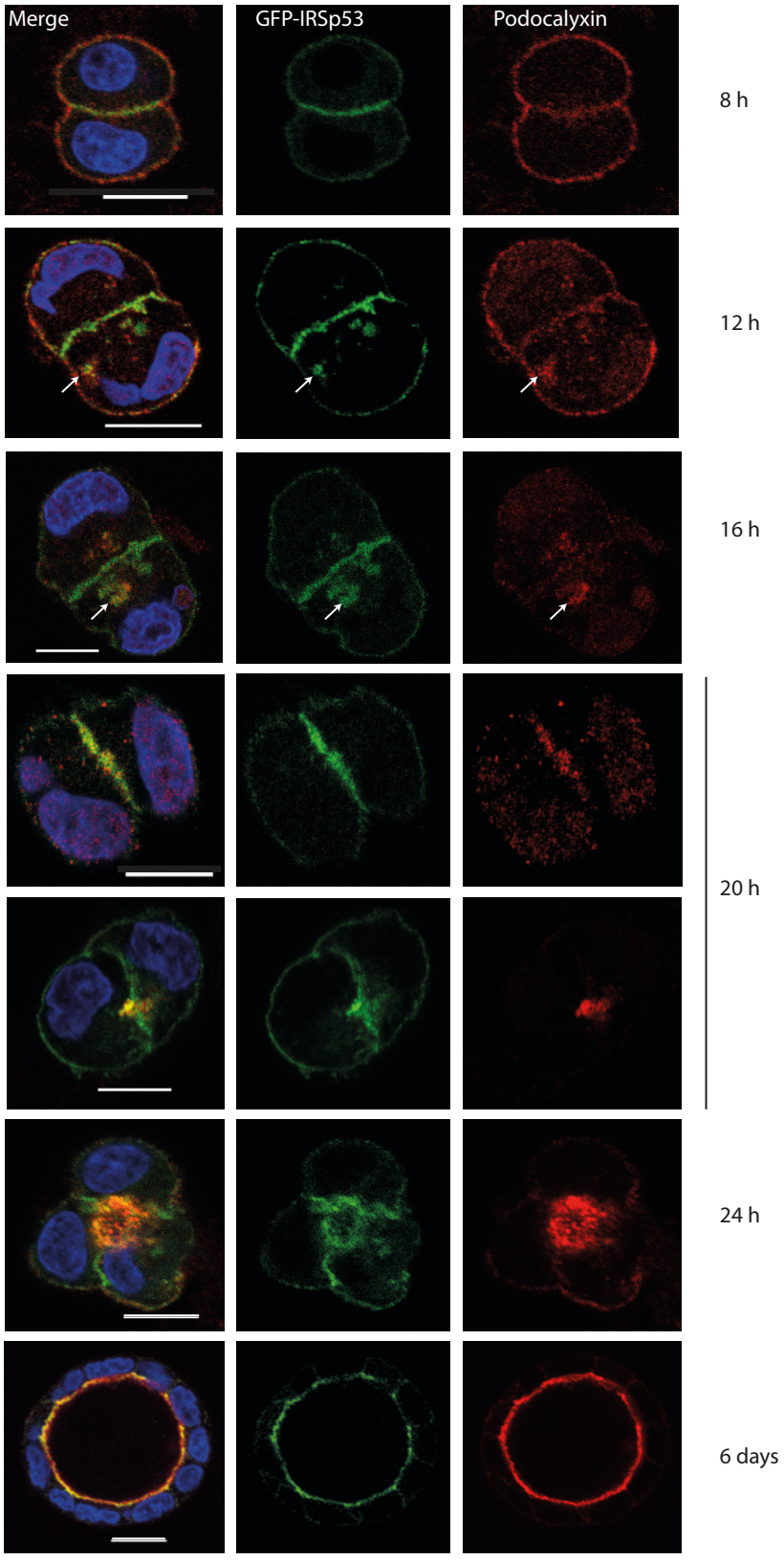

Figure 47. IRSp53 and podocalyxin localization during MDCK cystogenesis.

MDCK cells infected with GFP-IRSp53 were resuspended as single cells, plated on a Matrigel layer and fixed at the indicated time points. Cysts were stained with anti-podocalyxin antibody, DAPI was used to

detect nuclei. Images are confocal section of the central region of each cyst. Arrows highlight the areas of partial co-localization between GFP-IRSp53 and podocalyxin. Scale bar is 12 μm.

IRSp53 partially localizes in vesicles positive for phalloidin, podocalyxin, RAB7 and RAB11a

To get insight about the intracellular compartments in which we observed GFP-IRSp53 enrichment during the early phases of cyst formation, we performed co-staining of GFP-IRSp53 expressing MDCK cells with different markers (Figure 48). We observed GFP-IRSp53 in vesicular-like compartments, partially co-localizing with phalloidin, podocalyxin, RAB7 (which localizes in late endosomes) and RAB11a. We observed no co-localization between GFP-IRSp53 and EEA1 (early endosome antigen 1, an early endosomes marker), LAMP1 (lysosome-associated membrane glycoprotein 1, a late endosomes and lysosomes marker) nor Giantin (a Golgi marker).

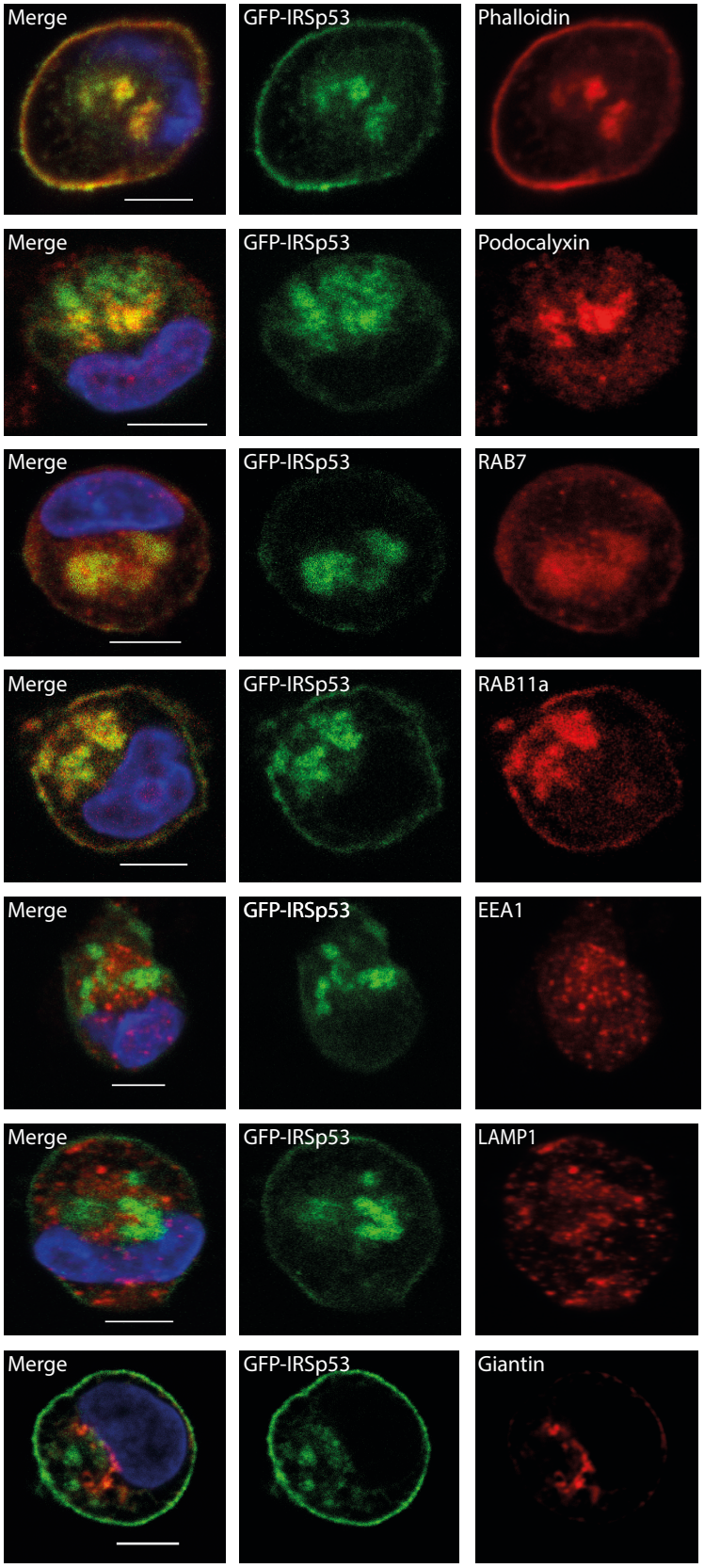

Figure 48. Co-localization analysis of GFP-IRSp53 positive vesicles.

MDCK cells were infected with GFP-IRSp53, resuspended as single cells and plated on a Matrigel layer. Cysts at one-cell stage were fixed at 8 hours after plating and stained with phalloidin, anti-podocalyxin, anti-RAB7, anti-EEA1, anti-LAMP1 or anti-Giantin antibodies. For RAB11a, cotrasfection with apple-

RAB11a construct was used. DAPI was used to detect nuclei. Images are sums projections of confocal sections containing GFP positive vesicles. Scale bar is 6 μm.

IRSp53 KD affects podocalyxin relocalization in the early phases of MDCK cyst formation

As shown above, IRSp53 is enriched at the cell-cell contact region and at the AMIS during the early phases of MDCK cystogenesis. We next asked whether IRSp53 removal affects cyst formation soon after cell plating on Matrigel, in order to investigate the possibility that IRSp53 might play a role in early polarity signalling program.

We observed that in WT cells, podocalyxin nicely accumulated at the AMIS in three-four cells cysts, and only 35% of them presented aberrant podocalyxin localization. Upon transient siRNA-mediated IRSp53 KD, podocalyxin was mislocalized and accumulated in discrete foci in 52% of the analysed cysts. Podocalyxin distribution was reverted to its correct localization upon GFP-IRSp53 re-expression into IRSp53 KD cells: in this case, only 22% of the cysts presented aberrant podocalyxin localization (Figure 49).

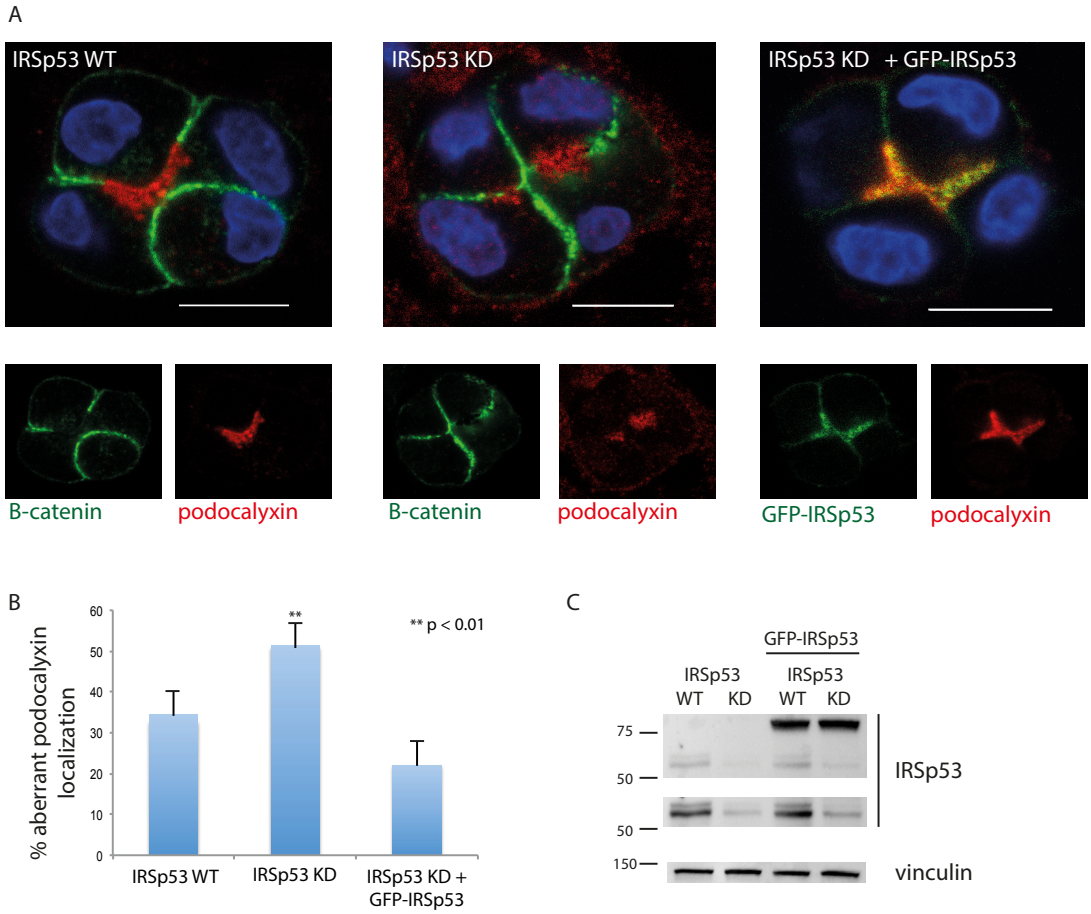

Figure 49. IRSp53 KD affects podocalyxin localization in three-four cells cysts.

A MDCK cells WT or infected with GFP-IRSp53 were treated with control or IRSp53 canine-targeted siRNA, to knock down IRSp53. Cells were resuspended as single cells and plated on a Matrigel layer for 24-30 hours. Cysts were then fixed and stained with anti-β-catenin and anti-podocalyxin antibodies, DAPI was used to detect nuclei. Images are confocal section of the central region of each cyst. Scale bar is 10 μm.

B Percentage of cysts presenting aberrant podocalyxin localization, in the conditions tested in panel A. The experiment was performed in triplicate, analysing at least 30 cysts per condition.

C Level of expression of IRSp53 in MDCK cells WT or infected with GFP-IRSp53, that were treated with control or IRSp53 canine targeted oligoes.

We then performed a structure-function analysis, to investigate which domain from IRSp53 was required to correctly localize podocalyxin in the early phases cysts. We used a siRNA approach to KD endogenous IRSp53 protein, in MDCK cells that have

been previously infected with GFP-IRSp53 mutated in I-BAR, CRIB, SH3 or PDZ-binding domains. We observed that both I-BAR, CRIB and SH3 domains mutation caused an aberrant localization of podocalyxin in cysts at 24-30 hours after plating (in 60%, 59% and 59% of cysts, respectively). On the contrary, PDZ-binding domain is dispensable for podocalyxin re-localization: in 24-30 hours time-frame, only 43% of cysts presented an altered distribution of this apical marker (Figure 50).

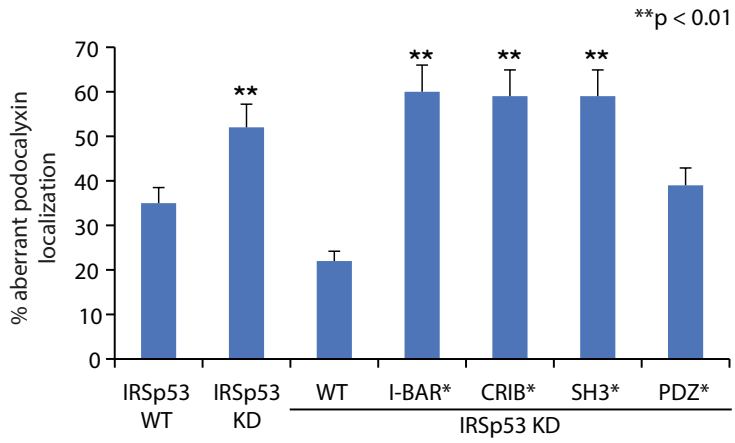

Figure 50. I-BAR, CRIB and SH3 domains are required for correct podocalyxin localization in early stages MDCK cysts.

Percentage of cysts presenting an aberrant podocalyxin localization. MDCK cells were infected with GFP-IRSp53 WT or mutated (*) in I-BAR, CRIB, SH3 and PDZ-binding domains. Infected and parental cells were treated with control or IRSp53 canine-targeted siRNA, to KD endogenous IRSp53. Cells were resuspended as single cells, plated on a Matrigel layer and fixed after 24-30 hours. At least 30 cysts were analysed for each condition.

Discussion and future plans

A model for filopodia initiation based on CDC42:IRSp53:VASP axis

To summarize our findings, we showed that i) IRSp53 possesses a weak capping activity, which is relieved by CDC42-GTP binding. ii) A CDC42:IRSp53 interaction is critical to induce a structural rearrangement of IRSp53 protein as well as for the formation of a CDC42:IRSp53:VASP complex. iii) *In vitro*, IRSp53 is able to mediate VASP clustering on functionalized surfaces and lipid bilayer, fostering VASP processive elongation activity. iv) The *in vitro* findings were mirrored by *in vivo* experiments in which we observed that IRSp53 is essential to promote the formation of VASP foci along discrete areas on the plasma membrane and to efficiently promote filopodia formation.

Based on the above-mentioned results, we propose the following model for filopodia formation. In the initial state, IRSp53 through its I-BAR domain, localizes preferentially along the plasma membrane. At this site, in resting or signalling off conditions, the weak capping activity of IRSp53 likely prevails and contributes to ensure that unfruitful, or uncontrolled, actin polymerization occurs. Actin polymerization inhibition, in this phase, might be reinforced by IRSp53 interaction with EPS8, due to EPS8 capping activity [160]. Upon CDC42 activation, two key biochemical events may take place. Firstly, IRSp53 inhibition of barbed end growth is relieved. Secondly, the protein switches to its open conformation: open IRSp53 is then able to interact with VASP. Indeed, immunoprecipitation experiments (not shown in this thesis, but included in Disanza et al., 2013 [191]) suggest that in the presence of active CDC42, IRSp53:EPS8 interaction is competed out and the association with others SH3 binders, and specifically VASP, is favored. IRSp53 then induces localized VASP clustering, which is, in turn, essential for promoting its processive actin elongation activity. Long actin filaments are consequently produced,

which cooperate with IRSp53 membrane bending activity to promote and sustain filopodia formation, in a spatially restricted and timely coordinated manner. Other proteins are concomitantly recruited and required, for example, to bundle linear actin filaments, such as the crosslinking protein fascin, thereby increasing the stiffness of the inner cytoskeletal core of the filopodia. This is though to be necessary to oppose the counter forces exerted either by the increase in membrane tension or by the extracellular environment (Figure 51).

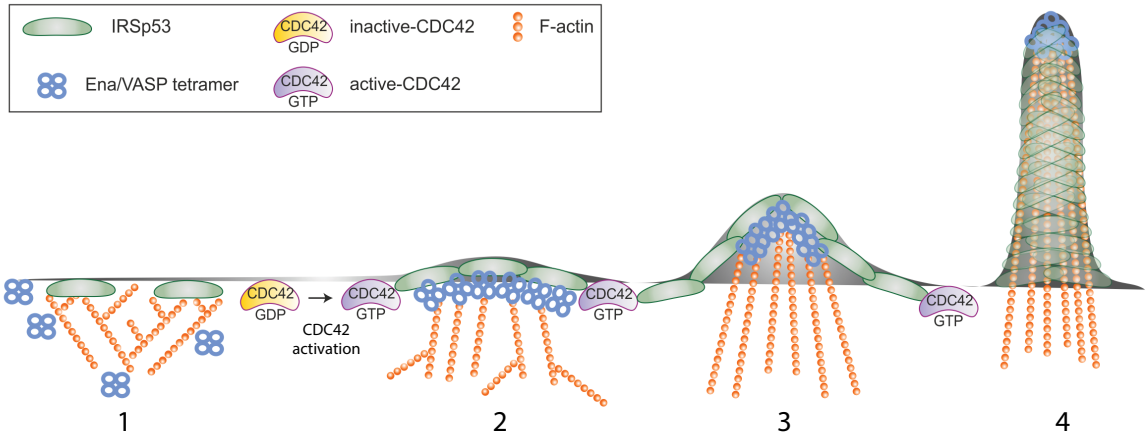

Figure 51. Model for filopodia initiation.

Here are depicted the proposed steps that characterize the initial phases of filopodia formation. Step 1: in the absence of stimuli, IRSp53 binds the plasma membrane and slows down barbed end elongation. Step 2: following CDC42 activation due to an external stimulus, CDC42 binds IRSp53 promoting IRSp53 shift to its open conformation and the interaction with VASP, forming a CDC42:IRSp53:VASP complex. Step 3: IRSp53 and VASP foci are formed at the plasma membrane, VASP clustering allows processive actin filament elongation. Step 4: membrane deforming activity of IRSp53 and processive actin filament elongation by VASP work in concert to promote filopodia initiation, in coordinated time and space (modified from Disanza et al., 2013 [191]).

Our observations are in agreement with the recently proposed model of IRSp53 conformational changes upon CDC42 binding, described by Kast et al., 2014 [115], and cited in the introduction of this thesis. Briefly, an intramolecular interaction

between IRSp53 CRIB and SH3 domains determines the formation of a "close" conformation. Upon active CDC42 binding, the intramolecular interaction is abrogated and IRSp53 switches to an "open" conformation. Thus, IRSp53 in the "close" conformation could exert capping activity over the actin filaments, while the formation of a complex between CDC42 and "open" IRSp53 will favor its interaction with the SH3 binder VASP, and consequently promotes filaments elongation. Interestingly, an independent report have linked IRSp53:VASP interaction to podosome formation in NIH-Src cells. Podosomes are another type of small cylindrical protrusion (1μm in diameter or less), rich in actin filaments and containing also focal adhesion molecules. Podosomes assemble in rosetta-like structures and are important for cell migration and ECM invasion [193]. These observations suggest that IRSp53:VASP interaction may be conserved and crucial for the emergence of different protrusive actin-based cellular structures.

It must be pointed out, however, that EGFP-IRSp53 in MV^{D7} Ena/VASP family deficient fibroblast cells still localizes to the tips of lamellipodia and filopodia [194], implying that IRSp53 localization is not affected by the loss of VASP, and, more importantly, that the IRSp53:VASP complex is not absolutely essential or uniquely required for filopodia formation. Additional mechanisms are likely to be operative in these cells to ensure filopodia formation, further pointing to the existence of multiple and independent pathways capable of stimulating filopodia elongation. This seems to be actually the case, as suggested by Goh et al., 2012 [195], which showed that mDia1 and WAVE2 interaction with IRSp53 may also participate in promoting filopodia in N1E-115 cells (mouse brain neuroblasts), independently of Ena/VASP family proteins. Of note, it was already known that mDia1/2 can directly induce filopodia formation [196] [23], but filopodia initiated by Ena/VASP or mDia2 proteins possess distinct properties, differing in their number, length and lifetime [197]. Goh et al.,

2012 [195], however, observed that RFP-IRSp53 acted in synergy with GFP-WAVE2 or GFP-mDia1 when the proteins are coexpressed, while depletion of mDia1 or WAVE2 decreased the ability of IRSp53 to induce filopodia in N1E-115 cells. Interestingly, mDia1 formin localizes along all the length of the filopodia, while VASP is rigorously restricted to the filopodia tips. Similarly, Gertler's group showed that the genetic removal of all the Ena/VASP family members in mice severely compromised filopodia extension in primary neurons, however, filopodia could still be induced by either plating cells on laminin or upon ectopic expression of mDia2 or myosin X [99]. The validity of the model described above finds further experimental and theoretical support in a more recent work by Prevost et al., 2015 [121]. The authors, using a variety of biochemical and *in vitro* reconstituted liposome-based systems, proposed that the I-BAR domain of IRSp53 is present at low concentration and density along the plasma membrane at the steady state. Local and transient fluctuations of the membrane are subsequently stabilized and amplified by IRSp53, through a feed forward loop. At moderate protein density, I-BAR intrinsic curvature can, indeed, favor negative curvature and the local recruitment of more IRSp53 proteins. As a consequence of IRSp53 accumulation, the protein will phase separate into coexisting domains of different curvature along the plasma membrane, explaining why IRSp53 may be the first protein to mark the nascent filopodia and to be required for the initial formation of protrusions.

Novel roles of IRSp53 in polarity determination

As shown in the second part of the results section, we observed that in models of 3-D cells cysts, IRSp53 is prominently enriched in the apical region, while IRSp53 depletion leads to a multilumen phenotype, suggesting a role of IRSp53 in the polarity program. Lumenogenesis is a fundamental step in the morphogenesis of many hollow

epithelial organs; interestingly, performing a tissue microarray (TMA) screening, we observed IRSp53 enrichment in the lumenal/apical region of different human tissues, as kidney, prostate and duodenum (Figure 52), providing support to our *in vitro* observations in organoids. We are currently investigating if our IRSp53 KO mice present defects in the structure and function of these tissues.

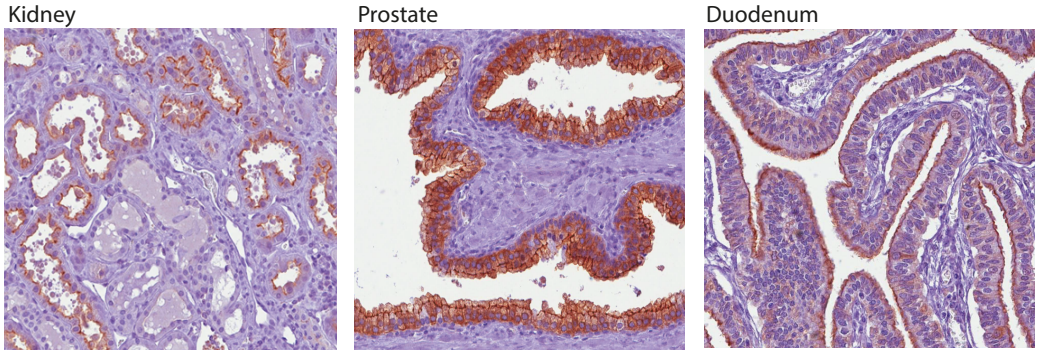

Figure 52. Immunohistochemistry analysis of human samples of different origin.

Tissues where stained with anti-IRSp53 polyclonal antibody.

We also observed an early enrichment of IRSp53 in the AMIS region of MDCK cysts at two-cells stage, that precedes in time podocalyxin enrichment in the same region. As reported in the introduction, podocalyxin relocalization to the AMIS region is a key event in the definition of polarity in MDCK cysts. Data presented here points to a role of IRSp53 in podocalyxin relocalization, possibly through the regulation of podocalyxin trafficking. This latter hypothesis is supported by the observations of aberrant podocalyxin localization upon IRSp53 loss in MDCK cysts at four-cells stage and of GFP-IRSp53 enrichment in vesicular-like compartments in MDCK cells plated on Matrigel. It must be pointed out, however, that the data collected so far are not enough to rule out a possible involvement of IRSp53 in functions of the polarity program other than the trafficking of polarity determinants.

A number of factors can cause multiple lumen and defective polarization in 3-D models of epithelial cells [176]:

1- alterated trafficking of apical proteins, that impedes the enlargement and consolidation of small lumens into one central lumen;

2- defective junctions between cells forming 3-D organoids;

3- mislocalization of pumps and channels, which generate the hydrostatic pressure that is required for lumen enlargement;

4- aberrant orientation of mitosis, that affects the spherical structure of the growing organoid. This effect could be due to defective localization and/or function of the proteins that regulates spindle orientation and cytokinesis, as CDC42 [181], aPKC and LGN.

IRSp53 may impinge on any or all of these processes, which we are currently investigating, in order to shed light on the mechanism by which IRSp53 is involved in the polarity program.

Interestingly, a structure-function analysis of IRSp53 to define the key domains that are required to guarantee a correct phenotype in Caco2 and in early phases MDCK cysts, showed that the I-BAR, CRIB and SH3 domains are all necessary, while the PDZ-binding domain is dispensable. These observations can all be rationalized within a framework whereby: i) the I-BAR domain recognizes PIP_2, which is known to be enriched at the apical membrane [169]. ii) The CRIB domain may link IRSp53 to the CDC42/PAR3/PAR6 complex, which is apically localized at the very early stages of lumen formation, and is involved in the establishment of polarity by regulating several processes of transcytosis, as well as spindle orientation. iii) The SH3 domain might exert its role through the recruitment of one or more effectors, unknown so far.

Investigation of novel IRSp53 interactors through proximity biotinylation and mass spectrometry analysis

To investigate if novel IRSp53 effectors are required by this protein to exert its role on polarity establishment, we took advantage of BioID strategy coupled to mass spectrometry analysis, as described in Roux et al., 2012 [198]. Briefly, the protein of interest is fused to a promiscous biotin protein ligase (BirA*), so that, after supplementation of cell culture medium with biotin, all the primary amine groups (predominantly lysines) around 15-20 nm from the bait are biotinylated. Biotinylated proteins are then selectively isolated and analysed by mass spectrometry.

Given the mechanism of BioID, biotinylated proteins can be direct interactors of the protein of interest, indirect interactors or only vicinal proteins. Due to the strong interaction between biotin and streptavidin, harsh condition can be used to lyse cells and in the subsequent passages, without compromising the efficiency of the *in vitro* binding.

In particular, we used HeLa cells infected with lentiviral constructs encoding for BirA*-IRSp53 or BirA*-GFP as control. In our experiments, BirA* approach was combined with stable isotope labelling with amino acids in cell culture (SILAC), to have a quantitative result of the protein enrichment in the two samples. Results are summarized in Table 1: proteins are ranked accordingly to the normalized heavy to light ratio, please note that the first entry is IRSp53 itself (BAIAP2).

Gene name	Protein name	Average H/L ratio	Ratio H/L normalized a	1/Ratio H/L normalized b	Sequence coverage a [%]	Sequence coverage b [%]	Mol. weight [kDa]
BAIAP2	Brain-specific angiogenesis inhibitor 1-associated protein 2	19,53	10,90	28,16	77,5	85,9	60,867
SHANK2;CORTBP1	SH3 and multiple ankyrin repeat domains protein 2	9,52	6,03	13,02	2,1	1,6	158,82
CGN	Cingulin	9,22	9,29	9,14	18,6	28,7	136,38
DLG1	Disks large homolog 1	9,05	8,77	9,33	10,1	10,6	100,45
BAIAP2L1	Brain-specific angiogenesis inhibitor 1-associated protein 2-like protein 1	8,24	7,82	8,65	17,4	43,2	56,882
MUC13	Mucin-13	7,39	7,75	7,03	9	12,9	54,603
TP53BP2	Apoptosis-stimulating of p53 protein 2	7,22	7,00	7,44	10,3	14,8	125,61
INADL	InaD-like protein	6,55	6,75	6,35	12,4	8,5	196,37
EPS8	Epidermal growth factor receptor kinase substrate 8	5,84	6,93	4,74	20	27	91,88
SLC3A2	4F2 cell-surface antigen heavy chain	4,35	4,35	4,35	23,7	26,7	64,872
MPDZ	Multiple PDZ domain protein	3,85	2,57	5,13	2,2	2,8	221,62
RAPH1	Ras-associated and pleckstrin homology domains-containing protein 1	3,77	3,51	4,03	13,8	11,2	135,25
APC	Adenomatous polyposis coli protein	3,51	3,88	3,14	5,6	0,9	311,64
SEC16A	Protein transport protein Sec16A	3,38	2,33	4,43	2,7	1,2	186,49
INPPL1	Phosphatidylinositol 3,4,5-trisphosphate 5-phosphatase 2	3,13	3,67	2,59	2,9	11	138,6
MPP5	MAGUK p55 subfamily member 5	2,98	3,25	2,72	5,9	3,3	77,293
EGFR	Epidermal growth factor receptor	2,84	2,63	3,05	3,1	10,6	125,8
ERBB2IP	Protein LAP2	2,82	2,94	2,70	2,3	3,1	158,3
TXNL1	Thioredoxin-like protein 1	2,81	2,70	2,92	25,6	28,7	32,251
TJP1	Tight junction protein ZO-1	2,72	2,62	2,82	15,8	18,6	189,67
LIN7C;LIN7A	Protein lin-7 homolog C;Protein lin-7 homolog A	2,64	2,38	2,91	13,7	26,9	21,834
NCK1	Cytoplasmic protein NCK1	2,64	3,10	2,17	9	21	42,864
WASF2	Wiskott-Aldrich syndrome protein family member 2	2,57	3,08	2,06	6,6	12,7	54,283
TACC2	Transforming acidic coiled-coil-containing protein 2	2,48	2,55	2,40	6,3	2,8	64,675
SEC24B	Protein transport protein Sec24B	2,30	2,40	2,20	2,7	2,6	137,42
ABI1	Abl interactor 1	2,12	2,52	1,71	11,9	28,4	42,637
UBAP2L	Ubiquitin-associated protein 2-like	1,99	2,10	1,87	6,1	8,8	113,5

Table 1. Summary of the combined data from two independent experiments using BirA*-IRSp53 approach to analyse proximal proteins by SILAC BioID in HeLa cells.

HeLa cells were infected with lentiviral constructs encoding for BirA*-IRSp53 or BirA*-GFP as control. The two populations have been treated with heavy (BirA*-GFP) and light (BirA*-IRSp53) labelled media for 6 passages, swap of labelling was performed in the replicate. Cells have been treated with 50

μM biotin for 24 hours and lysed in JS buffer, then biotinylated proteins were fished out with streptavidin-conjugated magnetic beads (Thermo Fisher Scientific). Beads were washed out from aspecific binders using 50 mM Tris pH 7.5, 1% SDS, protease inhibitors; elution was performed using SDS-PAGE Sample buffer 2X, coupled with 95°C boiling. Eluates were then subjected to SDS-PAGE, after colloidal blue staining bands were processed for trypsin digestion and mass spectrometry.

Among the identified potential IRSp53 interactors, we found a number of proteins related to polarity and junctions establishment (Table 2): cingulin, ZO-1, DLG1, INPPL1 (Phosphatidylinositol 3,4,5-trisphosphate 5-phosphatase 2), LIN7 (or MALS), INADL (or PATJ) and MPP5 (MAGUK p55 subfamily member 5). We are currently planning to validate these potential hits and to study whether these interactions are important in mediating IRSp53 involvement in the polarity program of epithelial cells.

Of particular interest is the presence, in this list, of tight junctions proteins, since we observed strong co-localization of IRSp53 with the tight junctions protein ZO-1 in Caco2 cysts (Figure 45), which was not abolished by mutation of any of the functional domains of IRSp53. Moreover, the correct junctional organization is a critical aspect for the proper morphogenesis of 3-D organoids, as discussed in the previous paragraph.

As shown in Table 2, the list of potential IRSp53 interactors also comprises proteins involved in scaffolding, signalling and trafficking functions. We are planning to validate also these hits. As cited before, trafficking of polarity determinants is crucial for the correct polarization of epithelial organoids. As expected, various actin-related proteins, known interactors of IRSp53, such as WASF2, ABI1 and EPS8 were also among the hits, validating the relevance of our proteomic analysis.

Gene name	Protein name	Notes and functions	
BAIAP2	Brain-specific angiogenesis inhibitor 1-associated protein 2	BirA* fusion	Junctions and/or polarity
CGN	Cingulin	Actin binding, involved in tight junction assembly	
TJP1	Tight junction protein ZO-1	Involved in tight junction assembly	
DLG1	Disks large homolog 1	Scaffold protein, involved in junction assembly, signal transduction, cell proliferation	
INPPL1	Phosphatidylinositol 3,4,5-trisphosphate 5-phosphatase 2	Negatively regulates PI3K pathway to produce PIP2	
LIN7C;LIN7A (MALS)*	Protein lin-7 homolog C;Protein lin-7 homolog A	Involved in cell polarity	
INADL (PATJ)	InaD-like protein	Scaffold protein, involved in cell polarity and tight junction assembly	
MPP5	MAGUK p55 subfamily member 5	Involved in cell polarity and tight junction assembly	
NCK1	Cytoplasmic protein NCK1	Scaffold protein, cytoskeletal adaptor	Adaptors
SHANK2;CORTBP1*	SH3 and multiple ankyrin repeat domains protein 2	Scaffold activity in postsynaptic density	
ERBB2IP	Protein LAP2	Adapter for the receptor ERBB2	
MPDZ	Multiple PDZ domain protein	Involved in NMDAR signaling	Signaling
APC	Adenomatous polyposis coli protein	Tumor suppressor involved in Wnt signaling	
MUC13	Mucin-13	Cell signaling	
EGFR	Epidermal growth factor receptor	Receptor tyrosine kinase	
SEC24B	Protein transport protein Sec24B	Required for traffic from ER to Golgi	Trafficking
SLC3A2	4F2 cell-surface antigen heavy chain	Required for amino-acids transport	
SEC16A	Protein transport protein Sec16A	Required for traffic from ER to Golgi	
RAPH1 (lamellipodin)	Ras-associated and pleckstrin homology domains-containing protein 1	Mediator of membrane signals, involved in lamellipodial dynamics	Actin architecture
WASF2*	Wiskott-Aldrich syndrome protein family member 2	Part of WAVE complex	
ABI1*	Abl interactor 1	Involved in cytoskeletal reorganization and EGFR signaling	
EPS8*	Epidermal growth factor receptor kinase substrate 8	Signaling adapter that regulates actin architecture	
BAIAP2L1	Brain-specific angiogenesis inhibitor 1-associated protein 2-like protein 1	Adapter protein involved in actin organization	
TACC2	Transforming acidic coiled-coil-containing protein 2	Role in organizing centrosomal microtubules	Others
TXNL1	Thioredoxin-like protein 1	Oxidoreductase activity	
TP53BP2	Apoptosis-stimulating of p53 protein 2	Apoptosis stimulation	
UBAP2L	Ubiquitin-associated protein 2-like	Regulates hematopoietic stem cells activity	

*known interactors

Table 2. List of the proteins reported in Table 1, organized according to their function.

IRSp53 involvement in angiogenesis and vasculogenesis

The identification of novel potential interactors of IRSp53 should help us also to discover additional biological processes in which IRSp53 may be involved. In fact, genetic and developmental analysis performed on *Irsp53* null mice revealed that its loss causes partially penetrant embryonic lethality at midgestation (with 80% lethality at embryonic day 12.5-14.5). In particular, *Irsp53* null embryos show delayed development, diffuse edema, cardiac malformation, haemorrhages and defective angiogenesis. In Figure 53 images of embryo WT or *Irsp53* null are shown, in which exemplar cases of localized pericardial effusion and edema defects are highlighted.

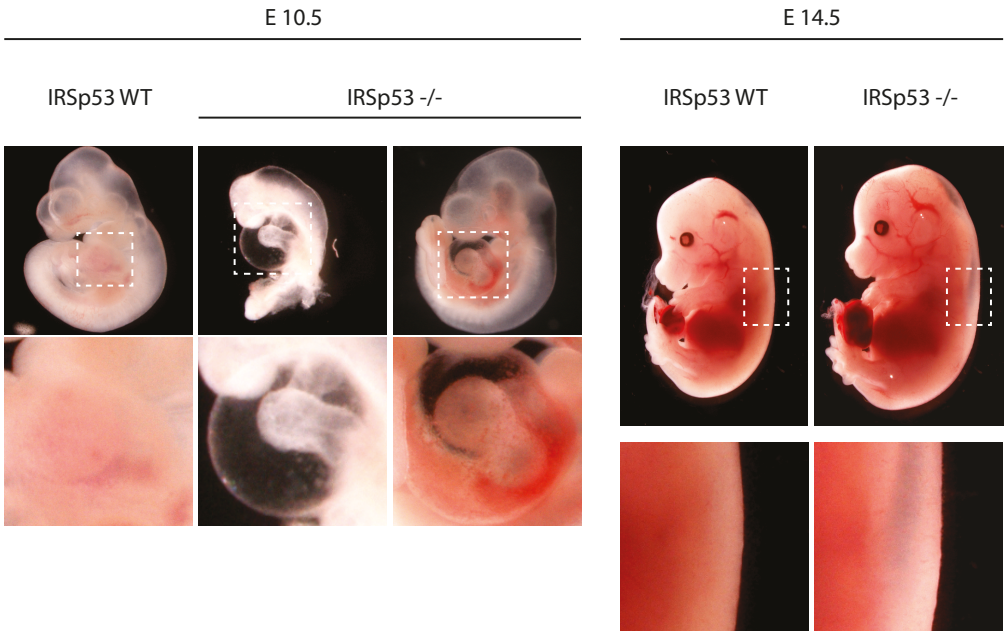

Figure 53. Stereo microscope images from embryo WT or *Irsp53* null, at embryonic day 10.5 or 14.5.

Lower panels are magnifications of the boxed regions.

Immunohistochemistry analysis on whole embryos at embryonic day 10.5, using an antibody against PECAM-1 (Platelet endothelial cell adhesion molecule), also known as cluster of differentiation 31 (CD31), revealed an aberrant architecture of the

vessels. In Figure 54 the dorsal and lateral somite staining is highlighted: in these regions, only the bigger vessels appear to form correctly, while the smaller, intervessel ones, that give rise to branched capillary networks, show severe defects and discontinuities.

Vascular defects were also found in the placenta from *Irsp53* null embryos (not shown), which presents diffuse hemorrhages and developmental abnormalities. In particular, we observed a severe reduction in the size of the labyrinth, which was also poorly vascularized by embryonic vessels, filled with large lacunae and lacking the spongiotrophoblasts layer.

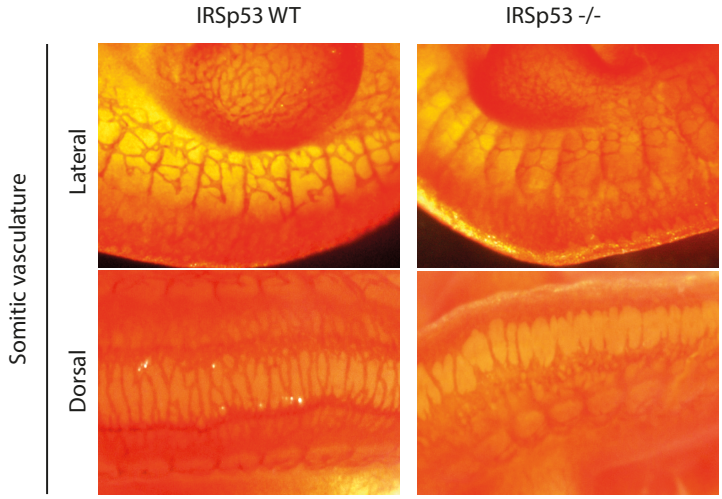

Figure 54. PECAM-1 (CD31) staining of whole mount embryos WT or *Irsp53* null at embryonic day 10.5.

The lateral and dorsal somite magnification are shown.

It is known that tip cells, at the forefront of vessel branches, extend numerous and long filopodia during sprouting angiogenesis. These filopodia are thought to constantly probe the microenvironment to guide the extension of novel vessels [199] [200], in a way similar to axonal growth cone in the nervous system. So *Irsp53* null mice phenotypes in angiogenesis and vasculogenesis could be, at least in part, due to

defective filopodia extension. However, the dynamic remodelling of endothelial cells is also crucial for these cells to get organized into tubular structures that later on mature into a vascular network: again migration, cell division, polarity establishment, junctional stabilization, as well as membrane and cytoskeleton remodeling [199] are all critical functions in which IRSp53 could be involved.

An alternative hypothesis is that IRSp53 could be primarily implicated in the formation of the lumen of the vessels, in analogy with the role or IRSp53 in lumenogenesis of epithelial cells, as shown in this thesis. It is known that lumenogenesis in vessels recapitulates to some extent lumenogenesis in epithelial cells. For example, in both MDCK and endothelial cells, ECM-integrin interaction activates cytoskeletal regulators (in particular, CDC42 and RAC1 are activated in endothelial cells), then apical determinants are delivered to the lumen initiation sites [201]. Moreover, Strilic et al., 2009 [185], proposed that two CD34-sialomucins, CD34 and podocalyxin, must relocalize to the site of lumen initiation in endothelial cells, with a mechanism dependent on VE-cadherin adhesion, in a manner similar to what has been proposed to occur during kidney lumenogenesis. Sialomucins relocalization is crucial to generate the repulsive forces required to open the lumen, with a mechanism similar to podocalyxin in MDCK cysts (see "Introduction"). Furthermore, F-actin and moesin became enriched at the future lumenal surface; upon PKC phosphorylation, moesin interacts with F-actin and promotes a reorganization of the actin cytoskeleton. As last step, VEGF-A and ROCK mediate the cell shape changes needed for lumen formation, again with mechanisms that are similar to the ones observed in MDCK cysts. Of note, a critical functional difference between epithelial and endothelial cells is the exposure of the latter cells to blood flow, high shear stress and pressures: these forces have ben shown to cause important changes in cell morphology and cell adhesion and to be critical for morphogenesis and

lumenogenesis [202].

Interestingly, a number of IRSp53 actin regulatory partners have been shown to be specifically important for various aspects of the endothelial morphogenetic program. A case in point is represented by the endothelial cells-specific genetic loss of RAC1 or its effector WAVE2, which both lead to defects in vascular development *in vivo* [203] [204]. Similarly, the formin formin-like 3 (FMNL3) interacts with CDC42 and RHOJ [205] and is required for vessel lumen formation: FMNL3 is essential to maintain a pool of F-actin at the endothelial cell junction, that regulates junctional stability [206]. FMNL3 is also involved in podocalyxin trafficking to the AMIS in vascular lumenogenesis [205].

Alternatively, IRSp53 could interact with not yet identified molecular partners that, in turn, affect its functions in angiogenesis and vasculogenesis. To this end, we performed mass spectrometry analysis also on HUVEC cells (human umbilical vein endothelial cells). These cells were infected with constructs encoding for BirA*-IRSp53 or BirA*-GFP as control. The results obtained are summarized in Table 3, in which we listed only the top ranking interactors candidates. Notably, some of these proteins were found in the previous analysis performed in HeLa cells, in particular DLG1, SEC16A and RAPH1 (also lamellipodin), suggesting that they might be crucial molecular partners to execute some of the IRSp53 functions. Our future plan is to validate these interactions in an attempt to decipher and dissect the key molecular mechanisms and players through which IRSp53 affects such a variety of cellular functions, ranging from polarity to vasculogenesis and angiogenesis.

To conclude, in this thesis novel roles of IRSp53 have been presented, in particular in capping the actin filaments, in inducing filopodia formation and in the establishment of polarity program in 3-D organoids. However, a lot of work is still needed, judging from the high complexity phenotypes emerging from *in vivo* data in *Irsp53* null mice.

Such a wide range of effects highlights the fact that proteins at the membrane-actin interface, as IRSp53, can be involved and crucial in many different cellular events, also in unobvious ways.

Gene name	Protein name	Notes and functions	
BAIAP2	Brain-specific angiogenesis inhibitor 1-associated protein 2	BirA* fusion	
DLG1	Isoform 3 of Disks large homolog 1	Scaffold protein, involved in junction assembly, signal transduction, cell proliferation	Junctions and/or polarity
SCRIB	Protein scribble homolog	Scaffold protein involved in polarization	
CTNND1	Isoform 1AC of Catenin delta-1	Role in Wnt signaling and cell adhesion	
CTNNA1	Catenin alpha-1	Forms cadherin/catenin adhesion complexes	
MCAM	Cell surface glycoprotein MUC18	Role in adhesion of endothelial cells	
MLLT4	Afadin	Role in adhesion and spindle orinetation, actin binder	
SHANK3	SH3 and multiple ankyrin repeat domains protein 3	Major scaffold postsynaptic density protein	Adaptors
DNMBP	Dynamin-binding protein	Scaffold protein	
EPHA2	Ephrin type-A receptor 2	Receptor tyrosine kinase	Signaling Trafficking
SEC16A	Protein transport protein Sec16A	Required for traffic from ER to Golgi	
DNAJC13	DnaJ homolog subfamily C member 13	Involved in membrane trafficking through early endosomes	
ANKRD50	Ankyrin repeat domain-containing protein 50	Involved in the endosome-to-plasma membrane trafficking	
AP3B1	AP-3 complex subunit beta-1	Role in protein sorting in the late-Golgi/trans-Golgi network and endosomes	
NCKAP1*	Nck-associated protein 1	Part of the WAVE complex	Actin architecture
RAPH1 (lamellipodin)	Ras-associated and pleckstrin homology domains-containing protein 1	Mediator of membrane signals, involved in lamellipodial dynamics	
UTRN	Utrophin	Anchors cytoskeleton to the plasma membrane	
ABI3	ABI gene family member 3	Regulators of cell migration	
CYFIP1*	Cytoplasmic FMR1-interacting protein 1	Part of the WAVE complex	
NAP1L4	Nucleosome assembly protein 1-like 4	Role in nucleosome assembly	Others
DYNC1H1	Cytoplasmic dynein 1 heavy chain 1	Microtubule motor activity	
IPO7	Importin-7	Nuclear protein import	

*known interactors

Table 3. Top 22 IRSp53 interactors in HUVEC cells, based on BirA* proximity ligation coupled to mass spectrometry.

Top ranking genes were evaluated according to a qualitative analysis performed on the unique peptide counts emerging from two independent experiments.

References

1. McMahon, H.T. and J.L. Gallop, *Membrane curvature and mechanisms of dynamic cell membrane remodelling.* Nature, 2005. **438**(7068): p. 590-6.
2. Zimmerberg, J. and M.M. Kozlov, *How proteins produce cellular membrane curvature.* Nat Rev Mol Cell Biol, 2006. **7**(1): p. 9-19.
3. McMahon, H.T. and E. Boucrot, *Membrane curvature at a glance.* J Cell Sci, 2015. **128**(6): p. 1065-70.
4. Hilpela, P., M.K. Vartiainen, and P. Lappalainen, *Regulation of the actin cytoskeleton by PI(4,5)P2 and PI(3,4,5)P3.* Curr Top Microbiol Immunol, 2004. **282**: p. 117-63.
5. Suetsugu, S., K. Toyooka, and Y. Senju, *Subcellular membrane curvature mediated by the BAR domain superfamily proteins.* Semin Cell Dev Biol, 2010. **21**(4): p. 340-9.
6. Qualmann, B., D. Koch, and M.M. Kessels, *Let's go bananas: revisiting the endocytic BAR code.* EMBO J, 2011. **30**(17): p. 3501-15.
7. Suetsugu, S., S. Kurisu, and T. Takenawa, *Dynamic shaping of cellular membranes by phospholipids and membrane-deforming proteins.* Physiol Rev, 2014. **94**(4): p. 1219-48.
8. Suetsugu, S., *The proposed functions of membrane curvatures mediated by the BAR domain superfamily proteins.* J Biochem, 2010. **148**(1): p. 1-12.
9. Scita, G., et al., *IRSp53: crossing the road of membrane and actin dynamics in the formation of membrane protrusions.* Trends in cell biology, 2008. **18**(2): p. 52-60.
10. Pantaloni, D., C. Le Clainche, and M.F. Carlier, *Mechanism of actin-based motility.* Science, 2001. **292**(5521): p. 1502-6.

11. Littlefield, R. and V.M. Fowler, *A minor actin catastrophe.* Nat Cell Biol, 2002. **4**(9): p. E209-11.

12. Ridley, A.J., et al., *Cell migration: integrating signals from front to back.* Science, 2003. **302**(5651): p. 1704-9.

13. Svitkina, T.M., et al., *Analysis of the actin-myosin II system in fish epidermal keratocytes: mechanism of cell body translocation.* J Cell Biol, 1997. **139**(2): p. 397-415.

14. Maiuri, P., et al., *Actin flows mediate a universal coupling between cell speed and cell persistence.* Cell, 2015. **161**(2): p. 374-86.

15. Aguda, A.H., L.D. Burtnick, and R.C. Robinson, *The state of the filament.* EMBO Rep, 2005. **6**(3): p. 220-6.

16. Pfaendtner, J., et al., *Nucleotide-dependent conformational states of actin.* Proc Natl Acad Sci U S A, 2009. **106**(31): p. 12723-8.

17. Holmes, K.C., *Structural biology: actin in a twist.* Nature, 2009. **457**(7228): p. 389-90.

18. Shekhar, S., J. Pernier, and M.F. Carlier, *Regulators of actin filament barbed ends at a glance.* J Cell Sci, 2016.

19. Svitkina, T.M. and G.G. Borisy, *Arp2/3 complex and actin depolymerizing factor/cofilin in dendritic organization and treadmilling of actin filament array in lamellipodia.* J Cell Biol, 1999. **145**(5): p. 1009-26.

20. Lim, K.B., et al., *The Cdc42 effector IRSp53 generates filopodia by coupling membrane protrusion with actin dynamics.* The Journal of biological chemistry, 2008. **283**(29): p. 20454-72.

21. Mattila, P.K. and P. Lappalainen, *Filopodia: molecular architecture and cellular functions.* Nat Rev Mol Cell Biol, 2008. **9**(6): p. 446-54.

22. Vignjevic, D. and G. Montagnac, *Reorganisation of the dendritic actin network during cancer cell migration and invasion.* Seminars in cancer biology, 2008. **18**(1): p. 12-22.

23. Yang, C., et al., *Novel roles of formin mDia2 in lamellipodia and filopodia formation in motile cells.* PLoS Biol, 2007. **5**(11): p. e317.

24. Vignjevic, D., et al., *Role of fascin in filopodial protrusion.* J Cell Biol, 2006. **174**(6): p. 863-75.

25. Lebrand, C., et al., *Critical role of Ena/VASP proteins for filopodia formation in neurons and in function downstream of netrin-1.* Neuron, 2004. **42**(1): p. 37-49.

26. Tokuo, H. and M. Ikebe, *Myosin X transports Mena/VASP to the tip of filopodia.* Biochem Biophys Res Commun, 2004. **319**(1): p. 214-20.

27. Le Clainche, C. and M.F. Carlier, *Regulation of actin assembly associated with protrusion and adhesion in cell migration.* Physiol Rev, 2008. **88**(2): p. 489-513.

28. Burnette, D.T., et al., *Filopodial actin bundles are not necessary for microtubule advance into the peripheral domain of Aplysia neuronal growth cones.* Nat Cell Biol, 2007. **9**(12): p. 1360-9.

29. Nobes, C.D. and A. Hall, *Rho, rac, and cdc42 GTPases regulate the assembly of multimolecular focal complexes associated with actin stress fibers, lamellipodia, and filopodia.* Cell, 1995. **81**(1): p. 53-62.

30. Ellis, S. and H. Mellor, *The novel Rho-family GTPase rif regulates coordinated actin-based membrane rearrangements.* Curr Biol, 2000. **10**(21): p. 1387-90.

31. Zhang, J., et al., *Rab35 controls actin bundling by recruiting fascin as an effector protein.* Science, 2009. **325**(5945): p. 1250-4.

32. Svitkina, T.M., et al., *Mechanism of filopodia initiation by reorganization of a dendritic network.* The Journal of cell biology, 2003. **160**(3): p. 409-21.

33. Faix, J., et al., *Filopodia: Complex models for simple rods.* The international journal of biochemistry & cell biology, 2009. **41**(8-9): p. 1656-64.

34. Bornschlogl, T., et al., *Filopodial retraction force is generated by cortical actin dynamics and controlled by reversible tethering at the tip.* Proc Natl Acad Sci U S A, 2013. **110**(47): p. 18928-33.

35. Breitsprecher, D., et al., *Cofilin cooperates with fascin to disassemble filopodial actin filaments.* J Cell Sci, 2011. **124**(Pt 19): p. 3305-18.

36. Kozma, R., et al., *The Ras-related protein Cdc42Hs and bradykinin promote formation of peripheral actin microspikes and filopodia in Swiss 3T3 fibroblasts.* Mol Cell Biol, 1995. **15**(4): p. 1942-52.

37. Hall, A., *Rho GTPases and the actin cytoskeleton.* Science, 1998. **279**(5350): p. 509-14.

38. Doherty, G.J. and H.T. McMahon, *Mediation, modulation, and consequences of membrane-cytoskeleton interactions.* Annual review of biophysics, 2008. **37**: p. 65-95.

39. Roy, P. and K. Jacobson, *Overexpression of profilin reduces the migration of invasive breast cancer cells.* Cell Motil Cytoskeleton, 2004. **57**(2): p. 84-95.

40. Cao, L.G., et al., *Effects of profilin and profilactin on actin structure and function in living cells.* J Cell Biol, 1992. **117**(5): p. 1023-9.

41. Pernier, J., et al., *Profilin Interaction with Actin Filament Barbed End Controls Dynamic Instability, Capping, Branching, and Motility.* Dev Cell, 2016. **36**(2): p. 201-14.

42. Mullins, R.D., J.A. Heuser, and T.D. Pollard, *The interaction of Arp2/3 complex with actin: nucleation, high affinity pointed end capping, and formation of branching networks of filaments.* Proceedings of the National Academy of Sciences of the United States of America, 1998. **95**(11): p. 6181-6.

43. Amann, K.J. and T.D. Pollard, *The Arp2/3 complex nucleates actin filament branches from the sides of pre-existing filaments.* Nature cell biology, 2001. **3**(3): p. 306-10.

44. Goley, E.D. and M.D. Welch, *The ARP2/3 complex: an actin nucleator comes of age.* Nature reviews. Molecular cell biology, 2006. **7**(10): p. 713-26.

45. Machesky, L.M., et al., *Purification of a cortical complex containing two unconventional actins from Acanthamoeba by affinity chromatography on profilin-agarose.* The Journal of cell biology, 1994. **127**(1): p. 107-15.

46. Welch, M.D., et al., *The human Arp2/3 complex is composed of evolutionarily conserved subunits and is localized to cellular regions of dynamic actin filament assembly.* The Journal of cell biology, 1997. **138**(2): p. 375-84.

47. Abella, J.V., et al., *Isoform diversity in the Arp2/3 complex determines actin filament dynamics.* Nat Cell Biol, 2016. **18**(1): p. 76-86.

48. Machesky, L.M., et al., *Scar, a WASp-related protein, activates nucleation of actin filaments by the Arp2/3 complex.* Proc Natl Acad Sci U S A, 1999. **96**(7): p. 3739-44.

49. Chereau, D., et al., *Actin-bound structures of Wiskott-Aldrich syndrome protein (WASP)-homology domain 2 and the implications for filament assembly.* Proc Natl Acad Sci U S A, 2005. **102**(46): p. 16644-9.

50. Panchal, S.C., et al., *A conserved amphipathic helix in WASP/Scar proteins is essential for activation of Arp2/3 complex.* Nat Struct Biol, 2003. **10**(8): p. 591-8.

51. Innocenti, M., et al., *Abi1 is essential for the formation and activation of a WAVE2 signalling complex.* Nat Cell Biol, 2004. **6**(4): p. 319-27.

52. Stradal, T.E. and G. Scita, *Protein complexes regulating Arp2/3-mediated actin assembly.* Curr Opin Cell Biol, 2006. **18**(1): p. 4-10.

53. Yan, C., et al., *WAVE2 deficiency reveals distinct roles in embryogenesis and Rac-mediated actin-based motility.* EMBO J, 2003. **22**(14): p. 3602-12.

54. Gorelik, R. and A. Gautreau, *The Arp2/3 inhibitory protein arpin induces cell turning by pausing cell migration.* Cytoskeleton (Hoboken), 2015. **72**(7): p. 362-71.

55. Maritzen, T., et al., *Gadkin negatively regulates cell spreading and motility via sequestration of the actin-nucleating ARP2/3 complex.* Proc Natl Acad Sci U S A, 2012. **109**(26): p. 10382-7.

56. Schonichen, A. and M. Geyer, *Fifteen formins for an actin filament: a molecular view on the regulation of human formins.* Biochim Biophys Acta, 2010. **1803**(2): p. 152-63.

57. Chhabra, E.S. and H.N. Higgs, *The many faces of actin: matching assembly factors with cellular structures.* Nat Cell Biol, 2007. **9**(10): p. 1110-21.

58. Kuhn, S. and M. Geyer, *Formins as effector proteins of Rho GTPases.* Small GTPases, 2014. **5**: p. e29513.

59. Romero, S., et al., *Formin is a processive motor that requires profilin to accelerate actin assembly and associated ATP hydrolysis.* Cell, 2004. **119**(3): p. 419-29.

60. Vavylonis, D., et al., *Model of formin-associated actin filament elongation.* Mol Cell, 2006. **21**(4): p. 455-66.

61. Li, F. and H.N. Higgs, *The mouse Formin mDia1 is a potent actin nucleation factor regulated by autoinhibition.* Curr Biol, 2003. **13**(15): p. 1335-40.

62. Jegou, A., M.F. Carlier, and G. Romet-Lemonne, *Formin mDia1 senses and generates mechanical forces on actin filaments.* Nat Commun, 2013. **4**: p. 1883.

63. Wear, M.A. and J.A. Cooper, *Capping protein: new insights into mechanism and regulation.* Trends Biochem Sci, 2004. **29**(8): p. 418-28.

64. Takeda, S., et al., *Two distinct mechanisms for actin capping protein regulation--steric and allosteric inhibition.* PLoS Biol, 2010. **8**(7): p. e1000416.

65. Pernier, J., et al., *Dimeric WH2 domains in Vibrio VopF promote actin filament barbed-end uncapping and assisted elongation.* Nat Struct Mol Biol, 2013. **20**(9): p. 1069-76.

66. Shekhar, S., et al., *Formin and capping protein together embrace the actin filament in a menage a trois.* Nat Commun, 2015. **6**: p. 8730.

67. Disanza, A., et al., *Eps8 controls actin-based motility by capping the barbed ends of actin filaments.* Nature cell biology, 2004. **6**(12): p. 1180-8.

68. Scita, G., et al., *EPS8 and E3B1 transduce signals from Ras to Rac.* Nature, 1999. **401**(6750): p. 290-3.

69. Lanzetti, L., et al., *The Eps8 protein coordinates EGF receptor signalling through Rac and trafficking through Rab5.* Nature, 2000. **408**(6810): p. 374-7.

70. Hertzog, M., et al., *Molecular basis for the dual function of Eps8 on actin dynamics: bundling and capping.* PLoS Biol, 2010. **8**(6): p. e1000387.

71. Claessens, M.M., et al., *Helical twist controls the thickness of F-actin bundles.* Proc Natl Acad Sci U S A, 2008. **105**(26): p. 8819-22.

72. McGough, A. and W. Chiu, *ADF/cofilin weakens lateral contacts in the actin filament.* J Mol Biol, 1999. **291**(3): p. 513-9.

73. Johnston, A.B., A. Collins, and B.L. Goode, *High-speed depolymerization at actin filament ends jointly catalysed by Twinfilin and Srv2/CAP.* Nat Cell Biol, 2015. **17**(11): p. 1504-11.

74. Kueh, H.Y., et al., *Actin disassembly by cofilin, coronin, and Aip1 occurs in bursts and is inhibited by barbed-end cappers.* J Cell Biol, 2008. **182**(2): p. 341-53.

75. Mikati, M.A., et al., *Coronin Enhances Actin Filament Severing by Recruiting Cofilin to Filament Sides and Altering F-Actin Conformation.* J Mol Biol, 2015. **427**(19): p. 3137-47.

76. Nadkarni, A.V. and W.M. Brieher, *Aip1 destabilizes cofilin-saturated actin filaments by severing and accelerating monomer dissociation from ends.* Curr Biol, 2014. **24**(23): p. 2749-57.

77. Kwiatkowski, A.V., F.B. Gertler, and J.J. Loureiro, *Function and regulation of Ena/VASP proteins.* Trends Cell Biol, 2003. **13**(7): p. 386-92.

78. Reinhard, M., et al., *The 46/50 kDa phosphoprotein VASP purified from human platelets is a novel protein associated with actin filaments and focal contacts.* EMBO J, 1992. **11**(6): p. 2063-70.

79. Gertler, F.B., et al., *Mena, a relative of VASP and Drosophila Enabled, is implicated in the control of microfilament dynamics.* Cell, 1996. **87**(2): p. 227-39.

80. Rottner, K., et al., *VASP dynamics during lamellipodia protrusion.* Nature cell biology, 1999. **1**(5): p. 321-2.

81. Vasioukhin, V., et al., *Directed actin polymerization is the driving force for epithelial cell-cell adhesion.* Cell, 2000. **100**(2): p. 209-19.

82. Scott, J.A., et al., *Ena/VASP proteins can regulate distinct modes of actin organization at cadherin-adhesive contacts.* Mol Biol Cell, 2006. **17**(3): p. 1085-95.

83. Gates, J., et al., *Enabled plays key roles in embryonic epithelial morphogenesis in Drosophila.* Development, 2007. **134**(11): p. 2027-39.

84. Li, Z., et al., *A predominant role for cAMP-dependent protein kinase in the cGMP-induced phosphorylation of vasodilator-stimulated phosphoprotein and platelet inhibition in humans.* Blood, 2003. **101**(11): p. 4423-9.

85. Boukhelifa, M., et al., *Palladin is a novel binding partner for Ena/VASP family members.* Cell Motil Cytoskeleton, 2004. **58**(1): p. 17-29.

86. Reinhard, M., et al., *Identification, purification, and characterization of a zyxin-related protein that binds the focal adhesion and microfilament protein VASP (vasodilator-stimulated phosphoprotein).* Proceedings of the National Academy of Sciences of the United States of America, 1995. **92**(17): p. 7956-60.

87. Brindle, N.P., et al., *The focal-adhesion vasodilator-stimulated phosphoprotein (VASP) binds to the proline-rich domain in vinculin.* Biochem J, 1996. **318 (Pt 3)**: p. 753-7.

88. Krause, M., et al., *Fyn-binding protein (Fyb)/SLP-76-associated protein (SLAP), Ena/vasodilator-stimulated phosphoprotein (VASP) proteins and the Arp2/3 complex link T cell receptor (TCR) signaling to the actin cytoskeleton.* J Cell Biol, 2000. **149**(1): p. 181-94.

89. Krause, M., et al., *Lamellipodin, an Ena/VASP ligand, is implicated in the regulation of lamellipodial dynamics.* Dev Cell, 2004. **7**(4): p. 571-83.

90. Grosse, R., et al., *A role for VASP in RhoA-Diaphanous signalling to actin dynamics and SRF activity.* EMBO J, 2003. **22**(12): p. 3050-61.

91. Chen, X.J., et al., *Ena/VASP proteins cooperate with the WAVE complex to regulate the actin cytoskeleton.* Dev Cell, 2014. **30**(5): p. 569-84.

92. Ferron, F., et al., *Structural basis for the recruitment of profilin-actin complexes during filament elongation by Ena/VASP.* The EMBO journal, 2007. **26**(21): p. 4597-606.

93. Hansen, S.D. and R.D. Mullins, *VASP is a processive actin polymerase that requires monomeric actin for barbed end association.* J Cell Biol, 2010. **191**(3): p. 571-84.

94. Kursula, P., et al., *High-resolution structural analysis of mammalian profilin 2a complex formation with two physiological ligands: the formin homology 1 domain of mDia1 and the proline-rich domain of VASP.* J Mol Biol, 2008. **375**(1): p. 270-90.

95. Lambrechts, A., et al., *cAMP-dependent protein kinase phosphorylation of EVL, a Mena/VASP relative, regulates its interaction with actin and SH3 domains.* J Biol Chem, 2000. **275**(46): p. 36143-51.

96. Furman, C., et al., *Ena/VASP is required for endothelial barrier function in vivo.* J Cell Biol, 2007. **179**(4): p. 761-75.

97. Krause, M., et al., *The Ena/VASP enigma.* J Cell Sci, 2002. **115**(Pt 24): p. 4721-6.

98. Han, Y.H., et al., *Requirement of a vasodilator-stimulated phosphoprotein family member for cell adhesion, the formation of filopodia, and chemotaxis in dictyostelium.* The Journal of biological chemistry, 2002. **277**(51): p. 49877-87.

99. Dent, E.W., et al., *Filopodia are required for cortical neurite initiation.* Nature cell biology, 2007. **9**(12): p. 1347-59.

100. Bear, J.E., et al., *Antagonism between Ena/VASP proteins and actin filament capping regulates fibroblast motility.* Cell, 2002. **109**(4): p. 509-21.

101. Barzik, M., et al., *Ena/VASP proteins enhance actin polymerization in the presence of barbed end capping proteins.* J Biol Chem, 2005. **280**(31): p. 28653-62.

102. Bear, J.E., et al., *Negative regulation of fibroblast motility by Ena/VASP proteins.* Cell, 2000. **101**(7): p. 717-28.

103. Goh, K.L., et al., *Ena/VASP proteins regulate cortical neuronal positioning.* Curr Biol, 2002. **12**(7): p. 565-9.

104. Trichet, L., C. Sykes, and J. Plastino, *Relaxing the actin cytoskeleton for adhesion and movement with Ena/VASP.* J Cell Biol, 2008. **181**(1): p. 19-25.

105. Pasic, L., T. Kotova, and D.A. Schafer, *Ena/VASP proteins capture actin filament barbed ends.* The Journal of biological chemistry, 2008. **283**(15): p. 9814-9.

106. Breitsprecher, D., et al., *Clustering of VASP actively drives processive, WH2 domain-mediated actin filament elongation.* The EMBO journal, 2008. **27**(22): p. 2943-54.

107. Chereau, D. and R. Dominguez, *Understanding the role of the G-actin-binding domain of Ena/VASP in actin assembly.* J Struct Biol, 2006. **155**(2): p. 195-201.

108. Hansen, S.D. and R.D. Mullins, *Lamellipodin promotes actin assembly by clustering Ena/VASP proteins and tethering them to actin filaments.* Elife, 2015. **4**.

109. Bockmann, J., et al., *ProSAP/Shank postsynaptic density proteins interact with insulin receptor tyrosine kinase substrate IRSp53.* J Neurochem, 2002. **83**(4): p. 1013-7.

110. Kim, M.H., et al., *Enhanced NMDA receptor-mediated synaptic transmission, enhanced long-term potentiation, and impaired learning and memory in mice lacking IRSp53.* J Neurosci, 2009. **29**(5): p. 1586-95.

111. Sawallisch, C., et al., *The insulin receptor substrate of 53 kDa (IRSp53) limits hippocampal synaptic plasticity.* J Biol Chem, 2009. **284**(14): p. 9225-36.

112. Kang, J., H. Park, and E. Kim, *IRSp53/BAIAP2 in dendritic spine development, NMDA receptor regulation, and psychiatric disorders.* Neuropharmacology, 2016. **100**: p. 27-39.

113. Offenhauser, N., et al., *Increased ethanol resistance and consumption in Eps8 knockout mice correlates with altered actin dynamics.* Cell, 2006. **127**(1): p. 213-26.

114. Chauhan, B.K., et al., *Cdc42- and IRSp53-dependent contractile filopodia tether presumptive lens and retina to coordinate epithelial invagination.* Development, 2009. **136**(21): p. 3657-67.

115. Kast, D.J., et al., *Mechanism of IRSp53 inhibition and combinatorial activation by Cdc42 and downstream effectors.* Nature structural & molecular biology, 2014. **21**(4): p. 413-22.

116. Roy, B.C., N. Kakinuma, and R. Kiyama, *Kank attenuates actin remodeling by preventing interaction between IRSp53 and Rac1.* The Journal of cell biology, 2009. **184**(2): p. 253-67.

117. Weiss, S.M., et al., *IRSp53 links the enterohemorrhagic E. coli effectors Tir and EspFU for actin pedestal formation.* Cell host & microbe, 2009. **5**(3): p. 244-58.

118. Suetsugu, S., et al., *The RAC binding domain/IRSp53-MIM homology domain of IRSp53 induces RAC-dependent membrane deformation.* The Journal of biological chemistry, 2006. **281**(46): p. 35347-58.

119. Yanagida-Asanuma, E., et al., *Synaptopodin protects against proteinuria by disrupting Cdc42:IRSp53:Mena signaling complexes in kidney podocytes.* Am J Pathol, 2007. **171**(2): p. 415-27.

120. Mattila, P.K., et al., *Missing-in-metastasis and IRSp53 deform PI(4,5)P2-rich membranes by an inverse BAR domain-like mechanism.* J Cell Biol, 2007. **176**(7): p. 953-64.

121. Prevost, C., et al., *IRSp53 senses negative membrane curvature and phase separates along membrane tubules.* Nat Commun, 2015. **6**: p. 8529.

122. Safari, F. and S. Suetsugu, *The BAR Domain Superfamily Proteins from Subcellular Structures to Human Diseases.* Membranes (Basel), 2012. **2**(1): p. 91-117.

123. Takei, K., et al., *Functional partnership between amphiphysin and dynamin in clathrin-mediated endocytosis.* Nat Cell Biol, 1999. **1**(1): p. 33-9.

124. Peter, B.J., et al., *BAR domains as sensors of membrane curvature: the amphiphysin BAR structure.* Science, 2004. **303**(5657): p. 495-9.

125. Frost, A., et al., *Structural basis of membrane invagination by F-BAR domains.* Cell, 2008. **132**(5): p. 807-17.

126. Saarikangas, J., et al., *Molecular mechanisms of membrane deformation by I-BAR domain proteins.* Curr Biol, 2009. **19**(2): p. 95-107.

127. Yamagishi, A., et al., *A novel actin bundling/filopodium-forming domain conserved in insulin receptor tyrosine kinase substrate p53 and missing in metastasis protein.* The Journal of biological chemistry, 2004. **279**(15): p. 14929-36.

128. Millard, T.H., et al., *Structural basis of filopodia formation induced by the IRSp53/MIM homology domain of human IRSp53.* The EMBO journal, 2005. **24**(2): p. 240-50.

129. Millard, T.H., J. Dawson, and L.M. Machesky, *Characterisation of IRTKS, a novel IRSp53/MIM family actin regulator with distinct filament bundling properties.* J Cell Sci, 2007. **120**(Pt 9): p. 1663-72.

130. Pykalainen, A., et al., *Pinkbar is an epithelial-specific BAR domain protein that generates planar membrane structures.* Nature structural & molecular biology, 2011. **18**(8): p. 902-7.

131. Zhao, H., A. Pykalainen, and P. Lappalainen, *I-BAR domain proteins: linking actin and plasma membrane dynamics.* Current opinion in cell biology, 2011. **23**(1): p. 14-21.

132. Lee, S.H., et al., *Structural basis for the actin-binding function of missing-in-metastasis.* Structure, 2007. **15**(2): p. 145-55.

133. Chen, Z., Z. Shi, and T. Baumgart, *Regulation of membrane-shape transitions induced by I-BAR domains.* Biophys J, 2015. **109**(2): p. 298-307.

134. Connolly, B.A., et al., *Tiam1-IRSp53 complex formation directs specificity of rac-mediated actin cytoskeleton regulation.* Molecular and cellular biology, 2005. **25**(11): p. 4602-14.

135. Govind, S., et al., *Cdc42Hs facilitates cytoskeletal reorganization and neurite outgrowth by localizing the 58-kD insulin receptor substrate to filamentous actin.* J Cell Biol, 2001. **152**(3): p. 579-94.

136. Miki, H. and T. Takenawa, *WAVE2 serves a functional partner of IRSp53 by regulating its interaction with Rac.* Biochemical and biophysical research communications, 2002. **293**(1): p. 93-9.

137. Krugmann, S., et al., *Cdc42 induces filopodia by promoting the formation of an IRSp53:Mena complex.* Current biology : CB, 2001. **11**(21): p. 1645-55.

138. Funato, Y., et al., *IRSp53/Eps8 complex is important for positive regulation of Rac and cancer cell motility/invasiveness.* Cancer Res, 2004. **64**(15): p. 5237-44.

139. Soltau, M., D. Richter, and H.J. Kreienkamp, *The insulin receptor substrate IRSp53 links postsynaptic shank1 to the small G-protein cdc42.* Molecular and cellular neurosciences, 2002. **21**(4): p. 575-83.

140. Chen, C.J., et al., *SH2B1 and IRSp53 proteins promote the formation of dendrites and dendritic branches.* J Biol Chem, 2015. **290**(10): p. 6010-21.

141. Matsuda, S., et al., *Insulin receptor substrate protein 53 (IRSp53) as a binding partner of antimetastasis molecule NESH, a member of Abelson interactor protein family.* Annals of oncology : official journal of the European Society for Medical Oncology, 2008. **19**(7): p. 1356-7.

142. Sekerkova, G., et al., *Novel espin actin-bundling proteins are localized to Purkinje cell dendritic spines and bind the Src homology 3 adapter protein insulin receptor substrate p53.* The Journal of neuroscience : the official journal of the Society for Neuroscience, 2003. **23**(4): p. 1310-9.

143. Teodorof, C., et al., *SPIN90-IRSp53 complex participates in Rac-induced membrane ruffling.* Experimental cell research, 2009. **315**(14): p. 2410-9.

144. Okamura-Oho, Y., et al., *Dentatorubral-pallidoluysian atrophy protein interacts through a proline-rich region near polyglutamine with the SH3 domain of an insulin receptor tyrosine kinase substrate.* Human molecular genetics, 1999. **8**(6): p. 947-57.

145. Oda, K., et al., *Identification of BAIAP2 (BAI-associated protein 2), a novel human homologue of hamster IRSp53, whose SH3 domain interacts with the cytoplasmic domain of BAI1.* Cytogenetics and cell genetics, 1999. **84**(1-2): p. 75-82.

146. Sanda, M., et al., *The postsynaptic density protein, IQ-ArfGEF/BRAG1, can interact with IRSp53 through its proline-rich sequence.* Brain research, 2009. **1251**: p. 7-15.

147. Misra, A., et al., *The mammalian verprolin, WIRE induces filopodia independent of N-WASP through IRSp53.* Experimental cell research, 2010. **316**(17): p. 2810-24.

148. Tourette, C., et al., *A large scale Huntingtin protein interaction network implicates Rho GTPase signaling pathways in Huntington disease.* The Journal of biological chemistry, 2014. **289**(10): p. 6709-26.

149. Barilari, M. and L. Dente, *The neuronal proteins CIPP, Cypin and IRSp53 form a tripartite complex mediated by PDZ and SH3 domains.* Biological chemistry, 2010. **391**(10): p. 1169-74.

150. Fujiwara, T., et al., *Rho small G-protein-dependent binding of mDia to an Src homology 3 domain-containing IRSp53/BAIAP2.* Biochemical and biophysical research communications, 2000. **271**(3): p. 626-9.

151. Chou, A.M., et al., *Dynamin1 is a novel target for IRSp53 protein and works with mammalian enabled (Mena) protein and Eps8 to regulate filopodial dynamics.* The Journal of biological chemistry, 2014. **289**(35): p. 24383-96.

152. Cohen, D., et al., *The serine/threonine kinase Par1b regulates epithelial lumen polarity via IRSp53-mediated cell-ECM signaling.* J Cell Biol, 2011. **192**(3): p. 525-40.

153. Robens, J.M., et al., *Regulation of IRSp53-dependent filopodial dynamics by antagonism between 14-3-3 binding and SH3-mediated localization.* Mol Cell Biol, 2010. **30**(3): p. 829-44.

154. Alpi, E., et al., *Channel-interacting PDZ protein, 'CIPP', interacts with proteins involved in cytoskeletal dynamics.* Biochem J, 2009. **419**(2): p. 289-300.

155. Hori, K., et al., *MALS is a binding partner of IRSp53 at cell-cell contacts.* FEBS letters, 2003. **554**(1-2): p. 30-4.

156. Choi, J., et al., *Regulation of dendritic spine morphogenesis by insulin receptor substrate 53, a downstream effector of Rac1 and Cdc42 small GTPases.* The Journal of neuroscience : the official journal of the Society for Neuroscience, 2005. **25**(4): p. 869-79.

157. Miki, H., et al., *IRSp53 is an essential intermediate between Rac and WAVE in the regulation of membrane ruffling.* Nature, 2000. **408**(6813): p. 732-5.

158. Ahmed, S., W.I. Goh, and W. Bu, *I-BAR domains, IRSp53 and filopodium formation.* Semin Cell Dev Biol, 2010. **21**(4): p. 350-6.

159. Nakagawa, H., et al., *IRSp53 is colocalised with WAVE2 at the tips of protruding lamellipodia and filopodia independently of Mena.* Journal of cell science, 2003. **116**(Pt 12): p. 2577-83.

160. Disanza, A., et al., *Regulation of cell shape by Cdc42 is mediated by the synergic actin-bundling activity of the Eps8-IRSp53 complex.* Nature cell biology, 2006. **8**(12): p. 1337-47.

161. Vaggi, F., et al., *The Eps8/IRSp53/VASP network differentially controls actin capping and bundling in filopodia formation.* PLoS computational biology, 2011. **7**(7): p. e1002088.

162. Connolly, B.A., et al., *Tiam1-IRSp53 complex formation directs specificity of rac-mediated actin cytoskeleton regulation.* Mol Cell Biol, 2005. **25**(11): p. 4602-14.

163. Suetsugu, S., et al., *Optimization of WAVE2 complex-induced actin polymerization by membrane-bound IRSp53, PIP(3), and Rac.* J Cell Biol, 2006. **173**(4): p. 571-85.

164. Abou-Kheir, W., et al., *Membrane targeting of WAVE2 is not sufficient for WAVE2-dependent actin polymerization: a role for IRSp53 in mediating the interaction between Rac and WAVE2.* J Cell Sci, 2008. **121**(Pt 3): p. 379-90.

165. Massari, S., et al., *LIN7 mediates the recruitment of IRSp53 to tight junctions.* Traffic, 2009. **10**(2): p. 246-57.

166. Rodriguez-Boulan, E. and I.G. Macara, *Organization and execution of the epithelial polarity programme.* Nat Rev Mol Cell Biol, 2014. **15**(4): p. 225-42.

167. Iden, S. and J.G. Collard, *Crosstalk between small GTPases and polarity proteins in cell polarization.* Nat Rev Mol Cell Biol, 2008. **9**(11): p. 846-59.

168. Gassama-Diagne, A., et al., *Phosphatidylinositol-3,4,5-trisphosphate regulates the formation of the basolateral plasma membrane in epithelial cells.* Nat Cell Biol, 2006. **8**(9): p. 963-70.

169. Martin-Belmonte, F., et al., *PTEN-mediated apical segregation of phosphoinositides controls epithelial morphogenesis through Cdc42.* Cell, 2007. **128**(2): p. 383-97.

170. Suzuki, A., et al., *Atypical protein kinase C is involved in the evolutionarily conserved par protein complex and plays a critical role in establishing epithelia-specific junctional structures.* J Cell Biol, 2001. **152**(6): p. 1183-96.

171. Hutterer, A., et al., *Sequential roles of Cdc42, Par-6, aPKC, and Lgl in the establishment of epithelial polarity during Drosophila embryogenesis.* Dev Cell, 2004. **6**(6): p. 845-54.

172. Smith, C.A., et al., *aPKC-mediated phosphorylation regulates asymmetric membrane localization of the cell fate determinant Numb.* EMBO J, 2007. **26**(2): p. 468-80.

173. Hao, Y., et al., *Par3 controls epithelial spindle orientation by aPKC-mediated phosphorylation of apical Pins.* Curr Biol, 2010. **20**(20): p. 1809-18.

174. Fogg, V.C., C.J. Liu, and B. Margolis, *Multiple regions of Crumbs3 are required for tight junction formation in MCF10A cells.* J Cell Sci, 2005. **118**(Pt 13): p. 2859-69.

175. Wang, Q., X.W. Chen, and B. Margolis, *PALS1 regulates E-cadherin trafficking in mammalian epithelial cells.* Mol Biol Cell, 2007. **18**(3): p. 874-85.

176. Bryant, D.M., et al., *A molecular network for de novo generation of the apical surface and lumen.* Nat Cell Biol, 2010. **12**(11): p. 1035-45.

177. Doyonnas, R., et al., *Anuria, omphalocele, and perinatal lethality in mice lacking the CD34-related protein podocalyxin.* J Exp Med, 2001. **194**(1): p. 13-27.

178. Bryant, D.M., et al., *A molecular switch for the orientation of epithelial cell polarization.* Dev Cell, 2014. **31**(2): p. 171-87.

179. Roland, J.T., et al., *Rab GTPase-Myo5B complexes control membrane recycling and epithelial polarization.* Proc Natl Acad Sci U S A, 2011. **108**(7): p. 2789-94.

180. Galvez-Santisteban, M., et al., *Synaptotagmin-like proteins control the formation of a single apical membrane domain in epithelial cells.* Nat Cell Biol, 2012. **14**(8): p. 838-49.

181. Jaffe, A.B., et al., *Cdc42 controls spindle orientation to position the apical surface during epithelial morphogenesis.* J Cell Biol, 2008. **183**(4): p. 625-33.

182. Sobajima, T., et al., *Rab11a is required for apical protein localisation in the intestine.* Biol Open, 2014. **4**(1): p. 86-94.

183. Sato, T., et al., *The Rab8 GTPase regulates apical protein localization in intestinal cells.* Nature, 2007. **448**(7151): p. 366-9.

184. Horikoshi, Y., et al., *Interaction between PAR-3 and the aPKC-PAR-6 complex is indispensable for apical domain development of epithelial cells.* J Cell Sci, 2009. **122**(Pt 10): p. 1595-606.

185. Strilic, B., et al., *The molecular basis of vascular lumen formation in the developing mouse aorta.* Dev Cell, 2009. **17**(4): p. 505-15.

186. Cohen, D., et al., *Mammalian PAR-1 determines epithelial lumen polarity by organizing the microtubule cytoskeleton.* J Cell Biol, 2004. **164**(5): p. 717-27.

187. Lazaro-Dieguez, F., et al., *Par1b links lumen polarity with LGN-NuMA positioning for distinct epithelial cell division phenotypes.* J Cell Biol, 2013. **203**(2): p. 251-64.

188. Temmerman, K. and W. Nickel, *A novel flow cytometric assay to quantify interactions between proteins and membrane lipids.* J Lipid Res, 2009. **50**(6): p. 1245-54.

189. Veniere, S., et al., *The interaction of proline-rich ligands with profilin probed with an enzyme-linked immunosorbent assay.* J Biomol Screen, 2009. **14**(4): p. 350-9.

190. Kuhn, J.R. and T.D. Pollard, *Real-time measurements of actin filament polymerization by total internal reflection fluorescence microscopy.* Biophys J, 2005. **88**(2): p. 1387-402.

191. Disanza, A., et al., *CDC42 switches IRSp53 from inhibition of actin growth to elongation by clustering of VASP.* EMBO J, 2013. **32**(20): p. 2735-50.

192. Breitsprecher, D., et al., *Molecular mechanism of Ena/VASP-mediated actin-filament elongation.* EMBO J, 2011. **30**(3): p. 456-67.

193. Oikawa, T., et al., *IRSp53 mediates podosome formation via VASP in NIH-Src cells.* PLoS One, 2013. **8**(3): p. e60528.

194. Nakagawa, H., et al., *IRSp53 is colocalised with WAVE2 at the tips of protruding lamellipodia and filopodia independently of Mena.* J Cell Sci, 2003. **116**(Pt 12): p. 2577-83.

195. Goh, W.I., et al., *mDia1 and WAVE2 proteins interact directly with IRSp53 in filopodia and are involved in filopodium formation.* The Journal of biological chemistry, 2012. **287**(7): p. 4702-14.

196. Goh, W.I., et al., *Rif-mDia1 interaction is involved in filopodium formation independent of Cdc42 and Rac effectors.* J Biol Chem, 2011. **286**(15): p. 13681-94.

197. Barzik, M., et al., *Ena/VASP regulates mDia2-initiated filopodial length, dynamics, and function.* Mol Biol Cell, 2014. **25**(17): p. 2604-19.

198. Roux, K.J., et al., *A promiscuous biotin ligase fusion protein identifies proximal and interacting proteins in mammalian cells.* The Journal of cell biology, 2012. **196**(6): p. 801-10.

199. Gerhardt, H., et al., *VEGF guides angiogenic sprouting utilizing endothelial tip cell filopodia.* J Cell Biol, 2003. **161**(6): p. 1163-77.

200. De Smet, F., et al., *Mechanisms of vessel branching: filopodia on endothelial tip cells lead the way.* Arterioscler Thromb Vasc Biol, 2009. **29**(5): p. 639-49.

201. Bayless, K.J. and G.E. Davis, *The Cdc42 and Rac1 GTPases are required for capillary lumen formation in three-dimensional extracellular matrices.* J Cell Sci, 2002. **115**(Pt 6): p. 1123-36.

202. Iruela-Arispe, M.L. and G.E. Davis, *Cellular and molecular mechanisms of vascular lumen formation.* Dev Cell, 2009. **16**(2): p. 222-31.

203. Tan, W., et al., *An essential role for Rac1 in endothelial cell function and vascular development.* FASEB J, 2008. **22**(6): p. 1829-38.

204. Yamazaki, D., et al., *WAVE2 is required for directed cell migration and cardiovascular development.* Nature, 2003. **424**(6947): p. 452-6.

205. Richards, M., C. Hetheridge, and H. Mellor, *The Formin FMNL3 Controls Early Apical Specification in Endothelial Cells by Regulating the Polarized Trafficking of Podocalyxin.* Curr Biol, 2015. **25**(17): p. 2325-31.

206. Phng, L.K., et al., *Formin-mediated actin polymerization at endothelial junctions is required for vessel lumen formation and stabilization.* Dev Cell, 2015. **32**(1): p. 123-32.

Supplementary material

Supplementary methods

SILAC BioID in HeLa cells

BirA* expressing vector was purchased from Addgene (plasmid # 35700). BirA* was cloned upstream of IRSp53 or GFP, as control, in lentiviral pLVX vector (Clonetech). HeLa cells were infected with lentiviral particles generated from pLVX BirA*-IRSp53 or pLVX-BirA*-GFP. The two populations have been treated with heavy (BirA*-GFP) and light (BirA*-IRSp53) labelled DMEM medium for SILAC (Thermo Fisher Scientific) (supplemented with dialyzed fetal bovine serum) for 6 passages; swap of labelling was performed in the replicate. Cells have been treated with 50 μM biotin for 24 hours and lysed in JS buffer, then biotinylated proteins were fished out with streptavidin-conjugated magnetic beads (Thermo Fisher Scientific). Beads were washed out from aspecific binders using 50 mM Tris pH 7.5, 1% SDS and protease inhibitors; elution was performed using SDS-PAGE Sample buffer 2X, coupled with 95°C boiling. Eluates were then subjected to SDS-PAGE; after colloidal blue staining, bands were excised and reduced with 10 mM dithiothreitol, alkylated with 55 mM iodoacetamide and finally digested overnight with 12.5 ng/μl of trypsin (Roche). After acidification, peptide mixtures were concentrated and desalted, dried in a Speed- Vac and resuspended in 12-15 μL of solvent A (2% acetonitrile, 0.1% formic acid). 5μl of each digested sample from the forward and reverse experiments were loaded on a LC (liquid chromatography)–ESI–MS/MS quadrupole Orbitrap QExactive mass spectrometer (Thermo Fisher Scientific). Peptides were separated on a linear gradient from 95% solvent A to 40% solvent B (80% acetonitrile, 0.1% formic acid) over 30 min and from 40 to 100% solvent B in 3 min at a constant flow rate of 0.25 μl/min on UHPLC Easy-nLC 1000 (Thermo Scientific), where the LC system was connected to a 25-cm fused-silica emitter of 75 μm inner diameter (New Objective,

Inc. Woburn, MA, USA), packed in-house with ReproSil-Pur C18-AQ 1.9 µm beads (Dr Maisch Gmbh, Ammerbuch, Germany). MS data were acquired using a data-dependent top 12 method for HCD fragmentation. Survey full scan MS spectra (300–1650 Th) were acquired in the Orbitrap with 70000 resolution, AGC target 3^{e6}, IT 60 ms. For HCD spectra, resolution was set to 17 500 at m/z 200, AGC target 1^{e5}, IT 120 ms; Normalized Collision energy 25% and isolation with 2.0 m/z. Technical replicates were conducted on the LC–MS-MS part of the analysis. Raw data were processed with MaxQuant ver. 1.4.1.2. Peptides were identified from the MS/MS spectra searched against the UniProt_Human_2014_10 database using the Andromeda search engine in which trypsin specificity was set up with a maximum of two missed cleavages. Cysteine carbamidomethylation was used as fixed modification, methionine oxidation and protein *N*-terminal acetylation as variable modifications. Mass deviation for MS/MS peaks was set at 20 ppm. The peptides and protein false discovery rates (FDR) were set to 0.01; the minimal length required for a peptide was six amino acids; a minimum of two peptides and at least one unique peptide were required for high-confidence protein identification. The lists of identified proteins were filtered to eliminate reverse hits and known contaminants. For quantitative analysis, "re-quantify" and "second peptide" options were selected. The statistical program Perseus (ver. 1.5.1.6) was used to quantify significantly up and down regulated proteins following the criteria: (i) significance A with a Benjamini-Hochberg FDR<0.05; (ii) ratio normalized values concordant in both forward and reverse experiments; (iii) minimum H/L ratio counts = 2.

BioID in HUVEC cells

HUVEC cells have been infected with lentiviral constructs encoding for BirA*-IRSp53 or BirA*-GFP. Cells have been treated with 50 µM biotin for 24 hours and lysed in JS buffer, then biotinylated proteins were fished out with streptavidin-conjugated

magnetic beads (Thermo Fisher Scientific). Beads were washed out from aspecific binders using 50 mM Tris pH 7.5, 1% SDS and protease inhibitors; elution was performed using SDS-PAGE Sample buffer 2X, coupled with 95°C boiling. Eluates were then subjected to SDS-PAGE; after colloidal blue staining, bands were excised and reduced with 10 mM dithiothreitol, alkylated with 55 mM iodoacetamide and finally digested overnight with 12.5 ng/µl of trypsin (Roche). After acidification, peptide mixtures were concentrated and desalted, dried in a Speed- Vac and resuspended in 12-15 µL of solvent A (5% acetonitrile, 0.1% formic acid). LC-ESI-MS/MS of 5 µL of each sample was performed on a Fourier transformed-LTQ mass spectrometer (FT-LTQ, Thermo Electron, San Jose, CA). Peptides separation was achieved on a linear gradient from 100% solvent A to 20% solvent B (80% acetonitrile, 0.1% formic acid) over 30 min and from 20% to 80% solvent B in 20 min at a constant flow rate of 0.3 µL/min on Agilent chromatographic separation system 1100 (Agilent Technologies, Waldbronn, Germany), where the LC system was connected to a 15 cm fused-silica emitter of 75 µm inner diameter (New Objective, Inc. Woburn, MA USA), packed in-house with ReproSil-Pur C18-AQ 3 µm beads (Dr. Maisch Gmbh, Ammerbuch, Germany), using a high-pressure bomb loader (Proxeon, Odense, Denmark). Survey MS scans were acquired in the FT from m/z 350-1650 with 100 000 resolution. The five most intense doubly and triply charged ions were automatically selected for fragmentation. Target ions already selected for the MS/MS were dynamically excluded for 60 s. Tandem mass spectra were extracted by RAW2MSM ver.1.10_2007_06.14, converted into peaklist (.msm) and analyzed using Mascot (Matrix Science, London, UK; ver. 2.3.02) searching against UniProt_CP_Human_20140709 database. Searches were performed assuming the digestion enzyme trypsin, a fragment ion mass tolerance of 0,50 Da and a parent ion tolerance of 10,0 PPM; carbamidomethyl of cysteine was specified as a fixed

modification, oxidation of methionine and acetyl of protein N-terminus as variable modifications. Scaffold (ver. 4.4.3, Proteome Software Inc., Portland, OR) was used to validate MS/MS based peptide and protein identifications. Peptide identifications were accepted if they could be established at greater than 95,0% probability by the Peptide Prophet algorithm with Scaffold delta-mass correction. Protein identifications were accepted if they could be established at greater than 99,0% probability and contained at least 2 identified peptides. Protein probabilities were assigned by the Protein Prophet algorithm. Proteins that contained similar peptides and could not be differentiated based on MS/MS analysis alone were grouped to satisfy the principles of parsimony.

Supplementary material

Disanza, A., et al.,

CDC42 switches IRSp53 from inhibition of actin growth to elongation by clustering of VASP.

EMBO J, 2013. **32**(20): p. 2735-50.

The EMBO Journal (2013) 32, 2735–2750
www.embojournal.org

SOURCE DATA | TRANSPARENT PROCESS

THE EMBO JOURNAL

CDC42 switches IRSp53 from inhibition of actin growth to elongation by clustering of VASP

Andrea Disanza[1,8], Sara Bisi[1,8], Moritz Winterhoff[2], Francesca Milanesi[1,9], Dmitry S Ushakov[2,10], David Kast[3], Paola Marighetti[1], Guillaume Romet-Lemonne[4], Hans-Michael Müller[5], Walter Nickel[5], Joern Linkner[2], Davy Waterschoot[6], Christophe Ampè[6], Salvatore Cortellino[1], Andrea Palamidessi[1], Roberto Dominguez[3], Marie-France Carlier[4], Jan Faix[2,*] and Giorgio Scita[1,7,*]

[1]IFOM, Fondazione Istituto FIRC di Oncologia Molecolare, Milan, Italy, [2]Hannover Medical School, Institute for Biophysical Chemistry, Hannover, Germany, [3]Department of Physiology, Perelman School of Medicine Philadelphia, University of Pennsylvania, Philadelphia, PA, USA, [4]Cytoskeleton Dynamics and Motility Group, Laboratoire d'Enzymologie et Biochimie Structurales, Centre de Recherche de Gif, CNRS, Gif-sur-Yvette, France, [5]Heidelberg University Biochemistry Center, Heidelberg, Germany, [6]Department of Biochemistry, Faculty of Medicine and Health Sciences, Ghent University, Ghent, Belgium and [7]Dipartimento di Scienze della Salute, Universita' degli Studi di Milano, Milan, Italy

Filopodia explore the environment, sensing soluble and mechanical cues during directional motility and tissue morphogenesis. How filopodia are initiated and spatially restricted to specific sites on the plasma membrane is still unclear. Here, we show that the membrane deforming and curvature sensing IRSp53 (Insulin Receptor Substrate of 53 kDa) protein slows down actin filament barbed end growth. This inhibition is relieved by CDC42 and counteracted by VASP, which also binds to IRSp53. The VASP:IRSp53 interaction is regulated by activated CDC42 and promotes high-density clustering of VASP, which is required for processive actin filament elongation. The interaction also mediates VASP recruitment to liposomes. In cells, IRSp53 and VASP accumulate at discrete foci at the leading edge, where filopodia are initiated. Genetic removal of IRSp53 impairs the formation of VASP foci, filopodia and chemotactic motility, while IRSp53 null mice display defective wound healing. Thus, IRSp53 dampens barbed end growth. CDC42 activation inhibits this activity and promotes IRSp53-dependent recruitment and clustering of VASP to drive actin assembly. These events result in spatial restriction of VASP filament elongation for initiation of filopodia during cell migration, invasion, and tissue repair.

The EMBO Journal (2013) **32,** 2735–2750. doi:10.1038/emboj.2013.208; Published online 27 September 2013
Subject Categories: cell & tissue architecture
Keywords: actin dynamics; cell migration; CDC42; filopodia; IRSp53

*Corresponding authors. J Faix, Hannover Medical School, Institute for Biophysical Chemistry, OE 4350, Carl-Neuberg-Str. 1, D-30625 Hannover, Germany. Tel.: +49 511 532 2928; Fax: +49 511 532 5966; E-mail: faix.jan@mh-hannover.de or G Scita, Dipartimento di Scienze della Salute, Universita' degli Studi di Milano, IFOM, Fondazione Istituto FIRC di Oncologia Molecolare, via Adamello, 16, Milan 20141, Italy. Tel.: +39 02574303277; Fax: +39 02574303231; E-mail: giorgio.scita@ifom.eu
[8]These authors contributed equally to this work
[9]Present address: Center for Genomic Science of IIT@SEMM, Istituto Italiano di Tecnologia, at the IFOM-IEO Campus, Milan, Italy
[10]Present address: Faculty of Biological Sciences, University of Leeds, Leeds, UK

Received: 22 March 2013; accepted: 30 August 2013; published online: 27 September 2013

Introduction

Cells move and interact with the environment by forming migratory structures composed of self-organized polymers of actin. These protrusions can be flat-sheet lamellipodia, or elongated, finger-like filopodia. Cells use lamellipodia as expanding membrane sheets driving cell locomotion (Wu *et al*, 2012), while filopodia act as compasses navigating cell migration (Faix *et al*, 2009; Yang and Svitkina, 2011a), as well as mechanical sensors (Chan and Odde, 2008).

In lamellipodia, actin is organized in networks of branched filaments (Svitkina *et al*, 2003; Yang and Svitkina, 2011b), generated by the concerted action of the Arp2/3 complex, capping proteins, and filament elongation factors (Svitkina and Borisy, 1999; Wiesner *et al*, 2003; Akin and Mullins, 2008). Conversely, filopodia are composed of parallel actin bundles that emanate from the cell periphery (Adams, 2004). However, in several cell types, filopodia and lamellipodia rapidly interchange during protrusion. Furthermore, filopodia are frequently embedded into, or arise from, pre-existing lamellipodia (Rottner *et al*, 1999; Svitkina *et al*, 2003). This finding suggests that filopodia form through a reorganization of the underlying actin network by convergent elongation of pre-existing filaments, or by *de novo* actin nucleation and elongation (Faix *et al*, 2009; Yang and Svitkina, 2011a). Whatever the case, the occurrence of lamellipodia-to-filopodia transition suggests commonalities between the two structures. For example, while it appears that capping proteins, including CP and EPS8, determine which actin-based protrusive organelle dominates at the cell periphery (Mejillano *et al*, 2004; Akin and Mullins, 2008; Vaggi *et al*, 2011), they do not function in isolation. The ENA/VASP family of proteins (Gertler *et al*, 1995; Reinhard *et al*, 1995; Gertler *et al*, 1996), which in mammals includes MENA, VASP, and EVL, also influence the underlying actin architecture of migratory protrusions (Bear *et al*, 2002). Notably, by cellular localization alone, ENA/VASP proteins appear to be vital to this lamellipodial–filopodial transition since they localize to active sites of actin assembly, such as the tips of protruding lamellipodia and filopodia (Lanier *et al*, 1999; Rottner *et al*, 1999). At the leading edge, the intensity of GFP-VASP has been shown to increase locally in puncta that subsequently give rise to filopodia, suggesting that higher

order clustering of this protein may be critical for generating linear filaments to support filopodia protrusions (Lanier *et al*, 1999; Rottner *et al*, 1999; Svitkina *et al*, 2003; Applewhite *et al*, 2007). Biochemical studies have recently shown that soluble VASP displays weak, processive polymerase activity (Hansen and Mullins, 2010). High-density VASP clustering, however, is required to enhance processive filament elongation, even in the presence of high concentrations of capping proteins (Breitspre**c**her *et al*, 2008, 2011). Not surprisingly, genetic evidence in various organisms showed that ENA/VASP proteins are essential players in filopodia formation (Schirenbe**c**k *et al*, 2006; Gates *et al*, 2007; Kwiatkowski *et al*, 2007). Whether and how the activity and higher order clustering of ENA/VASP family proteins is differentially tuned to control lamellipodia-to-filopodia transition remains, however, poorly defined.

Molecules sitting at the actin:membrane interface are predicted to be important in this process, albeit their nature and mechanisms of action remain unclear. One candidate is IRSp53 (Insulin Receptor Substrate of 53 kDa) (also called BAIAP2, brain angiogenic inhibitor interacting protein 2) (Abbott *et al*, 1999; Oda *et al*, 1999; Okamura-Oho *et al*, 1999). IRSp53 possesses an inverted Bin-Amphiphysin-Rvs167 (I-BAR) domain that binds to $PI(4,5)P_2$-rich lipid inducing negative curvatures, such as the ones required for filopodia protrusions (Zhao *et al*, 2011). Consistently, IRSp53 expression is sufficient to induce filopodia-like structures (Bockmann *et al*, 2002; Yamagishi *et al*, 2004; Disanza *et al*, 2006). Furthermore, IRSp53 binds activated CDC42 and, through its SH3 domain, a number of actin regulatory proteins that are involved in filopodia protrusions (Ahmed *et al*, 2010). Among them, IRSp53 was reported to bind to MENA *in vitro* (Krugmann *et al*, 2001) and to VASP in FRET-based and co-immunoprecipitation assays (Lim *et al*, 2008; Vaggi *et al*, 2011). Interestingly, the interaction between VASP and IRSp53 enhances the bundling activity of the former (Lim *et al*, 2008; Vaggi *et al*, 2011). However, it is unknown whether IRSp53 affects other key biochemical activities of MENA and VASP, and what the functional consequences of these interactions are.

Here, we show that IRSp53 alone slows down barbed end growth. Binding to CDC42 relieves this inhibition and promotes IRSp53-dependent recruitment and clustering of VASP to the plasma membrane to initiate processive F-actin elongation. These events result in spatial restriction of VASP activity to initiate filopodia, drive cell migration, and promote tissue repair.

Results

Characterization of the IRSp53–VASP interaction

We initially characterized the interaction between IRSp53 and VASP using purified proteins and various binding assays. IRSp53 associates with VASP, as well as EVL, through its SH3 domain (Supplementary Figure S1a–f) that contacts VASP on proline-rich sites partially overlapping, but distinct from the Profilin binding sites (Supplementary Figure S1c and g). Next, since VASP has recently been shown to acquire processive elongation activity upon clustering and IRSp53 can form dimer through its I-BAR domain (Millard *et al*, 2005), we tested whether in solution the two proteins can form high order oligomer by dynamic light scattering. Purified IRSp53 produced a single major species with a hydrodynamic radius of about 7.2 nm (Figure 1A) consistent with its dimeric structure (similar results were obtained by hydrodynamic measurements; Supplementary Figure S2a), while the VASP tetramer gave rise to a single species with a radius of about 14.3 nm (Figure 1A). Notably, the mixture of both proteins led to the formation of large clusters with an average diameter of about 200 nm (Figure 2A, left). Importantly, the VASP-ΔPRD mutant, which is unable to bind to IRSp53 (Supplementary Figure S1e), and the IRSp53 W413G mutant, which lacks VASP binding ability (Supplementary Figure S1c), did not form heterocomplexes (Figure 1A, right, and data not shown). In contrast, a VASP mutant lacking the central three GP_5 motifs (VASP-ΔGP_5), which retains IRSp53 binding ability, albeit with reduced affinity (Supplementary Figure S1d and f), was still able to hetero-oligomerize upon addition of IRSp53 (Figure 1A, middle). Thus, IRSp53 promotes clustering of VASP in solution, and might therefore be a decisive factor in the regulation of VASP function *in vitro* and *in vivo*.

IRSp53-mediated inhibition of barbed end growth is relieved by CDC42

Given the established role of VASP as an actin elongation factor with a relatively weak filament nucleation activity (Huttelmaier *et al*, 1999; Samarin *et al*, 2003; Barzik *et al*, 2005; Breitspre**c**her *et al*, 2008; Pasic *et al*, 2008), we next assessed whether IRSp53 regulates VASP filament elongation in bulk pyrenyl-actin polymerization assays. In this assay, VASP increased the rate (up to 2.5-fold) of spectrin-actin seeded barbed end growth from both ATP-G-actin (data not shown) and profilin-ATP-G-actin in an identical and dose-dependent fashion, under conditions in which its nucleating effect was negligible (Figure 1B). In contrast, IRSp53 slowed down barbed end growth by ∼10-fold, in a substoichiometric concentration range with respect to G-actin, indicating that the interaction of IRSp53 with barbed ends, rather than with G-actin, mediates this inhibitory effect (Figure 1C). The interaction of VASP and IRSp53 with barbed ends also inhibited dilution-induced depolymerization of filaments (Figure 1D).

A structure/function analysis of IRSp53 domains mediating barbed end growth inhibition revealed that the SH3 domain binding activity is dispensable. Indeed, an IRSp53-W413G mutant inhibited barbed end growth to the same extent as wild-type (WT) IRSp53, but bound to barbed ends instantaneously with a Kd of 0.29 μM (Figure 1E, scheme; Supplementary Figure S2b and c). In contrast, the isolated I-BAR domain of IRSp53 had no effect on barbed end growth (Figure 1E-scheme; Supplementary Figure S2b). We determined that the minimal region that mediates barbed end growth inhibition includes the I-BAR domain and a stretch of 30 amino acids just before the SH3 domain (Figure 1E, scheme; Supplementary Figure S2d). These results suggest that IRSp53 uses multiple interaction surfaces for inhibiting barbed end growth (e.g., the I-BAR domain to bind to filaments and additional surfaces to dock onto the barbed end protomers) or that it adopts an appropriate three-dimensional conformation centred on the dimeric I-BAR domain. Indeed, IRSp53 has recently been shown by the Dominguez group (in a work submitted elsewhere) to fold into a closed conformation held together by an intramolecular interaction between the SH3 domain and a proline-rich region that is part

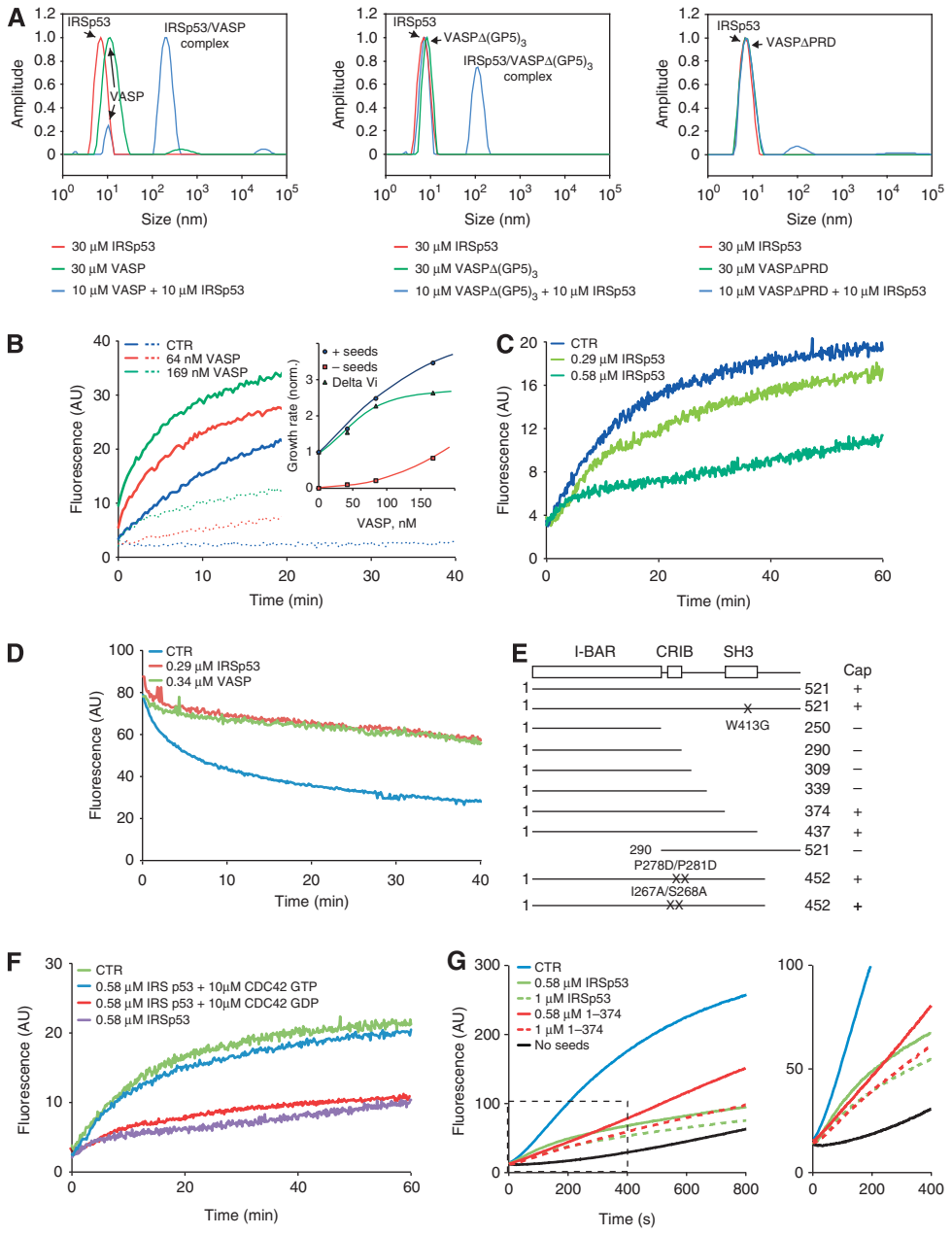

Figure 1 IRSp53 slows down barbed end growth: an effect relieved by CDC42. (**A**) IRSp53 and VASP form large clusters in solution. Intensity weighted diameter distributions for IRSp53 and VASP showed single species for either IRSp53 (red lines) or VASP WT and mutant proteins alone at concentrations of up to 30 μM (green lines). Aggregates formed in mixtures of 10 μM IRSp53 and 10 μM VASP WT or VASPΔ(GP5)$_3$, whereas no clusters were observed with VASP-ΔPRD (blue lines). (**B**) VASP increases the association rate constant of profilin-actin to barbed ends. Barbed end growth was measured in bulk pyrenyl-actin polymerization assays using 1.25 μM MgATP-G-actin (5% pyrenyl-labelled), 5 μM profilin, and VASP (V) at 0 (blue lines), 64 nM (red lines), and 169 nM (green lines), in the absence (dotted lines) or in the presence (continuous lines) of 0.16 nM spectrin-actin seeds. Inset shows cumulated data from additional assays performed with different VASP concentrations. (**C**) IRSp53 slows down actin polymerization by weakly capping barbed ends. Kinetics of actin polymerization induced by spectrin-actin seeds, measured as described in (**A**), in the presence of the indicated concentrations of IRSp53. (**D**) IRSp53 and VASP inhibit barbed end depolymerization. Depolymerization of actin filaments (2.5 μM F-actin, 50% pyrenyl-labelled) was induced by 50-fold dilution into polymerization buffer in the presence of 0.29 μM IRSp53 (red curve) or 0.34 μM VASP (green curve). (**E**) Summary of barbed end growth inhibition (Cap) by the indicated IRSp53 constructs and mutants (see also Supplementary Figure S2). (**F**) Active CDC42 relieves IRSp53 capping activity. Kinetics of actin polymerization induced by spectrin-actin seeds was measured as described in (**A**) in the presence of 0.58 μM IRSp53, alone or with 10 μM CDC42-GTP or CDC42-GDP. Control (CTR) sample contained no IRSp53. (**G**) Kinetics of actin polymerization induced by spectrin-actin seeds was measured as described in (**A**) in the presence of the indicated concentrations of IRSp53 or its truncated mutant 1–375. *Right graph* represents a magnification of the initial phase of elongation by seeds (inset in the *left graph*).

of an atypical CDC42 binding interface. Mutation of these prolines (P278DA, P281D) leads to an 'open' IRSp53 conformation, which was capable of inhibiting barbed end growth, albeit slightly less efficiently than WT IRSp53 (Supplementary Figure S2d). CDC42-GTPγS abolished the slowing down of barbed end growth by IRSp53-WT and the proline mutant, but not by a CDC42 binding-deficient mutant (IRSp53-I267A-S268A; Figure 1E; Supplementary Figure S2e). Importantly, only active GTP-loaded CDC42, but not the GDP-bound form, relieved IRSp53-mediated inhibition of

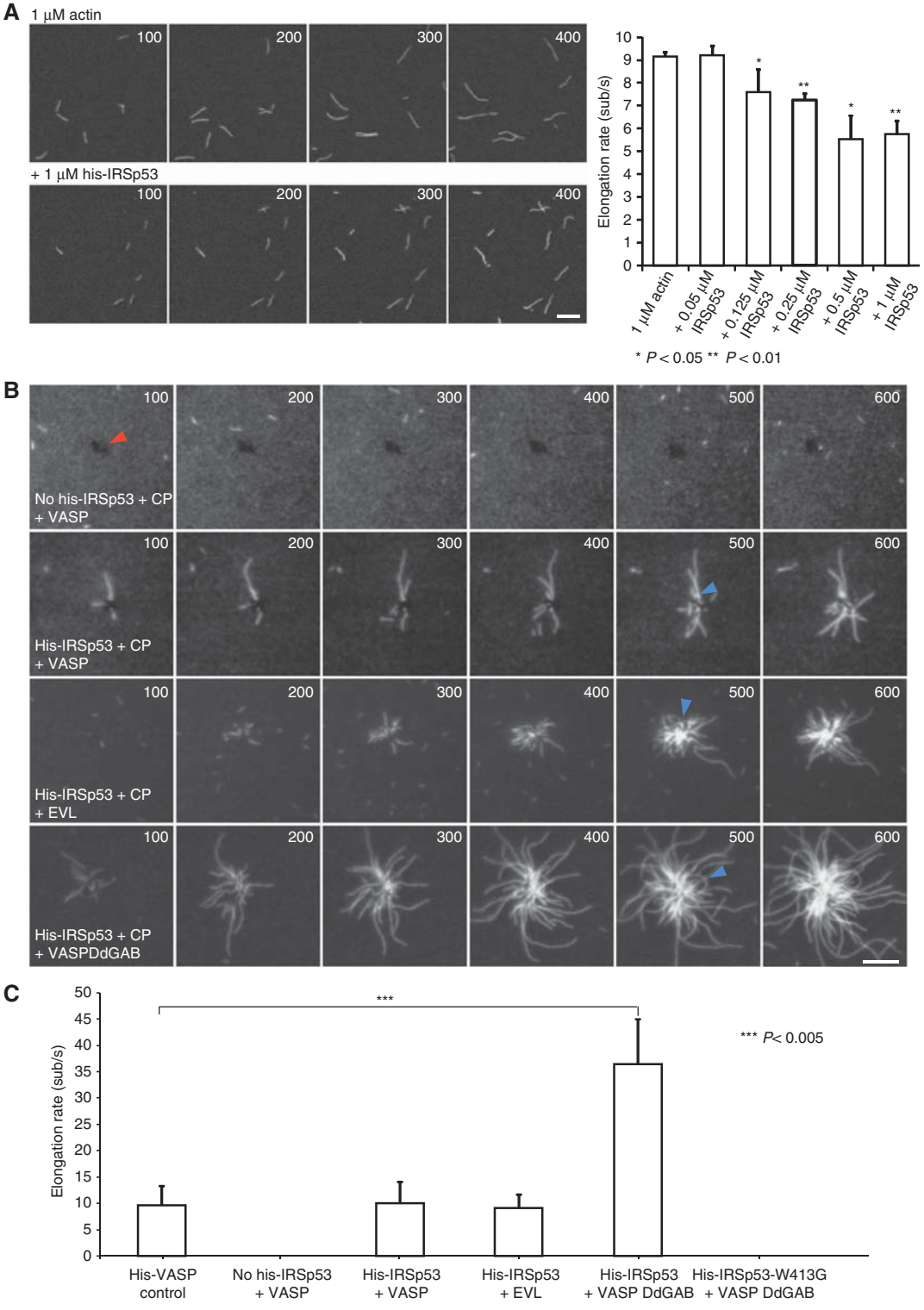

Figure 2 IRSp53 recruits and clusters Ena/VASP proteins to drive processive actin filament elongation in the presence of capping protein. (**A**) IRSp53 inhibits barbed end elongation. (*Left*) Polymerization of 1.0 μM G-actin (20% Atto-488 labelled) in the absence or presence of 1 μM IRSp53 in 1 × TIRF buffer monitored by TIRF microscopy. Time is indicated in seconds in the top right corner of each frame. Scale bar, 10 μm. (*Right*) Quantification of actin filament elongation rates in the absence or presence of IRSp53 as monitored by TIRF microscopy. Elongation rates are presented as mean ± s.e.m. from three independent experiments. At least 24 filaments per condition/experiment were measured. *, $P<0.05$ and **, $P<0.01$ (*T*-test, compared to 1 μM actin). (**B**) TIRF micrographs of the assembly of 1.0 μM G-actin (20% Atto-488 labelled) on uncoated (red arrowhead) or His-IRSp53-saturated Ni-NTA beads in the presence of 50 nM capping protein and 200 nM VASP, EVL, or hVASP DdGAB. Blue arrowheads indicate buckling filaments (also see Supplementary Movie 1). Only filaments that were attached with their barbed ends to the beads were observed, whereas capping protein largely abolished filament growth in solution. Time is indicated in seconds in the upper right corner of each frame. Scale bar, 10 μm. (**C**) Quantification of actin filament elongation rates from experiment shown in (**B**). Data are presented as mean ± s.d. of three independent experiments, in which at least 16 filaments/experiment were measured. ***, $P<0.005$ (*T*-test, compared to His-VASP control).

barbed end elongation (Figure 1F). Thus, IRSp53 can inhibit barbed end growth in both the 'closed' and 'open' conformation, and CDC42 relieves this inhibition presumably by sterically hindering the IRSp53:barbed end interaction.

Notably, inhibition of barbed end elongation by IRSp53 developed slowly during filament growth (Figure 1C). This finding is further supported by data showing that steady-state amounts of assembled actin were unaffected by the presence of IRSp53 and/or VASP at the concentrations tested (Supplementary Figure S2f). Furthermore, an IRSp53 mutant retaining the minimal surfaces for barbed end inhibition, but lacking the entire SH3 domain (and thus presumably adopting an open conformation) instantaneously inhibited barbed end growth (IRSp53-1–374; Figure 1G), similarly to IRSp53-W413G (Supplementary Figure S2b).

Finally, we monitored filament elongation in real time by *in vitro* TIRF microscopy in the presence of IRSp53. Similarly to our bulk spectrin-actin seed assays, addition of increasing concentrations of IRSp53 significantly slowed down barbed growth by ~30% (Figure 2A). This effect was reverted by the addition of activated CDC42 (Supplementary Figure S2g). It must be noted, however, that TIRF data were collected in the early phase of filament elongation, between 0 and 400 s. In this time frame, we also detected partial inhibition of growth in bulk polymerization spectrin-actin seed assays. These data provide further evidence for the slow kinetics of IRSp53 association to barbed ends. To detect more extensive barbed end growth inhibition by TIRF, we would need to use concentrations of IRSp53 much higher than those we can achieve given the relatively low Kd (~0.3 μM) of IRSp53 for barbed ends (Supplementary Figure S2c). The low affinity of IRSp53 for barbed ends could also result in short t1/2 of the IRSp53:barbed end complex, which may allow growth of barbed ends that are only transiently occupied by IRSp53. Alternatively, IRSp53 may bind slowly to barbed ends because it needs to undergo a slow conformational change for efficient binding, or a slow conformational change might follow IRSp53 binding to the sides of filaments, close to the barbed ends, resulting in a reduction in the rate of filament growth.

Although VASP and IRSp53 bind to each other, they have independent and opposing effects on barbed end growth. The addition of VASP to IRSp53-blocked barbed ends resulted in restoration of fast filament growth to rates obtained with VASP alone (Supplementary Figure S3a). Hence, in this assay, the possible association of VASP and IRSp53 to barbed ends does not change the kinetic behaviour of VASP-bound barbed ends. Thus, the formation of a VASP::IRSp53 complex has negligible effects on the filament elongation rate of VASP in solution.

IRSp53 promotes VASP recruitment and clustering on supported surfaces to drive processive filament elongation

High-density clustering of VASP onto functionalized beads allows processive, WH2 domain-mediated actin filament elongation, even in the presence of high concentrations of capping protein (Breitspre**c**her *et al*, 2008, 2011). Thus, we assessed whether beads saturated with IRSp53 could recruit and cluster VASP to drive processive actin assembly in the presence of capping protein using TIRF microscopy. To facilitate the visualization of actin filament growth, we initially used a chimaeric VASP (VASP-DdGAB), bearing the GAB motif of the *Dictyostelium discoideum* VASP homologue. This DdGAB motif, due to its high affinity for G-actin, markedly enhances filament elongation compared to WT mammalian VASP at the low G-actin concentration (1 μM) used in the TIRF assay (Figure 2B and C; Supplementary Figure S3d; Breitspre**c**her *et al*, 2011). We observed that high-density crowding or clustering of VASP-DdGAB on IRSp53-coated beads relieved inhibition of actin growth by capping protein and promoted marked processive filament elongation (Figure 2B and C; Supplementary Figure S3d). Buckling actin filaments grew away from the bead surfaces with elongation rates ranging from 37.1 ± 7 to 45.4 ± 5.5 actin subunits/s, which is comparable to the rate obtained with VASP-DdGAB-coated control beads (Figure 2B and C; Supplementary Figure S3d; Supplementary Movie 1). This elongation rate is about four times faster than the elongation rate (~10 actin subunits/s) of spontaneously growing actin control filaments (Breitspre**c**her *et al*, 2008, 2011). The recruitment of VASP-DdGAB to the beads was specifically mediated by IRSp53, since no filament growth was observed when uncoated beads were incubated with soluble VASP (Figure 2B and C). Likewise, no filament growth was observed when beads were coated with IRSp53-W413G, which possesses a defective SH3 domain (Supplementary Figure S3d). We extended these observations to human VASP (hVASP) and EVL (hEVL). In both cases, the recruitment of the proteins to IRSp53-coated beads in the presence of capping proteins promoted processive filament elongation in the presence of capping proteins (Figure 2B and C). As expected, the rate of filament elongation in the presence of hVASP or hEVL was 3- to 4-fold slower compared to that of hVASP-DdGAB, due to the lower affinities of their GAB domains for G-actin (Breitspre**c**her *et al*, 2011). Collectively, these results demonstrate that bead-immobilized IRSp53 is necessary and sufficient to recruit and cluster VASP from solution, which in turn drives processive actin filament assembly in the presence of CP.

CDC42 favours the formation of an IRSp53–VASP complex in vivo

IRSp53 can bind both activated RAC (Miki *et al*, 2000) and CDC42 (Govind *et al*, 2001; Krugmann *et al*, 2001). MENA, another member of the ENA/VASP family protein, has been shown to bind to IRSp53 in a CDC42-dependent manner *in vitro* (Krugmann *et al*, 2001). Using recombinant purified proteins, we first examined whether IRSp53 serves as a link between VASP and active CDC42. Binding of IRSp53 to GTP-CDC42 was readily detected, while VASP interacted with GTP-CDC42 in an IRSp53-dependent manner, indicating the existence of a CDC42–IRSp53–VASP complex (Figure 3A). Furthermore, the addition of saturating amounts of GTP-CDC42 increased the ability of IRSp53 to interact with VASP *in vitro* (Figure 3B). Similar results were obtained in co-immunoprecipitation experiments. The ectopic expression of active CDC42, but not of a dominant-negative mutant, significantly enhanced the amount of endogeneous IRSp53 co-immunoprecipitating with VASP (Figure 3C). The CDC42-dependent increase in the VASP:IRSp53 association was accompanied by a diminution of the EPS8:IRSp53 interaction (Figure 3C). Notably, VASP and EPS8 compete for binding to the SH3 domain of IRSp53, and in unstimulated conditions

EPS8, which contrary to VASP acts as a capper, binds more efficiently than VASP to IRSp53 (Menna *et al*, 2009; Vaggi *et al*, 2011). Thus, CDC42 binding promotes a switch in IRSp53-based molecular complexes that favours IRSp53 association with VASP, while reducing the interaction with EPS8, leading to the formation of an actin assembly promoting CDC42:IRSp53:VASP complex.

IRSp53-mediated association of VASP to PIP2-enriched membrane is required for proper clustering of VASP at the PM and filopodia formation

Filopodia initiation is preceded by localized accumulation of VASP into discrete foci along the PM (Rottner *et al*, 1999; Svitkina *et al*, 2003; Yang *et al*, 2007). IRSp53 also binds and localizes at the PM, accumulating at PIP2-rich sites (Zhao *et al*, 2011). Thus, IRSp53 may control and enhance VASP activity by recruiting and spatially restricting its localization on PIP2-rich, curved PM. We first tested this hypothesis using FACS-based *in vitro* assays that monitor the ability of fluorescently labelled (Alexa-488) proteins to bind PIP2-rich liposomes in solution (Temmerman and Nickel, 2009). Fluorescently labelled IRSp53 and IRSp53-W413G bound efficiently to liposomes only when PIP2 was included in the lipid mixture (Figure 4A; Supplementary Figure S4a). Alexa-488-VASP instead did not associate with liposomes. However, when PIP2 liposomes were incubated first with unlabelled

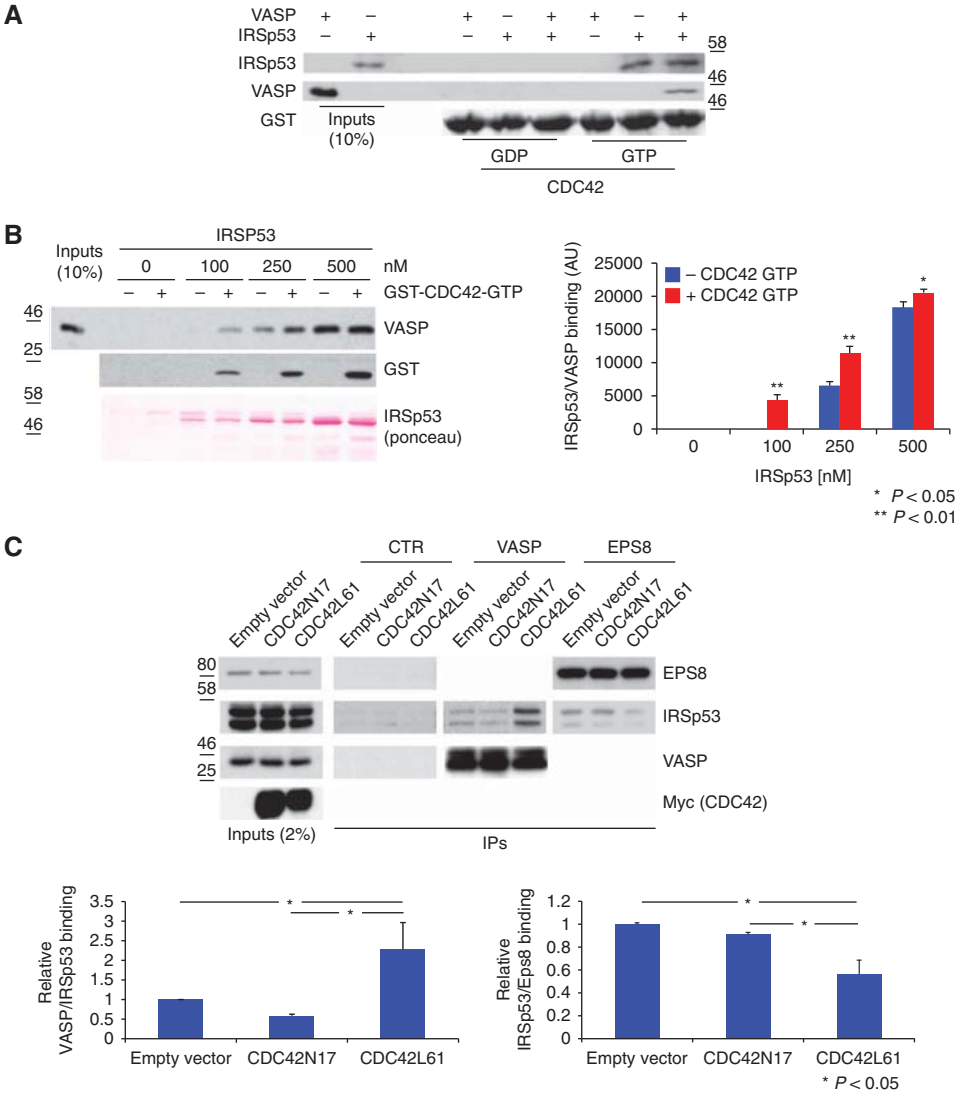

Figure 3 CDC42 modulates the interaction between IRSp53 and VASP. (**A**) IRSp53 connects VASP with CDC42. Equimolar concentrations (200 nM) of IRSp53and/or VASP were incubated with 1 μM GDP- or GTPγS-loaded GST-CDC42 immobilized on beads, as indicated. Inputs (10% of total) and bound material were analysed by immunoblotting to visualize VASP or by Ponceau staining to detect IRSp53 and CDC42. (**B**) Equal amounts of VASP were incubated with Ni-NTA agarose beads coating with increasing concentrations of recombinant purified His-IRSp53 (0, 100, 250, and 500 nM), in the absence or presence of saturating concentrations of GTP-loaded GST-CDC42. Inputs (10% of total) and bound material were immunoblotted with the indicated antibodies (Ponceau staining visualizes IRSp53). Right panel: Quantification of the fraction of VASP bound to His-IRSp53-Ni-NTA beads was determined by analysing blots with the ImageJ software. The fraction (bound/total) of VASP was plotted against the concentrations of IRSp53 (data are the mean ± s.d. of three independent experiments). (**C**) Lysates (2 mg) of HeLa cells, transfected with empty vector as a control (EV) or with either CDC42 dominant-negative (N17) or constitutively active (L61) mutants, were immunoprecipitated with an anti-VASP (VASP) or control antibody (CTR). Input lysates (40 μg) and immunoprecipitates (IPs) were immunoblotted with the indicated antibodies. *Right panel*: The amount of IRSp53 bound to VASP was determined using the ImageJ software. Relative binding between IRSp53 and VASP (data are the mean ± s.d. of five independent experiments). Source data for this figure is available on the online supplementary information page.

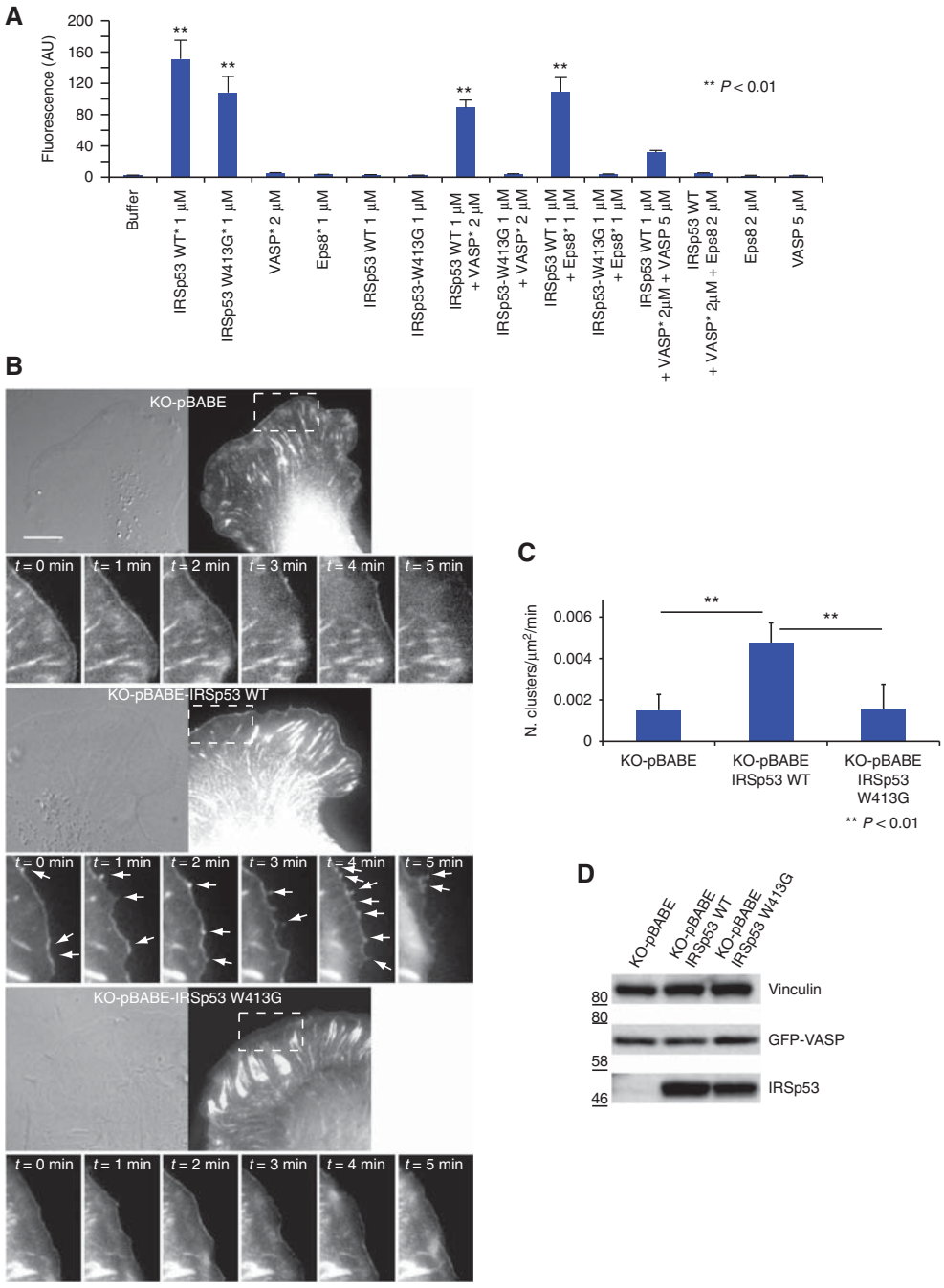

Figure 4 IRSp53 is required for VASP recruitment and clustering at the PM. (**A**) VASP is recruited to PIP2-containing liposomes through IRSp53. Unlabelled or labelled (*Alexa-488) IRSp53-WT, IRSp53-W413G, EPS8, and VASP, at the indicated concentrations and combinations, were added to 1 mM of 10% PIP2 containing liposomes. Interactions were analysed by FACS and data were processed with the CellQuest Pro software (Becton Dickinson) and expressed as mean ± s.e.m. of at least three independent experiments performed in duplicate. **Indicates $P<0.01$ (*t*-test, comparing each condition to control, buffer). (**B**) IRSp53 removal diminishes VASP clustering at the PM. Still images from differential interference contrast (DIC) and fluorescence time-lapse analysis of migrating cells. MEFs transfected with empty vector (KO-pBABE), KO-pBABE-IRSp53 WT, and KO-pBABE-IRSp53 W413G were electroporated with GFP-VASP and plated on laminin (40 μg/ml). Twenty-four hours after electroporation, cells were analysed by time-lapse imaging (5 min, time interval 5 s). Bar is 5 μm (2 μm for the insets). Arrows indicate VASP puncta (see also Supplementary Movies 2–5). (**C**) Quantification of the number (*N*) of clusters (mean ± s.e.m.) formed by GFP-VASP was obtained by analysing 20 cells for each condition. (**D**) The expression levels of EGFP-VASP, IRSp53, and vinculin were analysed by immunoblotting in KO-pBABE, KO-pBABE-IRSp53 WT, and KO-pBABE-IRSp53 W413G transfected MEFs.

IRSp53, Alexa-488-VASP readily bound to PIP2 lipids (Figure 4A). This interaction was abolished when unlabelled IRSp53-W413G was used instead of WT IRSp53 (Figure 4A), or by the addition of an excess of unlabelled EPS8 that competes with VASP for binding to IRSp53 (Disanza *et al*, 2006) (Figure 4A).

We next explored whether IRSp53 is required for the formation of VASP foci at the leading edge. We took advantage of MEF cells derived from IRSp53 null mice (Sawallisch *et al*, 2009; Weiss *et al*, 2009) stably infected with mock empty vector, or vectors expressing IRSp53-WT or -W413G to levels similar to the endogeneous protein (Figures 4D and 5C).

We analysed by time-lapse imaging the cellular dynamics of GFP-VASP in MEFs plated on laminin (Figure 4B–D; Supplementary Movies 2–5). In reconstituted WT IRSp53 MEFs, VASP was distributed to focal adhesions and prominently enriched along lamellipodia (Figure 4B). At this latter location, bright foci of GFP-VASP frequently moved laterally, merged, and fused. These foci invariably preceded the extension of filopodia that were also positive for fascin (Figure 4B; Supplementary Figure S4b and c; Supplementary Movies 7 and 8). Conversely, in MEFs devoid of IRSp53 or reconstituted with IRSp53-W413G mutant, the formation of leading edge-localized GFP-VASP foci was significantly reduced, while VASP localization and dynamics in lamellipodia and focal adhesion remained unaltered (Figure 4B; Supplementary Movies 2–5). We also tested whether IRSp53 accumulates along the leading edge in discrete foci together with VASP by dual-colour time-lapse microscopy using GFP-VASP and mCherry-IRSp53. Notably, both proteins accumulated into bright, dynamic puncta at sites of filopodia initiation (Supplementary Figure S4b; Supplementary Movie 7). Time-resolved analysis of the accumulation of cherry-IRSp53 and GFP-VASP into foci revealed that IRSp53 preceded the recruitment of VASP by 1.4 s on average. (Supplementary Figure S4c; Supplementary Movie 8). Notably, mDia1, another putative interactor of IRSp53 with filament elongation activity that is implicated in filopodia (Goh *et al*, 2012), as well as N-WASP and WAVE (data not shown), did not display any accumulation into foci at the leading edge (Supplementary Figure S4d). This finding suggests that these proteins are not required in the initial phase of filopodia formation. Thus, IRSp53 is specifically implicated in the recruitment of VASP to PIP2-rich membrane and in its apparent clustering along PM sites where filopodia are initiated, implying a requirement of the IRSp53:VASP complex in the formation of these protrusions.

To test the latter hypothesis, we monitored filopodia induced by the expression of active CDC42 or following the initial phases of cell spreading on extracellular matrix (ECM) substrates (Kozma *et al*, 1995; Applewhite *et al*, 2007). A >40% reduction in CDC42-induced filopodia was observed in MEFs devoid of IRSp53 compared with cells reconstituted with IRSp53-WT (Figure 5A–C). Of note, when IRSp53 is expressed, it displays a diffuse punctate distribution throughout the cytoplasm, but also decorates the shafts of protruding filopodia (Figure 5A–C). Similarly, in IRSp53-WT-reconstituted MEFs, VASP, as expected, was confined to filopodia tips. Conversely, removal of IRSp53 or re-expression of IRSp53-W413G in IRSp53 null MEFs prevented the proper localization of VASP (Supplementary Figure S5a–d). VASP localized at the tips of filopodia in ~80% of IRSp53-WT reconstituted cells, but only in 20 and 30% of empty vector and IRSp53-W314G reconstituted cells, respectively.

Filopodia protrusions are also typically formed during cell spreading onto ECM. Three different spreading modes have been described for mouse fibroblasts: smooth-edged, filopodial or ruffling (Applewhite *et al*, 2007). ENA/VASP proteins are known to increase the number of cells that form filopodia (Applewhite *et al*, 2007). We performed the same analysis in IRSp53 null MEFs infected with empty vector or IRSp53-WT shortly after plating on fibronectin (Figure 5D). We then scored cells into one of the phenotypic spreading modes (Figure 5E). Removal of IRSp53 does not affect cell adhesion (Figure 5E), but favours a smooth-edged/ruffling mode of spreading and significantly reduces the number of cells forming filopodia, mimicking VASP loss-of-function (Applewhite *et al*, 2007). Finally, functional interference of CDC42 by expression of a dominant-negative mutant significantly reduced VASP clustering at filopodia initiation sites and its subsequent localization at filopodia tips during cell spreading (Supplementary Figure S5e). Thus, IRSp53 is required for efficient filopodia formation during CDC42-dependent cell spreading, strengthening the notion that IRSp53 and VASP act in the same pathway.

IRSp53 drives cell directional migration and invasion, and is required for efficient epidermal wound healing in vivo

Filopodia drive directional migration and invasion into ECM (Vignjevic and Montagnac, 2008). Thus, we tested the impact of IRSp53 on these processes using our genetically modified MEFs in a battery of migration and invasion assays (Figure 6). In wound healing assays, IRSp53 null MEFs were defective in closing the wound when compared with IRSp53-reconstituted cells. Defective wound closure was due to reduced speed and impaired directional migration (Figure 6A; Supplementary Movie 9). Importantly, IRSp53 null MEFs were impaired in extending polarized protrusions

Figure 5 IRSp53 is required for CDC42-induced filopodia formation. (**A**) MEF KO-pB and KO-pB-IRSp53 cells, transfected with a constitutively active Myc-tagged CDC42 (Myc-CDC42 L61), were fixed and stained with anti-Myc or anti-IRSp53 antibodies and FITC-phalloidin to detect myc-CDC42 L61, IRSp53 (KO-pB-IRSp53), or F-actin, respectively. The right panels represent magnifications of the indicated areas of each corresponding image. Scale bar is 10 μm (2.5 μm for the magnifications). (**B**) Quantification of filopodia induced by CDC42 L61 in cells shown in (**A**). Upper panel. The number of cells expressing CDC42 L61 and presenting filopodia was counted. Data are expressed as the fraction of CDC42 L61-expressing cells presenting filopodia with respect to CDC42 L61-expressing KO-pB-IRSp53 cells (relative filopodia index). CDC42 L61 induced filopodia in ~80% of transfected KO-pB-IRSp53 cells. *Lower panel*: The number of filopodia/cell was counted. At least 100 cells were analysed in each experiment and three independent experiments were performed. Data are the mean ± s.e.m. (**C**) The expression levels of IRSp53, Myc-CDC42-L61, and vinculin were analysed by immunoblotting. There are four distinct splicing isoforms of IRSp53 (Scita *et al*, 2008), which differ only in the very C-terminal region, displaying either a WH2 domain or a PDZ binding motif. The isoform we introduced into IRSp53 KO MEFs was BAIAP2-S carrying a PDZ motif at its C-terminus. (**D**) IRSp53 controls the mode of cell spreading and increases the number of filopodia forming cells. MEFs KO-pB and KO-pB-IRSp53 were seeded on fibronectin-coated coverslips and fixed at 5 or 10 min after seeding. Cells were stained with FITC-phalloidin (green), anti-IRSp53 antibody (red) and Dapi (blue) to detect actin filaments, IRSp53 (pB-KO-IRSp53) and nuclei, respectively. The right panels represent magnifications of the indicated areas. Scale bar is 20 μm for the upper panels, 10 μm for the lower panels, and 5 μm for magnifications. (**E**) Upper panel: Quantification of spreading phenotypes. Normalized data ± s.e.m. of the number of cells displaying smooth-edged/ruffle (S-E/Ruffles) and filopodia spreading phenotypes in KO-pBABE and KO-pBABE-IRSp53 MEF cells, 5 and 10 min after seeding. At least 50 cells/experiment were analysed in three independent experiments. Lower panel: Quantification of adhering cells. The number of adhering cells/field ± s.e.m. in KO-pBABE and KO-pBABE-IRSp53 MEF cells, 5 and 10 min after seeding. At least 10 fields in each experiment were counted.

in the wound space and moved randomly rather than directionally (Supplementary Movie 9). Similar results were obtained in trans-well migration and invasion assays. IRSp53 removal also impaired chemotactic migration towards serum or PDGF (Figure 6B) and directed cell invasion in Matrigel-coated transwells (Figure 6C) as well as into native collagen type I chamber (Sabeh *et al*, 2009) (Supplementary Figure S6b; Supplementary Movie 10).

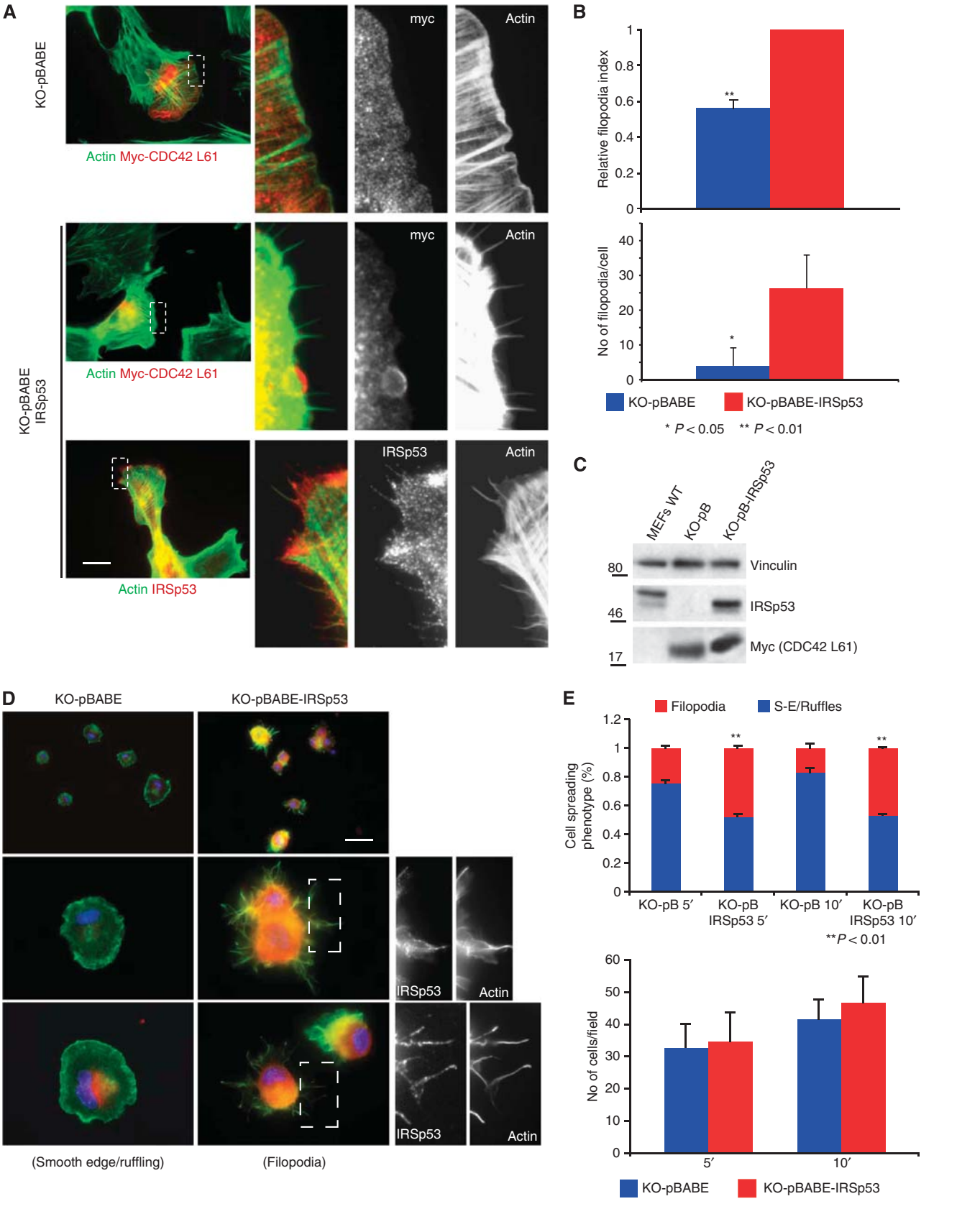

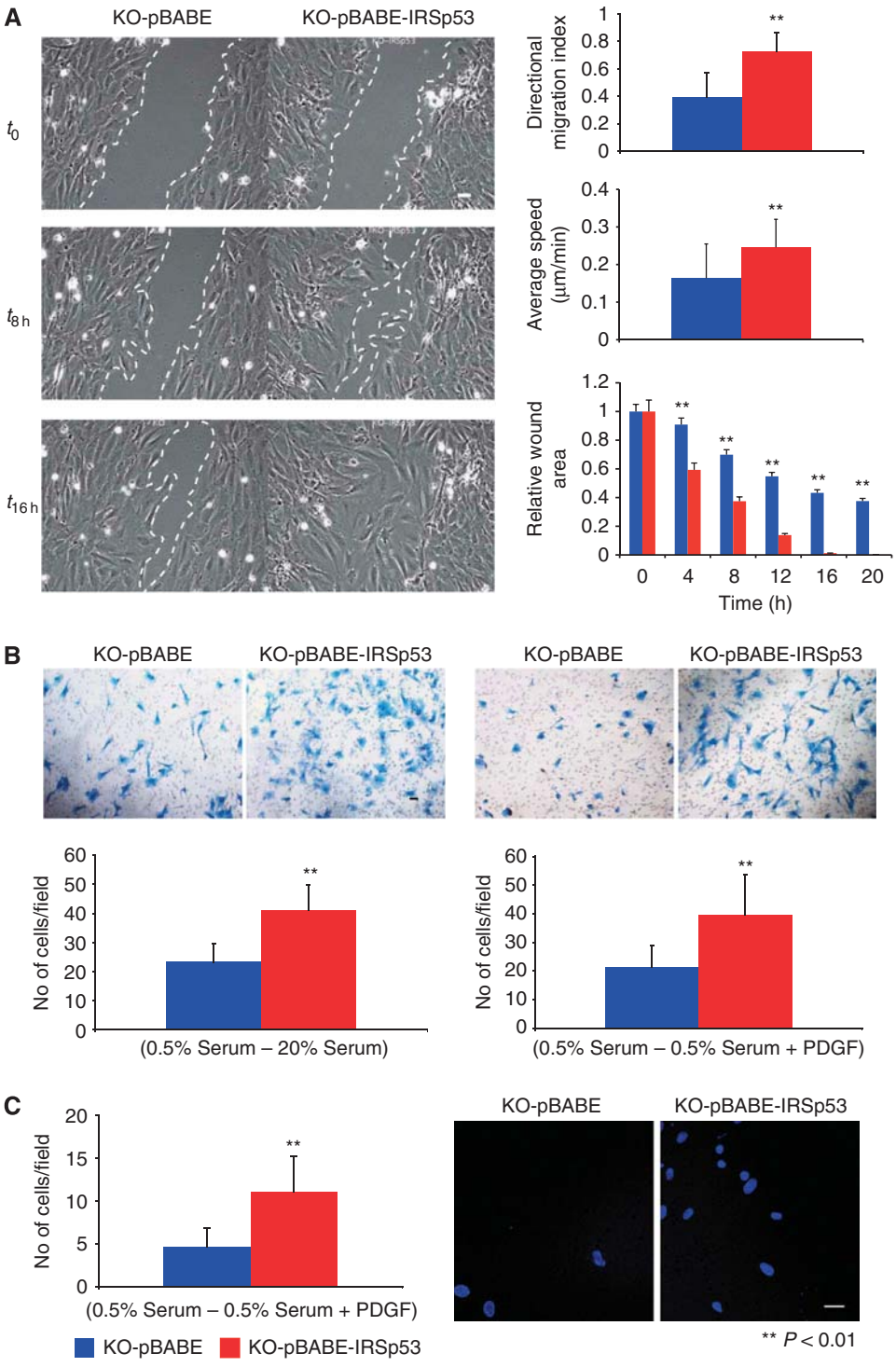

Figure 6 IRSp53 removal affects directional cell migration and invasion. (**A**) Wound healing assay. KO-pBABE and KO-pBABE-IRSp53 MEFs, seeded and grown to confluence, were scratched with a tip and analysed by DIC time-lapse imaging (20 h, 5 min time interval; see Supplementary Movie 9). Left panels: Still images taken at the indicated time points. Bar is 50 μm. White-dashed lines mark the front of migrating cells. Right panels: Single-cell migration was analysed using the ImageJ software. The directional migration index (upper panel) and the average speed (central panel) of cells were calculated. The directional migration index represents the ratio between the total distance covered by cells and the distance covered longitudinally towards the centre of the wound. At least 20 cells were analysed for each condition. Lower panel: Total wound area was measured at the indicated time points using the ImageJ software and relative wound closure was determined as described in Materials and methods. Data are the mean ± s.e.m. from $n = 5$ fields/experiment. Data are from three independent experiments. (**B**) Transwell assay. KO-pBABE and KO-pBABE-IRSp53 MEFs were seeded on fibronectin-coated chambers. Twenty percent serum (left panel) or 10 ng/ml PDGF (right panel) was added in the lower chamber to generate a chemo-attractive gradient. Cells were fixed after 6 h and stained with crystal violet. Bar is 50 μm. The number of cells passing the semi-permeable membrane was counted. At least 20 different fields were analysed for each condition. Data are the mean ± s.e.m. from three independent experiments. (**C**) Invasion assay. KO-pBABE and KO-pBABE-IRSp53 MEFs were seeded on Matrigel-coated chambers. PDGF was added in the lower chamber to generate a chemo-attractive gradient. Cells were fixed after 16 h and stained with Dapi to detect nuclei. Left panel: Quantification of the number of cells passing the semi-permeable membrane. At least 10 fields were analysed for each condition. Data are the mean ± s.e.m. from three independent experiments. Right panel: Representative images of invading cells. Bar is 10 μm.

To assess whether IRSp53 removal also resulted in an organismal migratory phenotype, we subjected 10-week-old IRSp53 KO and WT littermate mice to the dermal punch wound model of wound healing. During tissue repair keratinocytes, endothelial cells, macrophages, and mesenchymal cells, such as fibroblasts or myofibroblasts, migrate into the wound area (Gabbiani, 2003; Stappenbeck and Miyoshi, 2009). To assess epidermal wound healing, we

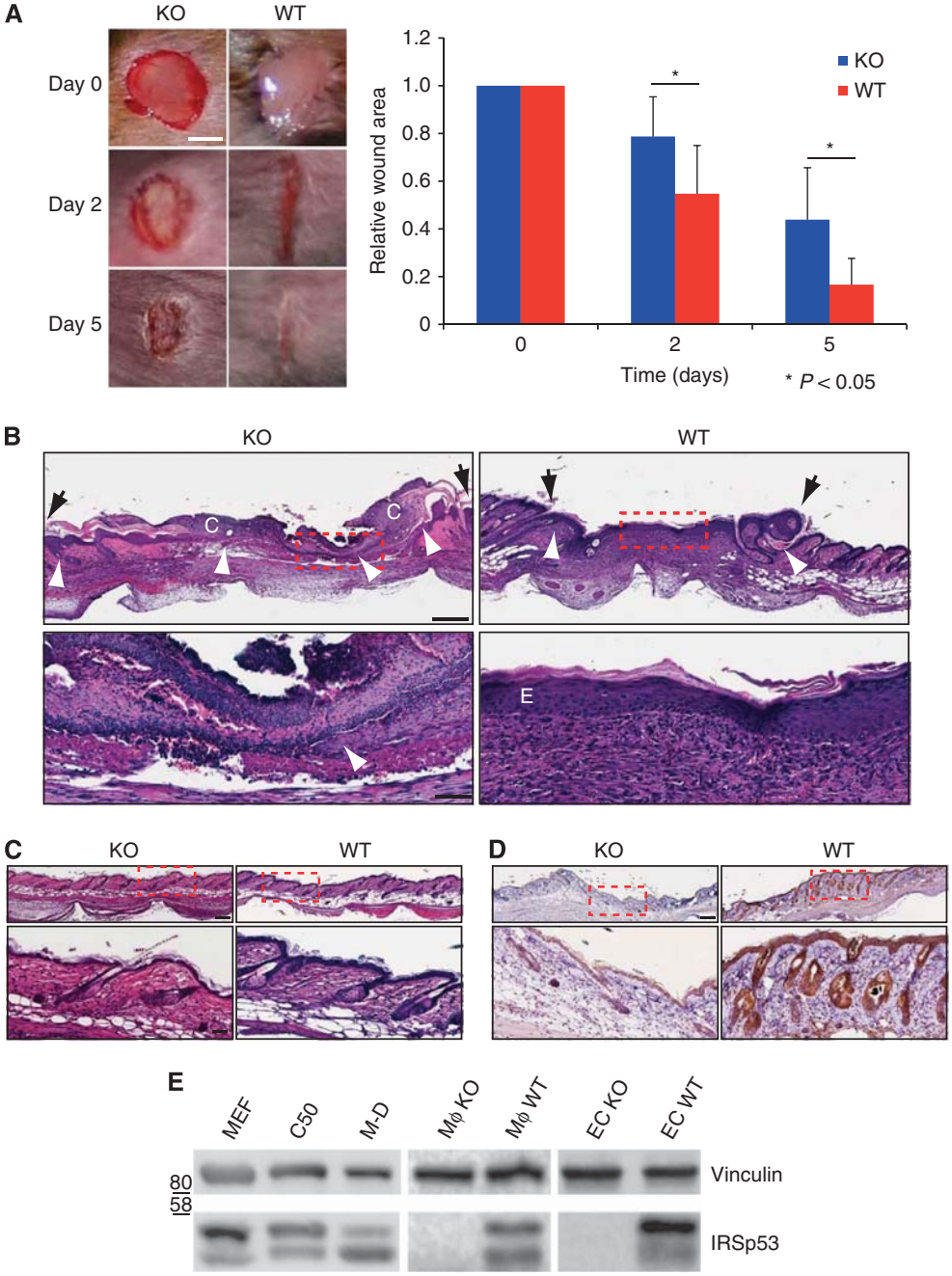

Figure 7 Genetic removal of IRSp53 in mice impairs wound repair. (**A**) Time course of wound closure. (*Left panels*) Microphotographs of wounds were captured on days 0, 1, 2, 4, 5, 6, and 7 after wounding to determine the degree of wound closure in IRSp53 KO and control WT mice. Representative images from days 0, 2, and 5 are shown. Right panel. Total wound area on days 0, 2, and 5 after wounding was measured using the ImageJ software and relative wound closure was quantified as described in Materials and methods. Data are the mean ± s.e.m. from $n = 6$ animals/group. Scale bar is 2 mm. (**B**) H&E analysis of back skin from IRSp53 KO and WT mice at day 7 after wounding. Black arrows denote the wound limits. White arrowheads denote the re-epithelialization regions. Lower panels represent × 5 magnifications of the insets (dashed red lines) in upper panels. C, clot; E, epithelium. Scale bar is 200 μm (higher magnifications, 40 μm). (**C**) H&E analysis of back skin from IRSp53 KO (*left*) and WT (*right*) mice. Lower panels represent × 5 magnifications of the insets (dashed red lines) in upper panels. Scale bar is 200 μm (lower panels, 40 μm). (**D**) IHC analysis of IRSp53 in back skin from IRSp53 KO (left) and WT (right) mice. Lower panels represent × 5 magnifications of the insets (dashed red lines) in upper panels. Scale bar is 200 μm (lower panels, 40 μm). (**E**) IRSp53 is expressed in mouse keratinocytes, dermal fibroblasts, macrophages, and endothelial cells. The expression levels of IRSp53 and vinculin were analysed by immunoblotting in MEFs and mouse keratinocyte (C50), dermal fibroblast (M Dunni, M-D) cell lines. Bone marrow macrophages (Mϕ) and lung endothelial cells (EC) derived from IRSp53 KO or WT mice were also analysed. Source data for this figure is available on the online supplementary information page.

punched four wounds on the back skin of 10-week-old IRSP53 KO and WT mice and monitored wound closure over a 7-day period. Microphotographs, morphometric quantification, and H&E analysis of wounds revealed that IRSp53 KO animals displayed a marked delay in wound closure relative to control animals (Figure 7A and B). Indeed, a thick clot was still present at 7 days after wounding and the wound limits were larger, while the re-epithelialization process was incomplete (Figure 7B). Notably, we detected no differences in the cellular composition and overall morphology between IRSP53 KO and WT mice, indicating that IRSp53 is dispensable for skin development, but required for wound re-epithelialization (Figure 7C). Importantly, IRSp53 is expressed in epidermal keratinocytes, macrophages, isolated dermal fibroblasts, and endothelial cells (Figure 7D and E). Removal of IRSp53 delayed wound closure by keratinocytes *in vitro* (data not shown). Furthermore, quantitative analysis of cells at wound sites revealed that while endothelial cells were recruited in similar numbers and generated blood vessels of similar size in IRSp53 KO and WT mice, macrophages were instead significantly reduced in IRSp53 KO mice (Supplementary Figure S7). This result is consistent with previous findings showing that IRSp53 removal impairs macrophage chemotactic cell motility (Abou-Kheir *et al*, 2008). Collectively, these data suggest that IRSp53 removal impairs the re-population of wound sites by epithelial keratinocytes, macrophages, and dermal fibroblasts, which are the major cells involved in wound healing *in vivo*.

Discussion

Our study identifies a signalling and molecular mechanism that controls, in a spatially confined manner, VASP actin regulatory activity during the initial phases of filopodia formation from lamellipodia sheets, in response to CDC42 activation. We show that the membrane deforming I-BAR-domain containing protein IRSp53 plays a critical role in this process and characterize the physiological relevance of IRSp53 regulation of filopodia in tissue repair and wound healing in mice. While CDC42 and VASP are established critical factors in filopodia formation, the signalling mechanisms regulating VASP activity and, in particular, its clustering-dependent processive elongation function, have remained elusive. Here, we show that the CDC42-IRSp53 axis is critical in mediating a switch from inhibition of actin barbed end growth (by IRSp53) to processive filament elongation following IRSp53-mediated clustering of VASP. Moreover, this signalling axis spatially restricts VASP activity along the leading edge of migrating cells, resulting in filopodia formation (Figure 8).

At the molecular level, IRSp53 exerts this function through a number of essential, biochemical, and signalling activities. First, via the I-BAR domain, IRSP53 can bind, sense, and promote PM deformation (Zhao *et al*, 2011). This property is entirely independent from forces generated by actin polymerization or protein:protein interactions (Zhao *et al*, 2011), suggesting that an initial step in the assembly of the machinery for filopodia formation is localized membrane evagination (Figure 8, step 1). These initial protrusions are subsequently, or concomitantly, stabilized and extended by actin filaments that elongate in a linear fashion (Figure 8, step 2). Importantly, in the absence of stimuli, IRSp53 slows down barbed end growth, thus safeguarding against unwanted growth of actin filaments that would occupy the free space of outwardly curved PM, leading to unrestrained, isotropic filopodia extensions. In this respect, it is well established that the expression of the isolated IRSp53 I-BAR domain, which is devoid of barbed end activity, elicits the formation of aberrant, isometrically distributed filopodia-like structures that are nearly devoid of F-actin (Yang *et al*, 2009). Intriguingly, the weak capping activity of IRSp53 may be reinforced by its association with EPS8 (Disanza *et al*, 2006), which caps barbed ends with nanomolar affinity (Disanza *et al*, 2004), suggesting that an EPS8:IRSp53 complex may be critical for proper control of filament growth at the leading edge. The inhibition of barbed end growth by IRSp53 is relieved by activated CDC42, which appears to compete

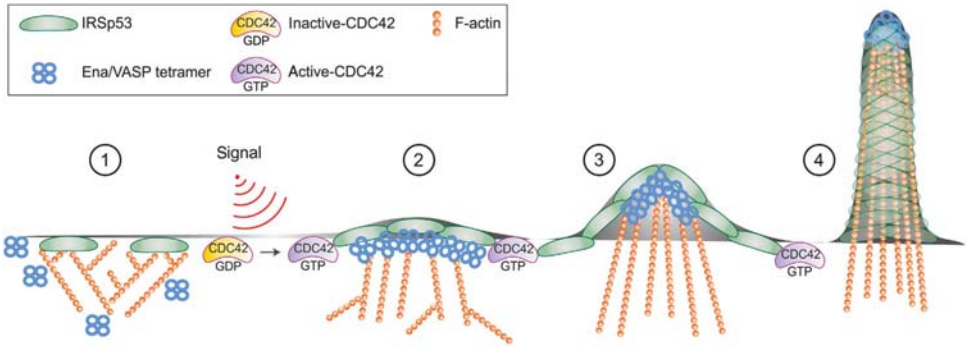

Figure 8 Model depicting how CDC42 switches IRSp53 from inhibition of actin assembly to filament elongation by clustering VASP during filopodia formation. A series of distinct signalling and biochemically defined steps characterize the initial phases of filopodia formation, mediated by the membrane deforming protein IRSp53 and its interactor VASP. Step 1: in the absence of stimuli, IRSp53 binds to the PM and slows down barbed end elongation. The constitutive association of IRSp53 with the capping protein EPS8 likely reinforces EPS8 capping activity (not shown) (Disanza *et al*, 2006; Vaggi *et al*, 2011). Step 2: following filopodia-inducing stimuli, activated CDC42 binds to IRSp53. This interaction relieves IRSp53-mediated inhibition of filament growth and promotes the formation of a CDC42:IRSp53:VASP complex, and simultaneously reduces the formation of the IRSP53:EPS8 complex. Step 3: binding to CDC42 further facilitates the formation of IRSp53 and VASP foci at the leading edge of the PM, in which VASP clustering allows processive actin filament elongation in the presence of capping protein. Step 4: membrane deforming activity of IRSp53 and processive filament elongation by VASP work in concert to extend actin filaments beyond the *x*, *y* plane of the membrane. During this process, the filaments become cross-linked by fascin (not shown), to resist counter membrane tension and extracellular compression forces.

with EPS8 for binding to IRSp53, as evidenced in co-immunoprecipitation experiments. This latter finding is remarkable from different points of view. At the biochemical level, it suggests that IRSp53 adopts different conformations controlled by CDC42 binding. In the absence of active CDC42, IRSp53 folds into a 'closed state' that negatively regulates actin polymerization. Binding of CDC42 induces a conformational switch that not only impedes barbed end association, but also promotes IRSp53 binding with some of its downstream targets (see below). Structural/biochemical evidence in this direction are provided by recent findings by Roberto Dominguez and colleagues (manuscript submitted elsewhere) that reveal how an SH3-CRIB-based intra-molecular interaction is critical in mediating the switch from a 'closed' to an 'open/active' state of IRSp53. One additional important feature of IRSp53 is that the conformational switch appears to be dependent on consecutive association with EPS8 and CDC42 that eventually assemble into an open heterohexamer. Under these conditions, the barbed capping activity of IRSp53 is prevented by CDC42, while SH3 interactors, such as VASP, may bind to IRSp53, compete out EPS8, and eventually switch the activity of the complex towards filament elongation. Notably, we have previously shown that IRSp53 may contribute to filopodia elongation by promoting the bundling activity of a CDC42–IRSp53–VASP complex through oligomerization (Vaggi *et al*, 2011). Thus, the formation of this complex may not only be required to promote processive filament elongation, an activity that is essential to initiate the growth of actin filaments and of filopodia, but also the bundling of filaments to sustain filopodia extension. This latter activity is thought to be primarily mediated by fascin (Vignjevic *et al*, 2006). Nevertheless, bundling particularly close to the barbed ends, where the IRSp53::VASP complex is restricted, may subsequently favour tighter cross-linking by fascin. This cross-linking may confer sufficient stiffness to filopodia that then allows them to resist counter PM tension and extracellular forces.

The regulation of IRSp53 barbed end capping activity by CDC42 is also important in the context of RHO family GTPase signalling, and more generally, in the regulation of filament barbed end growth since little is known about the mechanisms and signalling pathways that target this critical activity. Indeed, blockade of barbed end growth is viewed as a 'default process' that must immediately take place to avoid uncontrolled filament elongation that would otherwise occur on free barbed ends, given the high concentration of G-actin (or G-actin::profilin complex) in cells (Koestler *et al*, 2009). During filopodia initiation, instead, CDC42 actively and locally inhibits IRSp53 capping, further promoting a switch towards the formation of an active IRSP53::VASP complex driving filopodia formation.

Our data also shed light on how VASP activity is regulated in cells. First, we provide evidence that VASP, via IRSp53, is directly linked to CDC42, thus defining a CDC42–IRSp53–VASP signalling relay axis for actin assembly underlying filopodia formation. Second, we show that IRSp53 drives VASP clustering, which is essential for promoting sustained processive actin filament elongation of VASP at the PM in the presence of capping proteins (Breitsprecher *et al*, 2008, 2011). It has recently been shown, using single molecule TIRF analysis, that isolated VASP is also capable of promoting processive elongation in the presence of profilin (Hansen and Mullins, 2010). However, in solution, individual VASP tetramers are only weakly processive (Hansen and Mullins, 2010). Clustering of VASP into dense foci appears, therefore, to be necessary to enhance this activity for the extension of spatially restricted and timely coordinated filopodia. Consistently, we show that VASP is recruited to foci at the leading edge primarily via specific IRSp53-mediated protein: protein interactions. We cannot exclude that barbed end binding by VASP may also contribute to localization at the PM. However, VASP association to free barbed ends does not explain signalling-dependent VASP clustering as satisfactorily as IRSp53-mediated recruitment of VASP. In this latter respect, it is worth emphasizing that the binding of VASP to membrane-associated proteins, such as Mig-10/RIAM/Lamellipodin or CXCR2, has previously been reported (Krause *et al*, 2004; Neel *et al*, 2009). However, none of these proteins localized dynamically into discrete foci at filopodia initiation sites. Rather, they were distributed along the entire leading edge of lamellipodia, suggesting that they more likely contribute to the regulation of VASP activity in these migratory protrusions. Thus, it appears likely that distinct VASP-based protein complexes participate in the control of its multiple activities in different migratory structures, ultimately regulating the transition between lamellipodia-to-filopodia. It must be also pointed out that for this transition to be complete other activities, such as nucleation by formin family proteins (Peng *et al*, 2003; Pellegrin and Mellor, 2005; Schirenbeck *et al*, 2005) and bundling by fascin (Faix *et al*, 2009) are likely to be required to cooperate with the IRSp53::VASP filopodia initiation complex. Reconstituting the interplay between these factors will lead to a better understanding of how cells dynamically regulate the architecture of functional actin networks and their biological consequences.

Materials and methods

All animal experiments were conducted in accordance with national guidelines and were approved by the ethics committee of the Animal Welfare Office of the Italian Work Ministry and conformed to the legal mandates and Italian guidelines for the care and maintenance of laboratory animals.

Expression vectors, antibodies, reagents, and cells

Cytomegalovirus (CMV)-promoter-based and elongation factor-1 (EF1)-promoter-based eukaryotic expression vectors and GST bacterial expression vectors were generated by recombinant PCR. pEGFP–IRSp53 was from H Nakagawa (Austrian Academy of Sciences, Vienna, Austria), pmCherry-Fascin was from K Rottner (Institute of Genetics, University of Bonn, Germany) and JV Small (Institute of Molecular Biotechnology, Vienna, Austria), pmCherry-Eps8 (Addgene, One Kendall Sq, Cambridge, MA). All constructs were verified by sequencing.

The antibodies used were monoclonal anti-Eps8 (Transduction Laboratories, Lexington, KY); rabbit polyclonal anti-GST (Santa Cruz Biotechnology, Santa Cruz, CA); anti-Myc 9E10 (Babco, Berkeley, CA); anti-tubulin and rabbit polyclonal anti-IRSp53 (Sigma-Aldrich, St Louis, MO); rat monoclonal anti-F4/80 (AbD Serotec, Oxford, UK); rabbit polyclonal anti-CD31 (Abcam, Cambridge, UK). The monoclonal anti-IRSp53 was generated as described (Disanza *et al*, 2006). Immortalized fibroblasts from *IRSp53*+/+ and *IRSp53*−/− embryos were as described (Weiss *et al*, 2009). pBABE control, pBABE IRSp53 WT, and pBABE IRSp53 W413G re-expressing cells were obtained by infection of immortalized fibroblasts from *IRSp53*−/− embryos.

For additional detailed information on Materials and methods, see Supplementary data.

Actin polymerization assays

Actin polymerization was monitored by the increase in fluorescence of 10% pyrenyl-labelled actin. Seeded polymerization was induced by addition of 0.05 M KCl, 1 mM $MgCl_2$ and 0.2 mM EGTA to a solution of Ca-ATP–G-actin (1.25 μM) containing spectrin-actin seeds, 5 μM profilin, and various concentrations of purified proteins. Fluorescence measurements were performed at 20°C in a Safas Sfx or a Spex Fluorolog 2 spectrofluorimeter. Samples from seeded-polymerization assay were pelleted for 30 min at 400 000 *g* in a Beckman TL-100 tabletop ultracentrifuge. Equal amounts of starting materials, supernatants, and pellets were solubilized in loading buffer, boiled, and resolved on an SDS-PAGE gel. Each single assay was repeated at least five times with similar results. Representative experiments are shown.

Dilution-induced depolymerization of pyrenyl F-actin was monitored in a Spex Fluorolog 2 instrument. A 50% labelled F-actin solution (2.5 μM F-actin) was diluted 50-fold into polymerization buffer (5 mM Tris–HCl pH 7.8, 0.1 mM $CaCl_2$, 0.2 mM ATP, 1 mM DTT, 0.01% NaN_3, 50 mM KCl, 1 mM $MgCl_2$, and 0.5 mM EGTA) containing the desired amount of IRSp53 or VASP.

TIRF microscopy for monitoring of actin polymerization and elongation was performed with flow cells, essentially as described in Breitsprecher *et al* (2011) and Jegou *et al* (2011) (see Supplementary Experimental Procedures for details).

Statistical analysis

All data are presented as the mean ± standard errors of mean (s.e.m.), except when specified otherwise. A Student's *t*-test was used to calculate the *P*-values.

Supplementary data

Supplementary data are available at *The EMBO Journal* Online (http://www.embojournal.org).

Acknowledgements

We are indebted to Rosalind Gunby for critically editing the manuscript, to Frank B Gertler and Dorothy Schafer for providing VASP reagents, peptide arrays and critically reading the manuscript, and to Vic Small and Klemens Rottner for providing pmCherry-Fascin. Work in the authors' laboratory is supported by grants from the Associazione Italiana per la Ricerca sul Cancro (GS and AD), the European Research Council (Advanced-ERC-268836 to GS), the Italian Ministry of Education-University-Research (MIUR) (GS), the Association for International Cancer Research (GS), and the CARIPLO Foundation (GS and AD). MFC acknowledges grants from the ERC (Advanced-ERC-249982), from the EU (FP7 program MitoSys-# 241548, and from the Ligue Nationale contre le Cancer (équipe labellisée). CA is supported by fund G.0441.10N from the FWO-Vlaanderen. JF was supported by grants from the Deutsche Forschungsgemeinschaft (330/9-1 and 330/5-1). RD was supported by the National Institute of Health grant R01 MH087950. DK was supported by training grants T32 AR053461 from National Institute of Health and PF-13-033-01-DMC from the American Cancer Society.

Author contributions: AD, SB and M-FC wrote part of the manuscript, conceived and performed the experiments, and analysed the data. MW, FM, DSU, PM, H-MM, JL, DW, SC, and AP performed experiments and analysed the data. DJK and GR-L conceived and performed the experiments, and analysed the data. WN and CA conceived experiments and analysed the data. RD conceived and designed the experiments, and analysed the data. JF and GS wrote the manuscript, conceived and designed the experiments, and analysed the data.

Conflict of interest

The authors declare that they have no conflict of interest.

References

Abbott MA, Wells DG, Fallon JR (1999) The insulin receptor tyrosine kinase substrate p58/53 and the insulin receptor are components of CNS synapses. *J Neurosci* **19:** 7300–7308

Abou-Kheir W, Isaac B, Yamaguchi H, Cox D (2008) Membrane targeting of WAVE2 is not sufficient for WAVE2-dependent actin polymerization: a role for IRSp53 in mediating the interaction between Rac and WAVE2. *J Cell Sci* **121:** 379–390

Adams JC (2004) Roles of fascin in cell adhesion and motility. *Curr Opin Cell Biol* **16:** 590–596

Ahmed S, Goh WI, Bu W (2010) I-BAR domains, IRSp53 and filopodium formation. *Semin Cell Dev Biol* **21:** 350–356

Akin O, Mullins RD (2008) Capping protein increases the rate of actin-based motility by promoting filament nucleation by the Arp2/3 complex. *Cell* **133:** 841–851

Applewhite DA, Barzik M, Kojima SI, Svitkina TM, Gertler FB, Borisy GG (2007) Ena/VASP proteins have an anti-capping independent function in filopodia formation. *Mol Biol Cell* **18:** 2579–2591

Bachmann C, Fischer L, Walter U, Reinhard M (1999) The EVH2 domain of the vasodilator-stimulated phosphoprotein mediates tetramerization, F-actin binding, and actin bundle formation. *J Biol Chem* **274:** 23549–23557

Barzik M, Kotova TI, Higgs HN, Hazelwood L, Hanein D, Gertler FB, Schafer DA (2005) Ena/VASP proteins enhance actin polymerization in the presence of barbed end capping proteins. *J Biol Chem* **280:** 28653–28662

Bear JE, Svitkina TM, Krause M, Schafer DA, Loureiro JJ, Strasser GA, Maly IV, Chaga OY, Cooper JA, Borisy GG, Gertler FB (2002) Antagonism between Ena/VASP proteins and actin filament capping regulates fibroblast motility. *Cell* **109:** 509–521

Bockmann J, Kreutz MR, Gundelfinger ED, Bockers TM (2002) ProSAP/Shank postsynaptic density proteins interact with insulin receptor tyrosine kinase substrate IRSp53. *J Neurochem* **83:** 1013–1017

Breitsprecher D, Kiesewetter AK, Linkner J, Urbanke C, Resch GP, Small JV, Faix J (2008) Clustering of VASP actively drives processive, WH2 domain-mediated actin filament elongation. *EMBO J* **27:** 2943–2954

Breitsprecher D, Kiesewetter AK, Linkner J, Vinzenz M, Stradal TE, Small JV, Curth U, Dickinson RB, Faix J (2011) Molecular mechanism of Ena/VASP-mediated actin-filament elongation. *EMBO J* **30:** 456–467

Chan CE, Odde DJ (2008) Traction dynamics of filopodia on compliant substrates. *Science* **322:** 1687–1691

Disanza A, Carlier MF, Stradal TE, Didry D, Frittoli E, Confalonieri S, Croce A, Wehland J, Di Fiore PP, Scita G (2004) Eps8 controls actin-based motility by capping the barbed ends of actin filaments. *Nat Cell Biol* **6:** 1180–1188

Disanza A, Mantoani S, Hertzog M, Gerboth S, Frittoli E, Steffen A, Berhoerster K, Kreienkamp HJ, Milanesi F, Di Fiore PP, Ciliberto A, Stradal TE, Scita G (2006) Regulation of cell shape by Cdc42 is mediated by the synergic actin-bundling activity of the Eps8-IRSp53 complex. *Nat Cell Biol* **8:** 1337–1347

Faix J, Breitsprecher D, Stradal TE, Rottner K (2009) Filopodia: Complex models for simple rods. *Int J Biochem Cell Biol* **41:** 1656–1664

Ferron F, Rebowski G, Lee SH, Dominguez R (2007) Structural basis for the recruitment of profilin-actin complexes during filament elongation by Ena/VASP. *EMBO J* **26:** 4597–4606

Gabbiani G (2003) The myofibroblast in wound healing and fibrocontractive diseases. *J Pathol* **200:** 500–503

Gates J, Mahaffey JP, Rogers SL, Emerson M, Rogers EM, Sottile SL, Van Vactor D, Gertler FB, Peifer M (2007) Enabled plays key roles in embryonic epithelial morphogenesis in *Drosophila*. *Development* **134:** 2027–2039

Gertler FB, Comer AR, Juang JL, Ahern SM, Clark MJ, Liebl EC, Hoffmann FM (1995) Enabled, a dosage-sensitive suppressor of mutations in the *Drosophila* Abl tyrosine kinase, encodes an Abl substrate with SH3 domain-binding properties. *Genes Dev* **9:** 521–533

Gertler FB, Niebuhr K, Reinhard M, Wehland J, Soriano P (1996) Mena, a relative of VASP and *Drosophila* Enabled, is implicated in the control of microfilament dynamics. *Cell* **87:** 227–239

Goh WI, Lim KB, Sudhaharan T, Sem KP, Bu W, Chou AM, Ahmed S (2012) mDia1 and WAVE2 proteins interact directly with IRSp53

in filopodia and are involved in filopodium formation. *J Biol Chem* **287:** 4702–4714

Govind S, Kozma R, Monfries C, Lim L, Ahmed S (2001) Cdc42Hs facilitates cytoskeletal reorganization and neurite outgrowth by localizing the 58-kD insulin receptor substrate to filamentous actin. *J Cell Biol* **152:** 579–594

Hansen SD, Mullins RD (2010) VASP is a processive actin polymerase that requires monomeric actin for barbed end association. *J Cell Biol* **191:** 571–584

Huttelmaier S, Harbeck B, Steffens O, Messerschmidt T, Illenberger S, Jockusch BM (1999) Characterization of the actin binding properties of the vasodilator-stimulated phosphoprotein VASP. *FEBS Lett* **451:** 68–74

Jegou A, Niedermayer T, Orban J, Didry D, Lipowsky R, Carlier MF, Romet-Lemonne G (2011) Individual actin filaments in a microfluidic flow reveal the mechanism of ATP hydrolysis and give insight into the properties of profilin. *PLoS Biol* **9:** e1001161

Koestler SA, Rottner K, Lai F, Block J, Vinzenz M, Small JV (2009) F- and G-actin concentrations in lamellipodia of moving cells. *PLoS One* **4:** e4810

Kozma R, Ahmed S, Best A, Lim L (1995) The Ras-related protein Cdc42Hs and bradykinin promote formation of peripheral actin microspikes and filopodia in Swiss 3T3 fibroblasts. *Mol Cell Biol* **15:** 1942–1952

Krause M, Leslie JD, Stewart M, Lafuente EM, Valderrama F, Jagannathan R, Strasser GA, Rubinson DA, Liu H, Way M, Yaffe MB, Boussiotis VA, Gertler FB (2004) Lamellipodin, an Ena/VASP ligand, is implicated in the regulation of lamellipodial dynamics. *Dev Cell* **7:** 571–583

Krugmann S, Jordens I, Gevaert K, Driessens M, Vandekerckhove J, Hall A (2001) Cdc42 induces filopodia by promoting the formation of an IRSp53:Mena complex. *Curr Biol* **11:** 1645–1655

Kwiatkowski AV, Rubinson DA, Dent EW, Edward van Veen J, Leslie JD, Zhang J, Mebane LM, Philippar U, Pinheiro EM, Burds AA, Bronson RT, Mori S, Fassler R, Gertler FB (2007) Ena/VASP is required for neuritogenesis in the developing cortex. *Neuron* **56:** 441–455

Lanier LM, Gates MA, Witke W, Menzies AS, Wehman AM, Macklis JD, Kwiatkowski D, Soriano P, Gertler FB (1999) Mena is required for neurulation and commissure formation. *Neuron* **22:** 313–325

Lim KB, Bu W, Goh WI, Koh E, Ong SH, Pawson T, Sudhaharan T, Ahmed S (2008) The Cdc42 effector IRSp53 generates filopodia by coupling membrane protrusion with actin dynamics. *J Biol Chem* **283:** 20454–20472

Mejillano MR, Kojima S, Applewhite DA, Gertler FB, Svitkina TM, Borisy GG (2004) Lamellipodial versus filopodial mode of the actin nanomachinery: pivotal role of the filament barbed end. *Cell* **118:** 363–373

Menna E, Disanza A, Cagnoli C, Schenk U, Gelsomino G, Frittoli E, Hertzog M, Offenhauser N, Sawallisch C, Kreienkamp HJ, Gertler FB, Di Fiore PP, Scita G, Matteoli M (2009) Eps8 regulates axonal filopodia in hippocampal neurons in response to brain-derived neurotrophic factor (BDNF). *PLoS Biol* **7:** e1000138

Miki H, Yamaguchi H, Suetsugu S, Takenawa T (2000) IRSp53 is an essential intermediate between Rac and WAVE in the regulation of membrane ruffling. *Nature* **408:** 732–735

Millard TH, Bompard G, Heung MY, Dafforn TR, Scott DJ, Machesky LM, Futterer K (2005) Structural basis of filopodia formation induced by the IRSp53/MIM homology domain of human IRSp53. *EMBO J* **24:** 240–250

Neel NF, Barzik M, Raman D, Sobolik-Delmaire T, Sai J, Ham AJ, Mernaugh RL, Gertler FB, Richmond A (2009) VASP is a CXCR2-interacting protein that regulates CXCR2-mediated polarization and chemotaxis. *J Cell Sci* **122:** 1882–1894

Oda K, Shiratsuchi T, Nishimori H, Inazawa J, Yoshikawa H, Taketani Y, Nakamura Y, Tokino T (1999) Identification of BAIAP2 (BAI-associated protein 2), a novel human homologue of hamster IRSp53, whose SH3 domain interacts with the cytoplasmic domain of BAI1. *Cytogenet Cell Genet* **84:** 75–82

Okamura-Oho Y, Miyashita T, Ohmi K, Yamada M (1999) Dentatorubral-pallidoluysian atrophy protein interacts through a proline-rich region near polyglutamine with the SH3 domain of an insulin receptor tyrosine kinase substrate. *Hum Mol Genet* **8:** 947–957

Pasic L, Kotova T, Schafer DA (2008) Ena/VASP proteins capture actin filament barbed ends. *J Biol Chem* **283:** 9814–9819

Pellegrin S, Mellor H (2005) The Rho family GTPase Rif induces filopodia through mDia2. *Curr Biol* **15:** 129–133

Peng J, Wallar BJ, Flanders A, Swiatek PJ, Alberts AS (2003) Disruption of the Diaphanous-related formin Drf1 gene encoding mDia1 reveals a role for Drf3 as an effector for Cdc42. *Curr Biol* **13:** 534–545

Reinhard M, Jouvenal K, Tripier D, Walter U (1995) Identification, purification, and characterization of a zyxin-related protein that binds the focal adhesion and microfilament protein VASP (vasodilator-stimulated phosphoprotein). *Proc Natl Acad Sci USA* **92:** 7956–7960

Rottner K, Behrendt B, Small JV, Wehland J (1999) VASP dynamics during lamellipodia protrusion. *Nat Cell Biol* **1:** 321–322

Sabeh F, Shimizu-Hirota R, Weiss SJ (2009) Protease-dependent versus -independent cancer cell invasion programs: three-dimensional amoeboid movement revisited. *J Cell Biol* **185:** 11–19

Samarin S, Romero S, Kocks C, Didry D, Pantaloni D, Carlier MF (2003) How VASP enhances actin-based motility. *J Cell Biol* **163:** 131–142

Sawallisch C, Berhorster K, Disanza A, Mantoani S, Kintscher M, Stoenica L, Dityatev A, Sieber S, Kindler S, Morellini F, Schweizer M, Boeckers TM, Korte M, Scita G, Kreienkamp HJ (2009) The insulin receptor substrate of 53 kDa (IRSp53) limits hippocampal synaptic plasticity. *J Biol Chem* **284:** 9225–9236

Schirenbeck A, Arasada R, Bretschneider T, Schleicher M, Faix J (2005) Formins and VASPs may co-operate in the formation of filopodia. *Biochem Soc Trans* **33:** 1256–1259

Schirenbeck A, Arasada R, Bretschneider T, Stradal TE, Schleicher M, Faix J (2006) The bundling activity of vasodilator-stimulated phosphoprotein is required for filopodium formation. *Proc Natl Acad Sci USA* **103:** 7694–7699

Scita G, Confalonieri S, Lappalainen P, Suetsugu S (2008) IRSp53: crossing the road of membrane and actin dynamics in the formation of membrane protrusions. *Trends Cell Biol* **18:** 52–60

Stappenbeck TS, Miyoshi H (2009) The role of stromal stem cells in tissue regeneration and wound repair. *Science* **324:** 1666–1669

Svitkina TM, Borisy GG (1999) Arp2/3 complex and actin depolymerizing factor/cofilin in dendritic organization and treadmilling of actin filament array in lamellipodia. *J Cell Biol* **145:** 1009–1026

Svitkina TM, Bulanova EA, Chaga OY, Vignjevic DM, Kojima S, Vasiliev JM, Borisy GG (2003) Mechanism of filopodia initiation by reorganization of a dendritic network. *J Cell Biol* **160:** 409–421

Temmerman K, Nickel W (2009) A novel flow cytometric assay to quantify interactions between proteins and membrane lipids. *J Lipid Res* **50:** 1245–1254

Vaggi F, Disanza A, Milanesi F, Di Fiore PP, Menna E, Matteoli M, Gov NS, Scita G, Ciliberto A (2011) The Eps8/IRSp53/VASP network differentially controls actin capping and bundling in filopodia formation. *PLoS Comput Biol* **7:** e1002088

Vignjevic D, Kojima S, Aratyn Y, Danciu O, Svitkina T, Borisy GG (2006) Role of fascin in filopodial protrusion. *J Cell Biol* **174:** 863–875

Vignjevic D, Montagnac G (2008) Reorganisation of the dendritic actin network during cancer cell migration and invasion. *Semin Cancer Biol* **18:** 12–22

Weiss SM, Ladwein M, Schmidt D, Ehinger J, Lommel S, Stading K, Beutling U, Disanza A, Frank R, Jansch L, Scita G, Gunzer F, Rottner K, Stradal TE (2009) IRSp53 links the enterohemorrhagic E. coli effectors Tir and EspFU for actin pedestal formation. *Cell Host Microbe* **5:** 244–258

Wiesner S, Helfer E, Didry D, Ducouret G, Lafuma F, Carlier MF, Pantaloni D (2003) A biomimetic motility assay provides insight into the mechanism of actin-based motility. *J Cell Biol* **160:** 387–398

Wu C, Asokan SB, Berginski ME, Haynes EM, Sharpless NE, Griffith JD, Gomez SM, Bear JE (2012) Arp2/3 is critical for lamellipodia and response to extracellular matrix cues but is dispensable for chemotaxis. *Cell* **148:** 973–987

Yamagishi A, Masuda M, Ohki T, Onishi H, Mochizuki N (2004) A novel actin bundling/filopodium-forming domain conserved in

insulin receptor tyrosine kinase substrate p53 and missing in metastasis protein. *J Biol Chem* **279:** 14929–14936

Yang C, Czech L, Gerboth S, Kojima S, Scita G, Svitkina T (2007) Novel roles of formin mDia2 in lamellipodia and filopodia formation in motile cells. *PLoS Biol* **5:** e317

Yang C, Hoelzle M, Disanza A, Scita G, Svitkina T (2009) Coordination of membrane and actin cytoskeleton dynamics during filopodia protrusion. *PLoS ONE* **4:** e5678

Yang C, Svitkina T (2011a) Filopodia initiation: focus on the Arp2/3 complex and formins. *Cell Adh Migr* **5:** 402–408

Yang C, Svitkina T (2011b) Visualizing branched actin filaments in lamellipodia by electron tomography. *Nat Cell Biol* **13:** 1012–1013

Zhao H, Pykalainen A, Lappalainen P (2011) I-BAR domain proteins: linking actin and plasma membrane dynamics. *Curr Opin Cell Biol* **23:** 14–21

